Three-dimensional characterisation of clay-related porosity in geological reservoir systems by high-resolution imaging

Inauguraldissertation

zur

Erlangung des akademischen Grades

Dr. rer. nat. (Doctor rerum naturalium)

der

Mathematisch-Naturwissenschaftlichen Fakultät

der

Universität Greifswald

vorgelegt von
Markus Peltz

Greifswald, im März 2023

Dekan*in:	Prof. Dr. Gerald Kerth
1. Gutachter*in:	Prof. Dr. Laurence N. Warr
2. Gutachter*in:	Prof. Dr. Christoph Butscher
Tag der Promotion:	21.07.2023

Abstract

The deep geological underground represents an important georesource for the short-term storage of renewable energy and the long-term reduction of greenhouse gas emissions. To ensure the economic viability and safety of any subsurface storage project, detailed characterisation of the quality and integrity of the reservoir and its cap rock is required. This characterisation includes the accurate determination of the petrophysical properties, such as porosity and permeability, as well as the potential mineral reactions, such as the dissolution of reactive phases, which may occur during the lifespan of such a project. Clay minerals are common components of many reservoir systems and, depending on their type and structure, can have a significant impact on storage and transport properties. These processes are, however, currently not well understood. In order to address these issues, the main focus of this thesis is on mineralogical analyses using X-ray diffraction (XRD) and microstructural studies using focused ion beam scanning electron microscopy (FIB-SEM) together with micro X-ray computed tomography (μXCT) to gain a better understanding of the influence of clay minerals on reservoir and cap rock properties.

A central part of this thesis focuses on the analysis of clay minerals and pore structures of the Bebertal Sandstone of the Parchim Formation (Early Permian, Upper Rotliegend), which is considered a natural analogue for the tight reservoir sandstones of the North German Basin. Two illite polytypes with a variety of characteristic structures have been identified in the Bebertal sandstone. Disordered $1M_d$ illite forms the majority of the observed structures, which include omnipresent grain coatings, altered permeable feldspar grains and pore-filling meshwork structures. *Trans*-vacant $1M$ illite represents the second and youngest generation of authigenic illite and occurs as fibrous to lath-shaped particles that grew into open pore spaces and led to a significant reduction in porosity and permeability during late diagenesis. Based on these results, a model for the formation of illite polytypes in the aeolian layers of the Bebertal sandstone was developed that describes the temporal and spatial evolution of porosity and permeability during diagenesis. Information from this model was then used to improve the prediction of permeability of the Bebertal sandstone based on μXCT pore space models and direct numerical simulations. To achieve this, a micro-scale pore space model was created that allowed the simulation of permeability reduction by clay minerals by including nanoporous illite domains based on a novel morphological algorithm. By performing Navier-Stokes-Brinkman simulations, more accurate predictions of permeabilities with respect to experimentally determined values were obtained compared to conventional Navier-Stokes simulations.

The detailed characterisation of the Bebertal sandstone has shown that natural reservoir rocks are usually complex heterogeneous systems with small-scale variations in texture, composition, porosity and permeability. Flow-through experiments on the Bebertal sandstone revealed that the coupled geochemical and hydrodynamic processes that occur during the dissolution of calcite could not be predicted by reactive transport models. Therefore, as part of this thesis, a novel approach for developing synthetic sandstones at low temperatures based on geopolymer binder was developed. It is shown that simpler and more homogeneous porous materials can be produced with porosity and permeability values in the range of natural sandstones. These can be used to better understand the dynamic and coupled processes relevant to the storage of renewable energy in reservoir rocks through improved experimental constraints.

The final part of this thesis reports on a detailed clay mineral and pore space study of three shale formations and one mudstone that were identified as potential seals for the Mt.

Simon sandstone reservoir in the Illinois Basin. During the Illinois Basin - Decatur Project, this reservoir was used for the sequestration of one megaton of supercritical carbon dioxide. In order to better assess the quality of the sealing units and to better understand the role of the intergranular clay mineral matrix as potential pathway for fluid migration, a multi-scale evaluation was conducted that included thin section analysis, quantitative evaluation of minerals by scanning electron microscopy (QEMSCAN), mercury intrusion capillary pressure (MICP) measurements, quantitative XRD and high-resolution FIB-SEM. The results allow for the classification of the studied formations into primary and secondary seals and emphasise the importance of three-dimensional clay-mineral-related pore structure characterisations in cap rock studies. XRD proved the most reliable method for the identification and quantification of clay minerals in the studied cap rocks and mudstones. In contrast, FIB-SEM and QEMSCAN provided the spacial constraints for reconstructing fluid flow pathways within the clay mineral matrix.

Overall, this thesis highlights the importance of the precise identification of clay minerals in geological reservoirs and their cap rocks. It also illustrates the need for three-dimensional characterisation and modelling of the associated small pore structures for an improved understanding of the rocks diagenetic history as well as the prediction of the transport and storage properties of these crustal reservoir systems.

Zusammenfassung

Im Rahmen der Abkehr von fossilen Brennstoffen wird die Verwendung des tiefen geologischen Untergrundes zur Reduzierung von Treibhausgasemissionen und zur Speicherung erneuerbarer Energien eine wichtige Rolle spielen. Um eine sichere und ökonomische Nutzung von porösen Untergrundspeichern zu gewährleisten, sind präsize Charakterisierungen der Qualität von Reservoiren und Abdeckschichten erforderlich. Von besonderem Interesse sind hierbei sowohl die Bestimmung der petrophysikalischen Eigenschaften, wie Porosität und Permeabilität, als auch die Prognose reaktiver Prozesse, wie Lösungsreaktionen, welche infolge der Wechselwirkungen zwischen Reservoirgestein und Formationsfluid auftreten können. Tonminerale sind häufiger Bestandteil vieler Reservoirsysteme und können je nach Art und Struktur erheblichen Einfluss auf die Speicher- und Transporteigenschaften haben. Die genauen Auswirkungen sind jedoch unzureichend untersucht. Schwerpunkte dieser Arbeit bilden daher mineralogische Untersuchungen mittels Röntgendiffraktometrie (XRD) und strukturelle Analysen mittels Rasterlelektronenmikroskopie mit fokussierten Ionenstrahlpolituren (FIB-SEM) und Mikro-Computertomographie (μXCT), um ein besseres Verständniss des Einlusses von Tonmineralen auf die Eigenschaften von Reservoiren und Abdeckschichten zu erhalten.

Den zentralen Teil dieser Arbeit bilden die Untersuchungen der Tonmineralogie und der Porenstrukturen des Bebertal Sandsteines der Parchim Formation (Oberrotliegend, Perm), welcher als Analoggestein für geringdurchlässige Reservoirsandsteine des Norddeutschen Beckens gilt. Es konnte gezeigt werden, dass zwei Illit-Polytype mit charakteristischen räumlichen Strukturen im Bebertal Sandstein auftreten. Ungeordnete $1M_d$ Illite bilden den Großteil der beobachteten Strukturen, zu denen neben häufig auftretenden Kornüberzügen auch permeable, alterierte Feldspäte und porenraumfüllende Illit-Gitterstrukturen gehören. *Trans*-vakante $1M$ Illite stellen die zweite und jüngste Gruppe authigener Tonminerale dar und sind durch faserige bis lattige Kristalle gekennzeichnet, welche in den Porenraum hineinwachsen und eine starke Reduktion der Porosität und Permeabilität bewirken. Auf Grundlage der gewonnenen Ergebnisse wurde in Kombination mit direkten numerischen Modellierungen ein Modell zur Genese der Tonminerale der äolischen Schichten des Bebertal-Sandsteins entwickelt, das die zeitliche und räumliche Entwicklung von Porosität und Permeabilität infolge des Tonmineralwachstums während der Diagenese beschreibt. Informationen dieses Modells wurden genutzt, um eine Verbesserung der Vorhersagbarkeit der Gesamtpermeabilität des Bebertal Sandsteins auf Grundlage direkter numerischer Simulationen an μXCT Topologien zu ermöglichen. So konnte ein mikroskaliges Porenraummodell entwickelt werden, das die Permeabilitäten nanoskaliger Tonmineralstrukturen auf Basis eines neu entwickelten morphologischen Algorithmus berücksichtigt. Im Gegensatz zur konventionellen Navier-Stokes-Modellierungen konnten mit Navier-Stokes-Brinkmann-Simulationen genauere Vorhersagen der Permeabilitäten erzielt werden, deren Übereinstimmungen mit experimentell ermittelten Werten signifikant höher waren.

Im Rahmen der Arbeiten am Bebertal Sandstein wurde deutlich, dass dieser infolge der Diagenese ein komplexes System mit kleinskaligen Heterogenitäten in Textur, Zusammensetzung, Porosität und Permeabilität darstellt. Diese führen nach Experimenten häufig zu Diskrepanzen zwischen Beobachtungen und Modellierungen, da sich die gekoppelten geochemischen und hydrodynamischen Prozesse, welche zum Beispiel infolge von Lösungsreaktionen von Kalzitzementen auftreten, nicht über reaktive Transportmodelle abbilden lassen. Aus diesem Grund wurde als Teil dieser Arbeit eine neuartige Methode entwickelt,

welche Geopolymer-Bindemittel zur Herstellung synthetischer Sandsteine nutzt, um temperatursensitive Materialien in Experimenten besser untersuchen zu können. Die so angefertigten Analogmaterialien zeigten neben Porositäts- und Permeabilitätswerte im Bereiche natürlicher Sandsteine, eine deutlich homogenere Struktur bei definierter mineralogischer Zusammensetzung.

Im abschließenden Teil dieser Arbeit wurden detaillierte Porenraumanalysen an den Abdeckschichten und Barrieregesteinen des Mt. Simon Sandsteinreservoirs aus dem Illinois Becken durchgeführt. Im Rahmen des Illinois Basin - Decatur Projekts, welches eines der ersten großangelegten Testprojekte zur Untergrundspeicherung von Kohlendioxid war, wurden drei das Reservoir überlagernde Tonschieferformationen und eine Tonsteinformation innerhalb des Reservoirs als potentielle Barrieren und Puffer des Mt. Simon Reservoirs identifiziert. Ziel dieser Untersuchungen war es, mittels Dünnschliffanalysen, Quecksilberporosimetrie, quantitative Mineralbestimmung mittels Rasterlelektronenmikroskopie (QEMSCAN), XRD und FIB-SEM, ein besseres Verständnis der Tonmineralmatrix der Barrieregesteine zu erhalten, welche als potentielle Fluidmigrationspfade gelten. Die Ergebnisse ermöglichten eine Einstufung der untersuchten Formationen in primäre und sekundäre Barrieren und lieferten wichtige Implikationen und Einschränkungen für die Nutzung der angewandten Methoden bei der Studie von Abdeckschichten. So konnte unter anderem gezeigt werden, dass XRD die einzige angewandte Methode war, welche die quantitative und qualitative tonmineralogischen Zusammensetzung von Tonschiefern und Tonsteinen zuverlässig klären konnte. Weiterhin wurde deutlich, dass FIB-SEM und QEMSCAN komplementäre Methode darstellen, welche wichtige Informationen zu Wegsamkeiten innerhalb der Tonmineralmatrix liefern können.

Im Rahmen dieser Arbeit konnte gezeigt werden, dass die genaue Untersuchung der tonmineralogischen Zusammensetzung von Reservoirgesteinen und Abdeckschichten, eine wichtige Grundlage zur Bewertung der Qualität dieser Gesteine darstellt. Weiterhin wurde demonstriert, dass sich mit Hilfe von gezielten FIB-SEM-Untersuchungen an Tonmineralen im Gesteinsverbund, wichtige Informationen zu Transport- und Speichereigenschaften von Gesteinen des Rervoirsystems gewinnen lassen. Die Nutzung dieser Daten ermöglicht sowohl das Ziehen von Rückschlüsse auf diagenetische Prozesse, als auch eine bessere Prognose von petrophysikalischen Parametern über Porenraummodellierungen.

Contents

List of symbols and abbreviations

List of symbols

K	Permeability
ϕ	Porosity

Abbreviations

μXCT	Micro X-ray computed tomography
2D	Two-dimensional
3D	Three-dimensional
BIB	Broad ion beam
CAES	Compressed air energy storage
CCS	Carbon capture and storage
CFD	Computational fluid dynamics
CH_4	Methane
CO_2	Carbon dioxide
DNS	Direct numerical simulations
DRP	Digital Rock Physics
EDX	Energy-dispersive X-Ray spectroscopy
EsB	Energy-selective backscattered (detector)
FESEM	Field-emission scanning electron microscopy
FIB	Focussed ion beam
FIB-SEM	Focussed ion beam - scanning electron microscopy
H_2	Hydrogen
IBDP	Illinois Basin - Decatur Project
ICCS	Illinois Industrial Carbon Capture and Storage
interP	Interparticle (Pore)
intraP	Intraparticle (Pore)
MICP	Mercury injection capillary pressure
MIP	Mercury intrusion porosimetry
NGB	North German Basin
QEMSCAN	Quantitative evaluation of minerals by scanning electron microscopy
REA	Representative elementary area
REV	Representative elementary volume
SEM	Scanning electron microscopy
XRD	X-ray diffraction

1 Introduction

1.1 Background

The deep geological underground will play an important role in the transition to renewable energies and the reduction of greenhouse gas emissions. To lower global carbon dioxide (CO_2) emissions, the burning of fossil fuels must be reduced and the share of renewable energy sources has increased [1]. Between 2000 and 2021 the power generated from renewable sources increased from about 250 to 3657 TWh per year with an annual increase in 2021 of 15% [2]. As the production of renewable energies relies on wind and solar conditions, daily to seasonal fluctuations need to be buffered. Thus, energy storage and CO_2 sequestration become key aspects in achieving the European Union's energy and climate target of becoming climate neutral by 2050 [3].

Geological formations, such as depleted oil fields or deep saline aquifers, may be used for the sequestration of CO_2 in carbon capture and storage (CCS) projects, for the storage of gases synthesised from renewable energies and for heat. Currently, salt caverns are utilised in compressed air energy storage (CAES) projects and to store hydrogen (H_2) gas and methane (CH_4), but the limited occurrence of salt formations does not meet the local energy demands. Porous formations may provide the needed capacity for the sequestration of CO_2 and for the long-term storage of hydrogen or methane due to their wider distribution. For example, Gasanzade et al. [4] quantified the storage potential for the North German Basin (NGB) and found that the potential capacity exceeds the predicted local demand by far. However, regional stratigraphic differences require detailed characterisations of reservoirs and cap rocks at each individual site.

The quality of reservoirs is mainly determined by their porosity and permeability, as these properties control the storage capacity and the potential to release or absorb fluids [5]. In contrast, the quality of the cap rock is predominantly controlled by its lateral and vertical continuity, its sealing capacity and the seals integrity. Sealing capacity is defined as the column height of injected fluid that a cap rock can retain before leakage occurs by exceeding the rocks capillary entry pressure [6]. Column heights can be determined from mercury injection capillary pressure (MICP) measurements and are controlled by the geometry of the pore system and the properties of the fluids [7]. Seal integrity includes all factors that must be considered to maintain the petrophysical and mechanical properties of a rock under varying hydraulic and chemical conditions. A reliable evaluation of the seal integrity requires knowledge of key rock properties, such as permeability (K), porosity (ϕ) and mineralogical compo-

sition, and the processes that might affect them over geologic time. As the injection of gases is expected to shift the geochemical and geomechanical equilibrium within the reservoir [8], potential mineral reactions need to be considered. Thus, assessing the quality of reservoirs and cap rocks and studying the coupled processes of fluid-rock interactions and their impact on petrophysical properties of these systems is an important part of ensuring the economic viability and safety of any reservoir-based project.

1.2 Illite in sedimentary rocks

The properties of reservoirs and cap rocks are strongly controlled by sedimentary and diagenetic parameters, such as the environment and prevailing climatic conditions during deposition, the degree of chemical and mechanical compaction, fault zones, burial depth as well as temperature and pore fluid chemistry. The types and amounts of detrital and authigenic clay minerals present in the rock are key factors that are also important to consider [9, 10]. While the occurrence of early diagenetic chlorite rims in sandstones is known to preserve porosity during later stages of diagenesis, the presence of smectite, illite-smectite interstratifications and illite have been shown to have a more negative influence on porosity and permeability [e.g. 5].

Clays and clay minerals are an integral part of most sedimentary rocks and thus of the reservoir system. There are various definitions for both terms. The German Institute for Normalisation (DIN) defines clay in the context of soils strictly grain-size-related as particles with a diameter of less than 2 μm [11]. The two geological societies AIPEA (Association Internationale pour l'Etude des Argiles) and CMS (Clay Mineral Society) exclude grain sizes from their definitions and define clay as a naturally occurring material, such as a sediment or a rock, "*composed primarily of fine-grained minerals, which is generally plastic at appropriate water contents and will harden when dried or fired*" [12]. The term clay mineral refers to hydrous aluminosilicates of the phyllosilicate group and to minerals that provide the plasticity of clays and that harden when dried or fired [12]. Sandstones and mudrocks contain by weight an average of 15% and 46% clay minerals, respectively [13]. In sandstones, the clay fraction is on average composed of illite (56%), kaolinite (20%), chlorite and interstratified clay minerals (17%) and smectite (7%) and in mudrocks of illite (62%), kaolinite (21%), chlorite and interstratified clay minerals (9%) and smectite (7%) [13].

The building blocks of clay minerals are sheets of corner-linked tetrahedra and edge-linked octrahedra. In tetrahedral sheets, Si^{4+} is the dominant cation that is

frequently substituted by Al^{3+} and Fe^{3+}. These cations are surrounded by four O ions in the close packing arrangement. Each tetrahedron is linked to three neighbouring tetrahedra by a shared oxygen to form a planar sheet (Fig. 1a). Octahedral sheets are built by edge-linked octahedra that are formed by six anions, commonly oxygen and hydroxyl, arranged in the closest-packing (Fig. 1b). The three octahedral sites that exist in this arrangement are occupied by either two trivalent cations, similar to the structure of gibbsite, or three divalent cations, similar to the structure of brucite, to balance charges. This leads to the formation of dioctahedral and trioctahedral sheets, respectively. Common cations in these sheets are Al^{3+}, Fe^{3+}, Fe^{2+} and Mg^{2+}. As only two of the three symmetrically independent octahedral sites (referred to as M1 and M2) are occupied in dioctahedral sheets, two possible configurations exist in clay minerals for the vacant sites with respect to the mirror and the position of the OH-groups, namely *trans*- and *cis*-vacant [14]. In the *trans*-configuration, the M1 position is vacant and the OH groups lie on opposite sites with respect to the vacant position, while in the *cis*-configuration one of the two M2 sites is vacant and the OH groups form a shared edge [e.g. 15] (Fig. 1b+c).

Both, tetrahedral and octahedral sheets are extended infinitely in terms of the X-ray scattering domain size along the a and b crystallographic axes. By joining tetrahedral and octahedral sheets, layers of clay minerals form that are stacked along the crystallographic c axis (Fig. 1c). Polytypes, which are varieties of a clay mineral with the same chemical composition but different crystal structure, form by ordered and disordered stacking sequences of layers. The interlayer space, which is the pore space in between layers, can be occupied by mono- and divalent cations to balance charges that originate from the substitution of octahedral and tetrahedral cations by cations of lower valence.

Illite is a dioctahedral 2:1 clay mineral as its layers are composed of two tetrahedral enclosing one octahedral sheet (Fig. 1c). By definition pure illite has a layer charge of 0.88 charges per 10 oxygen [18], which originate from major tetrahedral substitutions of Si^{4+} by Al^{3+} and minor octahedral substitutions of Al^{3+} and Fe^{3+} by Mg^{2+}. The layer charge is commonly balanced by K^+ within the interlayer, which perfectly fits into the hexagonal holes of the tetrahedra sheets. This irreversibly fixes opposing 2:1 layers due to high attractive forces that prevent cation hydration. Thus, each layer has a thickness of approximately 1 nm. Three illite polytypes are commonly observed in sedimentary rocks, which are $1M$, $1M_d$ and $2M$ illite. In $1M$ illite, all layers are stacked in the same direction and shifted by a vector $\overrightarrow{a/3}$ resulting from the octahedral sheets monoclinic tilt. The $2M_1$ polytype is characterised by

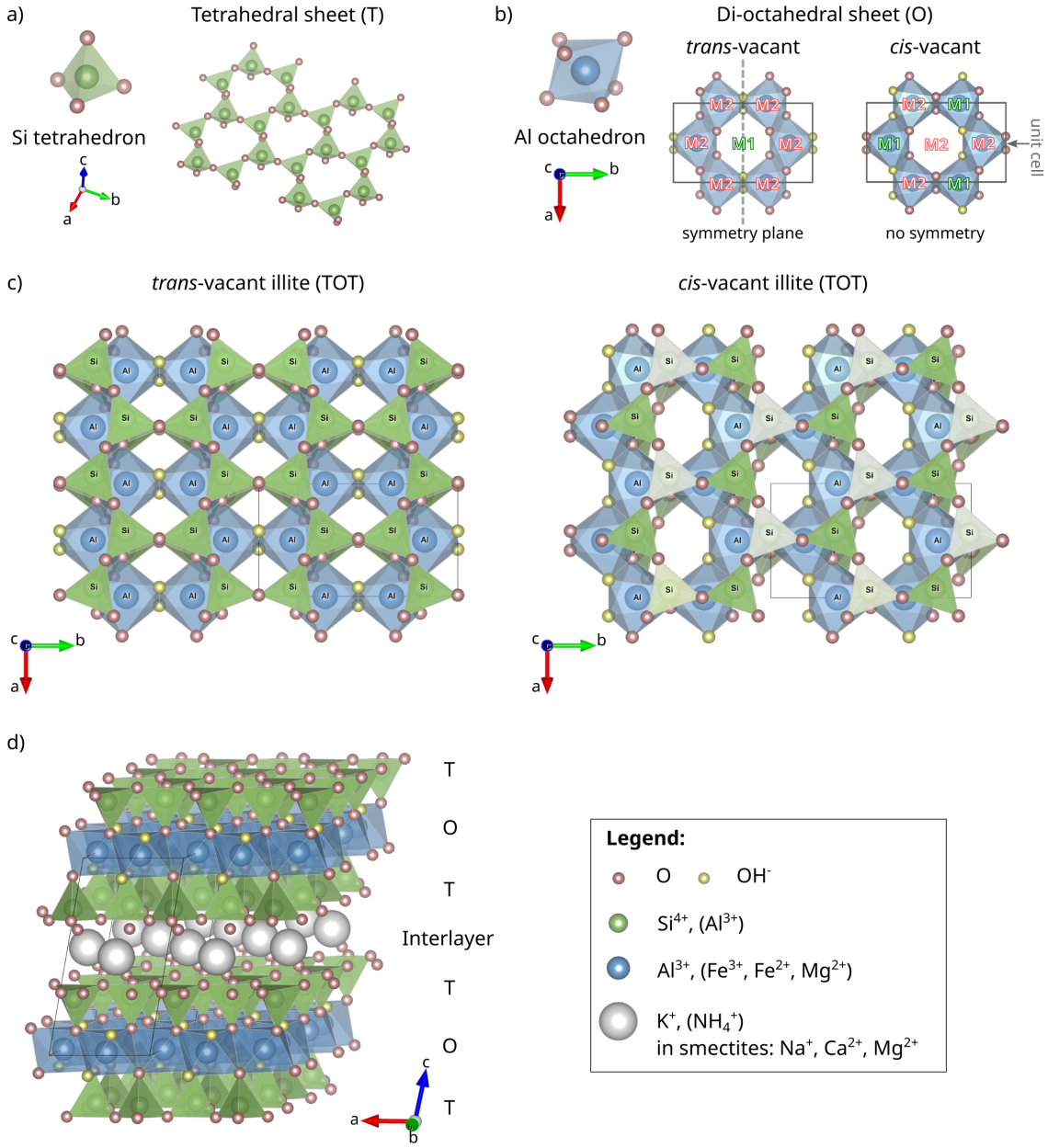

Figure 1: The building blocks of clay minerals are sheets of corner-linked tetrahedra (a) and edge-linked octahedra (b). In dioctahedral sheets, two of the three symmetrically independent octahedral sites (two M2 and one M1) are occupied and one is vacant. In the *trans*-configuration, the M1 position is vacant and the OH groups lie on opposite sites with respect to the vacant position, while in the *cis*-configuration one of the two M2 sites is vacant and the OH groups form a shared edge. (c) Top views of *trans*-vacant and *cis*-vacant illite TOT layers. *Trans*-vacant layers have a symmetry plane parallel to the *ac*-plane and *cis*-layers do not. (d) In illite, two tetrahedral sheets enclose one di-octahedral sheet. The interlayer space is commonly occupied by potassium to balance charges. (Visualised using VESTA [16] with illite structure models from Drits et al. [17].)

an alternating $\pm 120°$ rotation with respect to the mirror plane. In disordered $1M_d$ illite, layers are randomly stacked by $n \cdot 60°$ rotations. In addition, low amounts of interstratified smectite layers are common. Thus, $1M_d$ illite is often referred to as an illitic phase rather than pure illite.

Smectites are a group of di- and trioctahedral 2:1 clay minerals that have a negative layer charge between -0.2 to -0.6 per 10 oxygen. This reduces the attractive forces between layers, allowing smectites to swell due to the hydration of interlayer cations. Depending on the interlayer cation, air dried smectites show a layer thickness between 1.2 to 1.5 nm.

The formation of illite in sandstones and shales has been of interest for the oil and gas industry for decades for mainly two reasons. First, K-Ar isotopic dating of these minerals allows reconstruction of the thermal history of a basin. In source rocks, such as shales, the dating of illite can be used to constrain the onset of hydrocarbon formation, as it coincides with the temperature at which these particles begin to form [19]. However, because illite continues to grow after oil and gas have been displaced, accurate dating is complicated. However, in illite-bearing reservoir sandstones, K-Ar dating can be used to determine the timing when oil and gas were emplaced, as the growth of illite ceases after the formation water has been displaced [20]. The second reason is that the growth of authigenic illites in open pores is known to restrict fluid flow by reducing porosity and permeability of a reservoir [21], thus decreasing the reservoirs quality.

In sandstones, which are considered to be open systems that allow the influx and transport of chemical species by advection, the formation of illite is controlled by different sedimentary and diagenetic processes. $1M_d$ illite, often referred to as poorly crystalline illite, usually forms by the illitization of grain-coating dioctahedral smectite during burial diagenesis. This smectite either infiltrated during sedimentation or during early diagenesis, or developed from Fe^{3+}-rich precursor phases, such as Fe-oxyhydroxides, that formed under arid to semiarid conditions [21]. With increasing temperature during burial, smectite transforms into well-crystalline illite via smectite-rich disordered R0 illite-smectite, ordered R1 illite-smectite and illite-rich ($> 95\%$) R0 illite-smectite ($1M_d$) [e.g. 18, 22, 23]. The potassium required for the illitization during burial often comes from K-feldspar grains that experience intense dissolution with increasing temperature and degree of compaction.

Crystal habits can be diverse, from flaky over fibrous and lath-shaped to hexagonal and platy. Crystals of grain coatings, that are often of the $1M_d$ polytype, usually preserve the flaky shape of the initial smectite, as this illitization mechanism is driven

by solid state transformations [18]. However, as re-crystallisation is also known to occur during the transition of disordered R0 smectite-rich illite-smectite into ordered R1 illite-smectite, crystal habits can change [18]. Nonetheless, structures formed by smectite, such as honeycomb coatings, may be preserved even when the crystal habit is changed, as recently shown by Freiburg et al. [24].

Illites that nucleate and grow in the open pore spaces are predominantly fibrous to lath-shaped. The polytypes of these authigenic illites are often pure *trans*-vacant $1M$ illites, although it has been shown that R1 illite-smectites may also precipitate depending on chemical and thermal conditions [25]. The initiate crystal shapes are hairy to fibrous and evolve through lath-shaped particles to more hexagonal shapes with increasing temperature and depths. Complex irregular particle shapes are often observed and result from coalesced hexagonal crystals. The precipitation of illite can occur by illitization of K-feldspar and kaolinite. However, an additional source of K^+ is required to increase the K^+/H^+ activity ratio in order to supersaturate solutions with respect to illite. Therefore, the formation of illites in open pores is tied to the influx of potassium-rich fluids during hydrothermal events, as frequently observed in Permian North Sea reservoir sandstones [e.g. 26–29].

In contrast to sandstones, shales are considered closed systems due to their low and anisotropic permeability that is enhanced parallel to the lamination. Diffusive transport is the main mechanism controlling the flux of chemical species. Therefore, it is considered that the bulk chemical composition of shale does not change significantly during diagenesis. However, the formation of illite from a smectite precursors follows the same illitization sequence as in sandstones, but recrystallisations are more common.

1.3 Overview of approaches for porosity determination and microstructural analysis

Porosity is one the most important parameters to quantitatively assess the storage capacity of a reservoir and the sealing capacity of a cap rock. The effective porosity, i.e. the connected open pore volume of a rock, and the pore (throat) size distributions are of particular interest for reservoir studies, as they provide information on the size and volume of pathways for fluid migration. To determine these properties, different direct and indirect methods can be applied. Mercury intrusion porosimetry (MIP) is most commonly used by conducting mercury injection capillary pressure (MICP) measurements to determine bulk effective porosity values and pore throat

size distributions. The pressure P_c imposed on a sample to inject mercury into pores is a function of the associated pore throat radius r, the contact angle θ and the Hg-air interfacial surface tension γ and can be calculated by Young-Laplace equation for cylindrical pores, often referred to as the Washburn equation [30]:

$$P_c = \frac{2\gamma \cos(\theta)}{r} \tag{1}$$

Because high pressures are required to inject mercury through small throats, significant alterations of initial pore structures are known to occur in soft porous materials. However, the range of pore throat sizes that can be determined using this method is approximately between 3 nm and 1000 μm, which makes it an universal tool for probing a wide variety of porous rocks. Other common indirect methods include (I) gas adsorption measurements to determine surface area, effective porosity and the pore size distribution in the range between 2 to 350 nm and (II) helium pycnometry and (III) gravimetric water content measurements for most precise bulk porosity determinations [31].

Common techniques to directly image pore space are scanning electron microscopy (SEM) and micro X-ray computed tomography (μXCT). In recent years, X-ray and synchrotron radiation based computed tomography has become a routine analytical method for characterising porous rocks due to the rise of affordable laboratory micro X-ray computed tomography (μXCT) scanners and more available synchrotron radiation facilities [32, 33]. Theoretically, resolutions of 1 μm can be achieved at reasonable scan times, but require small samples sizes of a few millimetres in diameter. Typically, core diameters vary between 2 two 25 mm, which allows the study of a broad range of pore and grain sizes. Various investigations have shown that sandstone porosity determined by CT methods matches well with indirect methods if the sandstone is homogeneous and the amount of unresolved porosity is low [e.g. 34–36]. However, in order to precisely determine the total porosity of heterogeneous tight sandstones, which contain significant amounts clay minerals, detailed knowledge of the sub-micrometer porosity of clay-mineral-related structures is needed [37]. In shales, where most pore and grain sizes are at the nano-scale, μXCT is commonly used to study the distribution of organic matter and matrix minerals [38].

The potential applications of focussed ion beam - scanning electron microscopy (FIB-SEM) in the geosciences were first described by Wirth [39]. Since then, the combination of ion beam polishing and SEM has proven to be an efficient tool in quantifying porosity and analysing the sub-micrometer pore structures of clay minerals and their pore connectivity in tight rocks. Broad ion beam (BIB) polishing

systems using argon ions and focussed ion beam (FIB) polishing systems using gallium ions have been frequently used to study narrow pore structures in shales and mudstones [e.g. 40–47]. Based on early studies [e.g. 40–43] and their own work on North American shales, Loucks et al. [48] proposed a now well-accepted classification scheme for matrix-related pores types in argillaceous rocks. This classification is based on the differentiation between interparticle pores (interP), i.e. pores in between crystals and grains, and intraparticle pores (intraP), i.e. pores within a grain or organic matter. An important consequence of applying this scheme to the study of pore space in tight rocks is that systems dominated by interP pores are more likely to possess a high degree of pore space connectivity than systems with predominant intraP pores [48]. They further proposed an updated pore-size classification scheme based on the carbonate pore size classification of Choquette and Lloyd [49] that includes mudrock-relevant pore sizes below 62.5 μm. This scheme is considered more useful and intuitive to use for the description of pore sizes in tight sandstones and mudrocks than the IUPAC-accepted classification of Rouquerol et al. [50] as it allows improved differentiation between micro- and nanoporosity and is thus applied throughout this thesis.

BIB-SEM analyses can be used to examine relatively large areas of up to 3 mm^2, which were shown to lie within the representative elementary area (REA) of rocks dominated by a clay-mineral matrix [46]. Calculated REAs for such rocks are between 100×100 to 450×450 μm^2 [51]. Thus, BIB-SEM imaging can provide precise porosity values within the range of the SEM resolution as well as detailed information about the different minerals and pore types present in the rock. However, BIB-SEM images are usually two-dimensional (2D) and thus of limited use for the direct analysis of pore connectivity.

In contrast, FIB-SEM analyses provide three-dimensional (3D) information on pore shapes and connectivity and, if paired with EDX, on the distribution of minerals with spatial dimensions up to $20 \times 20 \times 20$ μm^3 and effective voxel sizes down to 5 nm. However, representative elementary volume (REV) sizes are difficult to obtain with this field of view as clay-rich rocks are notably heterogeneous. Thus, FIB-SEM analyses provide site-specific data and are best paired with additional imaging techniques and analytical methods.

Many ion beam studies of shales and mudstones have analysed the pore space of organic-rich formations due to their economic value as host rocks or unconventional hydrocarbon reservoirs [e.g. 44–46, 48]. The analysis of organic matter hosted nanoporosity provided valuable information on the degree of thermal maturation of the

rock. Other studies focused on deep shale formations, such as the Belgian Boom clay formation [40, 47] or the Swiss Opalinus clay [52], to determine their suitability for the disposal of radioactive waste. As depleted oil fields, which have already demonstrated their sealing integrity over geological times, are preferred gas storage sites, only a few studies have characterised the pore space of cap rocks outside the hydrocarbon system [e.g. 53, 54]. However, a detailed knowledge of the diverse structures and types of clay minerals observed in the matrix of potential seals and baffles could provide valuable information on potential fluid pathways and may help to better understand and evaluate the sealing capacity of cap rocks [e.g. 55, 56].

In this thesis (section 3.5), the different seals and reservoir-internal baffles of the Illinois Basin-Decatur CCS demonstration project were evaluated based on a combination of quantitative evaluation of minerals by scanning electron microscopy (QEMSCAN), FIB-SEM, MICP and XRD analyses and theoretical sealing capacity calculations. It is investigated how the methods complement each other by identifying differences and similarities in terms of pore space analyses and mineralogical composition to better understand their limitations in cap rock studies.

Bera et al. [57] were the first to realise that μXCT and FIB-SEM are complementary methods for studying porosity in sandstones. Although their FIB-SEM analyses on quartz grains of a polished Berea sandstone sample were of limited use, they have successfully demonstrated that the serial sectioning method can be applied to sandstone studies. Desbois et al. [58] presented a comprehensive pore space characterisation of a Rotliegend reservoir sandstone with a focus on clay mineral structures by conducting optical thin section, μXCT, BIB and FIB-SEM analyses. Their results provided valuable information about the diversity of illite structures and pore connectivity, but did not draw connections to the diagenetic processes that led to the formation of these structures and the illite polytypism. They further concluded that pore-scale modelling may be difficult to perform in tight reservoir sandstones due to the heterogeneity of pore sizes as a result of diagenetic illite growth. Markussen et al. [59] used μXCT- and SEM-imaging in combination with detailed clay mineral analyses to study pore spaces of tight reservoir rocks of the Edvard Grieg oil field (Norway). Their analyses on clay-rich conglomerates and aeolian sandstones showed that the type of clay mineral controls the amount of clay-hosted nanoporosity. However, their correlative μXCT-SEM approach did not allow a precise assessment of pore connectivity.

A central part of this thesis (section 3.2) was to conduct detailed XRD-based illite polytype analyses in combination with high resolution SEM and FIB-SEM imag-

ing to reconstruct the diagenetic processes and mechanisms that led the formation of the different, partially nanoporous illite structures characteristic for the Upper Rotliegend Bebertal sandstone from the Flechtingen High, Germany. It further investigates the impact of the observed pore structures on the permeability reduction during diagenesis by classifying pore types and pore connectivity in combination with permeability calculations.

1.4 Application of pore scale modelling to tight reservoirs

3D pore space imaging became a routine analytical method in the geoscience community and has led to the development of the so called Digital Rock Physics (DRP) concept [35]. This method involves the direct numerical simulations (DNS) on pore space models that can be used to calculate and analyse a variety of petrophysical properties, transport phenomena and fluid-rock interactions, such as absolute and relative permeability, multi-phase flow or reactive transport parameters. The most established concepts for image-based fluid flow modelling are Lattice-Boltzmann calculations, pore network modelling, and finite volume or finite element based computational fluid dynamics (CFD) simulations. A comprehensive review of common methods can be found in Bultreys et al. [60].

In this thesis (Articles 1-3), the software packages GeoDICT® and OpenFOAM® were used to conduct CFD simulations that utilise the finite volume approach. Using these tools, solutions of the (Navier-)Stokes equations can be approximated to predict the permeability K of tight sandstones, clay mineral structures and synthetic porous sandstone equivalents. A brief introduction of the equations used in CFD simulations is found in section 2.2.2 of this thesis.

Various studies have demonstrated that CFD simulations can be used to model single phase flow to calculate the permeability of natural homogeneous porous rocks based on CT images [e.g. 35, 61, 62]. However, most shales and tight sandstones are notably heterogeneous and contain a significant amount clay mineral structures with sub-micrometer porosity that cannot be resolved using μXCT. As shown by Peng et al. [62], not considering unresolved pores in CFD simulations could lead to calculated permeability values that differ by orders of magnitude from laboratory measurements. Soulaine et al. [63] demonstrated for a highly porous clay-poor Berea sandstone that clay mineral structures, depending on their assigned porosity, could affect calculated permeability tensors by a factor of two and higher. Callow et al. [37] analysed the pore space of a heterogeneous clay-rich sandstone using synchrotron CT and used pore network and finite element modelling approaches to calculate abso-

lute permeability values. They have shown that modelled permeabilities are either underestimated if clay domains were considered completely solid or overestimated by up to two orders of magnitude if clay voxels were considered as open pores.

To more precisely implement sub-resolution information into meshed open pore space models, finite volume micro-continuum models, such as the Navier-Stokes-Brinkman or Navier-Stokes-Darcy approach [63, 64], can be utilised. Here pore space models are subdivided into open pores and porous voxels, which are often referred to as Darcy or Brinkman domains. Flow is realised by solving the (Navier-)Stokes equation in open pores and the Darcy or Brinkman equation in porous domains. Various studies utilised a micro-continuum approach to analyse the potential impact of porous domains on permeability of sandstones and carbonates [63–66]. However, flow properties for the porous domains were either varied systematically by assuming different porosity and permeability values or assigned based on variations in grey-scale values and simplified Kozeny-Carman porosity-permeability relationships. While these approaches were proven to be valid for mono-mineralic rocks such as carbonates, the applicability for complex argillaceous rocks such as diagenetically altered sandstones must be questioned, as clay minerals often form complex pore structures that are likely not well represented by such simplified relationships. Therefore, detailed image-based knowledge of the porosity, pore structures and pore connectivity of unresolved nano-porous domains is required to assign them realistic permeability values derived from DNS.

This issue is addressed in this thesis (section 3.3) whereby a novel FIB-SEM-supported model was developed for the Upper Rotliegend Bebertal sandstone. This modelling was based on a detailed investigation of the distribution of illites in which correlative high resolution μXCT and SEM-EDX imaging was conducted to improve pore-scale permeability simulations by implementing Brinkman domains based on morphological observations.

The accurate modelling of flow is not only important for the characterisation of reservoirs and cap rock properties, but also provides the fundamental basis for the application of pore-scale reactive transport models to predict the behaviour of a system under varying chemical and hydraulic conditions. A common scenario is the dissolution of calcite following the injection of supercritical CO_2 into a reservoir [e.g. 67, 68]. Although numerous reactive transport codes exist to address this problem [e.g. 69–73], their validation is often problematic due to discrepancies between modelled predictions and experimental observations [e.g. 74].

During the ResKin project (section 2.1.1) it became apparent, that natural reser-

voir rocks are too complex and heterogeneous to study the effects of acidified pore fluids on properties of the rock. For example, Hale et al. [75] investigated the dissolution of calcite cements in the Upper Rotliegend Bebertal sandstone by flow-through experiments. They demonstrated that, although calcite dissolution was observed by monitoring effluents Ca^{2+} concentrations, even high resolution μXCT images were insufficient to detect the volume of calcite that dissolved over a period of 150 days. They concluded that the heterogeneity of the Rotliegend sandstone, which is characterised by low accessible calcite surface areas and complex flow patterns, prevents an efficient upscaling of the calcite reactivity from the mineral surface to the continuum or Darcy scale.

One promising approach to better constrain these coupled chemical and hydromechanical processes through experimentation is the use of simpler and more homogeneous synthetic materials. Different approaches of synthesising geomaterials have been developed in the past. Early studies by Rathore et al. [76] utilised epoxy resin cemented sand to study P- and S-wave propagation through cracks, which resulted in reasonable compressive strengths but provided a poor natural analogue. To better mimic quartz cementation, binders based on Na-silicate solution were often utilised [e.g. 77–79]. However, to produce strong silicate cementation these binders require heating to temperatures over 600°C which prevents studying thermally sensitive materials. More recently, Dimou et al. [80] utilised 3D-printed pore space models to study single phase flow and particle transport. While this technique can be used to study transport processes on well-defined topologies, the implementation of the reactive phase is not possible yet. Currently, there is no method available for creating synthetic rock mixtures that allows to study temperature- and pH-sensitive materials, such as clay minerals or carbonate cements, in a porous grain framework. Thus, there is a demand for developing such synthetic porous materials to improve our understanding of subsurface processes by advancing experimental studies. Therefore, an additional objective of this doctoral study (section 3.4) was to investigate the suitability of geopolymer binder for the preparation of synthetic porous materials that can be utilised in flow-through experiments to better constrain the coupled chemical and hydro-mechanical processes that occur in subsurface reservoirs.

2 Materials and methods

2.1 Materials and Projects

2.1.1 The ResKin Project

Three of the studies presented as part of this thesis (Articles 1-3) were prepared within the framework of the BMBF-funded *ResKin* project (Reaction Kinetics in Reservoir Rocks; grant number: 03G0871) and its successor *ResKin_Move* (grant number: 03G0900). In both joint projects, researchers from the University of Bremen, the University of Greifswald, the University of Mainz, ITWM Kaiserslautern, KIT Karlsruhe, and HZDR Dresden/Leipzig investigated the dissolution kinetics of calcite and the coupled particle mobilisation in reservoir rocks at different scales from the crystal surface at the nanometre-scale to core plugs at the centimetre-scale. The project resulted in a novel reactive transport model that includes the variability of dissolution rates observed at the crystal surface into pore scale simulations [73]. The strong inter-connectivity of the working packages of the project members is summarised in Figure 2. The main tasks of the research group of the University of Greifswald were the mineralogical characterisation of the sample materials before and after experimentation and the analysis of nano-porous clay structures using FIB-SEM to determine their impact on the flow of fluids in tight reservoir rocks.

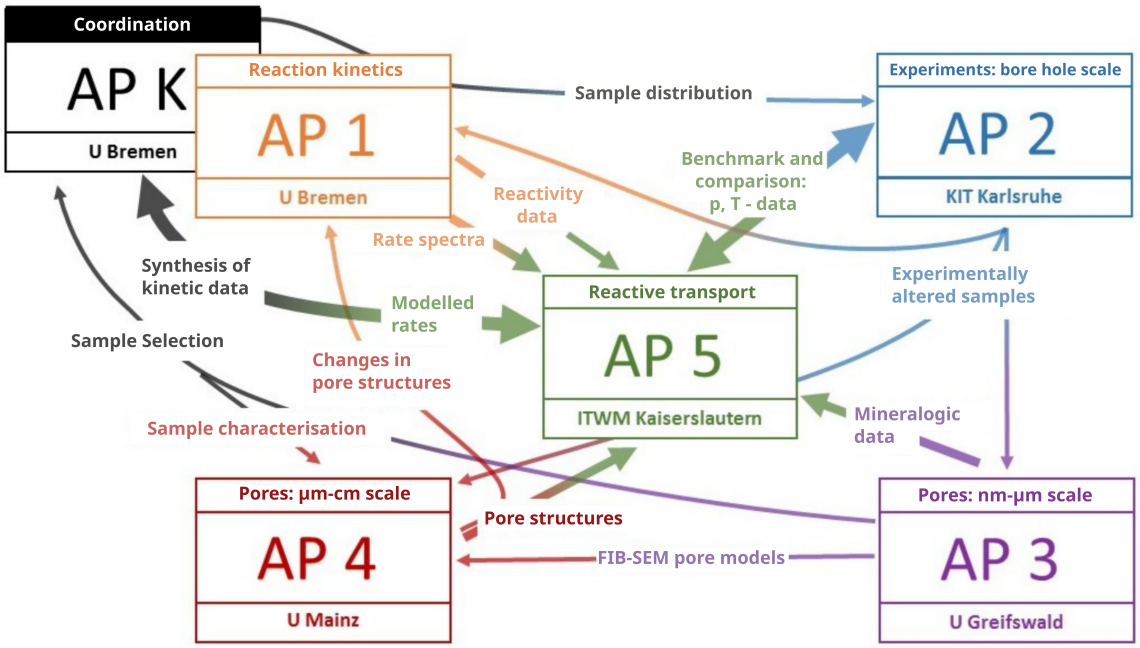

Figure 2: Web diagram illustrating the topics of the working packages of the ResKin project and their inter-connectivity.

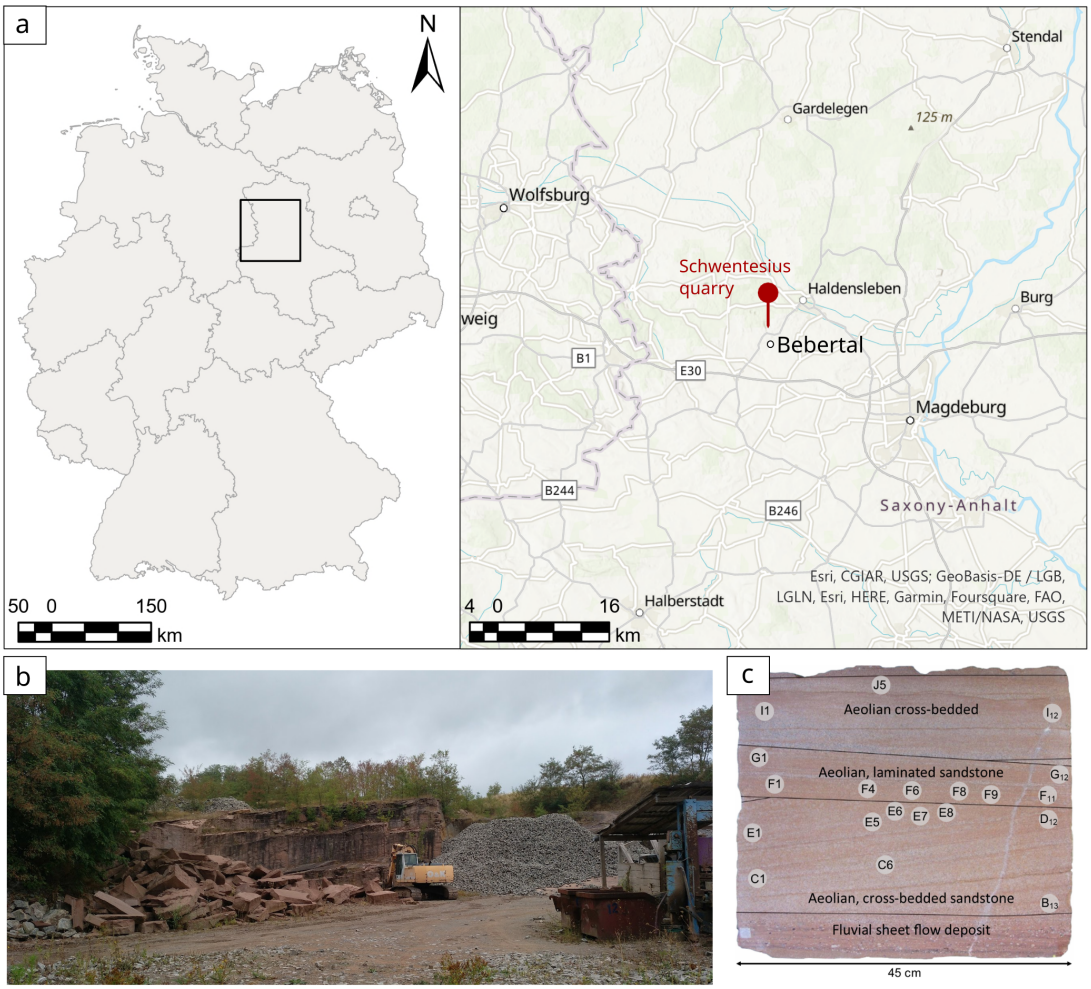

Figure 3: (a) Map of Germany with the location of the Schwentesius quarry near Bebertal. (b) Photograph of the Schwentesius quarry. (c) Sample block of the Bebertal sandstone used in the ResKin project.

The ResKin project used the aeolian sandstones of the Parchim Formation (Early Permian Upper Rotliegend) that were collected from the Schwentesius quarry near Bebertal (Flechtingen High, Northern Germany, N52.2564084°; E11.3361657°, Figure 3). The fluvial-aeolian sandstone succession found at this outcrop is considered a natural analogue for a deeply buried low-permeability Rotliegend gas reservoir sandstone of the North German Basin [81, 82].

2.1.2 The Illinois Basin - Decatur Project (IBDP)

The Illinois Basin - Decatur Project (IBDP) and the Illinois Industrial Carbon Capture and Storage (ICCS) project were demonstration projects used to determine the storage potential of the Cambrian Mt. Simon sandstone within the Illinois Basin

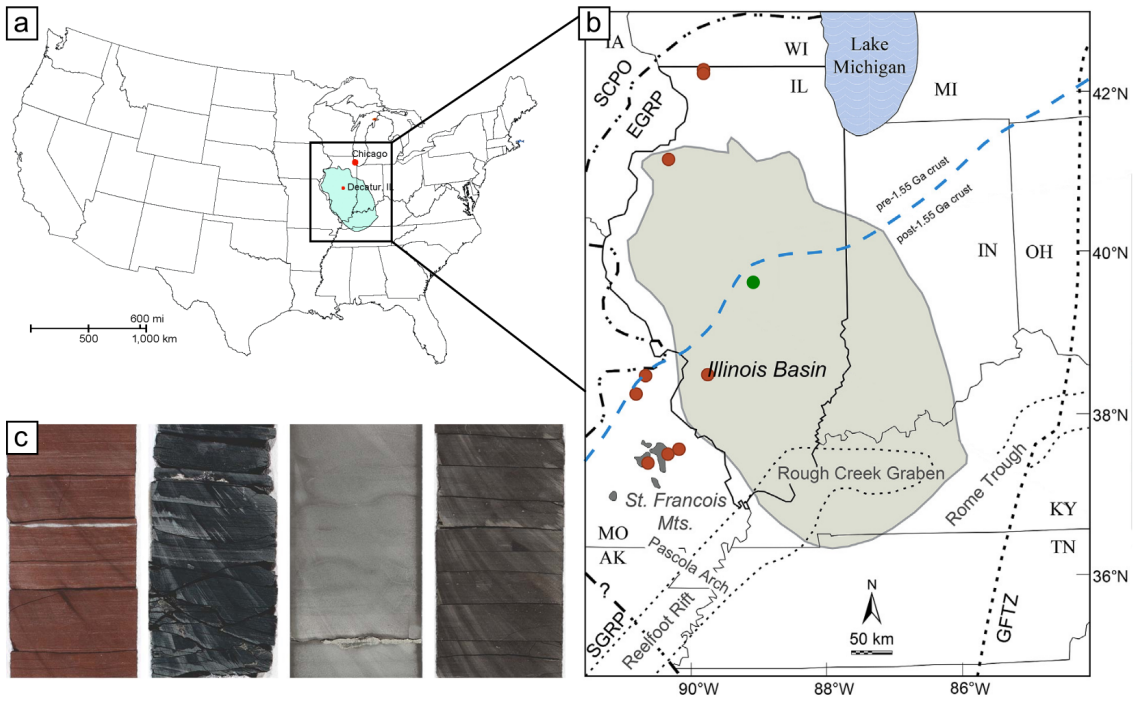

Figure 4: (a) Map of the United States with the location of the Illinois Basin and the Illinois Basin-Decatur Project in Decatur, Illinois. (b) Map of the Illinois Basin. The green circle marks the area of Decatur and the CO_2 injection well. (c) 4 inch core samples of the potential sealing units. From left to right: Mt. Simon mudstone (depth 2092m), Eau Claire shale (depth 1666m), Maquoketa shale (depth 858m) and New Albany shale (depth 657m). Modified from Freiburg et al. [89, 90].

(Figure 4a+b) and to evaluate the integrity of its three overlying seals for the large-scale underground storage of CO_2 from industrial sources [83, 84]. Between 2011 and 2014, a total of 1 Mt CO_2 were injected into the Mt. Simon with an average of 1100 tons per day. From 2016 on, the annual injection was increased to approximately 1 Mt (3300 tons per day) [85]. So far, no leakage or movement out of the injection zone has been detected by monitoring the spread of CO_2 plume. However, micro-seismic events have been reported to start two month after injection in the lowermost Mt. Simon sandstone and the underlying Precambrian basement [86].

Three overlying, laterally extensive shale units, namely the Eau Claire, the Maquoketa and the New Albany were identified as primary and secondary seals [83] and a Mt. Simon internal, discontinuous mudstone as potential pressure baffle [87, 88]. As part of this thesis (section 3.5), the seals and baffles (Figure 4c) overlying and within the Mt. Simon sandstone were investigated by combining detailed XRD clay mineral studies with high-resolution FIB-SEM pore space imaging, thin section analyses, QEMSCAN, MICP and theoretical sealing capacity calculations.

2.2 Methods

2.2.1 Focused ion beam scanning electron microscopy - a tool for studying the 3D structure and fabric of illite

Focussed ion beam - scanning electron microscopy (FIB-SEM) is the method of choice to directly study the 3D structure of nanomaterials at resolutions down to 5 nm. It combines high-resolution field-emission scanning electron microscopy (FESEM) with ultrafine gallium ion beam milling and polishing, allowing surfaces as small as 20×20 μm^2 to be sequentially captured. By combining a series of serially polished and imaged surfaces, a pseudo 3D volume can be reconstructed to study a variety of spatial properties of a material. A review of applications of FIB-SEM in the geosciences is given in section 1.3. In this thesis, FIB-SEM provides the basis for the structural analysis of clay structures in tight sandstones, mudrocks and shales. In the following, the method is briefly introduced by focusing on the applied workflow developed and refined during the studies of this thesis. It emphasised the various steps required to process large data sets, from image acquisition to machine-learning based phase segmentation.

All FIB-SEM analyses in the context of this thesis were conducted on a Zeiss Auriga crossbeam microscope equipped with a Gemini electron beam column and an Orsay Physics ion beam column at angle of 54° to each other (Fig. 5a). In comparison to conventional tungsten cathode SEM, the fine electron beam of a FESEM allowed fast acquisition of high resolution images at low beam energies down to 0.5 keV which minimised noise and charging artefacts. To collect images of ion-polished surfaces, SE2 secondary electron images were captured using an Everhart-Thornley detector, while an energy-selective backscattered (EsB) detector was used to form backscattered electron images. Unlike SE1 secondary electrons, which are generated near the surface of the sample and detected using an inlense detector, SE2 secondary electrons are generated deeper within the sample and reflected at lower angles, thus providing more compositional and less morphological information of the polished surface. The low reflection angle further enhances pore detection from polished surfaces by reducing shine through artefacts. In contrast to conventional backscattered electron (BSE) detectors, the acquired EsB images provide better site-specific compositional information at low beam energies, but require comparatively long scan times for reasonable noise levels, which occasionally introduced charging artefacts near grain boundaries. To correlate the different grey levels in EsB images to single mineral phases, the chemical composition of the polished surface was determined by energy-

dispersive X-Ray spectroscopy (EDX) mappings using an Oxford X-Max 80 mm^2 detector.

As FIB-SEM image stacks are a series of sequentially acquired cross sections, multiple processing steps are required to obtain geometrically correct 3D volumes. An illustrated workflow can be found in Fig 5b-f. Sample drift is the most common artefact that occurs during the acquisition of image stacks as the electron beam is blanked during each ion beam polishing step, which leads to minor drifts after refocusing the beam on the sample surface. Therefore, aligning the image sequence to correct for this drift is usually the first step, followed by cropping the image volume to delete image information outside the imaging planes (Fig. 5b-c). After alignment, various filters can be applied to improve the image quality. Shading artefacts are commonly observed and occur within a single image as a result of detector shadowing or between individual images as a result of varying imaging conditions. Both are often caused by insufficiently large trenches to the left of the sample wedge (Fig. 5a) and need to be corrected to achieve a homogeneous grey scale distribution (Fig. 5d). Other, less frequently observed artefacts include noise and stripes. Stripes result from pillars of material on the image planes that was not etched away by the gallium beam. These remnants often occur during the polishing of highly porous areas and only need to be removed if they are too large, as filtering attempts frequently introduce image distortions. Noise removal was found to be situational as the application of edge-preserving noise reduction filters, such as *Non-Local Means*, are computationally demanding and frequently remove important image information. Further, it was found that machine learning-based segmentation algorithms provided better results if noise was not removed in advance.

Different concepts exist for the automated segmentation of pore space from FIB-SEM data, which include grey value thresholding, Otsu thresholding, watershed segmentation and machine learning-based algorithms [e.g. 91, 92]. However, it was found that only machine learning segmentation was capable of reliably segmenting pores with strong shine-through artefacts (Fig. 5e+f). These artefacts appear especially in the area of larger pores (Fig. 5c+d) as the detector also collects electrons from behind the actual imaging plane. Furthermore, these artefacts are enhanced by the deposition of gallium on the surface of these pores, which, due to its high density, raises the grey level at these surfaces above that of the surrounding minerals. In most of the studies presented in this thesis, the machine learning segmentation software Ilastik [93] was used, which after intensive training provided fast and reliable pore space segmentations of μXCT and FIB-SEM data sets (Fig. 5f).

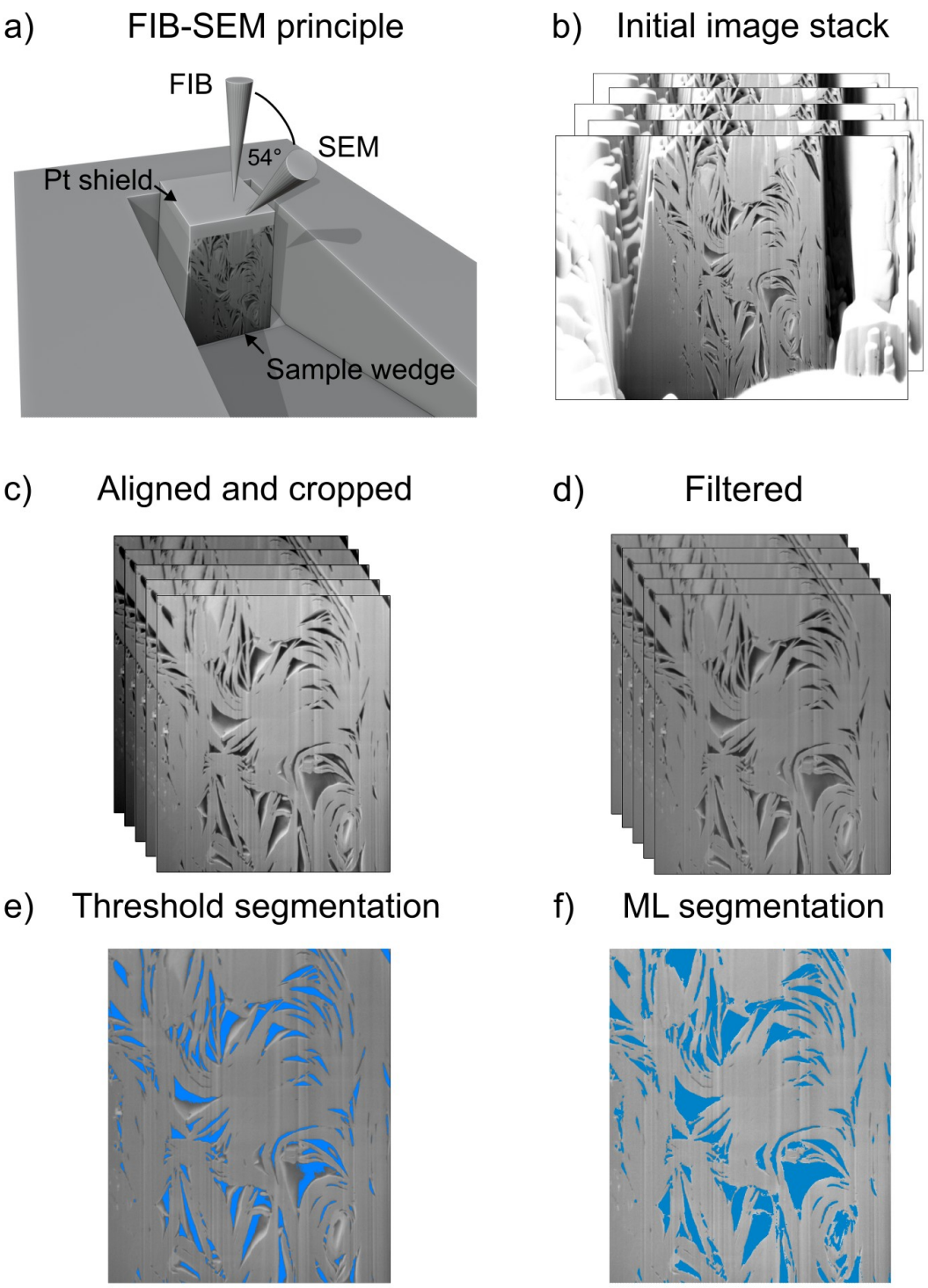

Figure 5: Visualised workflow for processing and segmentation of FIB-SEM image sequences. a) 3D rendering illustrating the principle of focused ion beam scanning electron microscopy. b) After image acquisition the image stack consists of a series of unaligned raw electron images. c+d) After the alignment and cropping, filtering is required to remove artefacts caused by shading, stripes and noise. e) Example of a conventional grey scale thresholding that fails segment pores with shine-through artefacts. f) Machine learning (ML) segmentation with Ilastik provides good results even in large pores.

2.2.2 Governing equations for fluid flow simulations

The Navier-Stokes equations are a set of two partial differential equations that can be used to simulate the free flow of Newtonian fluids. The two equations are the conservation of mass and the conservation of momentum. For laminar single phase flow the conservation of mass reads:

$$\frac{\partial \rho}{\partial t} + \nabla \cdot (\rho v) = 0, \tag{2}$$

where ρ is the density of the fluid and v is the velocity field. It implies that the volume of fluid within the system is constant over time as the flux of fluid out of the system is equal to the flux of fluid into the system. For incompressible fluids the density is constant and equation (2) simplifies to the divergence-free velocity field expression:

$$\nabla \cdot v = 0. \tag{3}$$

The conservation of momentum without external forces, such as gravity or buoyancy, is:

$$\mu \nabla^2 v - \nabla p = \rho \left(\frac{\partial v}{\partial t} + v \cdot \nabla v \right) \tag{4}$$

where μ is the dynamic fluid viscosity and p the pressure field. The left side of the equation describes the internal forces that a fluid exerts on itself. Thereby, the term $\mu \nabla^2 v$ corresponds to the viscous forces and ∇p to the pressure forces. The term $\rho \left(\frac{\partial v}{\partial t} + v \cdot \nabla v \right)$ describes the inertial forces. This term becomes larger the denser the fluid or the higher its velocity. The ratio between inertial and viscous forces can be expressed by the dimensionless Reynolds number

$$R_e = \frac{\rho v l}{\mu}, \tag{5}$$

where l is a characteristic linear dimension, i.e. the average length of pores. In sandstones, where laminar flow dominates, i.e. velocity of the fluid is low, R_e becomes very small ($\ll 1$) because viscous forces are high compared to the inertial forces. Thus, under the assumption of stationary conditions, the inertial term in equation (4) can be neglected, which results in the simplified steady Stokes equation

$$\mu \nabla^2 v = \nabla p. \tag{6}$$

The Navier-Stokes equation or the simplified Stokes equation are frequently used to calculate pressure and velocity fields in open pore structures, i.e. free flow domains, to describe the motion of fluids at the pore scale in sandstones.

A model that describes the macroscopic laminar flow of incompressible fluids through a porous material, e.g. the flow of groundwater through an aquifer, is provided by the Darcy equation. In his famous sand filter experiments, Darcy [94] found that the total discharge Q of water that flows through a cylindrical sand filter is proportional to the hydraulic gradient Δh between the inflow and the outflow reservoir, and the length L of the filter. It is further inversely proportional to the cross-sectional area A of the filter. Based on these findings a one-dimensional form of the Darcy equation reads:

$$Q = -k_f A \frac{\Delta h}{L}, \tag{7}$$

where the constant k_f is the hydraulic conductivity that depends on the properties of the fluid and the porous medium. The flux u, often referred to as the Darcy velocity, is defined as the total discharge per cross-sectional area and can be written as $u = \frac{Q}{A}$. With the hydraulic gradient defined as $\Delta H = \frac{\Delta p}{\rho g}$ and the permeability $K = k_f \frac{\mu}{\rho g}$, equation (7) becomes:

$$u = -\frac{K}{\mu} \frac{\Delta p}{L}, \tag{8}$$

where Δp is the pressure gradient between inflow and outflow reservoir.
In 3D dimensional space, a general form of the Darcy equation can be written as:

$$v = -\frac{K}{\mu} \nabla p \tag{9}$$

or

$$-\mu K^{-1} v = \nabla p. \tag{10}$$

At the pore scale, a combination of the Stokes (Eq. 6) and the Darcy equation (Eq. 10) can be used to realize coupled free and porous media flow. This equation is referred to as the Brinkman equation [95], which can be written as

$$\mu \nabla^2 v - \mu K_p^{-1} v = \nabla p, \tag{11}$$

where K_p is the permeability of the porous domain. The term $\mu K_p^{-1} v$ adds flow resistivity to the Stokes equation as the porosity in porous domains is < 1. An example for the application of the Brinkman equation are CT pore space models

of sandstones containing clay minerals [e.g. 63] in which free flow occurs in open intragranular pores and porous media flow in pores filled with clay minerals. As no solids reduce the local porosity in open pores, $K_p \to \infty$ and the Brinkman equation approximates the Stokes (Eq. 6) equation. In porous regions, however, clay minerals lead to a reduction of the local porosity and the flow resistivity term cannot be neglected. However, detailed knowledge of permeability of such porous regions is required to conduct realistic simulations.

3 Results and discussion

In section 3.1, the precise contributions by the author to the articles of this thesis are outlined. In sections 3.2-3.5, the key findings and conclusions of each study will be summarised before the results are discussed in a broader context in section 3.6.

3.1 Author contributions

Article 1: **Peltz, M.**, Jacob, A., Grathoff, G.H., Enzmann, F., Kersten, M. and Warr, L.N. (2022): A FIB-SEM Study of Illite Morphology in Aeolian Rotliegend Sandstones: Implications for Understanding the Petrophysical Properties of Reservoir Rocks. *Clays and Clay Minerals*, 70, 84-105. DOI: 10.1007/s42860-022-00174-9

MP conducted XRD analyses including Rietveld refinements, thin section analyses, FIB-SEM measurements and image processing. AJ performed permeability simulations. Data analysis and modelling was done by **MP**. **MP** prepared the initial version of the manuscript. LNW supervised the project. All authors contributed to reviewing and editing of the manuscript.

Article 2: Jacob, A., **Peltz, M.**, Hale, S., Enzmann, F., Moravcova, O., Warr, L.N., Grathoff, G.H., Blum, P. and Kersten, M. (2021): Simulating permeability reduction by clay mineral nanopores in a tight sandstone by combining computer X-ray microtomography and focussed ion beam scanning electron microscopy imaging. *Solid Earth*, 12, 1-14. DOI: 10.5194/se-12-1-2021

MP conducted FIB-SEM measurements, EDX mappings, XRD measurements and Rietveld refinements. **MP** developed the initial version of the Brinkmann-domain algorithm which was improved and translated to C++ in cooperation with AJ. AJ and **MP** developed the process methodology, conducted the programming and prepared the initial version of the manuscript. Visualisation of the results was conducted by AJ and **MP**. Study conceptualisation was done by AJ, **MP**, SH, FE, LNW, GGH, PB and MK. Review and editing was executed by AJ, **MP**, SH, FE, OM, LNW, GGH, PB and MK. Supervision was provided by FE, LNW, GGH, PB and MK. The project was administrated by FE, LNW, GGH, PB and MK.

Article 3: **Peltz, M.**, Warr, L.N., Hale, S. and Blum, P. (2023): Developing synthetic sandstones using geopolymer binder for constraining coupled processes in porous rocks. *SN Applied Sciences* 5, Article number 87. DOI: 10.1007/s42452-023-05301-2

Conceptualisation and methodology was developed by LNW and **MP**. **MP** prepared the samples and performed XRD analyses, SEM-EDX analyses and conducted all rock property measurements. CT scans were collected by SH. Pore space segmentation and permeability simulations were performed by **MP**. **MP** created all visuals. **MP** prepared the initial version of the manuscript. All authors contributed to reviewing and editing of the manuscript.

Article 4: Freiburg, J.T., **Peltz, M.**, Willette, D.C. and Grathoff, G.H. (2022): High-resolution pore space imaging, mineralogical characterization, and sealing capacity estimates of confining units at a geologic carbon storage demonstration: the Illinois Basin–Decatur Project, USA. *The Journal of Geology*, 130 (5), 335-355. DOI: 10.1086/722563

GGH and JTF developed and supervised the study. **MP** performed FIB-SEM analyses and XRD measurements including Rietveld refinements. DCW performed cap rock integrity calculations. JTF prepared the initial version of the manuscript. Visualisation was performed by **MP** and JTF. **MP** contributed significantly to the methodological discussion. All authors contributed to reviewing and editing of the manuscript.

Prof. Dr. Laurence N. Warr Markus Peltz

3.2 Article 1: A FIB-SEM Study of Illite Morphology in Aeolian Rotliegend Sandstones: Implications for Understanding the Petrophysical Properties of Reservoir Rocks

In this study, published in *Clays and Clay Minerals*, the growth of authigenic illites in the aeolian Bebertal sandstone of the Parchim formation (Early Permian Upper Rotliegend group) was studied. It was found that the multiple generations of illite that formed during diagenesis led to a significant reduction of porosity and flow paths. These changes were carefully reconstructed by a novel approach that combined detailed mineralogical XRD illite polytype studies with site-specific structural and chemical FIB-SEM and EDX analyses. Based upon the findings, an illite formation model was developed that can be used to provide more detail on the rocks paragenetic sequence as proposed by Fischer et al. [82]. It links the series of diagenetic events to the formation of disordered $1M_d$ and *trans*-vacant $1M_{tv}$ illite polytypes as well as their associated morphologies.

Thin section and FIB-SEM analyses revealed a variety of illite morphologies in the aeolian layers of the Bebertal sandstone that are characteristic of many Rotliegend sandstones. These are (1) tangential grain coatings, (2) altered and illitised K-feldspars including illite meshwork cements, and (3) pore-filling laths.

Tangential illite coatings are an omnipresent feature in the Bebertal sandstone. Its formation during burial likely commenced with the illitisation of smectite coatings that likely infiltrated during sedimentation or formed from Fe-rich precursor phases such as Fe-oxyhydroxides. During a Triassic to Early Jurassic fluid flow event, these thin tangential grain coatings served as a substrate for the expansive growth of a thicker fully grain-covering tangential illite coating. This thickening reduced the porosity and permeability of the rock by decreasing pore throat sizes and partly sealing porous K-feldspar grains. This was confirmed by FIB-SEM analyses that showed no connected porosity perpendicular to the coating surface and pores that were frequently filled by hematite crystals.

During the same event, porous K-feldspar cements formed in pores of altered detrital K-feldspar grains. As the activity of potassium decreased, the remaining pores were locally filled with authigenic illite. Although these cements generated interconnected pore clusters, the porosity was limited to 7%. The low permeabilities

of up to 13.4 μD, which were derived from DRP simulations on pore space models of these structures, further indicate that the initial open pore systems in detrital K-feldspar grains were successively cut off from the main flow paths of the rock. A further reduction of porosity and permeability was caused by the formation of illite meshworks that formed from such altered K-feldspar grains. These morphologies showed the highest porosity (13.9%) and characteristic slit- to triangular-shaped pores. Although the largest interconnected pore clusters were observed within these structures, their expansion into open pores had an overall negative effect on the permeability of the sandstone.

Both tangential illite coatings (1) and illite in altered K-feldspar and meshworks (2) were found to be of the $1M_d$ polytype, as confirmed by XRD and the irregularly shaped crystals that are common to all analysed structures. Structural analyses further indicate a generic relationship between the crystal growth mechanism and the resulting pore structures as both pore and crystallite sizes follow a log-normal trend. Comparisons to crystallite size distribution studies by Eberl et al. [96] also suggest that the main formation mechanism was dominated by continuous nucleation and crystal growth.

Pore-filling laths and fibres (3) represent the youngest generation of illites in the Rotliegend sandstone. These delicate, epitaxially grown structures, which primarily nucleated on tangential coatings and K-feldspar surfaces, likely formed during a Late Jurassic fluid flow event and are comprised of the $1M_{tv}$ polytype.

To assess the influence of the studied nanoporous morphologies on the permeability of the sandstone, permeability simulations were run on extracted connected pore volumes. These modelled permeabilities of illite and K-feldspar cements were three to four orders of magnitude smaller than those derived from core plug measurements and μXCT-scale simulations. Therefore, these systems are considered to be widely disconnected from the effective transport pathways measured under laboratory conditions. However, under reservoir conditions, nanoporous systems may become more relevant once the pore pressures exceed the capillary entry pressures of these structures, for example due to lithostatic compression of the pore systems, clogging of larger flow paths due to particle mobilisation or further crystal growth.

3.3 Article 2: Simulating permeability reduction by clay mineral nanopores in a tight sandstone by combining X-ray microtomography and focussed ion beam scanning electron microscopy imaging

Predicting the permeability of tight sandstones based on μXCT imaging is challenging due to the heterogeneity of pore sizes commonly observed in these rocks. Pore size distributions are broad and contain significant amounts of sub-micrometer porosity that is not resolvable by μXCT. As a result, pore space models of tight rocks are often characterised by high amounts of the smallest resolvable pores which are 1-2 voxels in size. Peng et al. [62] demonstrated that the inclusion of such voxel sizes frequently leads to an overestimation of the actual pore sizes, thus leading to inaccurate calculations of permeability.

This study, published in *Solid Earth*, provides an approach to correct for overestimated pore sizes by combining pore space models obtained from high-resolution synchrotron μXCT and nano-scale FIB-SEM to improve the prediction of permeability in a tight aeolian illite-rich Bebertal sandstone based on pore scale simulations.

As demonstrated in section 3.2, the formation of illite in the Bebertal sandstone led to a significant reduction of permeability and porosity during diagenesis. Although this sandstone was found to contain on average 13% illite, with a variety of nanoporous structures, neither illite grain coatings, illitised K-feldspar nor pore-filling illite laths were resolved using synchrotron μXCT imaging. This was attributed to missing density contrasts between detrital grains and authigenic illite as well as a lack of resolution. However, as demonstrated by correlative μXCT and SEM-EDX analyses on the same core section, the smallest resolved pores correlate with the occurrence of illite, indicating that these pores are partially filled with these clay minerals.

To simulate the reduction of permeability through these illite-rich regions, a multi-continuum pore space model was created that differentiated between void and porous voxels, which represent open pores and nanoporous illite structures, respectively. To identify illite-rich domains in the segmented μXCT pore space images, a distance map based algorithm was developed that masks all pores with local diameters of less than two voxels. Subsequently, permeability was calculated by modelling flow through the constructed pore space model. Simulations solved Navier-Stokes

equations extended by a Brinkman-term to add flow resistivity to porous illite domains. Flow properties for Brinkman domains were obtained from Navier-Stokes simulations on a pore space model of an illite meshwork structure, which was considered representative for illite structures in these regions.

In comparison to laboratory measurements, which showed an average permeability of 2.9 mD, results demonstrated that the distance map approach in combination with FIB-SEM informed Navier-Stokes-Brinkmann calculations provided more realistic simulated permeability values for the Bebertal sandstone than conventional Navier-Stokes simulations. While permeabilities determined by Navier-Stokes simulations on open pore space models were up to one order magnitude too high (+814%), the Navier-Stokes-Brinkman approach reduced the mismatch between measurements and simulations to -34.5% (-1 mD).

3.4 Article 3: Developing synthetic sandstones using geopolymer binder for constraining coupled processes in porous rocks

Studies of the Bebertal sandstone (section 3.2 and 3.3) demonstrated that natural reservoir rocks represent complicated heterogeneous systems. The variations in texture and composition, which formed as a result of the sedimentary environment and diagenetic history, led to small-scale heterogeneity in the porosity and permeability of these rocks [97]. During the ResKin project it became apparent that the Bebertal sandstone was too complex to easily constrain the geochemical and hydrodynamical processes that occured during calcite dissolution experiments in a flow-through cell. Within 150 days of experimentation, calcite dissolution was only observed chemically by monitoring the effluents Ca^{2+} concentrations [75]. The volume of calcite dissolved was too low to be detected by high-resolution μXCT, thus holding back the experimental validation of pore- and plug-scale reactive transport models. More intense dissolution was mainly prevented by the low accessible calcite surface area, complex flow paths, and low permeability of the rock, which was further reduced by the mobilisation of pore-filling illites.

Quantifying and predicting changes that occur in reservoir systems during fluid-rock interactions are important aspects to ensure an efficient and safe reservoir usage. To better constrain the dynamic and coupled processes relevant to the storage of

renewable energies in reservoir rocks, simpler porous analogue materials need to be used for improved experimentation. Past attempts at creating synthetic rock-like assemblages with realistic cement analogues commonly involved sintering or curing at temperatures above 600°C, thus preventing the study of thermally sensitive materials, such as carbonates or clay minerals, common to many reservoir rocks. In addition, high temperature treatment may also introduce artificial fluid pathways due to the formation of thermally induced micro-fractures or cracks formed during shrinkage.

In this proof-of-concept study, published in *SN Applied Sciences*, a novel approach for developing synthetic sandstones cured at low temperatures (<80°C) is presented. By utilising metakaolin-based geopolymer as binder, it was possible to prepare a homogeneous porous material with porosity and permeability values in the range of natural reservoir rocks. After curing, the binder was composed of crystalline zeolite NaP and minor amounts of amorphous geopolymer, which are considered valid analogues to cements formed during diagenesis, as authigenic zeolites are common to highly porous reservoir sandstones. The structure of the synthesised rock was further analysed by μXCT image analysis and direct numerical simulations. Inhomogeneities in porosity, permeability and mineral distribution are also considered to be minor when compared to the textural heterogeneity observed in the Bebertal and Berea sandstones, such as grading of sand grains, sedimentary boundary layers or uneven distributed cements. The synthetic sandstone prepared in this manuscript represents a simplified analogue of Upper Rotliegend reservoir rocks that can be used to more accurately constrain the coupled hydrodynamic and chemical processes that occur during calcite dissolution. Improved properties include, for example, higher porosity and permeability, a simpler mineralogical composition as well as a higher accessibility of calcite surfaces to fluids.

The published paper further highlights a range of parameters, such as grain size distribution, binder content, mineralogical composition and sample geometry. These can be easily adapted during sample preparation to attain specific properties, such as porosity, permeability and pore size distributions. Thus, the use of geopolymer-cemented synthetic sandstones containing thermally sensitive minerals is expected to advance future experimental studies leading to an improved understanding of coupled physico-chemical subsurface processes.

3.5 Article 4: High-resolution pore space imaging, mineralogical characterization, and sealing capacity estimates of confining units at a geologic carbon storage demonstration: the Illinois Basin - Decatur Project, USA

The IBDP was one of the first large-scale demonstration projects for subsurface storage of supercritical CO_2 worldwide. Three laterally continuous shale formations, which are the Eau Claire, the Maquoketa and the New Albany, were identified as potential seals, overlying the Lower Mt. Simon sandstone reservoir. Freiburg et al. [87, 88] further found laterally discontinuous mudstones within the Mt. Simon formation that were considered efficient baffles for lateral migration of CO_2. To better assess the sealing quality of these formations and thus ensure the safety of the CCS project, a detailed knowledge of the clay-mineral-associated pore- and micro-structure, and mineralogical composition of these rocks was required.

In this study, published in *The Journal of Geology*, thin section, QEMSCAN and MICP analyses were combined with quantitative XRD and high-resolution FIB-SEM to provide a multi-scale evaluation of the different cap rock lithologies with a focus on the intergranular clay-rich matrix as potential pathway for fluid migration. Based on the findings of this study, the Eau Claire as the primary seal provides the most effective sealing properties out of the three shale formations analysed. It shows the highest total clay content (71.3%) with about 60% illite-rich R0 illite-smectite, 6% chlorite and 5% authigenic $1M$ illite, and the lowest effective porosity. Based on FIB-SEM analyses, pores are observed as slit-shaped interP pores along detrital grain boundaries and as isolated spherical intraP pores within the clay matrix. The total porosity of the Eau Claire is minimal with 0.1% observed by FIB-SEM and 0.02% by MICP. Pore shapes and the spatial proximity of larger pore bodies to coarse detritus indicates that the visualised pore space was probably formed by desiccation or depressurisation after drilling and is likely not connected throughout the clay matrix.

The lower secondary confining unit, the Maquoketa shale, is, according to mineral quantification, an argillaceous dolomite and not a shale in the basal section of the formation. It contains by XRD 47.9% dolomite and only 28% clay minerals, which is in good agreement with QEMSCAN scan results (25%). Both methods identified $1M_d$ illite as the main clay mineral, with traces of chlorite and detrital muscovite. These low contents likely explain the highest observed values for porosity and capillary entry pressures of all the samples analysed. This is supported by FIB-SEM, which shows

abundant pores within the clay mineral matrix and large connected pore clusters within framboidal pyrites. The homogeneous distribution of pore bodies and the comparatively high total porosity indicates that pores are probably connected by throats below the FIB-SEM resolution, as confirmed by the relatively large MICP-detected median pore throat size of 9.1 nm. Thus, the Maquoketa is ranked the poorest seal of the three shale units overlying the Mt. Simon reservoir.

The New Albany shows the third lowest porosity and second highest capillary entry pressures based on MICP. It contains the highest amount of organic carbon (8.3%) and 53% clay minerals with abundant detrital $2M$ muscovite (24.1%), $1M_d$ illite (20.4%), chlorite (10.0%) and traces of $1M$ illite (1.6%). Muscovite and organic matter show a bedding parallel orientation and flow texture as observed by thin section analyses and FIB-SEM. The formation of the minimal porosity ($< 0.1\%$ by FIB-SEM and MICP) in the New Albany, which predominantly appears as large slit-shaped pores in close proximity to or inside organic matter, was mainly attributed to loss of volume that was generated during the transformation of organic macerals into solid bitumen. Although the thermal maturity, as determined by vitrinite reflectance measurements, is low, it is likely that some oil formation and migration has occurred. The New Albany is considered the most efficient secondary seal based on MICP and structural analysis.

The mudstone interval within the Mt. Simon reservoir shows the lowest total porosity and by far the highest capillary entry pressures. The mudstone is primarily composed of quartz (32.6%), K-feldspars (19.5% and $1M_d$ illite (39.3%) with minor amounts of $1M$ illite, hematite and dolomite. FIB-SEM shows a dense clay mineral matrix with pores being filled by large hematite crystals. Open pores are commonly observed to be isolated and in between hematite and clay. The broad spatial distribution of pores and the strong compaction of the clay matrix indicates that the minimal pore space observed by FIB-SEM is likely not connected by throats below the resolution. This is supported by the very low median pore throat size of 7.5 nm determined by MICP that probably occurs in between silica and clay-rich layers rather than the intergranular clay matrix. The Mt. Simon internal mudstone shows overall the best sealing properties but its lateral discontinuity prevents consideration as a reservoir seal. Nonetheless, these mudstones provide efficient baffles for the vertical migration of supercritical CO_2.

Based on the findings of this study, a number of important implications and constraints relevant to the study of cap rocks were derived for the methodologies applied to characterise pore space and mineralogy. It was shown that XRD provided

the most accurate identification and quantification mineral phases including clay minerals, but lacked determination of trace components with low crystallinity, such as apatites. QEMSCAN could be used to accurately quantify the clay mineral content if the intergranular matrix was predominantly single-phase, as observed in the Maquoketa, and was not enriched with nano-crystalline minerals, such as hematite in the Mt. Simon. QEMSCAN results became error prone if samples contained abundant chemically similar minerals, such as K-feldspar and illite (Mt. Simon) or calcite and dolomite (Maquoketa). FIB-SEM mineral reconstructions were found to be less accurate than QEMSCAN mappings due to limited chemical data acquisition. However, the higher resolution enabled the localisation of the effective porosity determined by MICP through the visualisation of 3D pore networks. Overall, integrating mineralogical and pore size related methods provided valuable information on the diversity of clay mineral structures in cap rocks, allowing for a better assessment of their sealing properties.

3.6 Discussion and outlook

Valuable information on the pore structures and transport properties of illitic clay minerals formed under diagenetic conditions was obtained from the FIB-SEM analyses presented in this thesis. In a novel approach, results from direct numerical simulations of fluid flow through nano-scale illite topologies were incorporated into pore scale models of tight reservoir sandstones derived from μXCT imaging. This advance in pore-scale modelling allowed the determination of more realistic permeability values for tight rocks, and is a direct adaptation of the elementary building block model proposed by Desbois et al. [58]. However, modelling relied on a single isotropic permeability value. As demonstrated in Article 1, a variety of characteristic illite structures can be observed in the aeolian Rotliegend sandstones, each with different pore space characteristics and transport properties. Therefore, it can be argued that the Navier-Stokes-Brinkman model proposed in Article 2 is an oversimplification, although the results were satisfactory. Recently, Carrillo et al. [64] systematically analysed the influence of varying permeability and porosity values of porous domains on the absolute permeability of a carbonate rock. They found that increasing the permeability of such domains from 10^{-13} to 10^{-12} m^2 enhanced the absolute permeability by only 7% and decreasing it from 10^{-13} to 10^{-15} m^2 led to a reduction of only 14%. The permeability values of the different illite textures observed in this thesis varied between 0.1 and 13.4 μD, or a total of two orders of magnitude. Therefore, it is reasonable to assume that the implementation of multiple

porous domains in the proposed Navier-Stokes-Brinkman model would not influence the results significantly.

The Navier-Stokes-Brinkman model proposed in Article 2 is based on morphological relationships between pore sizes and illite occurrence. For a more realistic implementation of the observed mineral-specific transport properties in a multi-continuum model, a precise segmentation of phases would be required. Preliminary tests with synchrotron data from Article 2 indicated that SEM-EDX, when correlated with synchrotron CT images, has the potential to provide ground truth phase images for training machine learning segmentation algorithms. However, more research is needed on the evaluation and benchmarking of the quality of such segmentation workflows. There is currently no study that distinguishes between different detrital grains, such as quartz and feldspar, as synchrotron radiation is required to obtain the necessary density contrasts.

The main problem of FIB-SEM is the size of the analysed domain between $10 \times 10 \times 10$ to $20 \times 20 \times 20$ μm^3 (see section 2.2.1), which very likely does not meet REV sizes of clay mineral structures. Kelly et al. [98] performed FIB-SEM analyses and Lattice-Boltzmann simulations on a variety of shale samples at different resolutions and concluded that this method was not capable of capturing representative domains for permeability simulations. To overcome this limitation, advances in the development of nano-tomographic techniques may provide the technical means to improve the comparatively low field of view of Ga-FIB systems. Menke et al. [66] conducted nano-CT analyses of a 65 μm long carbonate sample at a resolution of 50 nm. However, the preparation of such small samples has required complex cutting using a stand-alone laser micro-machine. Recently, electron microscope manufacturers have begun to add laser beams to their FIB-SEM systems, resulting in much higher ablation rates, leading to faster site-specific preparation of sample sites. This technical advance is likely to increase the number of nano-tomographic studies of geological materials, bridging the spatial gap between μXCT and FIB-SEM observations.

The studies presented in this thesis all used the same Rietveld approach to quantify the illite polytypes present in the fine fraction of the Upper Rotliegend reservoir sandstones as well as the mudstones and shales from the Illinois Basin. However, no systematic evaluation of the polytype composition of different size fractions, commonly performed in illite age analysis, has been undertaken. Future studies could verify the illite formation model proposed in Article 1 by ^{40}Ar-^{39}Ar or K-Ar dating of illites using Rietveld analyses as a modern alternative to the often performed full

pattern quantification of polytype weight fractions using WILDFIRE® [e.g. 99, 100]. Kuligiewicz et al. [101] have demonstrated the viability of the Rietveld approach by using a model very similar to that presented in this thesis to quantify the contents of $1M$, $1M_d$ and $2M_1$ polytypes in different size fractions to improve ^{40}Ar-^{39}Ar age dating analyses of clay gauges from the Tatra Mountains. Overall, the development of complex clay mineral structures [e.g. 102] for freely available Rietveld software such as BGMN provided a modern and reproducible method of quantifying illite polytypes that does not rely on proprietary software such as WILDFIRE®, NEWMOD® [103] or SYBILLA® [104].

3.7 Conclusion

FIB-SEM imaging for the 3D reconstruction of clay-mineral-related porosity is a challenging method that requires advanced data processing to provide reliable results. As demonstrated in this thesis, machine-learning-based segmentations offer a first step towards a more efficient application workflow for the study of reservoirs and cap rock. It was further shown that prescient and specific research questions are required to allow site-specific and representative results. This was achieved by specifically analysing illite structures in sandstones and by focusing on the intergranular matrix of shales. However, to avoid common problems regarding the representativeness of conducted analyses, complementary methods that allow a more general characterisation, such as BIB-SEM or μXCT, should be applied prior to FIB-SEM imaging.

Direct numerical simulations can be used to provide meaningful predictions of the permeability of tight reservoirs, when information from the nanometre to the centimetre scale and beyond is taken into account. The studies in this thesis were the first to improve permeability predictions of tight sandstones by using transport properties derived from FIB-SEM topologies as input to Navier-Stokes-Brinkman simulations performed on μXCT pore space models. Similar modelling approaches could be used to study transport in clay-rich rocks, such as shales or mudstones, relevant for example to radioactive waste disposal. However, further research is needed to better assess how and under what conditions the nano-scale pore space becomes transport relevant.

The analysis of polytypes and 3D structures of illite in the Bebertal sandstone provided information on transport properties and the diagenetic history of the rock. It was shown that the different polytypes formed characteristic structures, but only the $1M$ illite was considered susceptible to mobilisation. Further studies are needed

to investigate the transport properties of other clay minerals common to many reservoir rocks, such as kaolinite or chlorite, and to determine whether these particles and their associated structures are susceptible to mobilisation.

4 References

[1] R. K. Pachauri, M. R. Allen, V. R. Barros, J. Broome, W. Cramer, R. Christ, J. A. Church, L. Clarke, Q. Dahe, P. Dasgupta, et al. Climate change 2014: synthesis report. Contribution of Working Groups I, II and III to the fifth assessment report of the Intergovernmental Panel on Climate Change. 2014. doi: 10013/epic.45156.d001. URL https://epic.awi.de/id/eprint/37530/.

[2] bp. bp Statistical Review of World Energy. 2022. URL https://www.bp.com/en/global/corporate/energy-economics/statistical-review-of-world-energy.html.

[3] EU. Directive (EU) 2018/2001 of the European Parliament and of the council of 11 December 2018 on the promotion of the use of energy from renewable sources. *Official Journal of the European Union*, 2018. URL https://eur-lex.europa.eu/legal-content/EN/TXT/PDF/?uri=CELEX:32018L2001.

[4] F. Gasanzade, W. T. Pfeiffer, F. Witte, I. Tuschy, and S. Bauer. Subsurface renewable energy storage capacity for hydrogen, methane and compressed air – A performance assessment study from the North German Basin. *Renewable and Sustainable Energy Reviews*, 149:111422, Oct. 2021. doi: 10.1016/j.rser.2021.111422. URL https://doi.org/10.1016/j.rser.2021.111422.

[5] R. H. Worden, P. J. Armitage, A. R. Butcher, J. M. Churchill, A. E. Csoma, C. Hollis, R. H. Lander, and J. E. Omma. Petroleum reservoir quality prediction: overview and contrasting approaches from sandstone and carbonate communities. *Geological Society, London, Special Publications*, 435(1):1–31, Jan. 2018. doi: 10.1144/sp435.21. URL https://doi.org/10.1144/sp435.21.

[6] J. Kaldi, R. Daniel, E. Tenthorey, K. Michael, U. Schacht, A. Nicol, J. Underschultz, and G. Backe. Containment of CO2 in CCS: Role of Caprocks and Faults. *Energy Procedia*, 37:5403–5410, 2013. doi: 10.1016/j.egypro.2013.06.458. URL https://doi.org/10.1016/j.egypro.2013.06.458.

[7] R. F. Daniel and J. G. Kaldi. Evaluating Seal Capacity of Cap Rocks and Intraformational Barriers for CO_2 Containment. In *Carbon Dioxide Sequestration in Geological Media—State of the Science: PESA Eastern Australian Basins Symposium III*, volume 59, Dallas, Texas, 2008. American Association of Petroleum Geologists. doi: 10.1306/13171247St59227.

[8] S. Bauer, C. Beyer, F. Dethlefsen, P. Dietrich, R. Duttmann, M. Ebert, V. Feeser, U. Görke, R. Köber, O. Kolditz, W. Rabbel, T. Schanz, D. Schäfer, H. Würdemann, and A. Dahmke. Impacts of the use of the geological subsurface for energy storage: an investigation concept. *Environmental Earth Sciences*, 70(8):3935–3943, Nov. 2013. doi: 10.1007/s12665-013-2883-0. URL https://doi.org/10.1007/s12665-013-2883-0.

[9] R. H. Worden and S. Morad, editors. *Clay Mineral Cements in Sandstones*. Wiley, Oct. 1999. doi: 10.1002/9781444304336. URL https://doi.org/10.1002/9781444304336.

[10] S. Morad, K. Al-Ramadan, J. M. Ketzer, and L. F. D. Ros. The impact of diagenesis on the heterogeneity of sandstone reservoirs: A review of the role of depositional facies and sequence stratigraphy. *AAPG Bulletin*, 94(8): 1267–1309, Aug. 2010. doi: 10.1306/04211009178. URL https://doi.org/10.1306/04211009178.

[11] ISO 14688-1:2017. Geotechnical investigation and testing — Identification and classification of soil — Part 1: Identification and description. Standard, International Organization for Standardization, Geneva, CH, 2017.

[12] S. Guggenheim. Definition of Clay and Clay Mineral: Joint Report of the AIPEA Nomenclature and CMS Nomenclature Committees. *Clays and Clay Minerals*, 43(2):255–256, 1995. doi: 10.1346/ccmn.1995.0430213. URL https://doi.org/10.1346/ccmn.1995.0430213.

[13] L. N. Warr. Earth's clay mineral inventory and its climate interaction: A quantitative assessment. *Earth-Science Reviews*, 234:104198, Nov. 2022. doi: 10.1016/j.earscirev.2022.104198. URL https://doi.org/10.1016/j.earscirev.2022.104198.

[14] S. I. Tsipursky and V. A. Drits. The distribution of octahedral cations in the 2:1 layers of dioctahedral smectites studied by oblique-texture electron diffraction. *Clay Minerals*, 19(2):177–193, Apr. 1984. doi: 10.1180/claymin.1984.019.2.05. URL https://doi.org/10.1180/claymin.1984.019.2.05.

[15] V. A. Drits and B. B. Zviagina. Trans-vacant and cis-vacant 2:1 Layer Silicates: Structural Features, Identification, and Occurrence. *Clays and Clay Minerals*, 57(4):405–415, Aug. 2009. doi: 10.1346/ccmn.2009.0570401. URL https://doi.org/10.1346/ccmn.2009.0570401.

[16] K. Momma and F. Izumi. VESTA 3 for three-dimensional visualization of crystal, volumetric and morphology data. *Journal of Applied Crystallography*, 44(6):1272–1276, Oct. 2011. doi: 10.1107/s0021889811038970. URL https://doi.org/10.1107/s0021889811038970.

[17] V. A. Drits, B. B. Zviagina, D. K. McCarty, and A. L. Salyn. Factors responsible for crystal-chemical variations in the solid solutions from illite to aluminoceladonite and from glauconite to celadonite. *American Mineralogist*, 95(2-3):348–361, Feb. 2010. doi: 10.2138/am.2010.3300. URL https://doi.org/10.2138/am.2010.3300.

[18] A. Meunier and B. Velde. *Illite*. Springer Berlin Heidelberg, 2004. doi: 10.1007/978-3-662-07850-1. URL https://doi.org/10.1007/978-3-662-07850-1.

[19] D. R. Pevear. Illite and hydrocarbon exploration. *Proceedings of the National Academy of Sciences*, 96(7):3440–3446, Mar. 1999. doi: 10.1073/pnas.96.7.3440. URL https://doi.org/10.1073/pnas.96.7.3440.

[20] P. J. Hamilton. K-Ar Dating of Illite in Hydrocarbon Reservoirs. *Clay Minerals*, 24(2):215–231, 1989. doi: 10.1180/claymin.1989.024.2.08. URL https://doi.org/10.1180/claymin.1989.024.2.08.

[21] R. H. Worden and S. Morad. Clay Minerals in Sandstones: Controls on Formation, Distribution and Evolution. In *Clay Mineral Cements in Sandstones*, pages 1–41. Blackwell Publishing Ltd. doi: 10.1002/9781444304336.ch1. URL https://doi.org/10.1002/9781444304336.ch1.

[22] J. Hower, E. V. Eslinger, M. E. Hower, and E. A. Perry. Mechanism of burial metamorphism of argillaceous sediment: 1. Mineralogical and chemical evidence. *Geological Society of America Bulletin*, 87(5):725, 1976. doi: 10.1130/0016-7606(1976)87<725:mobmoa>2.0.co;2. URL https://doi.org/10.1130/0016-7606(1976)87<725:mobmoa>2.0.co;2.

[23] J. F. Burst. Diagenesis of Gulf Coast Clayey Sediments and Its Possible Relation to Petroleum Migration. *AAPG Bulletin*, 53, 1969. doi: 10.1306/5d25c595-16c1-11d7-8645000102c1865d. URL https://doi.org/10.1306/5d25c595-16c1-11d7-8645000102c1865d.

[24] J. T. Freiburg, M. Amer, K. Henkel, K. Wemmer, and G. H. Grathoff. Illitization in the Mt. Simon Sandstone, Illinois Basin, USA: Implications for carbon dioxide storage. *Marine and Petroleum Geology*, 146:105963, Dec. 2022. doi: 10.1016/j.marpetgeo.2022.105963. URL https://doi.org/10.1016/j.marpetgeo.2022.105963.

[25] A. Bauer, B. Velde, and R. Gaupp. Experimental constraints on illite crystal morphology. *Clay Minerals*, 35(3):587–597, June 2000. doi: 10.1180/000985500546909. URL https://doi.org/10.1180/000985500546909.

[26] K. W. Glennie, G. C. Mudd, and P. J. C. Nagtegaal. Depositional environment and diagenesis of Permian Rotliegendes sandstones in Leman Bank and Sole Pit areas of the UK southern North Sea. *Journal of the Geological Society*, 135 (1):25–34, Jan. 1978. doi: 10.1144/gsjgs.135.1.0025. URL https://doi.org/10.1144/gsjgs.135.1.0025.

[27] N. J. Hancock. Possible causes of Rotliegend sandstone diagenesis in northern West Germany. *Journal of the Geological Society*, 135(1):35–40, Jan. 1978. doi: 10.1144/gsjgs.135.1.0035. URL https://doi.org/10.1144/gsjgs.135.1.0035.

[28] H. Zwingmann, N. Clauer, and R. Gaupp. Timing of fluid flow in a sandstone reservoir of the north German Rotliegend (Permian) by K-Ar dating of related hydrothermal illite. *Geological Society, London, Special Publications*, 144(1):

91–106, Jan. 1998. doi: 10.1144/gsl.sp.1998.144.01.07. URL https://doi.org/10.1144/gsl.sp.1998.144.01.07.

[29] K. Ziegler. Clay minerals of the Permian Rotliegend Group in the North Sea and adjacent areas. *Clay Minerals*, 41(1):355–393, Mar. 2006. doi: 10.1180/0009855064110200. URL https://doi.org/10.1180/0009855064110200.

[30] E. W. Washburn. The Dynamics of Capillary Flow. *Physical Review*, 17(3):273–283, Mar. 1921. doi: 10.1103/physrev.17.273. URL https://doi.org/10.1103/physrev.17.273.

[31] A. Busch, K. Schweinar, N. Kampman, A. Coorn, V. Pipich, A. Feoktystov, L. Leu, A. Amann-Hildenbrand, and P. Bertier. Determining the porosity of mudrocks using methodological pluralism. *Geological Society, London, Special Publications*, 454(1):15–38, Jan. 2017. doi: 10.1144/sp454.1. URL https://doi.org/10.1144/sp454.1.

[32] R. A. Ketcham and W. D. Carlson. Acquisition, optimization and interpretation of X-ray computed tomographic imagery: applications to the geosciences. *Computers & Geosciences*, 27(4):381–400, May 2001. doi: 10.1016/s0098-3004(00)00116-3. URL https://doi.org/10.1016/s0098-3004(00)00116-3.

[33] V. Cnudde and M. Boone. High-resolution X-ray computed tomography in geosciences: A review of the current technology and applications. *Earth-Science Reviews*, 123:1–17, Aug. 2013. doi: 10.1016/j.earscirev.2013.04.003. URL https://doi.org/10.1016/j.earscirev.2013.04.003.

[34] A. E. Peksa, K.-H. A. Wolf, and P. L. Zitha. Bentheimer sandstone revisited for experimental purposes. *Marine and Petroleum Geology*, 67:701–719, Nov. 2015. doi: 10.1016/j.marpetgeo.2015.06.001. URL https://doi.org/10.1016/j.marpetgeo.2015.06.001.

[35] H. Andrä, N. Combaret, J. Dvorkin, E. Glatt, J. Han, M. Kabel, Y. Keehm, F. Krzikalla, M. Lee, C. Madonna, M. Marsh, T. Mukerji, E. H. Saenger, R. Sain, N. Saxena, S. Ricker, A. Wiegmann, and X. Zhan. Digital rock physics benchmarks—part II: Computing effective properties. *Computers & Geosciences*, 50:33–43, Jan. 2013. doi: 10.1016/j.cageo.2012.09.008. URL https://doi.org/10.1016/j.cageo.2012.09.008.

[36] N. Saxena, R. Hofmann, F. O. Alpak, S. Berg, J. Dietderich, U. Agarwal, K. Tandon, S. Hunter, J. Freeman, and O. B. Wilson. References and benchmarks for pore-scale flow simulated using micro-CT images of porous media and digital rocks. *Advances in Water Resources*, 109:211–235, Nov. 2017. doi: 10.1016/j.advwatres.2017.09.007. URL https://doi.org/10.1016/j.advwatres.2017.09.007.

[37] B. Callow, I. Falcon-Suarez, H. Marin-Moreno, J. M. Bull, and S. Ahmed. Optimal X-ray micro-CT image based methods for porosity and permeability quantification in heterogeneous sandstones. *Geophysical Journal International*, 223(2):1210–1229, June 2020. doi: 10.1093/gji/ggaa321. URL https://doi.org/10.1093/gji/ggaa321.

[38] T. Saif, Q. Lin, A. R. Butcher, B. Bijeljic, and M. J. Blunt. Multi-scale multi-dimensional microstructure imaging of oil shale pyrolysis using X-ray micro-tomography, automated ultra-high resolution SEM, MAPS Mineralogy and FIB-SEM. *Applied Energy*, 202:628–647, Sept. 2017. doi: 10.1016/j.apenergy.2017.05.039. URL https://doi.org/10.1016/j.apenergy.2017.05.039.

[39] R. Wirth. Focused Ion Beam (FIB) combined with SEM and TEM: Advanced analytical tools for studies of chemical composition, microstructure and crystal structure in geomaterials on a nanometre scale. *Chemical Geology*, 261(3-4):217–229, Apr. 2009. doi: 10.1016/j.chemgeo.2008.05.019. URL https://doi.org/10.1016/j.chemgeo.2008.05.019.

[40] G. Desbois, J. L. Urai, and P. A. Kukla. Morphology of the pore space in claystones – evidence from BIB/FIB ion beam sectioning and cryo-SEM observations. *eEarth*, 4(1):15–22, July 2009. doi: 10.5194/ee-4-15-2009. URL https://doi.org/10.5194/ee-4-15-2009.

[41] R. G. Loucks, R. M. Reed, S. C. Ruppel, and D. M. Jarvie. Morphology, Genesis, and Distribution of Nanometer-Scale Pores in Siliceous Mudstones of the Mississippian Barnett Shale. *Journal of Sedimentary Research*, 79(12):848–861, Nov. 2009. doi: 10.2110/jsr.2009.092. URL https://doi.org/10.2110/jsr.2009.092.

[42] M. Milner, R. McLin, and J. Petriello. Imaging Texture and Porosity in Mudstones and Shales: Comparison of Secondary and Ion-Milled Backscatter SEM Methods. In *All Days*. SPE, Oct. 2010. doi: 10.2118/138975-ms. URL https://doi.org/10.2118/138975-ms.

[43] J. Schieber. Common Themes in the Formation and Preservation of Intrinsic Porosity in Shales and Mudstones – Illustrated With Examples Across the Phanerozoic. In *All Days*. SPE, Feb. 2010. doi: 10.2118/132370-ms. URL https://doi.org/10.2118/132370-ms.

[44] M. Houben, A. Barnhoorn, M. Drury, C. Peach, and C. Spiers. Microstructural Investigation of the Whitby Mudstone (UK) As an Analog for Posidonia Shale (NL). In *Proceedings*. EAGE Publications BV, 2014. doi: 10.3997/2214-4609.20141056. URL https://doi.org/10.3997/2214-4609.20141056.

[45] M. Houben, N. Hardebol, A. Barnhoorn, Q. Boersma, A. Carone, Y. Liu, D. de Winter, C. Peach, and M. Drury. Fluid flow from matrix to fractures in Early Jurassic shales. *International Journal of Coal Geology*, 175:26–39, Apr.

2017. doi: 10.1016/j.coal.2017.03.012. URL https://doi.org/10.1016/j.coal.2017.03.012.

[46] J. Klaver, G. Desbois, R. Littke, and J. L. Urai. BIB-SEM characterization of pore space morphology and distribution in postmature to overmature samples from the Haynesville and Bossier Shales. *Marine and Petroleum Geology*, 59: 451–466, Jan. 2015. doi: 10.1016/j.marpetgeo.2014.09.020. URL https://doi.org/10.1016/j.marpetgeo.2014.09.020.

[47] S. Hemes, G. Desbois, J. L. Urai, B. Schröppel, and J.-O. Schwarz. Multi-scale characterization of porosity in Boom Clay (HADES-level, Mol, Belgium) using a combination of X-ray μ-CT, 2D BIB-SEM and FIB-SEM tomography. *Microporous and Mesoporous Materials*, 208:1–20, May 2015. doi: 10.1016/j.micromeso.2015.01.022. URL https://doi.org/10.1016/j.micromeso.2015.01.022.

[48] R. G. Loucks, R. M. Reed, S. C. Ruppel, and U. Hammes. Spectrum of pore types and networks in mudrocks and a descriptive classification for matrix-related mudrock pores. *AAPG Bulletin*, 96(6):1071–1098, June 2012. doi: 10.1306/08171111061. URL https://doi.org/10.1306/08171111061.

[49] P. W. Choquette and C. P. Lloyd. Geologic Nomenclature and Classification of Porosity in Sedimentary Carbonates. *AAPG Bulletin*, 54, 1970. doi: 10.1306/5d25c98b-16c1-11d7-8645000102c1865d. URL https://doi.org/10.1306/5d25c98b-16c1-11d7-8645000102c1865d.

[50] J. Rouquerol, D. Avnir, C. W. Fairbridge, D. H. Everett, J. M. Haynes, N. Pernicone, J. D. F. Ramsay, K. S. W. Sing, and K. K. Unger. Recommendations for the characterization of porous solids (Technical Report). *Pure and Applied Chemistry*, 66(8):1739–1758, Jan. 1994. doi: 10.1351/pac199466081739. URL https://doi.org/10.1351/pac199466081739.

[51] P. Cosenza, D. Prêt, A.-L. Fauchille, and S. Hedan. Representative elementary area of shale at the mesoscopic scale. *International Journal of Coal Geology*, 216:103316, Dec. 2019. doi: 10.1016/j.coal.2019.103316. URL https://doi.org/10.1016/j.coal.2019.103316.

[52] L. M. Keller, P. Schuetz, R. Erni, M. D. Rossell, F. Lucas, P. Gasser, and L. Holzer. Characterization of multi-scale microstructural features in Opalinus Clay. *Microporous and Mesoporous Materials*, 170:83–94, Apr. 2013. doi: 10.1016/j.micromeso.2012.11.029. URL https://doi.org/10.1016/j.micromeso.2012.11.029.

[53] J. Klaver, S. Hemes, M. Houben, G. Desbois, Z. Radi, and J. L. Urai. The connectivity of pore space in mudstones: insights from high-pressure Woods metal injection, BIB-SEM imaging, and mercury intrusion porosimetry. *Geofluids*, 15(4):577–591, Jan. 2015. doi: 10.1111/gfl.12128. URL https://doi.org/10.1111/gfl.12128.

[54] N. Kampman, P. Bertier, A. Busch, J. Snippe, J. Harrington, V. Pipich, A. Maskell, and M. Bickle. Validating Reactive Transport Models of CO2-brine-Rock Reactions in Caprocks Using Observations from a Natural CO2 Reservoir. *Energy Procedia*, 114:4902–4916, July 2017. doi: 10.1016/j.egypro.2017.03.1632. URL https://doi.org/10.1016/j.egypro.2017.03.1632.

[55] T. Ma, C. Yang, P. Chen, X. Wang, and Y. Guo. On the damage constitutive model for hydrated shale using CT scanning technology. *Journal of Natural Gas Science and Engineering*, 28:204–214, Jan. 2016. doi: 10.1016/j.jngse.2015.11.025. URL https://doi.org/10.1016/j.jngse.2015.11.025.

[56] L. Hou, Z. Yu, X. Luo, and S. Wu. Self-sealing of caprocks during CO2 geological sequestration. *Energy*, 252:124064, Aug. 2022. doi: 10.1016/j.energy.2022.124064. URL https://doi.org/10.1016/j.energy.2022.124064.

[57] B. Bera, S. K. Mitra, and D. Vick. Understanding the micro structure of Berea Sandstone by the simultaneous use of micro-computed tomography (micro-CT) and focused ion beam-scanning electron microscopy (FIB-SEM). *Micron*, 42(5):412–418, July 2011. doi: 10.1016/j.micron.2010.12.002. URL https://doi.org/10.1016/j.micron.2010.12.002.

[58] G. Desbois, J. L. Urai, S. Hemes, B. Schröppel, J.-O. Schwarz, M. Mac, and D. Weiel. Multi-scale analysis of porosity in diagenetically altered reservoir sandstone from the Permian Rotliegend (Germany). *Journal of Petroleum Science and Engineering*, 140:128–148, Apr. 2016. doi: 10.1016/j.petrol.2016.01.019. URL https://doi.org/10.1016/j.petrol.2016.01.019.

[59] Ø. Markussen, H. Dypvik, E. Hammer, H. Long, and Ø. Hammer. 3D characterization of porosity and authigenic cementation in Triassic conglomerates/arenites in the Edvard Grieg field using 3D micro-CT imaging. *Marine and Petroleum Geology*, 99:265–281, Jan. 2019. doi: 10.1016/j.marpetgeo.2018.10.015. URL https://doi.org/10.1016/j.marpetgeo.2018.10.015.

[60] T. Bultreys, W. D. Boever, and V. Cnudde. Imaging and image-based fluid transport modeling at the pore scale in geological materials: A practical introduction to the current state-of-the-art. *Earth-Science Reviews*, 155:93–128, Apr. 2016. doi: 10.1016/j.earscirev.2016.02.001. URL https://doi.org/10.1016/j.earscirev.2016.02.001.

[61] M. J. Blunt, B. Bijeljic, H. Dong, O. Gharbi, S. Iglauer, P. Mostaghimi, A. Paluszny, and C. Pentland. Pore-scale imaging and modelling. *Advances in Water Resources*, 51:197–216, Jan. 2013. doi: 10.1016/j.advwatres.2012.03.003. URL https://doi.org/10.1016/j.advwatres.2012.03.003.

[62] S. Peng, F. Marone, and S. Dultz. Resolution effect in X-ray microcomputed tomography imaging and small pore's contribution to permeability for a Berea sandstone. *Journal of Hydrology*, 510:403–411, Mar. 2014. doi: 10.1016/j.

jhydrol.2013.12.028. URL https://doi.org/10.1016/j.jhydrol.2013.12.028.

[63] C. Soulaine, F. Gjetvaj, C. Garing, S. Roman, A. Russian, P. Gouze, and H. A. Tchelepi. The Impact of Sub-Resolution Porosity of X-ray Microtomography Images on the Permeability. *Transport in Porous Media*, 113(1): 227–243, Apr. 2016. doi: 10.1007/s11242-016-0690-2. URL https://doi.org/10.1007/s11242-016-0690-2.

[64] F. J. Carrillo, C. Soulaine, and I. C. Bourg. The impact of sub-resolution porosity on numerical simulations of multiphase flow. *Advances in Water Resources*, 161:104094, Mar. 2022. doi: 10.1016/j.advwatres.2021.104094. URL https://doi.org/10.1016/j.advwatres.2021.104094.

[65] D. H. Kang, E. Yang, and T. S. Yun. Stokes-Brinkman Flow Simulation Based on 3-D μ-CT Images of Porous Rock Using Grayscale Pore Voxel Permeability. *Water Resources Research*, 55(5):4448–4464, May 2019. doi: 10.1029/2018wr024179. URL https://doi.org/10.1029/2018wr024179.

[66] H. P. Menke, Y. Gao, S. Linden, and M. G. Andrew. Using Nano-XRM and High-Contrast Imaging to Inform Micro-Porosity Permeability During Stokes–Brinkman Single and Two-Phase Flow Simulations on Micro-CT Images. *Frontiers in Water*, 4, July 2022. doi: 10.3389/frwa.2022.935035. URL https://doi.org/10.3389/frwa.2022.935035.

[67] Y. K. Kharaka, J. J. Thordsen, S. D. Hovorka, H. S. Nance, D. R. Cole, T. J. Phelps, and K. G. Knauss. Potential environmental issues of CO2 storage in deep saline aquifers: Geochemical results from the Frio-I Brine Pilot test, Texas, USA. *Applied Geochemistry*, 24(6):1106–1112, June 2009. doi: 10.1016/j.apgeochem.2009.02.010. URL https://doi.org/10.1016/j.apgeochem.2009.02.010.

[68] S. Ó. Snæbjörnsdóttir, B. Sigfússon, C. Marieni, D. Goldberg, S. R. Gislason, and E. H. Oelkers. Carbon dioxide storage through mineral carbonation. *Nature Reviews Earth & Environment*, 1(2):90–102, Jan. 2020. doi: 10.1038/s43017-019-0011-8. URL https://doi.org/10.1038/s43017-019-0011-8.

[69] S. Molins, D. Trebotich, L. Yang, J. B. Ajo-Franklin, T. J. Ligocki, C. Shen, and C. I. Steefel. Pore-Scale Controls on Calcite Dissolution Rates from Flow-through Laboratory and Numerical Experiments. *Environmental Science & Technology*, 48(13):7453–7460, June 2014. doi: 10.1021/es5013438. URL https://doi.org/10.1021/es5013438.

[70] O. Iliev, Z. Lakdawala, K. H. Neßler, T. Prill, Y. Vutov, Y. Yang, and J. Yao. On the pore-scale modeling and simulation of reactive transport in 3D geometries. *Mathematical Modelling and Analysis*, 22(5):671–694, Sept. 2017. doi: 10.3846/13926292.2017.1356759. URL https://doi.org/10.3846/13926292.2017.1356759.

[71] C. Soulaine, S. Roman, A. Kovscek, and H. A. Tchelepi. Pore-scale modelling of multiphase reactive flow: application to mineral dissolution with production of. *Journal of Fluid Mechanics*, 855:616–645, Sept. 2018. doi: 10.1017/jfm.2018.655. URL https://doi.org/10.1017/jfm.2018.655.

[72] J. Maes and H. P. Menke. GeoChemFoam: Direct Modelling of Multiphase Reactive Transport in Real Pore Geometries with Equilibrium Reactions. *Transport in Porous Media*, 139(2):271–299, Aug. 2021. doi: 10.1007/s11242-021-01661-8. URL https://doi.org/10.1007/s11242-021-01661-8.

[73] T. Prill, C. Fischer, P. Gavrilenko, and O. Iliev. Implementing the Variability of Crystal Surface Reactivity in Reactive Transport Modeling. *Transport in Porous Media*, 140(2):535–557, Oct. 2021. doi: 10.1007/s11242-021-01697-w. URL https://doi.org/10.1007/s11242-021-01697-w.

[74] A. S. Abd and A. S. Abushaikha. Reactive transport in porous media: a review of recent mathematical efforts in modeling geochemical reactions in petroleum subsurface reservoirs. *SN Applied Sciences*, 3(4), Mar. 2021. doi: 10.1007/s42452-021-04396-9. URL https://doi.org/10.1007/s42452-021-04396-9.

[75] S. Hale, E. T. Pedrosa, A. Jacob, M. Reinhardt, F. Enzmann, M. Kersten, C. Butscher, and P. Blum. Upscaling calcite dissolution rates in a tight reservoir sandstone. *Environmental Earth Sciences*, 81(11), May 2022. doi: 10.1007/s12665-022-10399-5. URL https://doi.org/10.1007/s12665-022-10399-5.

[76] J. Rathore, E. Fjaer, R. Holt, and L. Renlie. P- and S-wave anisotropy of a synthetic sandstone with controlled crack geometryl1. *Geophysical Prospecting*, 43(6):711–728, Aug. 1995. doi: 10.1111/j.1365-2478.1995.tb00276.x. URL https://doi.org/10.1111/j.1365-2478.1995.tb00276.x.

[77] S. W. den Brok, C. David, and Y. Bernabé. Preparation of synthetic sandstones with variable cementation for studying the physical properties of granular rocks. *Comptes Rendus de lAcadémie des Sciences - Series IIA - Earth and Planetary Science*, 325(7):487–492, Oct. 1997. doi: 10.1016/s1251-8050(97)89866-7. URL https://doi.org/10.1016/s1251-8050(97)89866-7.

[78] E. S. Al-Homadhi. Artificial Sandstone Cores Production with a Wide Range of Petrophysical Properties. *Journal of King Saud University - Engineering Sciences*, 14(1):95–117, 2002. doi: 10.1016/s1018-3639(18)30747-5. URL https://doi.org/10.1016/s1018-3639(18)30747-5.

[79] A. Kozhagulova, A. Shabdirova, N. H. Minh, and Y. Zhao. An integrated laboratory experiment of realistic diagenesis, perforation and sand production using a large artificial sandstone specimen. *Journal of Rock Mechanics and Geotechnical Engineering*, 13(1):154–166, Feb. 2021. doi: 10.1016/j.jrmge.2020.09.004. URL https://doi.org/10.1016/j.jrmge.2020.09.004.

[80] A. P. Dimou, H. P. Menke, and J. Maes. Benchmarking the Viability of 3D Printed Micromodels for Single Phase Flow Using Particle Image Velocimetry and Direct Numerical Simulations. *Transport in Porous Media*, 141(2):279–294, Dec. 2021. doi: 10.1007/s11242-021-01718-8. URL https://doi.org/10.1007/s11242-021-01718-8.

[81] C. Fischer, R. Gaupp, M. Dimke, and O. Sill. A 3D high resolution model of bounding surfaces in aeolian-fluvial deposits: an outcrop analogue study from the Permian Rotliegend, Northern Germany. *Journal of Petroleum Geology*, 30 (3):257–273, July 2007. doi: 10.1111/j.1747-5457.2007.00257.x. URL https://doi.org/10.1111/j.1747-5457.2007.00257.x.

[82] C. Fischer, I. Dunkl, H. von Eynatten, J. R. Wijbrans, and R. Gaupp. Products and timing of diagenetic processes in Upper Rotliegend sandstones from Bebertal (North German Basin, Parchim Formation, Flechtingen High, Germany). *Geological Magazine*, 149(5):827–840, Jan. 2012. doi: 10.1017/s0016756811001087. URL https://doi.org/10.1017/s0016756811001087.

[83] R. J. Finley. An overview of the Illinois Basin - Decatur Project. *Greenhouse Gases: Science and Technology*, 4(5):571–579, Sept. 2014. doi: 10.1002/ghg.1433. URL https://doi.org/10.1002/ghg.1433.

[84] R. A. Bauer, R. Will, S. E. Greenberg, and S. G. Whittaker. Illinois Basin–Decatur Project. In *Geophysics and Geosequestration*, pages 339–370. Cambridge University Press, Apr. 2019. doi: 10.1017/9781316480724.020. URL https://doi.org/10.1017/9781316480724.020.

[85] S. E. Greenberg, R. Bauer, R. Will, R. L. II, M. Carney, H. Leetaru, and J. Medler. Geologic Carbon Storage at a One Million Tonne Demonstration Project: Lessons Learned from the Illinois Basin – Decatur Project. *Energy Procedia*, 114:5529–5539, July 2017. doi: 10.1016/j.egypro.2017.03.1913. URL https://doi.org/10.1016/j.egypro.2017.03.1913.

[86] R. A. Bauer, R. Will, G. El-Kaseeh, P. Jaques, S. Greenberg, and M. Carney. Microseismic Monitoring, Event Location, and Focal Mechanisms at the Illinois Basin–Decatur Project, Decatur, Illinois, USA, Mar. 2022. URL https://doi.org/10.1002/9781119156871.ch19.

[87] J. T. Freiburg, D. G. Morse, H. E. Leetaru, R. P. Hoss, and Q. Yan. A depositional and diagenetic characterization of the Mt. Simon sandstone at the Illinois Basin-Decatur Project carbon capture and storage site, Decatur, Illinois, USA. *Illinois State Geological Survey Circular*, 583, 2014.

[88] J. T. Freiburg, R. W. Ritzi, and K. S. Kehoe. Depositional and diagenetic controls on anomalously high porosity within a deeply buried CO2 storage reservoir—The Cambrian Mt. Simon Sandstone, Illinois Basin, USA. *International Journal of Greenhouse Gas Control*, 55:42–54, Dec. 2016. doi: 10.1016/j.ijggc.2016.11.005. URL https://doi.org/10.1016/j.ijggc.2016.11.005.

[89] J. T. Freiburg, J. H. McBride, D. H. Malone, and H. E. Leetaru. Petrology, geochronology, and geophysical characterization of Mesoproterozoic rocks in central Illinois, USA. *Geoscience Frontiers*, 11(2):581–596, Mar. 2020. doi: 10.1016/j.gsf.2019.07.004. URL https://doi.org/10.1016/j.gsf.2019.07.004.

[90] J. T. Freiburg, M. Peltz, D. C. Willette, and G. H. Grathoff. High-resolution pore space imaging, mineralogical characterization, and sealing capacity estimates of confining units at a geologic carbon storage demonstration: the Illinois Basin–Decatur Project, USA. *The Journal of Geology*, Sept. 2022. doi: 10.1086/722563. URL https://doi.org/10.1086/722563.

[91] M. Andrew. A quantified study of segmentation techniques on synthetic geological XRM and FIB-SEM images. *Computational Geosciences*, 22(6):1503–1512, Aug. 2018. doi: 10.1007/s10596-018-9768-y. URL https://doi.org/10.1007/s10596-018-9768-y.

[92] A. Kazak, K. Simonov, and V. Kulikov. Machine-Learning-Assisted Segmentation of Focused Ion Beam-Scanning Electron Microscopy Images with Artifacts for Improved Void-Space Characterization of Tight Reservoir Rocks. *SPE Journal*, 26(04):1739–1758, Mar. 2021. doi: 10.2118/205347-pa. URL https://doi.org/10.2118/205347-pa.

[93] S. Berg, D. Kutra, T. Kroeger, C. N. Straehle, B. X. Kausler, C. Haubold, M. Schiegg, J. Ales, T. Beier, M. Rudy, K. Eren, J. I. Cervantes, B. Xu, F. Beuttenmueller, A. Wolny, C. Zhang, U. Koethe, F. A. Hamprecht, and A. Kreshuk. ilastik: interactive machine learning for (bio)image analysis. *Nature Methods*, 16(12):1226–1232, Sept. 2019. doi: 10.1038/s41592-019-0582-9. URL https://doi.org/10.1038/s41592-019-0582-9.

[94] H. Darcy. Les fontaines publiques de la ville de Dijon. Dalmont, Paris, 1856.

[95] H. C. Brinkman. Calculations on the flow of heterogeneous mixtures through porous media. *Flow, Turbulence and Combustion*, 1(1), Dec. 1949. doi: 10.1007/bf02120339. URL https://doi.org/10.1007/bf02120339.

[96] D. D. Eberl, V. A. Drits, and J. Srodon. Deducing growth mechanisms for minerals from the shapes of crystal size distributions. *American Journal of Science*, 298(6):499–533, June 1998. doi: 10.2475/ajs.298.6.499. URL https://doi.org/10.2475/ajs.298.6.499.

[97] M. Heidsiek, C. Butscher, P. Blum, and C. Fischer. Small-scale diagenetic facies heterogeneity controls porosity and permeability pattern in reservoir sandstones. *Environmental Earth Sciences*, 79(18), Sept. 2020. doi: 10.1007/s12665-020-09168-z. URL https://doi.org/10.1007/s12665-020-09168-z.

[98] S. Kelly, H. El-Sobky, C. Torres-Verdín, and M. T. Balhoff. Assessing the utility of FIB-SEM images for shale digital rock physics. *Advances in Water*

Resources, 95:302–316, Sept. 2016. doi: 10.1016/j.advwatres.2015.06.010. URL https://doi.org/10.1016/j.advwatres.2015.06.010.

[99] G. H. Grathoff. Illite Polytype Quantification using WILDFIRE© Calculated X-Ray Diffraction Patterns. *Clays and Clay Minerals*, 44(6):835–842, 1996. doi: 10.1346/ccmn.1996.0440615. URL https://doi.org/10.1346/ccmn.1996.0440615.

[100] Y. Song and H. Sim. Illite-Age-Analysis (IAA) for the Dating of Shallow Faults: Prerequisites and Procedures for Improvement. *Minerals*, 11(11):1162, Oct. 2021. doi: 10.3390/min11111162. URL https://doi.org/10.3390/min11111162.

[101] A. Kuligiewicz, M. Skiba, M. Szczerba, C. M. Hall, and D. Bakowska. Correction: Extraction of 40Ar-39Ar ages from a multicomponent mixture: a case study from the Tatra Mountains, Poland. *Clays and Clay Minerals*, 70(2):305–305, Apr. 2022. doi: 10.1007/s42860-022-00182-9. URL https://doi.org/10.1007/s42860-022-00182-9.

[102] K. Ufer, R. Kleeberg, J. Bergmann, and R. Dohrmann. Rietveld Refinement of Disordered Illite-Smectite Mixed-Layer Structures by a Recursive Algorithm. II: Powder-Pattern Refinement and Quantitative Phase Analysis. *Clays and Clay Minerals*, 60(5):535–552, Oct. 2012. doi: 10.1346/ccmn.2012.0600508. URL https://doi.org/10.1346/ccmn.2012.0600508.

[103] D. M. Moore, R. C. Reynolds Jr, et al. *X-ray Diffraction and the Identification and Analysis of Clay Minerals.* Oxford University Press (OUP), 1989.

[104] E. Zeelmaekers, D. McCarty, and K. Mystkowski. SYBILLA user manual. *Chevron proprietary software, unpublished manual, Houston, Texas, USA, 16pp*, 2007.

5 Publications

5.1 List of peer-reviewed thesis publications

- **Article 1**

  Peltz, M., Jacob, A., Grathoff, G.H., Enzmann, F., Kersten, M. and Warr, L.N. (2022): A FIB-SEM Study of Illite Morphology in Aeolian Rotliegend Sandstones: Implications for Understanding the Petrophysical Properties of Reservoir Rocks. *Clays and Clay Minerals*, 70, 84-105.

  DOI: 10.1007/s42860-022-00174-9

- **Article 2**

  Jacob, A., **Peltz, M.**, Hale, S., Enzmann, F., Moravcova, O., Warr, L.N., Grathoff, G.H., Blum, P. and Kersten, M. (2021): Simulating permeability reduction by clay mineral nanopores in a tight sandstone by combining computer X-ray microtomography and focussed ion beam scanning electron microscopy imaging. *Solid Earth*, 12, 1-14.

  DOI: 10.5194/se-12-1-2021

- **Article 3**

  Peltz, M., Warr, L.N., Hale, S. and Blum, P. (2023): Developing synthetic sandstones using geopolymer binder for constraining coupled processes in porous rocks. *SN Applied Sciences*, 5, Article number 87.

  DOI: 10.1007/s42452-023-05301-2

- **Article 4**

  Freiburg, J.T., **Peltz, M.**, Willette, D.C. and Grathoff, G.H. (2022): High-resolution pore space imaging, mineralogical characterization, and sealing capacity estimates of confining units at a geologic carbon storage demonstration: the Illinois Basin–Decatur Project, USA. *The Journal of Geology*, 130 (5), 335-355.

  DOI: 10.1086/722563

5.2 Full texts of thesis publications

5.2.1 Article 1

A FIB-SEM Study of Illite Morphology in Aeolian Rotliegend Sandstones: Implications for Understanding the Petrophysical Properties of Reservoir Rocks

Markus Peltz, Arne Jacob, Georg H. Grathoff, Frieder Enzmann, Michael Kersten, and Laurence N. Warr

Clays and Clay Minerals

Volume 70 (84-105)

Published: April 07, 2022
DOI: https://doi.org/10.1007/s42860-022-00174-9

Clays Clay Miner.,Vol. 70, No. 1:84–105, 2022
https://doi.org/10.1007/s42860-022-00174-9

ORIGINAL PAPER

A FIB-SEM Study of Illite Morphology in Aeolian Rotliegend Sandstones: Implications for Understanding the Petrophysical Properties of Reservoir Rocks

Markus Peltz · Arne Jacob · Georg H. Grathoff · Frieder Enzmann · Michael Kersten · Laurence N. Warr

Accepted: 13 January 2022

Abstract Diagenetic illite growth in porous sandstones leads to significant modifications of the initial pore system which result in tight reservoirs. Understanding and quantifying these changes provides insight into the porosity-permeability history of the reservoir and improves predictions on petrophysical behavior. To characterize the various stages of diagenetic alteration, a focused ion beam – scanning electron microscopy (FIB-SEM) study was undertaken on aeolian sandstones from the Bebertal outcrop of the Parchim Formation (Early Permian Upper Rotliegend group). Based on 3D microscopic reconstructions, three different textural types of illite crystals occur, common to many tight Rotliegend sandstones, namely (1) feldspar grain alterations and associated illite meshworks, (2) tangential grain coats, and (3) pore-filling laths and fibers. Reaction textures, pore structure quantifications, and numerical simulations of fluid transport have revealed that different generations of nano-porosity are connected to the diagenetic alteration of feldspars and the authigenic growth of pore-filling illites. The latter leads to the formation of microstructures that range from authigenic compact tangential grain coatings to highly porous, pore-filling structures. K-feldspar replacement and initial grain coatings of illite are composed primarily of disordered $1M_d$ illite whereas the epitaxially grown illite lath- and fiber-shaped crystals occurring as pore-filling structures are of the *trans*-vacant $1M_{tv}$ polytype. Although all analyzed 3D structures offer connected pathways, the largest reduction in sandstone permeability occurred during the initial formation of the tangential illite coatings that sealed altered feldspars and the subsequent growth of pore-filling laths and fibrous illites. Analyses of both illite pore-size and crystallite-size distributions indicate that crystal growth occurred by a continuous nucleation and growth mechanism probably controlled by the multiple influx of potassium-rich fluids during late Triassic and Jurassic times. The detailed insight into the textural varieties of illite crystal growth and its calculated permeabilities provides important constraints for understanding the complexities of fluid-flow in tight reservoir sandstones.

Keywords Illite morphology · Focused ion beam polishing · Computational fluid dynamic simulations · Pore-size distributions · Clay mineral diagenesis

M. Peltz (✉) · G. H. Grathoff · L. N. Warr
Institute of Geography and Geology, University of Greifswald, F.-L.-Jahn-Str. 17a, 17489 Greifswald, Germany
e-mail: markus.peltz@uni-greifswald.de

A. Jacob · F. Enzmann · M. Kersten
Institute of Geosciences, Johannes Gutenberg-University, J.-J. Becherweg 21, 55099 Mainz, Germany

Introduction

Aeolian sandstones from the Early Permian Upper Rotliegend group constitute important geological reservoirs for natural gas in the Southern Permian Basin (SPB) and, once exploited, present potential sites for future gas storage. To assess reliably the storage potential of these rocks and to determine their petrophysical

properties (e.g. porosity and permeability), detailed knowledge of the pore-filling diagenetic-mineral inventory and its associated pore-space characteristics is required. These properties were initially controlled by the depositional environment and then altered during multiple stages of burial diagenesis and subsequent regional-scale fluid-flow events (Darby et al., 1997; Bjørlykke, 2014).

Claymineral paragenesis represents an important indicator of reservoir quality. Whereas the presence of chlorite rims is often related to high permeability and the preservation of porosity (Morad et al., 2010), the occurrence of smectite, mixed-layer illite-smectite, or pure illite generally reflects more restrictive changes to the initial pore system such as a reduction in flow paths within sandstones. Illites and illitic minerals found in reservoir sandstones from the North Sea area and the North German Basin have been studied extensively in the past (Glennie et al., 1978; Hancock, 1978; Seemann, 1982; Ziegler, 2006; Gaupp & Okkerman, 2011; Weibel et al., 2020). Based on their origin, they can be divided into (1) detrital illite/muscovite, (2) illitic minerals that form by solid-state transformations of different precursor phases, and (3) authigenic illite crystals grown in the pore space.

Tangential grain coatings of illite are observed frequently in sandstones. They are described commonly as composed initially of either detrital illite/muscovite or amorphous to smectitic precursor phases (Griffiths et al., 2018) that infiltrated during deposition by aeolian transport or during early diagenesis by colloidal suspensions (Ziegler, 2006; Tang et al., 2018). Illites of detrital origin in these environments are usually of the $2M_1$ polytype and form thicker crystallites compared to other types of illite (Aldega & Eberl, 2005). With increasing burial, and temperatures >70°C (Merriman & Kemp, 1996), a well studied diagenetic illitization sequence starts with smectites transforming progressively through different stages of illite-smectite interstratifications to form illite with minor amounts (<5%) of interstratified smectite (Gharrabi, 1998). These illites are also referred to as poorly crystalline illites (Meunier & Velde, 2004) or $1M_d$ illite (Aldega & Eberl, 2005). Small et al. (1992) synthesized similar illite coatings from solution at various temperatures and with various morphologies that contain the ordered $1M$ as well as the $1M_d$ polytypes. None of the coatings observed showed a strictly tangential structure thought to indicate allochthonous infiltrated particles, however (Wilson, 1992).

The formation of late diagenetic authigenic illite is well documented in Mesozoic and Cenozoic porous sandstones across central and northwest Europe and has been related to basin-wide hydrothermal fluid-flow events linked to the opening of the Atlantic ocean (Zwingmann et al., 1998; Wilkinson et al., 2014). In contrast to burial-related illitization, these illites typically neocrystallized directly from formation fluids that were super-saturated in potassium. The crystal morphology of these precipitates has long been recognized and ranges from platy through lath-shaped to fibrous particles (Wilson & Pittman, 1977). K-feldspars, kaolinite, detrital mica grains, or grain-coating illites are known to serve as a substrate for subsequent illite growth, which commonly produces the trans-vacant (tv) $1M$ polytype variety with fibrous and lath-shaped crystal habits (Meunier & Velde, 2004; Lander & Bonnell, 2010). In contrast, the cis-vacant (cis) $1M$ polytype variety is considered to form at higher temperatures and is often associated with greater crystallinity and platy crystal shapes (Lanson et al., 2002). Lath- to fiber-shaped particles are interpreted to grow more rapidly in potassium-enriched fluids (Wilkinson et al., 2014), which is in accordance with the diverse crystal shapes synthesized in the laboratory under varying chemical conditions at a fixed temperature (Bauer et al., 2000). In terms of the petrophysical properties of the reservoir rock, the occurrence of fibrous illite is known as the main cause of permeability reduction in reservoir sandstones (Weibel et al., 2020). The occurrence of multiple generations of illite in porous rocks has also provided an ideal opportunity to determine the K-Ar ages of these hydrothermal mineralization events across Europe, which has revealed numerous fluid-flow events spanning a period of 200 million years that affected both sedimentary basins and underlying basement rocks (Zwingmann et al., 1998; Schleicher et al., 2006).

Although the mechanism of crystallization and the relationships between fluid composition and crystal growth are now well studied, the interaction between the growth of illite crystals in the pores of reservoir sandstones and the subsequent changes in pore space and fluid flow behavior is quantitatively less well understood. Desbois et al. (2016) analyzed illite-related microstructures in a German Rotliegend sandstone by broad ion beam polishing (BIB), focused ion beam polishing (FIB), and scanning electron microscopy (SEM), and proposed a fundamental building block model for quantifying the influence of nanoporous

structures on fluid flow. Currently, most conventional rock models used for computational fluid dynamic simulations differentiate between the void pore space and the solid mineral matrix at the μm-scale only, while the proposed digital rock model of Desbois et al. (2016) includes mineral-specific properties derived from nm-scale observations. Jacob et al. (2021) adapted this idea and developed a conceptual fluid-flow model to calculate flow parameters for illite-dominated sandstones based on FIB-SEM and micro-CT-generated 3D pore-space reconstructions, although the various nano-porous textural groups common to these rocks were not considered.

To address the influence of microtextural variability, the purpose of the present study was to combine XRD-based polytype quantifications with SEM and site-specific FIB-SEM studies to understand better the relationship between the different types of illite crystal growth features and dynamic fluid flow-related changes that occurred in the pore space of a well-studied Rotliegend sandstone sample block from the Bebertal outcrop, northern Germany. The objectives were (1) to determine the reaction textures and petrophysical properties of the selected FIB-SEM domains relevant to porosity, permeability, and simulated fluid flow, and (2) to place these results in the context of the rock's diagenetic history marked by initial burial and Triassic and Jurassic fluid-flow events that spanned at least 50 million years of geological time.

Material

The ~265 Ma old Upper Rotliegend sandstones from the Parchim Formation (Havel sub-group) present an ideal natural analogue for deeply buried gas-bearing reservoirs (Menning et al., 2006; Gaupp & Okkerman, 2011). They are located at the southern margin of the Northern German Basin (NGB), which formed as a sub-basin of the Southern Permian Basin (SPB). The Bebertal outcrop exposed in Schwentesius quarry (N 52.2564084°; E 11.3361657°) represents the northernmost exposure of this formation and is located close to Magdeburg, Germany. The upper 12 m of the quarry is composed of aeolian cross-bedded and laminated sandstone with thin layers of clay-rich fluvial sheet-flow deposits (Fischer et al., 2012). The main lithology consists of moderate- to well-sorted, medium- to fine-grained, subarkosic sandstones (Fischer et al., 2007).

Heidsiek et al. (2020) reported that the reservoir quality of the formation is limited by the distribution of diagenetic cements, which are composed of poikilitic calcite, illite, and iron oxide grain coatings as well as K-feldspar and quartz overgrowths. ^{40}Ar–^{39}Ar laser spot dating of authigenic K-feldspar recognized two age clusters at 222±2 Ma and 186±14 Ma, respectively (Fischer et al., 2012). Based on the partial annealing of zircons, the rocks probably reached temperatures of 170–190°C before Late Cretaceous–Early Tertiary uplift (post 92 Ma). Although the illites at this location have not been dated, two clusters of illite ages have been reported in Rotliegend sandstones of the region with K-Ar age groupings of 210–180 Ma and 155–190 Ma (Zwingmann et al., 1998).

Measurements of intrinsic permeabilities of the sample block derived from the quarry ranged between 1.1 and 5.4 md using a helium permeameter (Jacob et al., 2021) and between 0.1 and 13.7 md using an air-permeameter (Heidsiek et al., 2020). The latter measurements also included local anomalies of up to 140.26 md, attributed to localized channel flow behavior.

Numerous cores with a diameter of 2.5 cm were drilled out of the 45 cm × 39 cm × 11 cm sample block (Fig. 1). These were located in both cross-bedded and laminated parts of the aeolian facies. To include the natural heterogeneity within the sedimentary layer, a set of 20 samples was extracted and sectioned into two consecutive discs each 5 mm thick. One of the discs was used for XRD study and the other for FIB-SEM investigations. Most FIB-SEM analyses were undertaken using the cores F4 and E6. The small-scale facies heterogeneity of the sample block and its impact on petrophysical properties was studied in detail by Heidsiek et al. (2020) and Jacob et al. (2021). However, as shown by investigations of quarry-wide thin sections reported by Fischer et al. (2012), the structures observed were considered to be representative of and characteristic of the cross-bedded and parallel laminated layers of the aeolian deposits of the Parchim Formation at this location.

Methods

X-ray Diffraction and Rietveld Refinements

The average bulk mineralogical composition of the aeolian sandstone layer was analyzed using 20 micronized powder samples (Fig. 1). For a detailed clay-mineral

study, the <2 μm size fraction was separated from a rock fragment (~100 g) by ultrasonic dispersion followed by gravitational settling. The illite fraction was then purified by first dissolving carbonate minerals using 0.3 M citric acid solution, and second by dissolving iron oxides using the citrate/bicarbonate/dithionite method of Mehra and Jackson (1960). Repeated centrifugation and redispersion was used to obtain a purified <1 μm size fraction. Between each centrifugation step, the >1 μm fraction at the base of the centrifuge tube was discarded and the clay-in-suspension redispersed using an ultrasonic bath. After seven repetitions, XRD quantification of the fine fraction separated thus, prepared as a random powder on zero-background sample holders, showed it to be ~95% pure illite with only traces of quartz and feldspar. The high purity of the separates was confirmed by transmission electron microscopy examination using a JEOL JEM-2100Plus instrument (Tokyo, Japan). The fraction was also analyzed as an oriented preparation on a glass slide to characterize in more detail the nature of the illite minerals. Note that the durations for the gravitational grain-size separation were determined by Stokes' law, which, strictly, is valid only for spherical particles. Nonetheless, diagenetic illite laths and fibers of 10+ μm lengths were still present in the separated and purified <1 μm size fraction.

XRD data were collected using a Bruker D8 Advance diffractometer (Karlsruhe, Germany) with CoKα radiation, a Lynxeye 1D stripe detector, and primary and secondary Soller collimators. Bulk samples were measured between 3 and 80°2θ using an aluminum sample holder and a fixed divergence slit with a 0.5° opening angle. The XRD pattern of the purified powder was obtained using zero-background sample holders, a variable divergence slit to avoid beam spilling, and a 6 mm radiated sample length. Oriented mounts were prepared with a load of 4 mg/cm^2 and measured between 3 and 40°2θ in the air-dried and ethylene glycol-saturated state.

Quantifications were performed by Rietveld full profile modeling using the BGMN/Profex software package (Bergmann et al., 1998; Doebelin & Kleeberg, 2015). Structure files were taken from the internal database. Additionally, an R0 illite-smectite interstratification model by Ufer et al. (2012) was used to model the PCI/1M_d illite structure. This model includes the quantification of n·60° and n·120° layer rotations as well as trans-vacant (tv) and cis-vacant (cv) layers and interstratified smectite. Bulk random powder Rietveld

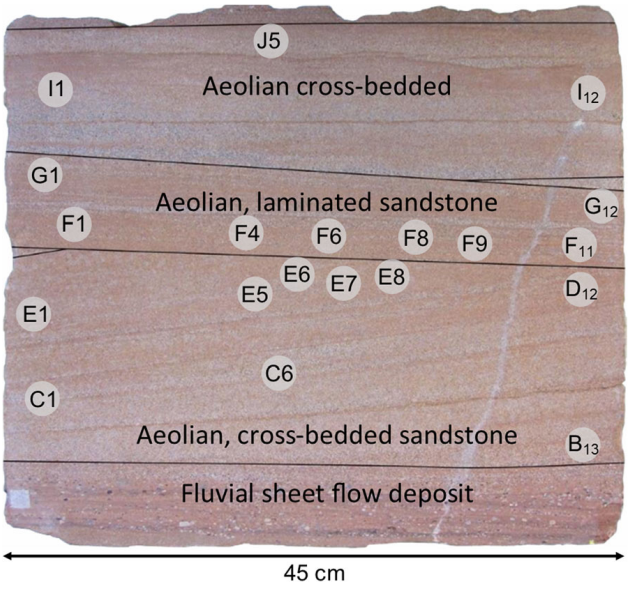

Fig. 1 Sample block with locations of drilled sample discs. Facies assignment is based on Heidsiek et al. (2020)

refinements were run with a fixed background polynomial of 5th order (RU=5) while purified pattern modeling was undertaken without background restrictions. XRD patterns collected using a variable divergence slit were divided by sin(θ) before refinement, which resulted in a reasonable approximation to fixed slit measurements.

In addition to Rietveld refinements, the illite crystallite size distribution (CSD) of the <1 μm size fraction was determined by the Warren-Averbach method using the program *MudMaster* (Eberl et al., 1996). For analyses, the (002) basal reflection of illite was selected, which was obtained by a slow scan of a thin, oriented clay preparation. For the calculation, appropriate intensity corrections were made assuming a pure K-illite phase and by applying the autocorrection mode. The range for the Fourier analyses was 15–25°2θ and the quality of the results verified by examining the shape of the interference function. The lognormal parameters of the calculated CSD expressed as α and β are equivalent to μ and σ defined in Eq. 1 (see 'Pore-size distribution' below).

FIB-SEM

FIB-SEM was used to image the illite-specific, submicrometer porosity of the Rotliegend sandstone. The study was conducted with a Zeiss (Oberkochen, Germany) Auriga crossbeam field emission microscope with a Gemini electron and Orsay Physics (Fuveau, France)

FIB column. The ion-beam sectioning was performed at 30 kV with beam currents of between 1 and 2 nA and a feed between 25 and 35 nm for each slice. The exact settings were chosen depending on the pore structure and its susceptibility to curtaining artefacts. Polished sections were electron imaged at 1 kV with a secondary electron (SE2) detector to minimize charging artefacts. The internal microscope tilt correction was utilized to account for the 54° sample tilt. Slices were collected at an image resolution of 2048×1536 pixels. The voxel and image stack dimensions for each sample are given in Table 1. The elemental compositions of sites of interest were probed by energy-dispersive X-ray spectroscopy (EDX) using an 80 mm^2 Oxford Instruments (Wiesbaden, Germany) X-Max detector.

Image Processing and Segmentation

All image processing was undertaken using the Thermo Fisher software *Avizo 9.3* (Waltham, Massachusetts, USA). A workflow for the collected FIB-SEM image stacks was established to improve the geometry and image quality of the datasets. First, a pre-alignment of the image stack was carried out to decrease the coarse image shift along the sectioning direction. Subsequently, the dataset was cropped to remove information outside the imaging plane. Then a fast Fourier-transform filter was utilized to remove curtaining artefacts. A second slice alignment was performed resulting in a dataset without observable image translation. Shading artefact correction and a gray-scale histogram normalization along the milling direction were performed to correct for gray-scale fluctuations during the sectioning. Noise reduction was achieved using a non-local means filter in 2D mode to remove noise while preserving grain and pore edges.

The automated segmentation of pores in ion polished images was challenging due to the variety of artefacts that occurred along edges (electron charging) or with large pores (shine through artefacts). A recent study by Berg et al. (2018) demonstrated the advantages of machine-learning segmentation over conventional thresholding or watershed techniques. Jacob et al. (2021) utilized successfully the machine-learning software *Ilastik 1.3.3* (Berg et al., 2019) to segment pores in a highly porous FIB-SEM derived illite structure. In the present study, the *Ilastik* program and its 2D pixel classification workflow were used to mask the porosity of all analyzed structures. Therefore, training datasets for each volume were generated by combining conservative gray-scale thresholding and manual masking of the first and last slice of each volume plus every 100th image. The resulting training mask included two phases: (1) the solid mineral matrix; and (2) the pores. After the segmentation, the labeled images were exported and transformed into binary images for further analyses.

Pore-size Distribution

The algorithm of Münch and Holzer (2008) was used to calculate 3D continuous pore-size distributions (PSD) from binary segmentation images and the total porosity (φ). The PSDs thus obtained showed a log-normal trend. To analyze further and compare the measured datasets, non-linear least-squares curve fitting was used to fit a probability density function (PDF) to the log-normal distributions. This approach allowed direct comparison of PSDs as they are independent of the total porosity (φ) and the volume analyzed. For porous media applications, Zydney et al. (1994) and references therein, showed that the general form of the PDF can be given as:

$$f(r) = \frac{1}{\sigma r\sqrt{2\pi}} exp\left(-\frac{(ln(r)-\mu)^2}{2\sigma^2}\right) \quad (1)$$

Where r is the pore radius; μ, the mean; and σ, the standard deviation. Note that μ and σ are the mean and standard deviation of the normal distributed variable ln(r) and not the PDF. By fitting μ and σ in Eq. 1 to the given pore-size distribution, the mean R_m of the pore-size distribution can be calculated by:

$$R_m = e^{\mu+\frac{\sigma^2}{2}} \quad (2)$$

the most probable pore radius R_p by:

$$R_p = e^{\mu-\sigma^2} \quad (3)$$

and the median R^* of the distribution by:

$$R^* = e^{\mu} \quad (4)$$

Modeling

To estimate the matrix flow properties of the connected pore systems within the analyzed structures, computational fluid dynamics (CFD) simulations were run by solving the Navier-Stokes equation on different

Table 1 Size properties of FIB-SEM volumes analyzed (*after processing, φ – total porosity)

Sample	Voxel size (*x*×*y*×*z*) (nm)	Grid dimension* (voxels)	Physical dimensions* (μm)
Meshwork illite	12.5×12.5×25	879×1043×370	11.0×13.0×9.3
Tangential illite	10×10×35	824×1298×73	8.2×13.0×2.6
Na-feldspar	17.5×17.5×35	951×930×297	16.6×16.3×10.4
K-feldspar (high φ)	12×12×35	1227×906×351	14.7×10.9×12.3
K-feldspar (low φ)	12×12×35	2236×1669×212	26.8×20.0×7.4

extracted sub-volumes. Calculations were realized using the *FlowDict* module of the software package *GeoDict* by Math2Market (Kaiserslautern, Germany). Simulations were run for water viscosity at 21°C. A pressure gradient of 100 Pa was applied between the inflow and outflow plane, and symmetric boundary conditions were defined for all other faces. Simulations were run in the *x*, *y*, and *z* directions successively. A detailed description of analogue calculations can be found in Jacob et al. (2021). Because the pore systems of the analyzed volumes are strongly heterogeneous and do not build up connected clusters across the analyzed volume, cubic domains with edge lengths between 192 and 384 voxels were extracted from the binarized pore-space models. This was undertaken in all volumes studied except for the tangential illite sample, where the whole coating region was treated as one computational domain. To achieve cubic domains, the binarized data were resampled to cubic voxel sizes in advance.

Results

X-ray Diffraction

The main mineral components of the Rotliegend sandstone are quartz, illite, feldspars (K- and Na-), and calcite (Fig. 2a, Table 2). Hematite and baryte occur in traces of <1 wt.%. Illite and calcite contents fluctuated widely, whereby low calcite often correlated with high illite content and vice versa. In most samples, two calcite generations were distinguished by their different *d*-spacings due to the enrichment of Mn in the youngest-generation calcite (Pedrosa et al., 2021).

Oriented aggregates of the purified <1 μm size fraction were used to determine the types of clay mineral present (Fig. 2b). The oriented patterns showed a 15 Å and a 10 Å phase. For the 10 Å illite phase, a shift of the 10.08 Å (001) reflection towards smaller *d*-spacings (9.92 Å), together with an intensified asymmetry towards smaller diffraction angles, was observed after EG saturation. The (002)-spacing (4.97 Å) did not change significantly and the (003)-spacing (3.31 Å) increased slightly to 3.32 Å. The basal spacing of the 15 Å phase increased to ~17 Å after EG treatment, which is characteristic of a two water-layer smectite containing a bivalent interlayer cation (e.g. Ca^{2+} or Mg^{2+}).

The reduced intensity of the 10 Å (001) reflection combined with the increase of intensity of the 3.3 Å (003) reflection after EG saturation was attributed to small amounts of intercalated smectite layers. Based on the intensity ratio of the (001)/(003) reflections for the air-dried and EG saturated states, a value of 1.4 suggests an average of 4% interlayered smectite occurred in the illite crystals (Moore & Reynolds, 1997; Środoń & Eberl, 2018).

The XRD patterns of the purified <1 μm fraction combined with quantitative Rietveld refinements were used to determine illite polytypes. This fraction contains only minor amounts of accessory phases with 4 wt.% quartz and 3 wt.% feldspars. Smectite was not observed in random powder patterns, and thus not included in the refinements. The XRD pattern (Fig. 3) showed two illitic phases: (1) a trans-vacant 1*M* polytype and (2) a disordered $1M_d$ illite. The $1M_d$ illite is characterized by broad reflections and an "illite hump" in the angular region between 22 and 46°2θ (green line in Fig. 3b) (Grathoff & Moore, 1996). The refined $1M_d$ model consists of 64% tv and 36% cv layers. The probability *p0* for 0° rotations reached the lower boundary value of 1/3, equivalent to a maximum degree of disorder. The probability for rotations of $n{\cdot}60°$ is 0.17 and for $n{\cdot}120°$ is 0.49. The amount of interstratified smectite layers was 5%, which was consistent with the oriented aggregate result. The $1M_{tv}$ illite was identified by its sharper overlaying reflections (i.e. $(\overline{1}\overline{1}\,1)$: 4.35 Å, $(\overline{1}\,1\,2)$: 3.65 Å, (112): 3.07 Å) that do not match the broad peak shape of

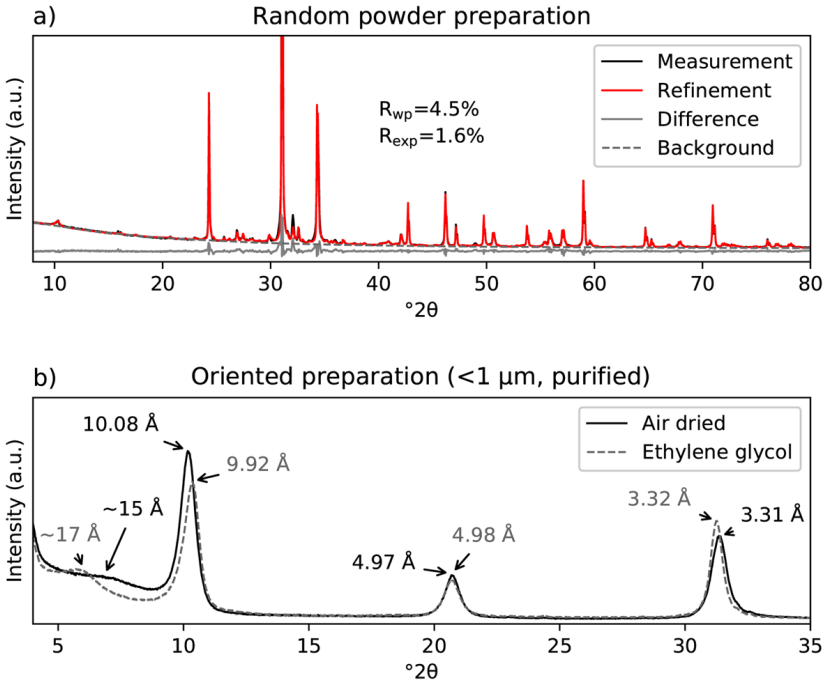

Fig. 2 **a** Rietveld refinements of the random powder preparations of the micronized bulk material. **b** Oriented aggregate of the purified fraction in air-dried (AD) and ethylene glycol-saturated (EG) state

the underlying $1M_d$ polytype. For the $1M_{tv}$ structure, crystallite size peak broadening and microstrain were refined. The total weight fractions were 77 wt.% $1M_d$ and 16 wt.% $1M_{tv}$ illite for the purified <1 µm fine fraction.

Calculations of the illite CSD for the purified <1 µm size fraction obtained using the *MudMaster* program by Fourier analyses of the (002) reflection produced a thickness distribution of crystallites (Eberl et al., 1996). These ranged (in the crystallographic *c* direction) between 1 and 80 nm. The average illite crystallite thickness was 24.7 nm with log-normal parameters of µ = 2.89 and σ = 0.77.

Microscopy

The SEM analyses of rock fragments and ion-polished surfaces revealed the diversity of illite-related textural and structural features whereby analyses of rock fragment showed an undisturbed image of delicate illite structures within the open pore space. The distribution of illite structures and the relationship between feldspar alteration and illite growth were studied further by light microscopy imaging (Fig. 4). Three types of illite textures were observed: (1) as illites replacing K-feldspar grains and meshwork textures; (2) as grain coatings (cutans or tangential illites); and (3) as pore fillings between grains.

K-feldspars occurred as detrital grains and diagenetically grown cement, both of which were associated with extensive secondary porosity caused by dissolution and nanocrystalline cement precipitates (Figs 5a and 7a). Na-feldspars (albite) occurred only as cements and contained unfilled porosity. In contrast, in most K-feldspars, grain-replacing illite crystals were observed. Calcite precipitated commonly within the pore space of K-feldspar grains (Fig. 5b). The surface structure of K-feldspar grains showed two specific characteristics: (1) illite crystals that extended out of altered K-feldspar grains to form thin sheets around most of the K-

Table 2 Average mineralogical composition of the aeolian Rotliegend sandstone layer analyzed (n = 20, SD – standard deviation)

	Quartz	Na-Feldspar	K-Feldspar	Calcite	Hematite	Baryte	Illite
Mean (wt.%)	63.7	7.6	8.6	5.9	0.5	0.5	13.2
Minimum (wt.%)	57.4	4.5	7.1	1.1	0.3	0.2	10.3
Maximum (wt.%)	68.5	9.6	10.2	18.2	0.7	1.3	15.9
SD 2σ	5.1	2.6	1.7	8.6	0.2	0.6	3.1

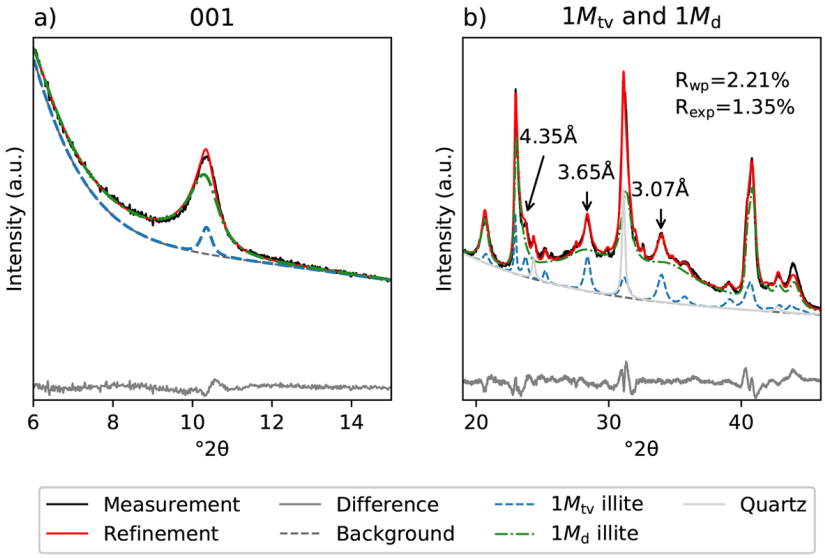

Fig. 3 XRD patterns and refined Rietveld model of the purified <1 μm size fraction. **a** The 1M_{tv} (001)-reflection is sharper with a slightly smaller *d* spacing compared to the 1M_d (001) spacing. The larger spacing of the disordered reflection is caused by minor amounts of interstratified smectite. **b** Decomposition of the angular range between 19 and 46°2θ. 1M_{tv} polytype specific peaks are highlighted

feldspar grain surfaces (Fig. 5c); and (2) layers that were formed by aggregated lath-shaped crystals that were interconnected to form sheets (Fig. 5d). The orientation of the crystals to each other appeared to be random. Hematite crystals <100 nm in size were often found on top of these layers.

Illite meshwork structures formed grain replacements >100 μm in size and extended commonly over the initial grain boundaries and grew into the intergranular pore space (Fig. 5e). These curly illite crystals formed honeycomb-like structures with lenticular- to slit-shaped internal pores (Fig. 5f). In some regions, these structures had a preferred tangential orientation surrounding grains. Compared to other honeycomb structures, which are observed commonly in other illite-bearing sandstones (Weibel et al., 2020), the thickness of the twisted sheets is >100 nm. Crystals observed on the surface of these sheets were flaky and had irregular shapes. Dissolved K-feldspar remnants were observed commonly within these structures.

Polished specimens and thin sections showed quartz and feldspar grains that were sub-rounded to rounded. Grain coatings were observed along most grain boundaries (Figs 4 and 6a). These coatings were formed by μm-thick layers of illite particles (Fig. 6b–d), which are often referred to as tangential illites (Desbois et al., 2016). Menisci between two coatings were observed rarely. Coating growth was also seen around authigenic microquartz crystals (Fig. 6c). The outer visible layer of the coating was covered by idiomorphous lath- to hexagonal-shaped illite crystals (Fig. 6b, c). The coating thickness was greater in intragranular and angular regions and was frequently thicker in regions with no calcite cementation. In regions with poikilitic calcite,

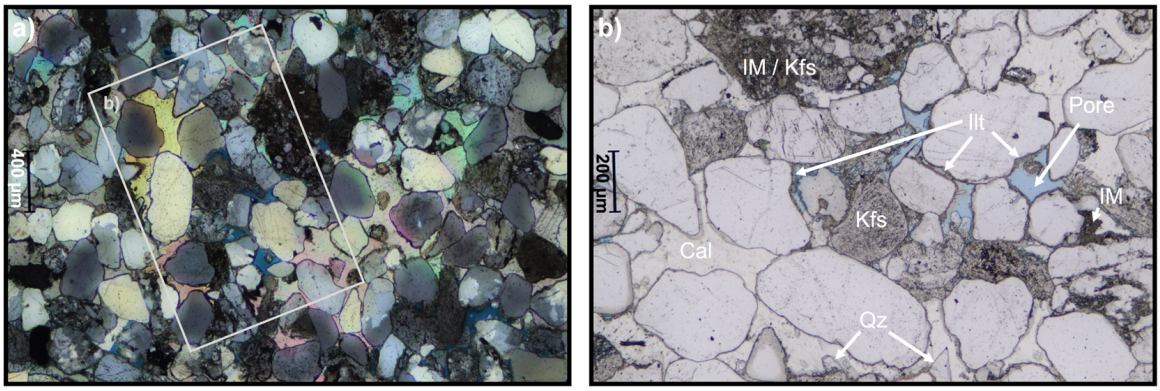

Fig. 4 **a** Cross-polarized thin section micrograph showing the distribution and thickness of illite grain coatings and poikilitic calcite cement. **b** Illite coatings in open pores are often thicker and cover whole grain surfaces whereas coatings in areas of poikilitic calcite are generally thinner and visibly enriched in grain depressions and on rough grain surfaces. Cal – calcite, Kfs – K-feldspar, Ilt – illite, IM – illite meshworks, Qz – quartz. Abbreviations after Warr (2020)

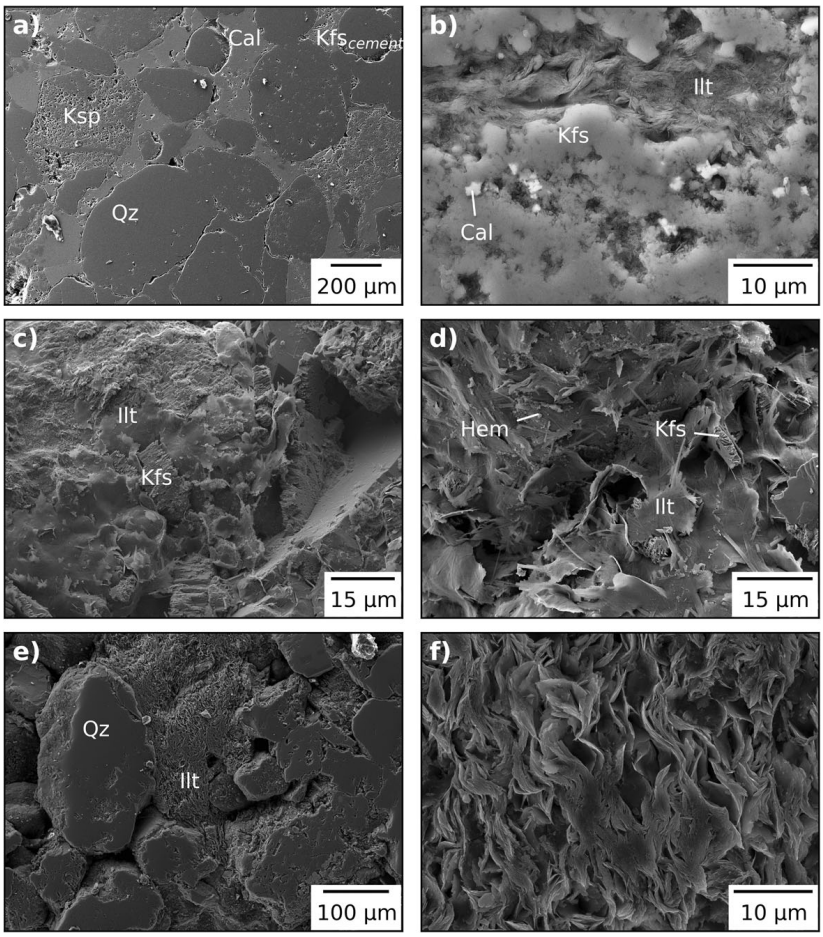

Fig. 5 **a** Hand-polished surface of Bebertal sandstone showing the diversity of diagenetic textures. As well as large poikilitic calcite (Cal) cements, K-feldspar (Kfs) and quartz (Qz) cements are common. Both Kfs detrital grains and cements show alteration to meshwork illite. **b** Close-up of a polished section of a diagenetically altered Kfs grain. Within the pores of the grain, Cal and illite (Ilt) precipitates are common. **c** Fractured rock fragment image showing an altered Kfs grain surface. Thin sheets of lath-shaped Ilt have grown and cover large parts of the Kfs grain surface. **d** Aggregated Ilt laths occupying the intergranular pore space. Hematite nanoparticles are commonly observed on these layers. **e**, **f** Hand-polished section of illite meshworks that form honeycomb structures with thick curly Ilt sheets. Irregular crystals were observed in these pore-filling structures that predate the Ilt laths and fibers. Abbreviations after Warr (2020)

thinner coatings were observed on smooth quartz surfaces, which thicken commonly with increasing surface roughness (Fig. 4b). Pores are notably common at the interface between angular quartz grains and the coating. At the interface between K-feldspar and the tangential illite, illitized K-feldspar was common (Fig. 6d). Crystals on grain coatings seemed to be oriented randomly; however, the image resolution used in this study was not sufficient to determine potential nucleation sites.

Pore-filling illite had idiomorphous fibrous- to lath-shaped crystal habits that extended commonly from the illite substrate into the open pore space. Within these assemblages, the crystal sizes and shapes were notably homogeneous (Fig. 6e). Crystals were elongated along the crystallographic *a* axis and reached lengths of up to 50 µm with breadths of up to 2 µm along the *b* axis (Fig. 7b). Between the different pores, crystal sizes varied, especially in the *b* direction. The agglomeration of laths to form crystal mats was observed frequently. Pore-bridging fibrous crystals that nucleated on illite coatings were common near grain contacts (Fig. 6f).

Elemental Analyses

The EDX analyses of the different types of illite were performed on selected FIB-SEM ion-polished sections. Each of the textural varieties described was analyzed, namely the illite replacing K-feldspar, meshwork illite, and the grain coating of illites (Table 3). Only the fibrous pore-filling illites could not be measured. To reduce interference from surrounding mineral grains, EDX maps were collected on hand- and ion-polished sites that appeared homogeneous. No maps were collected in the vicinity of calcite grains. As no Ca-feldspar was present in the samples, the observed calcium was assigned to intercalated Ca-smectite in the illite crystals. Some of the spectra from illite may have been contaminated by signals from surrounding grains, however, because the volume of X-ray generation exceeds the size of the analyzed illite structures. Further inaccuracies may arise from surface roughness. EDX measurements of the purified <1 µm fraction were also acquired for comparison. An idealized structural formula for this sample was calculated and is presented in Table 3.

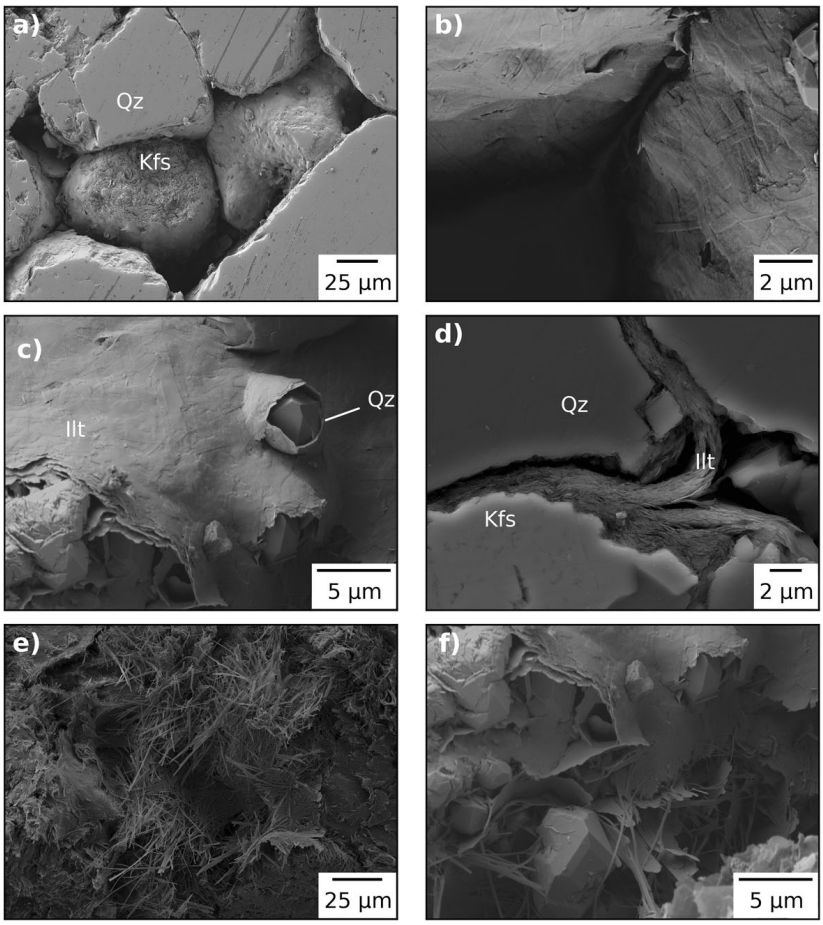

Fig. 6 **a** Hand-polished section of uncemented detrital grains, including the altered K-feldspar (Kfs) grain containing grain-enveloping coatings of illite. **b** Contact areas between two detrital quartz grains that are covered by illite coatings comprised of interlocking lath-shaped crystals. Menisci between coatings are rarely observed. **c** Open pore spaces with the growth of illite coating around authigenic microquartz crystals. Pore-bridging illite fibers in the lower region of the image (f) are seen to post-date the quartz crystals. **d** Polished section showing a junction between three grains. Pores are commonly found between the quartz (Qz) surface and the coating. No pores were found between Kfs surfaces and illite coatings. **e** Illite lath- to fiber-shaped crystals growing into open pores. The laths are often stacked together to form dense and twisted mats. **f** Pore-bridging laths and fibers that nucleate on illite substrate. Abbreviations after Warr (2020)

Overall, the measured compositions appeared very similar. Values that differed substantially from the purified <1 µm analyses could be attributed to contaminations of the grain-size assemblage used which contained traces of quartz and feldspar. Elevated K_2O values of the illites in K-feldspars and the meshwork illites were probably caused by the presence of K-feldspar grains and their remnants. The elemental data of the coating illites showed the greatest variability with large fluctuations in FeO, K_2O, and SiO_2 contents probably caused

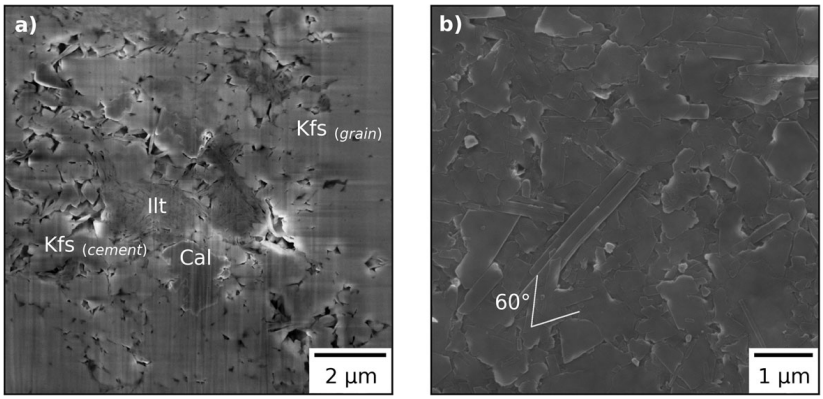

Fig. 7 **a** SE image of an ion-polished section scanned at 5 kV of the low φ K-feldspar (Fig. 8e) which shows structural features such as illite (Ilt) distribution and K-feldspar (Kfs) and calcite (Cal) precipitates. After a period of feldspar dissolution, the second generation of K-feldspar cements partially filled the generated pore. Subsequent calcite and illite precipitation further decreased the pore volume within the grain. IntraP and InterP pores occur mainly in the feldspar matrix. **b** Crystal shape analyzed on the purified illite fraction. Elongate, lath-shaped to fibrous crystals are common. 120° growth steps indicate a surface spreading growth mechanism

by the various substrates on which these structures were found. The largest FeO values were probably caused by hematite accumulations and the increased SiO_2 values by quartz substrates. Meshwork and coating illites showed no Na_2O whereas CaO was observed throughout all samples and probably reflected some intercalation of smectite layers within the minerals. Structures without Na_2O showed notably higher CaO values suggestive of varying smectite interlayer compositions. The composition of illite in K-feldspar differed least from the bulk purified fraction that was analyzed.

Pore-structure Analysis

Five nanoporous zones were identified that are characteristic of the studied Rotliegend sandstone. For each of the five zones, locations were chosen for FIB-SEM serial sectioning and 3D reconstructions (Table 1). A typical secondary electron (SE) image for each analysis is shown in Fig. 8 and 3D renderings of each volume including the segmented pore space are plotted in Fig. 9. Most nanoporous structures can be related to the occurrence of illitic clay minerals and feldspar cements. Pore structures are described based on the classification of Loucks et al. (2012), which differentiates between intraparticular (IntraP) and interparticular (InterP) pores.

Meshwork illites were uncommon but were the largest structures observed with the spatial dimension of >100 μm and high total porosities as shown in Figs 8a and 9a–c. These structures were found (1) as grain replacements of K-feldspar grains and (2) as replaced K-feldspar cements indicated by their intragranular occurrence. The characteristic of this type of pore structure was slit- and triangular-shaped pores, which were found within and between distinct clay mineral lamellae. Within these structures, InterP pores were visually larger than IntraP pores. Because these types are often interconnected within larger 3D pore clusters, however, the transitions cannot be defined clearly. A recurring feature in these regions was the twisted thin curly illite crystals that nucleated within and around K-feldspar grains the remnants of which were often <1 μm in size. An example of a cross-section of this type of structure can be found in the InterP pores of Fig. 8a. Meshwork illites form well connected nanoporous clusters that appear evenly distributed.

Na- and K-feldspar both contained significant amounts of porosity. The absence of diagenetic illite crystals within its pore space was characteristic of Na-feldspar (Fig. 8c). The reconstructed volume contained ~5.1 vol.-% porosity, which was aligned along the cleavage planes of the feldspar. These types of structures were exclusively IntraP pores. The Na-feldspars analyzed showed the largest range of pore sizes with radii of >1 μm (Fig. 10). The connectivity of these pore clusters was low with no axis connectivity at the observational scale, however. Porosity within Na-feldspar is, therefore, likely to be primary and developed during the formation of the cement.

In contrast to Na-feldspars, K-feldspars contain secondary porosity. Generally, the porosity in K-feldspars is caused by feldspar dissolution and feldspar and illite precipitation. The porosity observed in the present study had a channel structure and was distributed heterogeneously within the dissolved feldspar grain volume (Fig. 9j–o). The total porosity in the K-feldspar grains varied between 3 and 6.7 vol.%. Various types of pore shapes and sizes could be distinguished based on the total porosity of these grains (Fig. 9d–f). High φ grains showed complex pore shapes with systems built up by InterP- and IntraP-illite pores. The illite particles in these subsystems were thin platy to fibrous in habit. The associated pores were irregularly shaped and differed in size. The degree of connectivity within these clusters was high (Fig. 9l). Low φ grains contained less diverse shapes. Two main types of structures were found: (1) IntraP pores in K-feldspar caused by dissolution and/or the precipitation of tiny K-feldspar cement crystals; and (2) InterP/IntraP pores associated with illite precipitates. The latter were dominated by slit to triangular-shaped pores. Further, calcite precipitates were found within regions dominated by K-feldspar cement pores (Fig. 5b).

Tangential illites formed grain coatings around the borders of detrital grains. The characteristic of these rims were low internal porosities (<1 vol.%) and pores that were frequently filled with hematite (Fig. 8a,b). The rim thickness was up to 1 μm in regions with early diagenetic cements and visibly larger in open pores (Fig. 6a). Between tangential illites and the early diagenetic poikilitic calcite cement, slit-shaped pores were common. Tangential illite structures showed the lowest total porosity and the lowest degree of connectivity out of all analyzed structures.

A transition from the grain coating tangential illite into meshwork illite was recognized in some cases with a zone 2–3 μm thick. These areas were characterized by low pore cluster connectivity but large pore and illite laminae sizes (Figs. 8a and 9a–c).

Table 3 Energy dispersive X-ray analyses (values ± 2σ standard deviation, n.d. – not detected)

	Na_2O	MgO	Al_2O_3	SiO_2	K_2O	CaO	FeO
Meshwork Ilt (N=5)	n.d.	1.6 ± 0.1	29.4 ± 0.3	52.9 ± 0.4	11.0 ± 0.3	0.7 ± 0.2	4.4 ± 0.4
Ilt in Kfs (N=9)	0.12 ± 0.07	2.4 ± 0.8	29.0 ± 1.8	55.2 ± 1.4	9.1 ± 0.3	0.5 ± 0.3	3.6 ± 1.0
Coating Ilt (N=4)	n.d.	0.9 ± 0.3	20.1 ± 3.5	61.6 ± 5.4	9.3 ± 2.9	1.0 ± 0.1	7.3 ± 4.4
Purified <1 μm (N=11) *	0.35 ± 0.05	2.2 ± 0.1	28.9 ± 0.2	56.6 ± 0.3	8.3 ± 0.2	0.3 ± 0.1	3.4 ± 0.1

*corresponding formula unit: $Ca_{0.07}Na_{0.04}K_{0.64}(Al_{1.53}Fe_{0.38}Mg_{0.09})[Si_{3.45}Al_{0.55}]O_{10}(OH)_2$

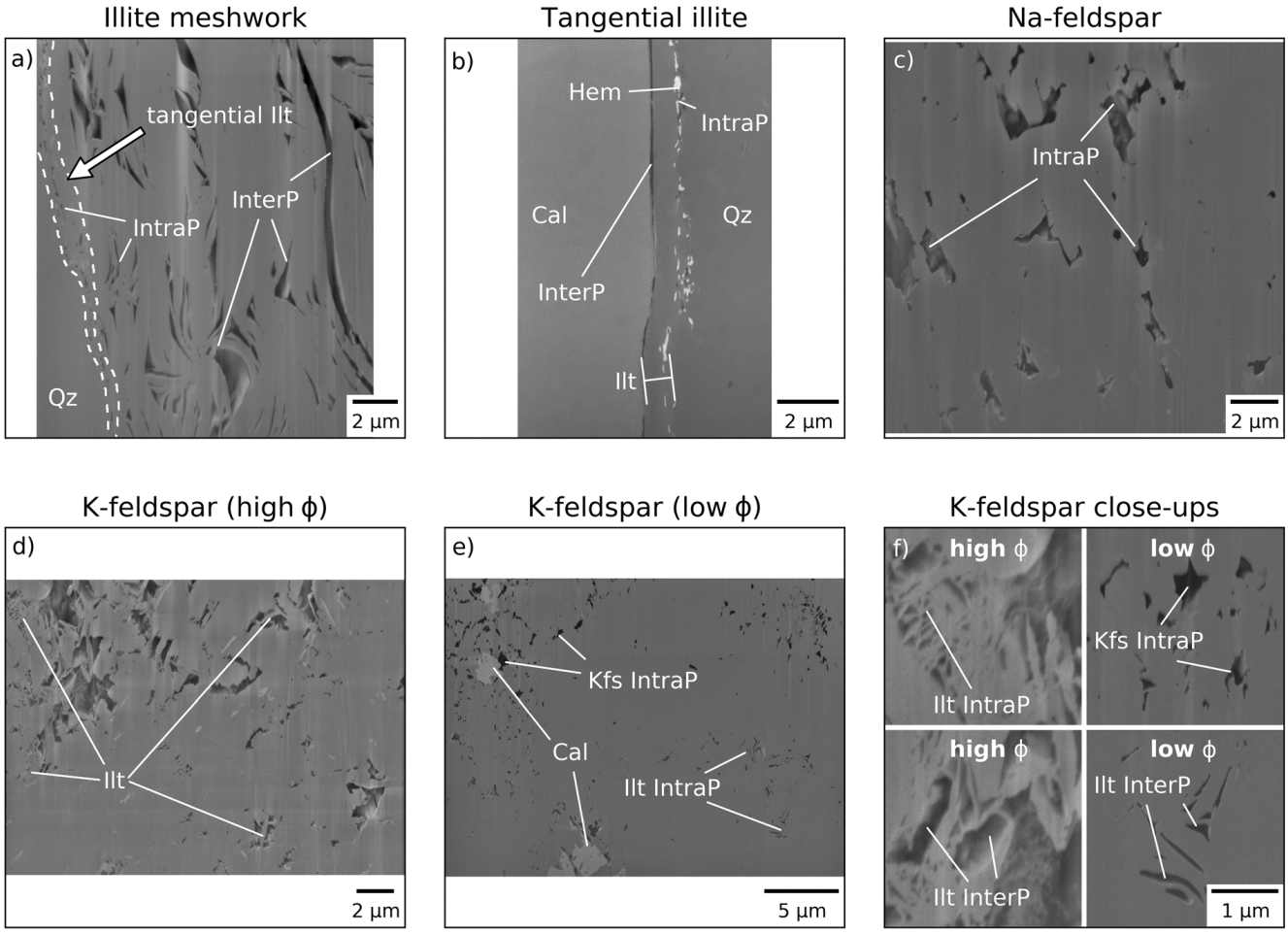

Fig. 8 Selected slices of FIB-SEM volumes. **a** Illite (Ilt) meshwork structures show predominantly slit- to triangular-shaped pores of varying size. These structures evolve from grain coating tangential illite. Twisted thin radial illite structures are marked in the bottom part of the image. **b** Tangential illite covers all detrital grain surfaces and shows little to no internal porosity. Slit-shaped pore structures between calcite (Cal) cement and illite point toward pressure dissolution or minor shrinking. Tangential illite is commonly cemented by Fe-oxides. **c** Na-feldspar shows large pore sizes that are oriented along crystal planes. No connectivity of pores was observed at the scale used, however. **d–f** K-feldspars (Kfs) are heavily altered with a deep-reaching pore system. The pore structures are diverse, depending on the type of pore filling. Kfs cement within Kfs grains is common and intraparticle (IntraP) pores are irregularly shaped. Pores related to illite depend on the amount of precipitated illite. Highly porous structures are dominated by IntraP and interparticle (InterP) with larger pore radii and irregular shapes. Heavily cemented areas show slit- to triangular-shaped pores. Abbreviations after Warr (2020)

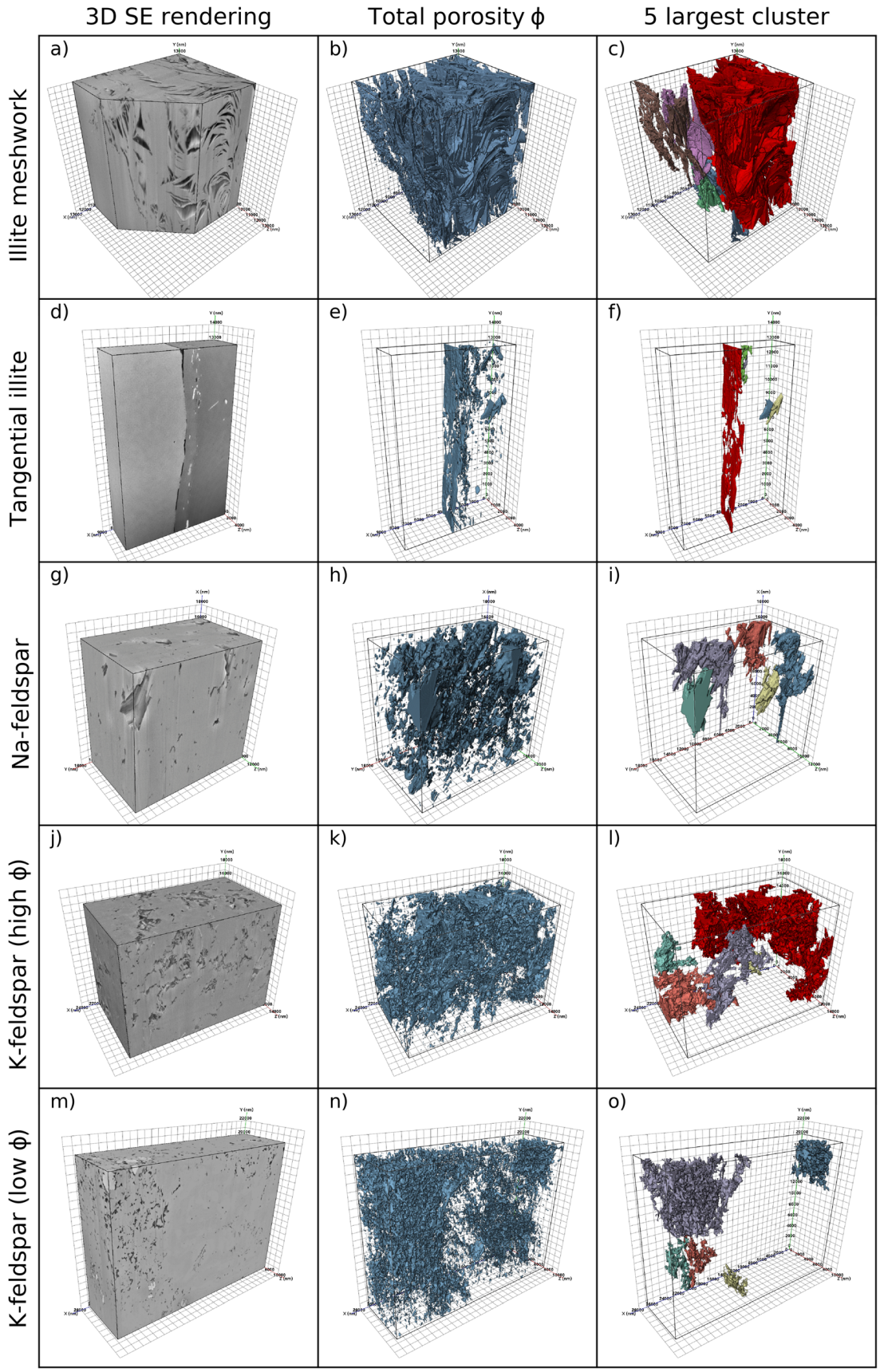

Fig. 9 Comparison of analyzed FIB-SEM structures. The left column displays 3D renderings based on SE images, the middle column a rendering of the extracted pore structure and the right column the five largest pore clusters, where axis-connecting clusters are shown in a deep red color (**c**, **f**, **l**). No axis connectivity was observed for Na-feldspar and K-feldspar (low φ)

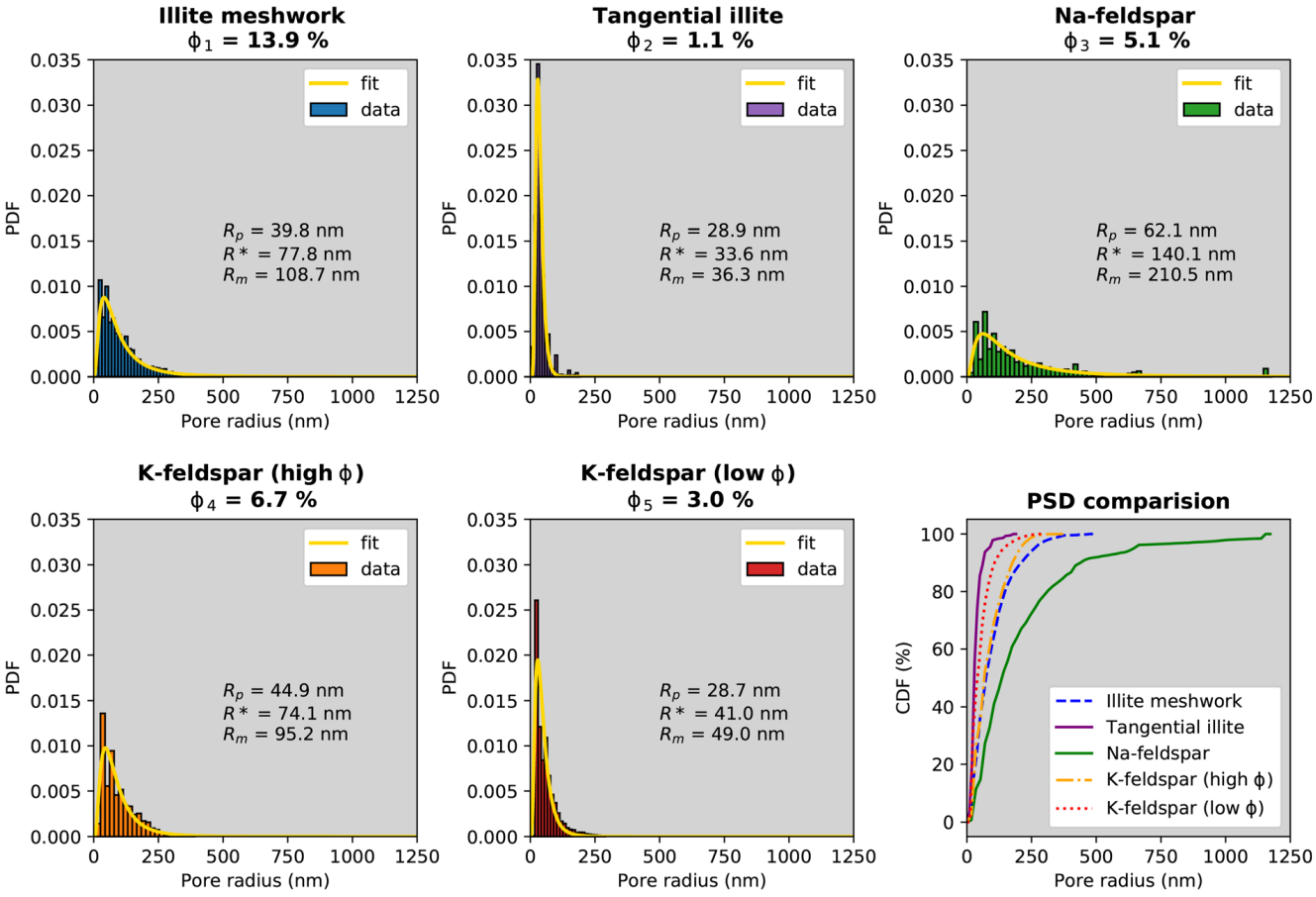

Fig. 10 Calculated geometric continuous PSDs of all five FIB-SEM pore space models plotted as probability density functions (PDFs). The yellow line shows the fitted log-normal curve. The illite meshwork and the Na-feldspar structures show the largest distribution of pore radii and the largest mean pore radii (Table 4). The bin-size is determined by the voxel size

Pore-size Distributions

The measured and calculated pore-size distributions as well as the results of the fitted PDF are shown in Table 4 and Fig. 10. The narrowest range of pore sizes combined with the lowest total porosities was associated with the tangential illites. The total porosity of this analyzed volume was 1.1 vol.%. The most probable pore radius was 28.9 nm, and the mean value was 36.3 nm. Note that most pore voxels in this structure were associated with a large slit-shaped pore network between the coating and the calcite cement and not within the actual coating itself (Fig. 9f). Low φ K-feldspars showed a similar R_p value (28.7 nm), but the range of pore radii was much larger as indicated by a higher median radius R* of 41.0 nm. Additionally, the illite meshwork and high φ K-feldspar structures showed similar pore-size statistics. The R_p values were slightly lower in illite meshworks (39.8 vs. 44.9 nm) but the pore-size range was marginally larger (R_m: 108.7 vs. 95.2 nm). Visually, this trend can be seen in the cumulative distribution function (CDF) plot in Fig. 10. The main difference between the two structures was the total porosity, which was more than two times higher in the illite meshwork compared to the high φ K-feldspar (13.9 vs. 6.7 vol.%). Na-feldspar showed the largest pore radii (R_p: 62.1 nm, R_m: 210 nm).

Permeability Simulations

The sub-domains for computational fluid dynamic simulations were extracted from the binarized resampled pore space volumes. As previously indicated, the analyzed volumes do not represent homogeneous pore systems. This is because they are either located within one mineral grain (Na- and K-Feldspar) that was subject to dissolution and precipitation during its burial history or within a mineral assemblage (e.g. tangential illites). Therefore, these pores are concentrated within certain regions. By extracting sub-domains from these areas,

Table 4 Fitted curve parameters, μ and σ (detailed description in section 'Pore-size distribution'), and statistical radii values for log-normal pore-size distribution curves

Sample	μ	σ	R_p (nm)	R^* (nm)	R_m (nm)	Φ (%)
Illite meshwork	4.35	0.82	39.8	77.8	108.7	13.9
Tangential illite	3.52	0.39	28.9	33.6	36.3	1.1
Na-feldspar	4.94	0.90	62.1	140.1	210.5	5.1
K-feldspar (high φ)	4.31	0.71	44.9	74.1	95.2	6.7
K-feldspar (low φ)	3.71	0.60	28.7	41.0	49.0	3.0

μ mean, σ standard deviation, R_p most probable radius, R^* median radius, R_m mean radius, Φ total porosity

generating connected pore clusters was possible. Modeled permeabilities are, therefore, not representative of the whole rock, but instead, provide information on matrix flow paths of various textural domains relevant to the circulation of diagenetic fluids.

Numerical calculations of permeabilities ranged between 0.1 and 13.4 μd (Table 5). Illite meshwork values varied between 0.1 and 6.2 μd with a noticeable enhancement in the *y*-direction. No flow was recognized in the *x*-direction in the tangential illite sample as it represents the direction perpendicular to the layered coating. Values in the *y*- and *z*-directions ranged between 0.1 and 1.4 μd. The tangential illite structure was the most heterogenous volume analyzed because it contained solid voxels of the surrounding calcite and quartz grains. The high-φ K-feldspar values ranged between 0.7 and 2.2 μd. The low-φ K-feldspar samples showed the greatest anisotropy within the modeled data with values between 0.1 and 13.4 μd (note that ROI6-8 partially overlap). These pore clusters were chosen because no further sub-domains >256^3 voxels existed within the dataset.

Discussion

Based on the results presented, a conceptual model summarizing the evolution of illite neocrystallization and the development of nano-porous systems in the Bebertal sandstone is illustrated in Fig. 11. The various aspects of the sandstone's diagenetic reactions, pore-size characteristics, and porosity-permeability evolution are discussed in the context of its geological history, as outlined in the thermal burial model of Fischer et al. (2012; fig. 8).

New Constraints on the Diagenetic History and Pore Evolution of the Bebertal Sandstone

According to the diagenetic sequence proposed by Fischer et al. (2012), the oldest generation of feldspar cement in the Upper Rotliegend sandstones was associated with a period of enhanced fluid flow following the rapid burial of the sandstone during Late-Permian to Early-Triassic times. The subsequent intense dissolution of feldspar grains and cements led to the formation of

Table 5 Results of CFD simulations run on extracted sub-domains. No flow path exists in the *x*-direction of tangential illite as it is the direction perpendicular to the coating surface

Sample	ROI	Domain size *x y z*	k_{xx} (μd)	k_{yy} (μd)	k_{zz} (μd)
Illite meshwork	1	384^3	0.1	5.0	1.5
Illite meshwork	2	384^3	0.6	6.2	0.3
Tangential illite	3	212×1298×256	no path	0.1	1.4
K-feldspar (high φ)	4	384^3	0.7	2.0	2.2
K-feldspar (high φ)	5	256^3	no path	1.1	1.4
K-feldspar (low φ)	6	384^3	0.2	9.4	1.2
K-feldspar (low φ)	7	384^3	0.1	10.0	1.1
K-feldspar (low φ)	8	384^3	0.3	13.4	1.1

ROI region of interest

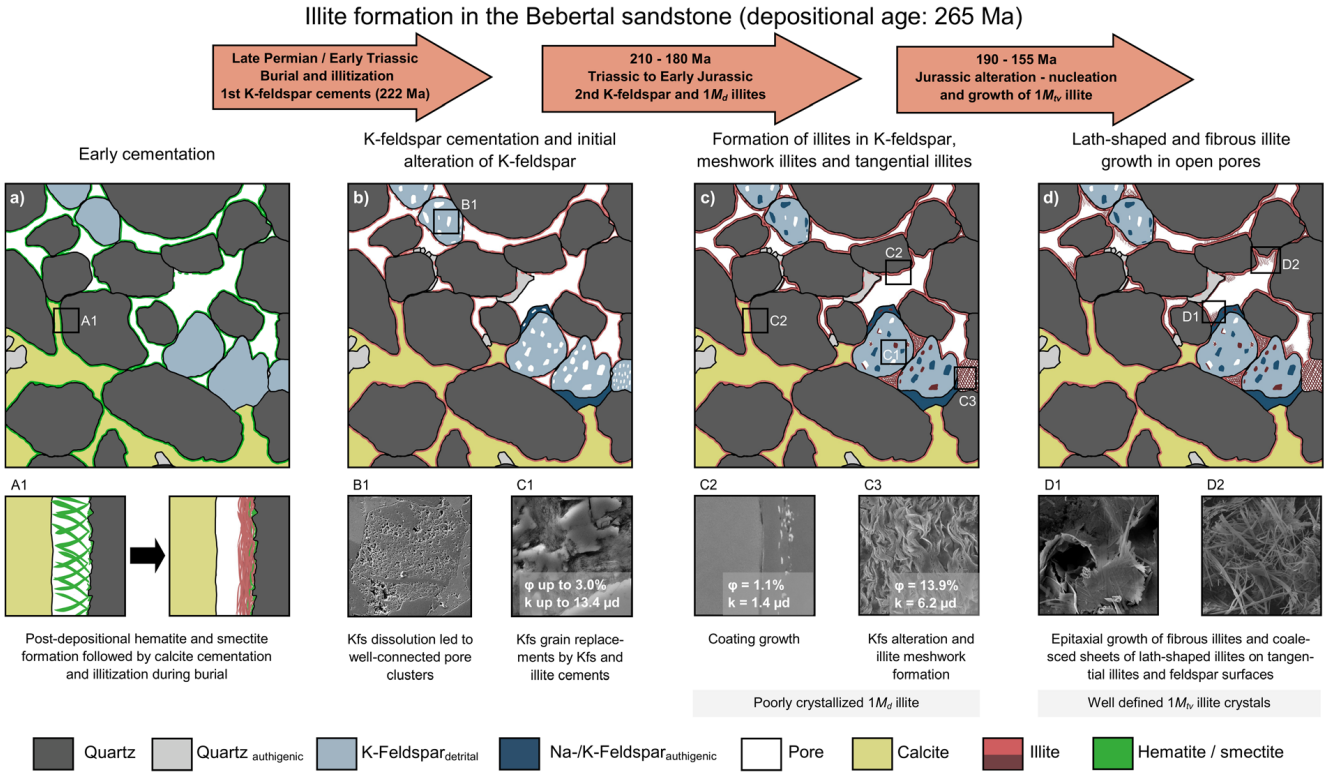

Fig. 11 Schematic diagram illustrating the development of illite-related porosity in the Bebertal sandstone. **a** Post-depositional hematite and smectite formation led to the development of thin initial grain coatings, which were subsequently illitized and compacted during burial. **b** Late Permian to Early Triassic K-feldspar alteration was characterized by the dissolution of detrital grains and the formation of authigenic K-feldspar and K-feldspar-replacing illite which all contain nano-porous pathways for diagenetic fluids. **c** As K-feldspar cementation faded, illite precipitation led to the formation of thin tangential coatings and illite meshwork structures. Meshworks formed within highly porous K-feldspar grains and as K-feldspar grain replacements. **d** The youngest generation of illites is composed of lath- to fiber-shaped crystals that nucleated preferably on older illite substrates and K-feldspar surfaces

large intragranular pore networks with local diameters of several micrometers (Fig. 11b). These networks, which formed in K-feldspar (Fig. 9), probably enhanced the flow properties of the reservoir at that time. This stage of dissolution and strong alteration of detrital K-feldspar grains with cement overgrowths resulted in authigenic ^{40}Ar-^{39}Ar ages of 222±2 Ma (Fischer et al., 2012).

The younger, second generation of K-feldspar cement dated at ~190–180 Ma (Fischer et al., 2012) indicates that a second mineral precipitation event affected these rocks, which has been linked to a Triassic to Early Jurassic phase of increased tectonic activity with the influx of hydrothermal K-rich fluids (Gaupp et al., 1993; Zwingmann et al., 1998). This stage of mineral formation probably reduced the secondary porosity by further K-feldspar cementation. This can be observed in the analyzed K-feldspar grains in regions with high porosities and irregularly shaped InterP pores. These regions are filled with K-feldspar cement composed of nm-sized crystals (Fig. 7a). Similar structures were described by Weibel et al. (2019) who attributed these to an abrupt supersaturation of the pore fluids with K.

Although the illites in this sample have not yet been dated, the occurrence of these minerals within K-feldspar grains, the illite meshworks, and the tangentially arranged platy illite coatings probably corresponds to the older group of illites described in the Rotliegend sandstone of this region. These have been dated as late Triassic to Early Jurassic with K-Ar ages in the range 210–180 Ma (Zwingmann et al., 1998) and crystallized following the previously described second generation of Jurassic K-feldspar cementation (Fig. 11c). That a second influx of K-rich fluids was responsible for both the younger generation of authigenic K-feldspar cement and the illite crystals found in and around K-feldspar grains (including meshworks and grain coatings) is partially supported by the general similarities in chemical composition and high concentrations of K. Crystallization probably commenced with K-feldspar growth and was

followed by some calcite precipitation as described by Heidsiek et al. (2020). This is confirmed by the observed intragranular K-feldspar and calcite precipitates (Fig. 5b). As the $a(K^+)/a(H^+)$ activity ratio decreased either by the precipitation of K-feldspar or by decreasing K^+ supply, conditions favored the precipitation of illite (Yuan et al., 2019). Based on the small number of intercalated smectite layers, as indicated by the elemental composition analyses and the irregular shapes of crystals edges, the replacement of K-feldspar grains, the illite meshwork textures, and the first generation of tangential coatings are all suggested to be composed of $1M_d$ illite.

The tangential illite coatings around detrital grains are an omnipresent feature of the Bebertal sandstone. In the literature, the origin of tangential clay coatings is often related to the mechanical infiltration of colloidal smectite-rich suspensions (Storvoll et al., 2002). However, based on the textural findings of the current study, this process is unlikely to be the origin of the complete coatings observed in the Bebertal sandstone, as none of the characteristic features, such as grain bridging menisci, preferred directions of deposition, or crinkly to flaky surfaces were observed (Worden & Morad, 2002; Ziegler, 2006). In contrast, tangential illite coatings, as shown in Fig. 6, generally follow the grain boundaries as opposed to bridging the grains. Therefore, the coating formation likely commenced with the local precipitation or deposition of thin but widespread syn-depositional smectite and hematite (Fig. 11a), as indicated by the thinner coatings in areas with early calcite cements (Fig. 4). Subsequently, these precursor smectites were illitized and compacted during burial and prevented extensive quartz cementation after burial. During the Triassic to Early Jurassic fluid flow event, these coatings likely served as important substrates for the expansive growth of the grain-covering tangential illite in open pores (Fig. 11c). The authigenic growth of these grain-covering coatings is indicated by the enclosed authigenic micro-quartz crystals (Fig. 6c), which are likely to be older than the post-illite crystallization of quartz proposed by Fischer et al. (2012). The tangential orientation of the predominantly lath- and irregular-shaped illite crystals are unusual and could well be the effect of pervasive fluid flow over tens of millions of years (Gaupp et al., 1993; Zwingmann et al., 1998). The post-growth alteration may also have then led to further thickening and amalgamation (Wilkinson et al., 2014).

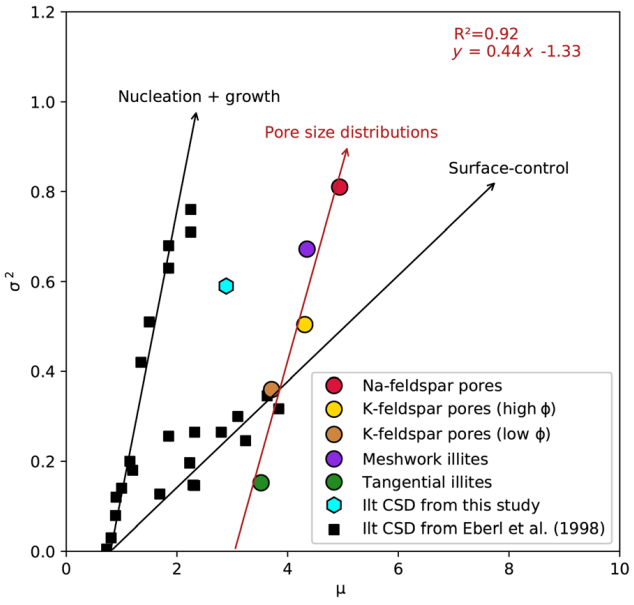

Fig. 12 Crystal-growth mechanism diagram from Eberl et al. (1998) expanded by the PSDs and the illite CSD from the present study. When plotting μ against σ^2, parameters deduced from the log-normal distribution parameters of the PSDs, a trend similar but parallel-shifted to the nucleation and growth mechanism was observed. Some data points from the original figure were excluded for visual reasons

The texturally younger pore filling-illites can be linked to the second generation of illite crystallization that has been regionally dated at 190–155 Ma (Zwingmann et al., 1998). These pore-filling lath-shaped to fibrous crystals nucleated on both tangential coatings and K-feldspar surfaces and formed coalesced sheets or open-pore fillings (Figs. 6e,f and 11d). Due to their well defined crystal shapes, the $1M_{tv}$ polytype recognized in random powder XRD patterns (Fig. 3b) likely corresponds to this second generation of illite crystals. This polytype is common to similar crystal shapes observed in a variety of sandstones characterized by K-rich pure illites where K-bearing detrital minerals acted as precursors (Meunier & Velde, 2004). In these cases, a significant amount of the K was probably derived from local, grain-scale dissolution and neocrystallization reactions.

Pore-size Distributions and Relationships to Illite Crystal Growth

The pore structures in K-feldspar grains and the illite-replacements are notably heterogeneous. The large differences between low- and high-φ K-feldspars are probably related to the porosity established during the initial stage of feldspar dissolution. In larger intragranular

pores, illites form more fibrous crystals compared to the more compacted curly illites observed in the low-φ sample. The total porosity, φ, of all analyzed textural domains varies significantly due to the occurrence of channeled structures or intergranular porosity. The PDF transformations allow a direct comparison of matrix-related pore-size parameters (Table 4). Differences between the textural domains are also revealed by the shapes of their PSDs, as expressed by the log-normal parameters of μ and σ. Increasing μ values correspond to larger mean pore radii and higher σ values to a broader range of the pore-size distributions. Importantly, these two parameters show a strong linear correlation whereby the larger the pore radii the broader the pore-size distributions (Fig. 12). Interestingly, the pore-size distributions for high-φ K-feldspar and meshwork illite show remarkably similar characteristics. This supports the idea that the meshwork textures represent intensely altered K-feldspars where the grain boundaries are no longer evident. These illite-rich areas contrast with the PSDs of: (1) the low-φ K-feldspar being dominated by pores within the K-feldspar cement; (2) the Na-feldspar containing IntraP pores; and (3) the tangential illite coatings characterized by grain-boundary pore space located at the interface with calcite crystals (Fig. 8b).

When plotted on the crystal growth mechanism diagram of Eberl et al. (1998), the linear correlation between the μ and σ^2 parameters of the different PSDs defines a trend that can be compared with the different growth mechanisms based on changes in CSDs (Fig. 12). Assuming the pore spaces are linked primarily to the growth mechanism of illite crystals, i.e. monomineralic growth within the pores and the different textural types represent a pore-filling crystal growth sequence, then this trend can be used to predict the mechanism of illite crystal growth. Based on these assumptions, continuous nucleation and growth mechanisms are indicated. That the curve is shifted towards larger mean sizes and intercepts the horizontal axis at μ = 3 (R_p = 20.1 nm) could reflect the starting pore size at the time of the initial nucleation. This is likely to represent the average pore sizes inside the unaltered K-feldspar crystals or within any substrate material that initially coated the grains (e.g. smectite or illite-smectite precursors). Plotting the log-normal parameters of the CSD determined by *MudMaster* for the total population of illites in the <1 μm size fraction, as expected, does not lie along the PSD line but is shifted toward small sizes. This reflects the smaller dimensions of the illite crystallite thicknesses (mean 24.7 nm) compared to the size of the pores between the crystals. However, assuming the CSD falls along a common trend parallel to the various PSD determinations, it indicates that illite nucleation commenced with particles ~5 nm in size (μ = 1.6, Fig. 12).

Even though two distinct phases of illite formation are recognizable in the Bebertal sandstone, the common trend in the PSDs of the different textural sites is indicative of common crystal growth mechanisms. Eberl and Velde (1989) proposed this growth mechanism may induce many stacking faults within the illite crystals as new particles nucleate on existing illite layers. This corresponds to a large amount of $1M_d$ illite as quantified by Rietveld refinements. The similar compositions of the illite in K-feldspars, the illite meshworks, and the grain coatings of illite all indicate similar amounts of interlayer cations that correspond to ~5% of intercalated smectite layers within the $1M_d$ illite. The grain coatings also include well-developed sheets containing randomly oriented laths, which according to Güven (2001) nucleate on substrates showing a high degree of disorder. Other areas of these grain coatings also contain intergrown lath crystals at 60° and 120° of the $1M_{tv}$ polytype similar to those described by Pevear (1999), Schleicher et al. (2006), and Laverret et al. (2006). The agglomeration of diverse crystal shapes is also similar to those observed by Lanson and Champion (1991), which were attributed to the post-growth alteration of lath-shaped illites transforming into hexagonal crystals. Although the analysis of different textural types of illite did not cover the fibrous pore-filling illites, which were not possible to study due to their delicate structures, the common trend of PSDs for all the textural pore types studied do indicate the younger stage of lath-shaped illite growth, which contributed to grain coatings and pore-fillings, also formed by continuous nucleation and growth from circulating fluids during the Jurassic.

As the PSD values for the primary pores of albite fall along the same crystal growth trend as those observed for the illite pores (Fig. 12), this approach may be applicable to other diagenetic minerals. For example, Worden and Rushton (1992) described similar diagenetic feldspar overgrowths with small primary pores, which were also considered to have formed by continuous nucleation and growth. However, note that the single PSD value for diagenetic albite of the Bebertal sandstone is currently insufficient to establish a reliable PSD trend and more data is required to verify this interpretation.

Porosity and Permeability Characteristics and Relationships to Reservoir Properties

In terms of permeability, the modeled nanoscale transport properties in this study are 3 to 4 orders of magnitude smaller than those obtained from CT-scale simulations and direct measurements (Heidsiek et al., 2020; Jacob et al., 2021). This indicates that the nanoporous systems are, at the plug scale, widely detached from the effective transport pathways measured under laboratory conditions. However, under the lithostatic pressures of the subsurface environment, significantly lower, plug-scale permeabilities can be expected due to compression of the pore systems and enhanced pore pressures. Nanoporous illite structures are, therefore, considered to become more relevant once pore pressures exceed the capillary entry pressures of these structures (Busch & Amann-Hildenbrand, 2013) or as tight reservoir sandstones lose more permeability as a consequence of further crystal growth or particle mobilization in the diagenetic environment.

The permeabilities of the analyzed nano-porous structures range from 13.4 to 1.4 μd and their growth significantly altered flow paths over time (Fig. 11). The generation of nano-porous systems commenced with the second generation of K-feldspar cementation, which formed permeable and connected-channel pore networks within the nanocrystalline cement matrix. This led to a reduction of porosity and permeability, both of which reached its lowest level after the Late Permian dissolution event. The subsequent formation of widespread tangential grain coatings, which do not exhibit perpendicular pore paths, further lowered the porosity and permeability by the reduction of intergranular pore-throat sizes and by sealing intragranular pore networks. Although the formation of K-feldspar replacing illite meshworks generated intergranular permeable porosity, the expansive nature of these structures into the open pore space negatively affected the overall rock permeability.

As the older generations of illite formed more stable, coalesced layers up to 2 μm thick, the younger generation of pore-filling illite laths and fibers are the phases that represent the more fragile structures within this sandstone. These crystals appear in places only weakly attached to substrate surfaces and commonly project out into the open pore space. Because these illites are of $1M_{tv}$ polytype, quantification of the bulk polytype composition, and their crystal shapes and sizes, provide important information for predicting any future mobilization of them. Such mobilization is relevant when new fluids are injected into these reservoir rocks for future gas-storage purposes.

Conclusions

1. Detailed 3D pore-space analyses by FIB-SEM combined with modeling of the fluid flow through the different textural sub-domains of a tight reservoir sandstone provide a powerful tool for reconstructing diagenetic history and for predicting in more detail microstructurally dependent petrophysical properties.
2. Two distinct events of illite crystallization were distinguished that have characteristic textural and petrophysical properties such as porosity and permeability. The older generation of illites of probable Early Jurassic age formed locally: illites in K-feldspar grains; more extensively altered meshwork structures; and thin but widespread grain coatings. These structures were formed by crystals of the $1M_d$ polytype. A younger generation of illites of probable Late Jurassic age formed overgrowths comprising delicate pore-filling lath-shaped and fibrous varieties of the $1M_{tv}$ polytype.
3. The nanoporous structure of the various illite reaction textures indicate a genetic relationship between their pore-size distribution and a common crystal-growth mechanism. A comparison with models based on crystallite-size distributions indicated that the main mechanism was dominated by continuous nucleation and crystal growth. The linear relationship between mean pore radii and the width of the pore-size distributions may be of interest for future modeling and upscaling approaches of reactive transport processes. The results further indicated that the observed trend may apply to a wider range of authigenic minerals, which needs to be confirmed in future studies.

Acknowledgments The authors are grateful to David Awwiller and David Quirt for their constructive feedback which helped to

improve the manuscript. This work was supported by the German Federal Ministry of Education and Research (BMBF) "Geological Research for Sustainability (GEO:N)" program of the BMBF "Research for Sustainable Development (FONA3)" activities. It is part of the project ResKin (Reaction kinetics in reservoir rocks, 03G0871B). The authors also thank Cornelius Fischer for his feedback on an earlier version of this manuscript and the continuous support of the ResKin team. This study used DFG-funded XRD, FIB-SEM, and TEM instrumentation (project numbers 108031954, 173095180, and 428027021).

Author Contribution Conceptualization: Markus Peltz, Laurence N. Warr; Formal analysis: Markus Peltz, Arne Jacob; Investigation: Markus Peltz, Arne Jacob; Methodology: Markus Peltz; Project administration: Laurence N. Warr, Michael Kersten; Software: Markus Peltz, Arne Jacob; Supervision: Michael Kersten, Laurence N. Warr; Validation: Georg H. Grathoff, Frieder Enzmann, Michael Kersten, Laurence N. Warr; Visualization: Markus Peltz; Writing – original draft: Markus Peltz; Writing – review & editing: Arne Jacob, Georg H. Grathoff, Frieder Enzmann, Michael Kersten, Laurence N. Warr

Funding Open Access funding enabled and organized by Projekt DEAL.

Funding sources are as stated in the Acknowledgments.

Data Availability FIB-SEM datasets are available upon reasonable request.

Declarations

Consent to Participate Not applicable.

Consent for Publication Not applicable.

Conflict of Interest The authors declare that they have no conflict of interest.

References

Aldega, L., & Eberl, D. D. (2005). Detrital illite crystals identified from crystallite thickness measurements in siliciclastic sediments. *American Mineralogist, 90*(10), 1587–1596. https://doi.org/10.2138/am.2005.1823

Bauer, A., Velde, B., & Gaupp, R. (2000). Experimental constraints on illite crystal morphology. *Clay Minerals, 35*(3), 587–597. https://doi.org/10.1180/000985500546909

Berg, S., Kutra, D., Kroeger, T., Straehle, C. N., Kausler, B. X., Haubold, C., Schiegg, M., Ales, J., Beier, T., Rudy, M., Eren, K., Cervantes, J. I., Xu, B., Beuttenmueller, F., Wolny, A., Zhang, C., Koethe, U., Hamprecht, F. A., & Kreshuk, A. (2019). Ilastik: Interactive machine learning for (bio)image analysis. *Nature Methods, 16*(12), 1226–1232. https://doi.org/10.1038/s41592-019-0582-9

Berg, S., Saxena, N., Shaik, M., & Pradhan, C. (2018). Generation of ground truth images to validate micro-CT image-processing pipelines. *The Leading Edge, 37*(6), 412–420. https://doi.org/10.1190/tle37060412.1

Bergmann, J., Friedel, P., & Kleeberg, R. (1998). BGMN – a new fundamental parameters based Rietveld program for laboratory X-ray sources, its use in quantitative analysis and structure investigations. *CPD Newsletter*, (20), 5–8.

Bjørlykke, K. (2014). Relationships between depositional environments, burial history and rock properties. Some principal aspects of diagenetic process in sedimentary basins. *Sedimentary Geology, 301*, 1–14. https://doi.org/10.1016/j.sedgeo.2013.12.002

Busch, A., & Amann-Hildenbrand, A. (2013). Predicting capillarity of mudrocks. *Marine and Petroleum Geology, 45*, 208–223. https://doi.org/10.1016/j.marpetgeo.2013.05.005

Darby, D., Wilkinson, M., Fallick, A. E., & Haszeldine, R. S. (1997). Illite dates record deep fluid movements in petroleum basins. *Petroleum Geoscience, 3*(2), 133–140. https://doi.org/10.1144/petgeo.3.2.133

Desbois, G., Urai, J. L., Hemes, S., Schröppel, B., Schwarz, J.-O., Mac, M., & Weiel, D. (2016). Multi-scale analysis of porosity in diagenetically altered reservoir sandstone from the Permian Rotliegend (Germany). *Journal of Petroleum Science and Engineering, 140*, 128–148. https://doi.org/10.1016/j.petrol.2016.01.019

Doebelin, N., & Kleeberg, R. (2015). Profex: A graphical user interface for the Rietveld refinement program BGMN. *Journal of Applied Crystallography, 48*(Pt 5), 1573–1580. https://doi.org/10.1107/S1600576715014685

Eberl, D. D., & Velde, B. (1989). Beyond the Kübler index. *Clay Minerals, 24*(4), 571–577. https://doi.org/10.1180/claymin.1989.024.4.01

Eberl, D. D., Drits, V. A., & Srodon, J. (1998). Deducing growth mechanisms for minerals from the shapes of crystal size distributions. *American Journal of Science, 298*(6), 499–533. https://doi.org/10.2475/ajs.298.6.499

Eberl, D. D., Drits, V. A., Srodon, J., & Nüesch, R. (1996). *MUDMASTER: A Program for Calculating Crystalline Size Distributions and Strain from the Shapes of X-Ray Diffraction Peaks* (Open-File Report). US Geological Survey.

Fischer, C., Dunkl, I., von Eynatten, H., Wijbrans, J. R., & Gaupp, R. (2007). A 3D high resolution model of bounding surfaces in aeolian-fluvial deposits: An outcrop analogue study from the Permian Rotliegend, Northern Germany. *Journal of Petroleum Geology, 30*(3), 257–273. https://doi.org/10.1111/j.1747-5457.2007.00257.x

Fischer, C., Dunkl, I., von Eynatten, H., Wijbrans, J. R., & Gaupp, R. (2012). Products and timing of diagenetic processes in Upper Rotliegend sandstones from Bebertal (North German Basin, Parchim Formation, Flechtingen High, Germany). *Geological Magazine, 149*(5), 827–840. https://doi.org/10.1017/S0016756811001087

Gaupp, R., & Okkerman, J. A. (2011). Diagenesis and reservoir quality of Rotliegend sandstones in the northern Netherlands—a review. In J. Grötsch (Ed.), *SEPM special publication: Vol. 98. The Permian Rotliegend of the Netherlands* (Vol. 98). Society for Sedimentary Geology.

Gaupp, R., Matter, A., Platt, J. D., Ramseyer, K., & Walzebuck, J. (1993). Diagenesis and fluid evolution of deeply buried Permian (Rotliegende) gas reservoirs, Northwest Germany. *AAPG Bulletin*, *77*. https://doi.org/10.1306/BDFF8E0C-1718-11D7-8645000102C1865D

Gharrabi, M. (1998). The transformation of illite to muscovite in pelitic rocks: Constraints from X-ray diffraction. *Clays and Clay Minerals, 46*(1), 79–88. https://doi.org/10.1346/CCMN.1998.0460109

Glennie, K. W., Mudd, G. C., & Nagtegaal, P. J. C. (1978). Depositional environment and diagenesis of Permian Rotliegendes sandstones in Leman Bank and Sole Pit areas of the UK southern North Sea. *Journal of the Geological Society, 135*(1), 25–34. https://doi.org/10.1144/gsjgs.135.1.0025

Grathoff, G. H., & Moore, D. M. (1996). Illite polytype quantification using Wildfire© calculated X-ray diffraction patterns. *Clays and Clay Minerals, 44*(6), 835–842. https://doi.org/10.1346/CCMN.1996.0440615

Griffiths, J., Worden, R. H., Wooldridge, L. J., Utley, J. E. P., & Duller, R. A. (2018). Detrital clay coats, clay minerals, and pyrite: A modern shallow-core analogue for ancient and deeply buried estuarine sandstones. *SEPM Journal of Sedimentary Research, 88*(10), 1205–1237. https://doi.org/10.2110/jsr.2018.56

Güven, N. (2001). Mica structure and fibrous growth of illite. *Clays and Clay Minerals, 49*(3), 189–196. https://doi.org/10.1346/CCMN.2001.0490301

Hancock, N. J. (1978). Possible causes of Rotliegend sandstone diagenesis in northern West Germany. *Journal of the Geological Society, 135*(1), 35–40. https://doi.org/10.1144/gsjgs.135.1.0035

Heidsiek, M., Butscher, C., Blum, P., & Fischer, C. (2020). Small-scale diagenetic facies heterogeneity controls porosity and permeability pattern in reservoir sandstones. *Environmental Earth Sciences, 79*(18). https://doi.org/10.1007/s12665-020-09168-z

Jacob, A., Peltz, M., Hale, S., Enzmann, F., Moravcova, O., Warr, L. N., Grathoff, G., Blum, P., & Kersten, M. (2021). Simulating permeability reduction by clay mineral nanopores in a tight sandstone by combining computer X-ray microtomography and focussed ion beam scanning electron microscopy imaging. *Solid Earth, 12*(1), 1–14. https://doi.org/10.5194/se-12-1-2021

Lander, R. H., & Bonnell, L. M. (2010). A model for fibrous illite nucleation and growth in sandstones. *AAPG Bulletin, 94*(8), 1161–1187. https://doi.org/10.1306/04211009121

Lanson, B., & Champion, D. (1991). The I/S-to-illite reaction in the late stage diagenesis. *American Journal of Science, 291*(5), 473–506. https://doi.org/10.2475/ajs.291.5.473

Lanson, B., Beaufort, D., Berger, G., Bauer, A., Cassagnabère, A., & Meunier, A. (2002). Authigenic kaolin and illitic minerals during burial diagenesis of sandstones: A review. *Clay Minerals, 37*(1), 1–22. https://doi.org/10.1180/0009855023710014

Laverret, E., Mas, P. P., Beaufort, D., Kister, P., Quirt, D., Bruneton, P., & Clauer, N. (2006). Mineralogy and geochemistry of the host-rock alterations associated with the shea creek unconformity-type uranium deposits (Athabasca Basin, Saskatchewan, Canada). Part 1. Spatial variation of illite properties. *Clays and Clay Minerals, 54*(3), 275–294. https://doi.org/10.1346/CCMN.2006.0540301

Loucks, R. G., Reed, R. M., Ruppel, S. C., & Hammes, U. (2012). Spectrum of pore types and networks in mudrocks and a descriptive classification for matrix-related mudrock pores. *AAPG Bulletin, 96*(6), 1071–1098. https://doi.org/10.1306/08171111061

Mehra, O. P., & Jackson, M. L. (1960). Iron oxide removal from soils and clays by a dithionite-citrate system buffered with sodium bicarbonate. In A. Swineford (Ed.), *Clays and clay minerals: proceedings of the seventh national conference on clays and clay minerals* (pp. 317–327). Elsevier Science. https://doi.org/10.1016/B978-0-08-009235-5.50026-7

Menning, M., Gast, R., Hagdorn, H., Käding, K.-C., Simon, T., Szurlies, M., & Nitsch, E. (2006). Zeitskala fur Perm und Trias in der stratigraphischen Tabelle von Deutschland 2002, zyklostratigraphische Kalibrierung der Hoheren Dyas und Germanischen Trias und das Alter der Stufen Roadium bis Rhaetium 2005. *Newsletters on Stratigraphy, 41*(1-3), 173–210. https://doi.org/10.1127/0078-0421/2005/0041-0173

Merriman, R. J., & Kemp, S. J. (1996). Clay minerals and sedimentary basin maturity. *Mineralogical Society Bulletin*, (111), 7–8. https://doi.org/10.1127/0935-1221/2005/0017-0007

Meunier, A., & Velde, B. (2004). *Illite: Origins, Evolution and Metamorphism*. Springer. https://doi.org/10.1007/978-3-662-07850-1

Moore, D. M., & Reynolds, R. C. (1997). *X-ray diffraction and the identification and analysis of clay minerals* (2nd ed.). Oxford University Press.

Morad, S., Al-Ramadan, K., Ketzer, J. M., & de Ros, L. F. (2010). The impact of diagenesis on the heterogeneity of sandstone reservoirs: A review of the role of depositional facies and sequence stratigraphy. *AAPG Bulletin, 94*(8), 1267–1309. https://doi.org/10.1306/04211009178

Münch, B., & Holzer, L. (2008). Contradicting geometrical concepts in pore size analysis attained with electron microscopy and mercury intrusion. *Journal of the American Ceramic Society, 91*(12), 4059–4067. https://doi.org/10.1111/J.1551-2916.2008.02736.X

Pedrosa, E. T., Fischer, C., Morales, L. F., Rohlfs, R. D., & Luttge, A. (2021). Influence of chemical zoning on sandstone calcite cement dissolution: The case of manganese and iron. *Chemical Geology, 559*, 119952. https://doi.org/10.1016/j.chemgeo.2020.119952

Pevear, D. R. (1999). Illite and hydrocarbon exploration. *Proceedings of the National Academy of Sciences of the United States of America, 96*(7), 3440–3446. https://doi.org/10.1073/pnas.96.7.3440

Schleicher, A. M., Warr, L. N., Kober, B., Laverret, E., & Clauer, N. (2006). Episodic mineralization of hydrothermal illite in the Soultz-sous-Forêts granite (Upper Rhine Graben, France). *Contributions to Mineralogy and Petrology, 152*(3), 349–364. https://doi.org/10.1007/s00410-006-0110-7

Seemann, U. (1982). Depositional facies, diagenetic clay minerals and reservoir quality of Rotliegend sediments in the Southern Permian Basin (North Sea): A review. *Clay Minerals, 17*(1), 55–67. https://doi.org/10.1180/claymin.1982.017.1.06

Small, J. S., Hamilton, D. L., & Habesch, S. (1992). Experimental simulation of clay precipitation within reservoir sandstones; 2, mechanism of illite formation and controls on morphology. *SEPM Journal of Sedimentary Research, 62*(3), 520–529. https://doi.org/10.2110/jsr.62.520

Środoń, J., & Eberl, D. D. (2018). 12. Illite. In S. Bailey (Ed.), *Reviews in Mineralogy & Geochemistry: Vol. 13. Micas* (pp. 495–544). De Gruyter. https://doi.org/10.1515/9781501508820-016

Storvoll, V., Bjørlykke, K., Karlsen, D., & Saigal, G. (2002). Porosity preservation in reservoir sandstones due to grain-coating illite: A study of the Jurassic Garn Formation from the Kristin and Lavrans fields, offshore mid-Norway. *Marine and Petroleum Geology, 19*(6), 767–781. https://doi.org/10.1016/S0264-8172(02)00035-1

Tang, L., Gluyas, J., & Jones, S. (2018). Porosity preservation due to grain coating illite/smectite: Evidence from Buchan Formation (Upper Devonian) of the Ardmore field, UK North Sea. *Proceedings of the Geologists' Association, 129*(2), 202–214. https://doi.org/10.1016/j.pgeola.2018.03.001

Ufer, K., Kleeberg, R., Bergmann, J., & Dohrmann, R. (2012). Rietveld refinement of disordered illite-smectite mixed-layer structures by a recursive algorithm. I: One-dimensional patterns. *Clays and Clay Minerals, 60*(5), 507–534. https://doi.org/10.1346/CCMN.2012.0600507

Warr, L. N. (2020). Recommended abbreviations for the names of clay minerals and associated phases. *Clay Minerals, 55*(3), 261–264. https://doi.org/10.1180/clm.2020.30

Weibel, R., Nielsen, M. T., Therkelsen, J., Jakobsen, F. C., Bjerager, M., Mørk, F., Mathiesen, A., Hovikoski, J., Pedersen, S. S., Johannessen, P. N., & Dybkjær, K. (2020). Illite distribution and morphology explaining basinal variations in reservoir properties of Upper Jurassic sandstones, Danish North Sea. *Marine and Petroleum Geology, 116*, 104290. https://doi.org/10.1016/j.marpetgeo.2020.104290

Weibel, R., Olivarius, M., Jakobsen, F. C., Whitehouse, M., Larsen, M., Midtgaard, H., & Nielsen, K. (2019). Thermogenetic degradation of early zeolite cement: An important process for generating anomalously high porosity and permeability in deeply buried sandstone reservoirs? *Marine and Petroleum Geology, 103*, 620–645. https://doi.org/10.1016/j.marpetgeo.2019.02.006

Wilkinson, M., Haszeldine, R. S., & Fallick, A. E. (2014). Authigenic illite within Northern and Central North Sea oilfield sandstones: Evidence for post-growth alteration. *Clay Minerals, 49*(2), 229–246. https://doi.org/10.1180/claymin.2014.049.2.06

Wilson, M. D. (1992). Inherited grain-rimming clays in sandstones from eolian and shelf environments: Their origin and control on reservoir properties. In D. W. Houseknecht & E. D. Pittman (Eds.), *Origin, diagenesis, and petrophysics of clay minerals in sandstones* (pp. 209–225). SEPM (Society for Sedimentary Geology). https://doi.org/10.2110/pec.92.47.0209

Wilson, M. D., & Pittman, E. D. (1977). Authigenic clays in sandstones: Recognition and influence on reservoir properties and paleoenvironmental analysis. *SEPM Journal of Sedimentary Research, 47*. https://doi.org/10.1306/212F70E5-2B24-11D7-8648000102C1865D

Worden, R. H., & Morad, S. (Eds.). (2002). *Special publication number 34 of the International Association of Sedimentologists. Clay mineral cements in sandstones*. Blackwell Pub. https://doi.org/10.1002/9781444304336

Worden, R. H., & Rushton, J. C. (1992). Diagenetic K-feldspar textures: A TEM study and model for diagenetic feldspar growth. *SEPM Journal of Sedimentary Research, Vol., 62*. https://doi.org/10.1306/D42679D8-2B26-11D7-8648000102C1865D

Yuan, G., Cao, Y., Schulz, H.-M., Hao, F., Gluyas, J., Liu, K., Yang, T., Wang, Y., Xi, K., & Li, F. (2019). A review of feldspar alteration and its geological significance in sedimentary basins: From shallow aquifers to deep hydrocarbon reservoirs. *Earth-Science Reviews, 191*, 114–140. https://doi.org/10.1016/j.earscirev.2019.02.004

Ziegler, K. (2006). Clay minerals of the Permian Rotliegend Group in the North Sea and adjacent areas. *Clay Minerals, 41*(1), 355–393. https://doi.org/10.1180/0009855064110200

Zwingmann, H., Clauer, N., & Gaupp, R. (1998). Timing of fluid flow in a sandstone reservoir of the North German Rotliegend (Permian) by K-Ar dating of related hydrothermal illite. *Geological Society, London, Special Publications, 144*(1), 91–106. https://doi.org/10.1144/GSL.SP.1998.144.01.07

Zydney, A. L., Aimar, P., Meireles, M., Pimbley, J. M., & Belfort, G. (1994). Use of the log-normal probability density function to analyze membrane pore size distributions: Functional forms and discrepancies. *Journal of Membrane Science, 91*(3), 293–298. https://doi.org/10.1016/0376-7388(94)80090-1

5.2.2 Article 2

Simulating permeability reduction by clay mineral nanopores in a tight sandstone by combining computer X-ray microtomography and focussed ion beam scanning electron microscopy imaging

Arne Jacob, **Markus Peltz**, Sina Hale, Frieder Enzmann, Olga Moravcova, Laurence N. Warr, Georg H. Grathoff, Philipp Blum, and Michael Kersten

Solid Earth

Volume 12 (1-14)

Published: January 11, 2021
DOI: https://doi.org/10.5194/se-12-1-2021

Solid Earth, 12, 1–14, 2021
https://doi.org/10.5194/se-12-1-2021

Solid Earth Open Access EGU

Simulating permeability reduction by clay mineral nanopores in a tight sandstone by combining computer X-ray microtomography and focussed ion beam scanning electron microscopy imaging

Arne Jacob[1], Markus Peltz[2], Sina Hale[3], Frieder Enzmann[1], Olga Moravcova[1], Laurence N. Warr[2], Georg Grathoff[2], Philipp Blum[3], and Michael Kersten[1]

[1]Geosciences Institute, Johannes Gutenberg-University, J.-J. Becherweg 21, 55099 Mainz, Germany
[2]Institute of Geography and Geology, University Greifswald, Friedrich-Ludwig-Jahn-Str. 17a, 17487 Greifswald, Germany
[3]Institute of Applied Geosciences (AGW), Karlsruhe Institute of Technology (KIT),
Kaiserstraße 12, 76131 Karlsruhe, Germany

Correspondence: Arne Jacob (a.jacob@uni-mainz.de)

Received: 9 September 2020 – Discussion started: 30 September 2020
Revised: 23 November 2020 – Accepted: 25 November 2020 – Published: 11 January 2021

Abstract. Computer X-ray microtomography (µXCT) represents a powerful tool for investigating the physical properties of porous rocks. While calculated porosities determined by this method typically match experimental measurements, computed permeabilities are often overestimated by more than 1 order of magnitude. This effect increases towards smaller pore sizes, as shown in this study, in which nanostructural features related to clay minerals reduce the permeability of tight reservoir sandstone samples. Focussed ion beam scanning electron microscopy (FIB-SEM) tomography was applied to determine the permeability effects of illites at the nanometre scale, and Navier–Stokes equations were applied to calculate the permeability of these domains. With these data, microporous domains (porous voxels) were defined using microtomography images of a tight reservoir sample. The distribution of these domains could be extrapolated by calibration against size distributions measured in FIB-SEM images. For this, we assumed a mean permeability for the dominant clay mineral (illite) in the rock and assigned it to the microporous domains within the structure. The results prove the applicability of our novel approach by combining FIB-SEM with X-ray tomographic rock core scans to achieve a good correspondence between measured and simulated permeabilities. This methodology results in a more accurate representation of reservoir rock permeability in comparison to that estimated purely based on µXCT images.

1 Introduction

Depositional environment and subsequent diagenetic alterations are two key factors that influence the bulk mineralogical composition and the authigenic clay mineral inventory of a reservoir (Wilson and Pittman, 1977; Worden and Morad, 1999), and therefore the fluid-flow properties of the porous rock. A well-established technique to image and analyse rapidly the 3D physical properties of porous rocks is computer X-ray microtomography (µXCT) combined with the concept of digital rock physics (Andrä et al., 2013a, b; Okabe and Blunt, 2004). By applying monochromatic synchrotron radiation, it is possible to overcome conventional µXCT artefacts like beam hardening and problems that arise due to limited phase contrast, lack of resolution and edge preservation, as well as low signal-to-noise ratios (Brunke et al., 2008; Kling et al., 2018; Lindquist et al., 2000; Mayo et al., 2015; Spanne et al., 1994). Synchrotron-based µXCT scans with image resolutions in the order of 1 µm can provide a sound basis for flow and transport modelling of tight sandstones as suggested by Peng et al. (2014). They found that synchrotron µXCT imaging is necessary for tight sandstones when the connectivity of the pore space is low and pore throats cannot be resolved using a conventional µXCT scanner. They further concluded that a high abundance of the smallest resolvable pores falsifies modelled permeabilities due to an overestimation of actual pore sizes. Several studies have shown sub-micrometre pore structures to be a

frequent feature of tight reservoir rocks (Jiang, 2012; Shah et al., 2016; Soulaine et al., 2016). Most of these nanostructures are related to different types of clay minerals; most commonly illite, kaolinite, chlorite and smectite (e.g. Wilson and Pittman, 1977; Worden and Morad, 1999; Desbois et al., 2016).

Although known for years, considering such structural features below µXCT resolution in pore-scale models remains challenging (Alyafei et al., 2015; Guan et al., 2019; Liu and Mostaghimi, 2018; Liu et al., 2020; Menke et al., 2019; Peng et al., 2012). Soulaine et al. (2016) systematically analysed the effect of sub-resolution domains with varying permeabilities on the simulated permeabilities of Berea sandstone (20 vol % porosity, 2 vol % sub-resolution domains) and found that calculated permeabilities can be reduced by up to 50 %, if microporous domain permeabilities converge towards zero. Thus, it is evident that neglecting sub-resolution information can lead to a significant overestimation of rock permeability in such simulations (e.g. Saxena et al., 2018, 2017). Menke et al. (2019) utilized a multi-scale Brinkman area approach, applying different permeabilities for each microporous domain to simulate flow in mono-mineralic carbonate rock. They showed that Stokes–Brinkman models are in good agreement with experimental data, whereas Stokes and/or Navier–Stokes models alone were not able to predict permeability in a conventional flow scenario. They also demonstrated that for pure carbonates, a direct correlation can be established between observed density contrasts and specific physical properties, such as porosity and permeability. However, this approach is not applicable in a system with more than one rock-forming mineral, such as a tight sandstone, where density contrasts relate to different mineral phases as well as sub-resolution porosities.

The lack of distinct material information for a voxel is often ascribed to the *partial volume effect* (e.g. Kessler et al., 1984; Ketcham and Carlson, 2001). To overcome the impact of this effect on physical properties of a rock, imaging techniques that can resolve the pore structure at different length scales have to be applied. For estimating the permeability of reservoir rocks, the resolution achieved by synchrotron radiation imaging lies within an acceptable range (Saxena et al., 2018). Several studies have demonstrated that, by combining X-ray and scanning electron imaging, the pore space of tight clay-bearing rocks can be spatially resolved from the millimetre down to the nanometre scale (e.g. Desbois et al., 2016; Hemes et al., 2015; Markussen et al., 2019).

In this study, we aim to demonstrate a new approach by combining synchrotron-based µXCT imaging with focussed ion beam scanning electron microscopy (FIB-SEM) to improve flow simulations in a tight sandstone formation with high clay mineral content. First, we used machine learning-based image segmentation to enhance pore space segmentations of artefact-rich FIB-SEM topologies. Then, we conducted Navier–Stokes simulations on FIB-SEM topologies. Finally, we subsequently used these simulations as input data for sub-resolution domains in µXCT-based Stokes–Brinkman models (Brinkman, 1949; Neale and Nader, 1974). This novel morphology-based approach for sub-resolution-rich materials results in simulated permeabilities that fit experimental results significantly better than using Navier–Stokes simulations alone.

2 Sample preparation and characterization

In this study, a well-characterized illite-bearing Upper Rotliegend sandstone from Germany was used, which was sampled from the quarry Schwentesius near Bebertal village (Heidsiek et al., 2020). This well-known location exposes an analogue of the Permian gas reservoir sandstone of the Flechtingen High, which formed part of the North German Basin. Thin section analyses of this reservoir rock have shown that illite is the main clay mineral, which primarily occurs as a coating along detrital grains, illite meshworks grown on coatings, diagenetically altered K-feldspar and illitized lithoclasts (Fischer et al., 2012).

Samples were taken from a large sandstone block displaying a variety of different aeolian and fluvial depositional facies (Fig. 1a). We identified several facies denoted A to J from four different types of sedimentary depositional layers. The samples of the different facies were numbered from left to right. Samples were drilled out and extracted from marked locations in the form of plugs with a diameter of 2.5 cm. The plugs were cut into three segments which were used for X-ray diffraction analyses, helium porosimetry measurements and FIB-SEM imaging. Mini plugs were drilled directly beside the plugs with a diameter of 3 mm and a length between 10 and 20 mm. The larger plugs were used for mineralogical and geochemical analysis, and to measure permeabilities experimentally. The mini plugs were scanned at the synchrotron radiation-based µXCT imaging beamline P05 at the PETRA of DESY Hamburg (Germany). After the synchrotron measuring campaign, the mini plugs were additionally examined by FIB-SEM and energy dispersive X-ray spectroscopy (EDX) imaging to obtain qualitative and quantitative information about the clay mineral particles found within the rock pore space. Microporous structures in the Rotliegend sandstone sample could be resolved by comparing µXCT and FIB-SEM images. The term "microporous" refers to the definition of sub-micrometre porosity by Soulaine et al. (2016), who differentiated between void, solid and microporous voxels in µXCT images. According to for example Tinet et al. (2020), the term "nanoporous" is used to describe structures with predominant pore sizes in the nanometre range (0.2–1000 nm). In this range, the clay minerals often appear as a greyish pore-filling phase in µXCT images.

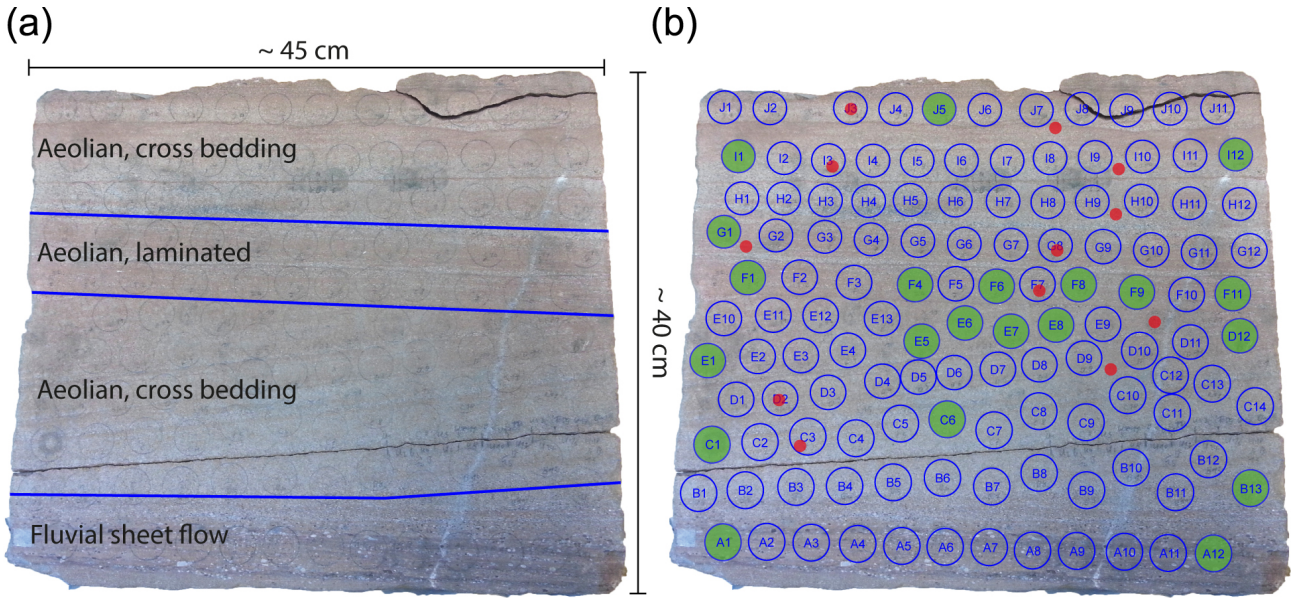

Figure 1. (a) Upper Rotliegend sandstone block showing four main deposition facies. **(b)** Sampling locations and sizes of the extracted plugs (green) and the mini plugs (red) extracted.

3 Analytical procedures

3.1 Mineralogical characterization

X-ray diffraction analyses using the Rietveld analysis program Profex 4.0 (Doebelin and Kleeberg, 2015; Ufer et al., 2012) have shown a homogenous mineralogical composition along the layers of the sample block with only slight variations in content (Fig. 2).

The main components are quartz (58 wt %–69 wt %), authigenic and diagenetic feldspars (12 wt %–20 wt %), calcite (1 wt %–18 wt %), and illite (10 wt %–17 wt %). In the <0.2 µm size fraction, we observed traces of swelling smectite interpreted as contaminants from surface weathering. Accessory hematite and barite particles also occur with abundances of <1 wt %. In the Bebertal tight sandstone, illite is by far the most abundant clay mineral and makes up ∼95 wt % of the <2 µm fraction. Commonly, the nanometre-scale microstructural features of reservoir rocks containing significant amounts of clay minerals are usually not detectable at µXCT resolution due to a low absorption contrast (Ahmad et al., 2018).

3.2 Permeability measurements and pore size distribution

A helium gas-driven permeameter under steady-state conditions was used to experimentally obtain permeability values for the individual plugs (e.g. Filomena et al., 2014). Compressed air was used to apply a pressure of 10 bar to the core samples that were coated by a latex membrane. A Bronkhorst F-111C-RBB-33-V was used as a flowmeter. It was calibrated by polynomial calibration and has a measuring accuracy of ±0.5 % plus ±0.1 % of the full scale. To measure the differential pressure, an Emerson Rosemount 3051S Ultra was used with an accuracy of ±0.045 %. To control the inflow and outflow, two pressure sensors (Brooks 5866) with an accuracy of ±0.5 % were installed. For permeability measurements, the inflow and outflow pressures of the helium flux were sequentially increased in up to six pressure steps. The differential pressure was kept constant at 200–500 mbar depending on the sample properties. The intrinsic sample permeability was derived from the apparent gas permeability, K_g, determined for each pressure step using Darcy's law (Liu et al., 2017):

$$K_g = \frac{2Qp_2\eta L}{A(p_1^2 - p_2^2)}, \quad (1)$$

where Q is the measured gas flow rate, η is the dynamic viscosity of the permeant, L is the sample length, A is the sample cross section, and p_1 and p_2 are the inflow and outflow pressures. By plotting K_g against $\frac{1}{(p_1+p_2)/2}$, the data can be fitted by a straight line. The intercept of the best-fit line at the K_g axis corresponds to the intrinsic sample permeability, K_{int} (Gao and Li, 2016; Klinkenberg, 1941). Also, MICP measurements were conducted with an Autopore IV Series (Micromeritic Instrument Corp.) to determine the pore size distribution of a dried sub-sample with a weight of ∼2.5 g, which was taken from a cross-bedded aeolian layer of the sandstone block. Based on the capillary law, MICP enables the analysis of a wide spectrum of pore sizes (3 nm to >900 µm), corresponding to a pressure range of 0–414 MPa. As a non-wetting liquid with a high contact angle

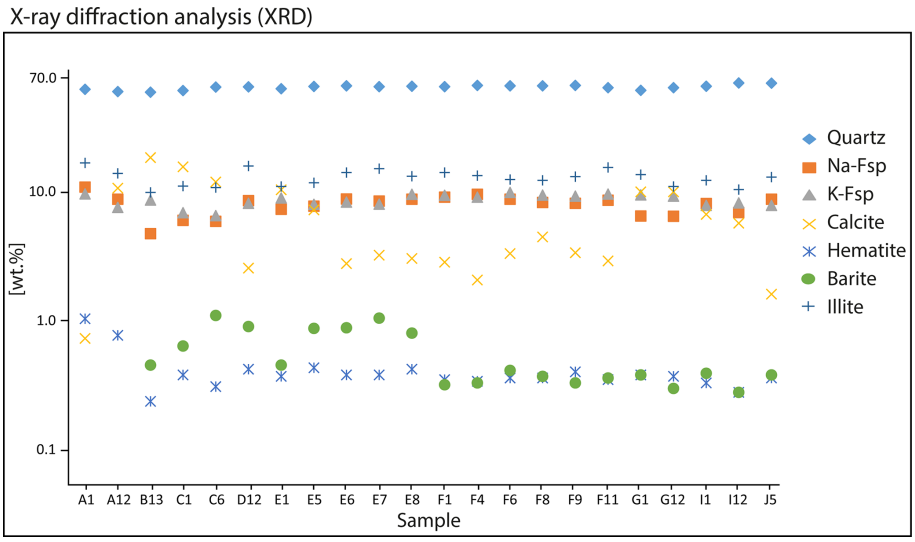

Figure 2. XRD analysis of the main minerals in the plugs based on Rietveld calculations, determined for several samples of facies A to J of the sandstone block.

(130–140°), mercury only penetrates a pore when pressure is applied. Under the assumption of cylindrical pores, the applied pressure is directly proportional to the pore throat diameter as described by the Washburn equation (Washburn, 1921):

$$D = \frac{-4\gamma \cdot \cos\theta}{P}, \tag{2}$$

where D is pore throat diameter, γ is the surface tension, θ is the contact angle and P is the applied pressure.

3.3 Synchrotron-based µXCT

For synchrotron tomography, a beam energy of 29.87 KeV was used while the sample-detector distance was 1.2 cm. The effective image resolution of the detector equipped with a CCD camera was 1.22 µm per pixel, while the image size was 3056 × 3056 pixels. We used an advanced reconstruction script described in Moosmann et al. (2014) with the MATLAB® software and binned the images by a factor of 2 before reconstruction to increase the signal-to-noise ratio. This decreased the voxel resolution to 2.43 µm and changed the image size to 1528 × 1528 pixels. The number of projections was 1200, with the information of five subsequent images used to calculate an average for every projection image. After reconstruction of the 3D image stacks, the scans were denoised using the non-local means filter of the GeoDict 2020 software package (Buades et al., 2011). Image segmentation of the mini plugs was realized by conventional greyscale thresholding. The greyscale values for each phase on a 16 bit intensity range were 0–8550 for pores, 8551–12 880 for grains, 12 881–25 000 for cements and 25 001–65 535 for high-density cements and oxides. Since the best threshold values for each phase varied slightly from sample to sample, these values were adjusted for each segmentation within a small range of ±50. A qualitative comparison with machine learning segmentation revealed a better pore-to-solid segmentation and resolving of small pore throats by thresholding (Fig. 3). Since the main goal was to achieve the best possible permeability estimation, the differentiation between pore and solid is more important for permeability estimation than the accurate segmentation into different phases (Khan et al., 2016). Leu et al. (2014) point out that even a small variation in pore throat morphology can have a large impact on the estimation of permeability.

For permeability simulations, we either used the fast Fourier transformation (SIMPLE-FFT) or the left-identity-right (LIR) solvers, both implemented in the FlowDict module of the GeoDict software package (Linden et al., 2015; Moulinec and Suquet, 1995). While the SIMPLE-FFT solver is fast for calculating low-porosity domains, the LIR solver is better suited for high-porosity domains and requires less memory. Both iterative finite volume solvers can apply Navier–Stokes and Navier–Stokes–Brinkman equations. Derived from these equations, Darcy's law (Eq. 1) is used to calculate the permeability of a material (Darcy, 1856):

$$\boldsymbol{u} = -\frac{K}{\eta}(\nabla p - \boldsymbol{f}). \tag{3}$$

In Eq. (3), $\boldsymbol{u}$ is the three-dimensional average fluid-flow velocity, K is the permeability, η is the fluid viscosity, p is the intrinsic average pressure tensor and f is the force density field, which was defined using the Navier–Stokes conservation of momentum equation for all three dimensions (Eq. 4):

$$-\eta\Delta\boldsymbol{u} + (\boldsymbol{u}\cdot\nabla)\,\boldsymbol{u} + \nabla p = \boldsymbol{f}. \tag{4}$$

The Brinkman term can be added to the Navier–Stokes equation where porous voxels are required. These voxels include

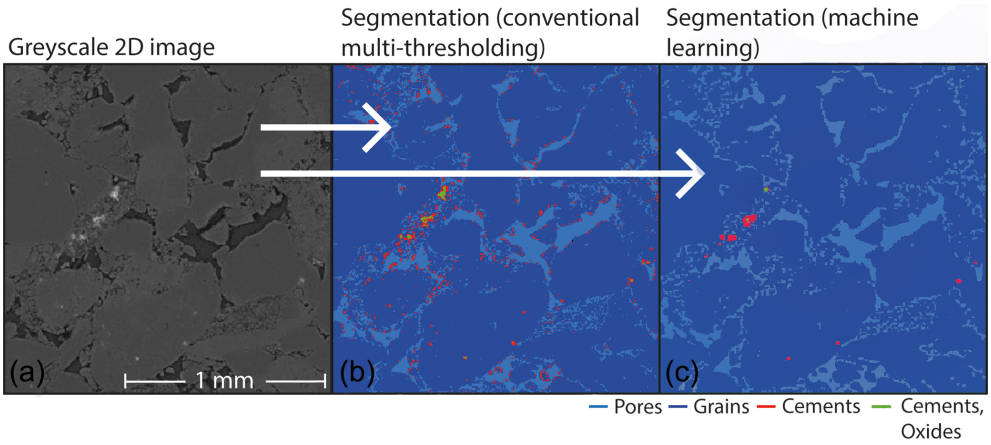

Figure 3. (a) Greyscale 2D µXCT image of a mini plug. **(b)** Segmented phases using multi thresholding. **(c)** Segmented phases using the machine learning image classification module of the software ilastik (Version 1.3.3) by Berg et al. (2019).

the nanoporous flow resistivity:

$$-\eta\Delta\boldsymbol{u} + (\boldsymbol{u}\cdot\nabla)\boldsymbol{u} + \eta K^{-1}\boldsymbol{u} + \nabla p = \boldsymbol{f}, \quad (5)$$

where K^{-1} is the inverse of the permeability tensor and ηK^{-1} the flow resistivity. The applicability and robustness of combining Navier–Stokes equations with the Brinkman term has been validated by Iliev and Laptev (2004).

We calculated the permeability with symmetric boundary conditions in tangential and flow direction with a pressure drop of 20 370 Pa. The symmetric boundary conditions are valid for low-porosity structures with non-periodic pore throat geometries. The differential pressure value was set to be able to compare the results with helium permeation flux measurements where similar values have been used. As a convergence stopping criterion, a low error bound of 0.05 was chosen. The error bound criterion uses the result of a previous iteration to predict the final solution by linear and quadratic extrapolation. This stops the iteration when the relative difference regarding the prediction is smaller than 5 %. During this process, the solver recognizes oscillations and local minima or maxima which prevents a premature stopping of the solver during the iteration process.

3.4 FIB-SEM measurements

In this study, a Zeiss Auriga crossbeam electron microscope equipped with a Gemini electron column and an Orsay Physics ion beam was used. SEM images were taken at 1 kV with an in-lens secondary electron (SE2) detector, and FIB slicing was executed with a beam current between 0.5 and 2 nA and a voltage of 30 kV. This resulted in a slice thickness of 25 nm. A large FOV of $\sim$ 20 µm could be reached. To derive structural information from the FIB-SEM images, extensive post-processing of the data was required. Following image alignment and cropping, stripes and shadow artefacts were filtered out before image segmentation. The Slice Alignment operation of the module ImportGeo of the GeoDict 2020 software package was used to align the images, while the Curtaining Filter was used for stripes correction (Fig. 4). In general, the segmentation of pores in FIB-SEM images was not straightforward since scans of porous polished sections are pseudo-2D and contain information from behind the actual imaging plane (De Boever et al., 2015).

As multi-thresholding and watershed segmentation algorithms have problems with shine-through artefacts (Prill et al., 2013), capturing the correct 3D pore space geometry is of crucial importance for the determination of a realistic permeability. Recent advances have shown that machine learning image segmentation software can successfully be utilized to segment pore space in CT scans (Berg et al., 2018).

The software ilastik, an interactive learning and segmentation toolkit by Berg et al. (2019), was used for the interactively supervised machine learning segmentation of the phases in our FIB-SEM images (Fig. 4). The built-in pixel classification module groups the probability of each pixel to be assigned to a phase according to their different imaged features. The software provides a set of different images based on features derived from the original image (filtering and smoothing, edge detection, etc.). Examples of the correct class (phase) provided by the user builds a decision surface in feature space. Based on these features, a random forest classifier assigns each pixel or voxel to a certain phase. This method works for both 2D and 3D data. The accuracy of this method increases with the number of user-provided training data. In a manually controlled workflow, it was possible to reach high segmentation accuracies with only minor over- or underestimations of the pore space (Fig. 4c, d).

3.5 Defining microporous domains

The need to define microporous domains results from the mismatch of permeability between µXCT simulations and gas-driven permeameter tests. While the simulation of per-

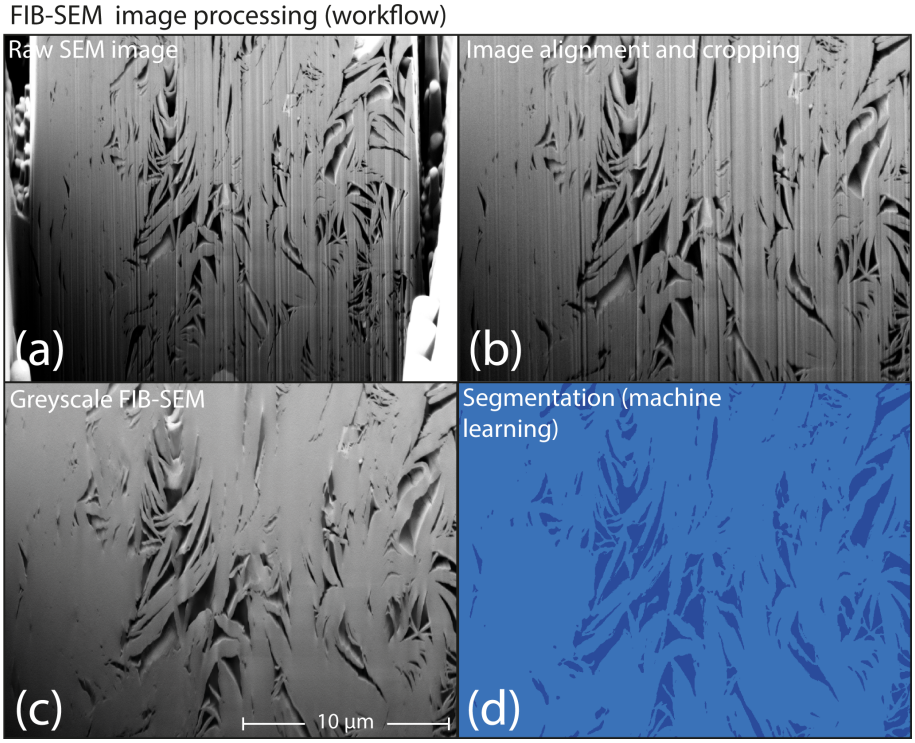

Figure 4. **(a)** Raw SEM image of secondary illite growth in a porous feldspar with streaks and shadow artefacts. **(b)** Images with aligned slices of a cropped region of interest. **(c)** Filtered greyscale SEM image of the illite meshworks. **(d)** The binarized result after image segmentation with pixel classification algorithms of the software *ilastik*.

meability in structures with high permeability and porosity obtained by µXCT scans is precise, the effect of nanoporosity below resolution on permeability increases with decreasing permeability (Pittman and Thomas, 1979; Saxena et al., 2018). When comparing backscattered electron (BSE) images with µXCT images of the same slice, it becomes apparent that the smallest pores in µXCT images simplify the real pore structure (Fig. 5). Furthermore, SEM and EDX images revealed that most of the pores are filled with clay minerals. Since both void and microporous regions share similar greyscale values, it is impossible to correctly differentiate upon segmentation. In this approach, the segmentation of the pores includes clay minerals with a low absorption contrast. To determine the distribution of illite in µXCT scans, we used correlative µXCT, SEM and EDX measurements. For this, a 3 mm plug was embedded into epoxy resin and then ground and polished until the region of interest was reached. Two sites were chosen for EDX mappings (Fig. 5). Comparing EDX mappings with CT images shows that the distribution of illite agrees with the textural findings of Fischer et al. (2012).

Furthermore, it becomes apparent that illite enrichments coincide with regions that are usually referred to as void pore space in µXCT images. The mismatch between real pore structure and segmented pore space is highest in small pores and throats. An average size of $\sim 5\,\mu m$ was measured for illites which cover the surfaces of the quartz and feldspar grains. This corresponds to approximately two voxels in the µXCT images. To refine flow and reduce the influence of overestimated pore sizes in these specific regions, we define all pores with a diameter ≤ 2 voxels as microporous domains. The Brinkman term accounts for small pores, where grains are porous themselves (Brinkman, 1949). To extract these regions from the initial pore space segmentation F_{p*} we calculated Euclidian distance maps as used by Maurer et al. (2003):

$$d = \sqrt{(x_2 - x_1) + (y_2 - y_1) + (z_2 - z_1)}, \quad (6)$$

where d is the distance between two points; x_1, y_1 and z_1 are the coordinates of the first point; and x_2, y_2 and z_2 are the coordinates of the second point. By selecting $d(\leq 2)$ all pore voxels with the nearest distance of ≤ 2 voxels to the next solid surface are masked, including the outer rim of larger pores (Fig. 6b). To obtain a mask with pores ≤ 2 voxels, this rim layer surplus must be removed. This was realized by performing a morphological dilation operation on $d(> 2)$ using a structure element SE2 of 2^3 voxels. By subtracting the dilated image from $d\,(> 2)$, the microporous domain data $F_{\mu 2}$ (Fig. 6c) can be obtained.

$$F_{\mu 2} = d\,(\leq 2) - \delta_{\mathrm{SE2}}\,(d(> 2)) \quad (7)$$

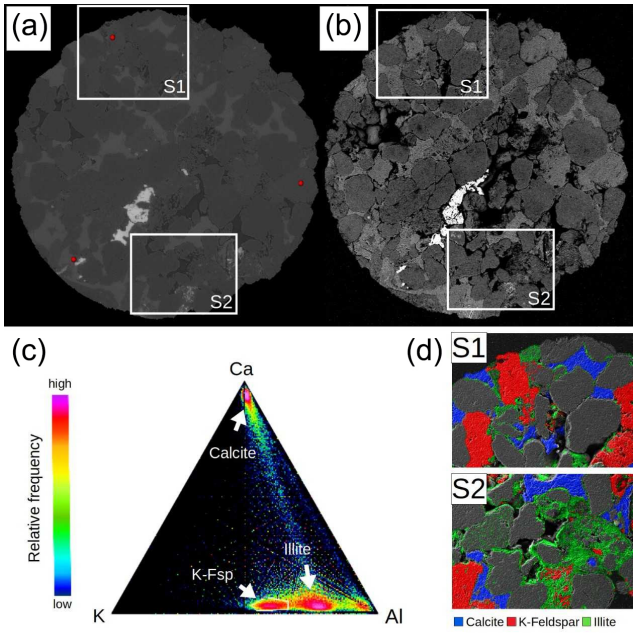

Figure 5. **(a)** µXCT and corresponding **(b)** BSE image of the polished section including the close-up regions S1 and S2 that were used for EDX mapping to analyse the distribution of illites. **(c)** Ternary plot of Ca, K and Al content of each pixel in the mappings. Calcite, illite and K-feldspar plot in three distinct regions. By selecting these areas, a phase map overlay was created that visualizes the location of these phases in SE images. **(d)** Region S1 and S2 with phase map overlays. Illite is predominantly found in the vicinity of altered feldspars, as coating along grain boundaries and as authigenic pore filling.

In GeoDict the permeabilities of the microporous domains are calculated with the Brinkman term. Based on flow simulations on 3D FIB-SEM images of illite meshworks, an isotropic permeability was assigned to the microporous domains (Fig. 6). Yoon and Dewers (2013) confirmed the validity of the approach of extrapolating structural features of clays measured by FIB-SEM to the pore scale. The complete workflow for a precise permeability simulation is illustrated in Fig. 7.

4 Results and discussion

4.1 Permeability measurements and pore size distribution

Four to six pressure stages were applied to the plug samples to determine their gas permeability. In Table 1, parameters which were used for the permeameter test are shown for sample F8. These values yield a Klinkenberg factor of 0.56 and a quadratic regression coefficient of 0.94.

Overall, the measured intrinsic permeabilities range between 1.1 and 5.4 mD with an average value of 2.9 mD for both aeolian facies (Table 2; Fig. 1, sample series E and F). The quadratic regression coefficient ranges from 0.732 to 0.998, which indicates a high accuracy of the permeameter test. The small variation of the physical rock properties between the main layers is induced by different angles of the grain layering in each plug sample and small-scale variations in grain and pore size distributions. The observed variance is in the typical range of observed permeability fluctuations for tight reservoir sandstones (Lis-Śledziona, 2019). Considering the observed permeability, the studied rock samples are at the lower end of the permeability range known for sedimentary reservoir rocks (Gluyas and Swarbrick, 2004).

The pore size distribution of the sub-sample analysed by mercury intrusion porosimetry (Sect. 3.2) was obtained by a semi-logarithmic representation of the normalized intrusion volume achieved per pressure interval (Fig. 8). The consumed capillary stem intrusion volume of 27 % was within the acceptable range needed for precise measurements. We discovered a major peak at approximately 1 µm, representing the most common pore throat diameter.

In addition to the mercury porosimetry results, calculations of the pore size distribution of FIB-SEM and µXCT mini plug images were conducted using the GeoDict module PoroDict. This module provides an algorithm that virtually pushes spheres of different sizes into a medium to determine the 3D pore size distribution (Münch and Holzer, 2008). FIB-SEM measurements of the pore size distribution cover the small pores related to the illite nanoporosity, while µXCT porosimetry illustrates the pore size distribution of the larger-scale intergranular pore space skeleton.

The µXCT pore volume analysis shows a constant rise towards the smallest observed pore diameters (2.44 µm; Fig. 9). The steepest slope is observed between 7.3 and 12.2 µm, which indicates that the largest volume of pore bodies is observed in that range. The calculated pore size distribution from nanoporous 3D structures of illite meshworks obtained by FIB-SEM imaging shows three distinct peaks at 75, 125 and 250 nm. This illustrates that the most common inscribed pore diameters are relatively small compared to the actual extent of the pores, which is considered typical for slit-shaped pore systems where the pore axial ratio is high (Desbois et al., 2016). Ultimately, this results from the different thicknesses of clay platelets and heterogeneity in the alignment of the illite nanostructure (Aplin et al., 2006).

An apparent gap exists between diameters observed by MICP and 3D imaging with FIB-SEM and µXCT. While MICP peaks at around 1 µm, diameters observed by µXCT start at 2.4 µm and the largest inscribed diameters observed by FIB-SEM are below 700 nm. However, it must be noted that pressure-controlled MICP generally gives information about the dimension of pore throats, whereas pore size distributions provided by imaging techniques give information about pore body volumes (Zhao et al., 2015). Furthermore, pore shielding may cause an underestimation of larger pores for MICP (Abell et al., 1999; Gane et al., 2004). The occur-

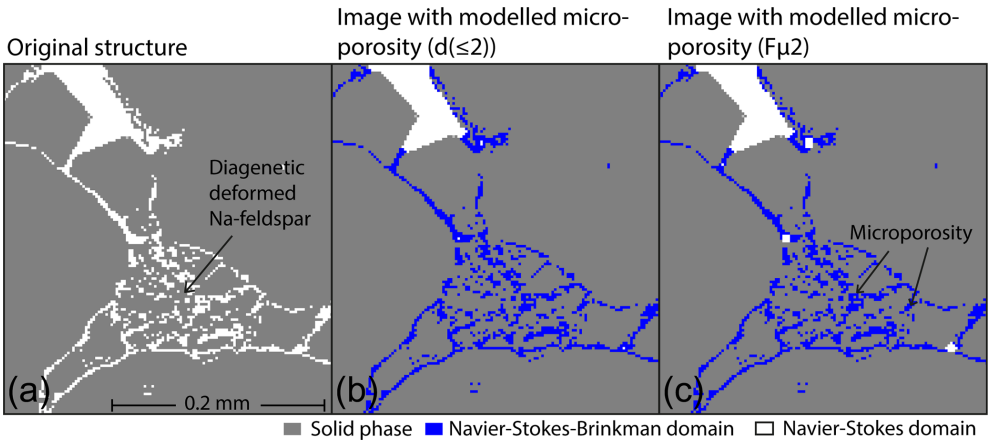

Figure 6. **(a)** Segmented μXCT image of the pore space of a mini plug. **(b)** Image with applied microporous domain using the Euclidian distance map approach. **(c)** Image with removed outer rim layer of larger pores.

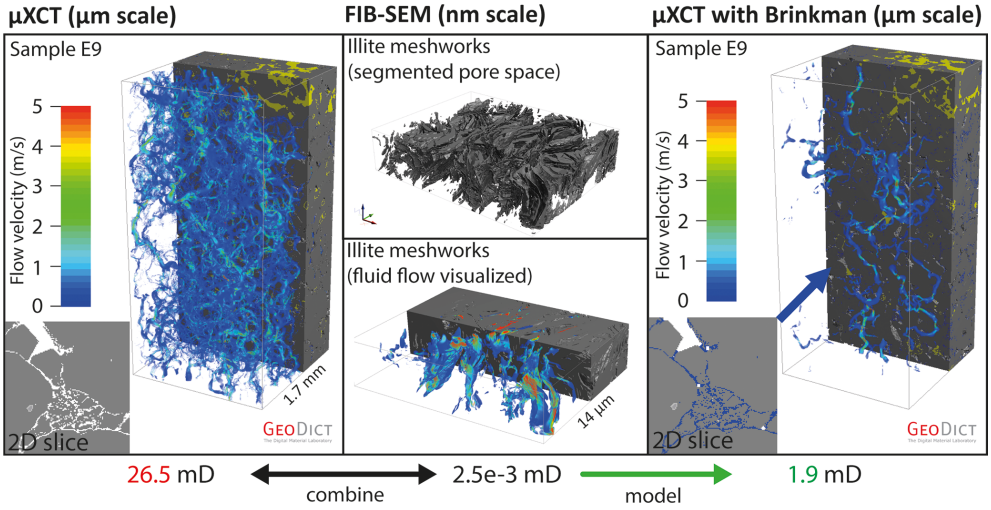

Figure 7. Workflow for microporous domain modelling combining FIB-SEM nanoporosity with μXCT scans. Sample E9 of the aeolian layer with well-distributed flow paths was selected for visualization. Upon the modelling of the microporous domains, the total fluid-flow velocity decreases. Displayed simulated permeabilities include the mean values of five samples with the best distribution of percolation paths. Fluid-flow velocities close to zero are transparent.

rence of authigenic illites is the likely cause of this effect as they are commonly found in pore throat areas. Since the Washburn equation assumes ideal pore throats of cylindrical shape, the underestimation of larger pores becomes more evident with the increasing complexity of the pore throat system at both the millimetre and nanometre scale (Washburn, 1921). Therefore, a direct comparison between the used methods is unlikely to result in compatible results.

4.2 Permeability simulation

A calculated isotropic permeability of 2.53×10^{-3} mD was used for the microporous domains based on the Navier–Stokes fluid-flow simulations of permeability of FIB-SEM scans of the illite meshworks. The number of porous voxels resulting from clay mineral modelling ranges between 3.3 vol % and 7.1 vol % of the total structure volume for all μXCT scans considered. A comparison of the modelled clay minerals in μXCT scans with XRD mass balancing highlights a large difference between the mineral abundances measured (Table 3, Fig. 2).

While the mean amount of clay minerals based on XRD measurements was 12.7 wt % (about 11.3 vol % within a structure with 8 % porosity), an average amount of 5.4 vol % was modelled by the distance map algorithm. This is expected since the illite content inside grains was not modelled since it has no effect on permeability. We simulated permeability of 12 mini plug samples that were scanned by μXCT and compared them with measurements from gas permeameter experiments. As a first step, we extracted and illustrated

Table 1. Parameters of the gas permeameter flux experiment (sample F8), including measured helium gas flow rate, recorded inflow and outflow pressures as well as calculated apparent gas permeability for each pressure stage. For evaluating the intrinsic sample permeability, the sample cross section (0.025 m) and length (0.05 m) as well as the dynamic viscosity of helium (18.4×10^{-6} Pas) is also needed.

Pressure stage	Inflow pressure (Pa)	Outflow pressure (Pa)	Flow rate ($m^3\ s^{-1}$)	Apparent permeability (mD)
1	129 522.3	109 151	2.8803e−08	2.38
2	149 587.1	129 167.9	2.8401e−08	2.38
3	174 634.9	154 120.4	2.7072e−08	2.28
4	224 581.7	204 228.1	2.5041e−08	2.16
5	324 516.8	304 066.2	2.4409e−08	2.13

Table 2. Intrinsic permeabilities and porosities of the measured sandstone plug samples.

	E5	E6	E7	E8	E13	F4	F6	F8	F9	Mean	Standard deviation ($\pm 1\sigma$)
Permeability (mD)	1.1	5.1	5.4	2.2	4.2	2.3	2.3	1.9	1.4	2.9	1.5

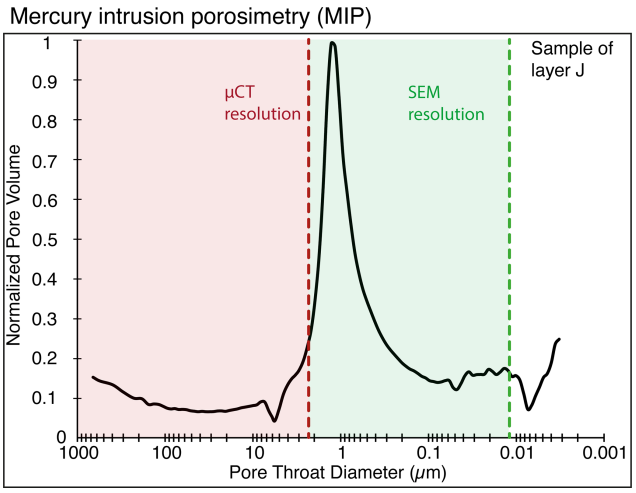

Figure 8. Distribution of the pore throat diameters of a sample of the aeolian facies in layer J obtained from mercury intrusion porosimetry (MICP).

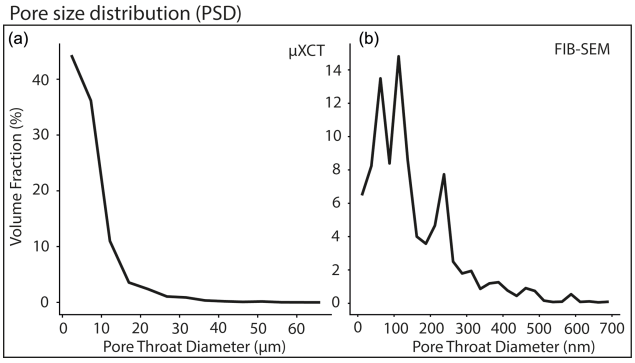

Figure 9. Pore throat diameters from µXCT **(a)** and FIB-SEM images **(b)**.

the 10 largest and 100 largest open flow paths through the pore space of all mini plug cores before the modelling of the microporous domains (Fig. 10). This yields information concerning the heterogeneity of the flow fields and allows the validity of the Navier–Stokes simulations to be checked. Structures with flow impingement often cause numerical problems, which results in an artificial underestimation of the permeability simulations. Significant underestimations of permeability after clay mineral modelling were also found in areas where the percolation paths in the samples were limited to a few voxels in the structure before modelling.

This effect leads to an artificial permeability drop, which renders calculations less precise. Since evenly distributed flow paths are necessary to determine the true permeability of a volume of a rock, we considered only permeability calculations of samples which show no flow impingement for modelling (Bear, 1972; Leu et al., 2014; Zhang et al., 2000). The validity of the simulations was ensured by applying the variance algorithm on the flow fields discussed in Jacob et al. (2019).

The mean value of the experimentally obtained intrinsic gas permeabilities was 2.9 mD (Table 2, Fig. 11a). Samples with no flow impingement had an initial mean permeability of 26.5 mD, whereas the mean permeability simulated on µXCT images was 26.5 mD (Fig. 11b). With applied microporous domains, a mean permeability of 1.9 mD was calculated (Fig. 11c).

The mismatch between measured and simulated permeabilities could be decreased to 1 mD (−34.5 %) compared to 23.6 mD (+813.8 %) prior to the modelling. Hence, our approach significantly improved the match between measured and simulated permeabilities and lies within the standard deviation of the permeabilities measured by the gas permeame-

Table 3. Modelled clay mineral content within the microporous domains in µXCT scans.

	C3	D2	D9	E9	F7	G2	G8	H9	I3	I9	J3	J7	Mean	Standard deviation ($\pm 1\sigma$)
Clay mineral content (vol %)	4.7	3.3	5.0	5.4	7.1	5.0	6.0	6.3	4.1	6.2	6.2	6.1	5.4	1.0

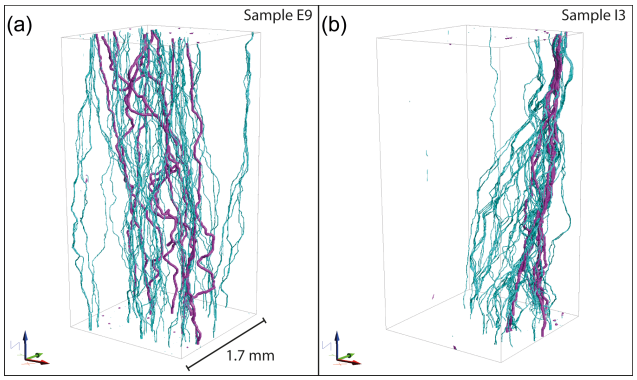

Figure 10. Comparison of percolation paths in two µXCT reconstructions of the 3D imaging data without microporous domain modelling. **(a)** Well distributed percolation paths in a µXCT reconstruction of mini plug sample E9 without microporous domain modelling. **(b)** Constricted percolation paths with flow impingement limited to a small region of the structure in mini plug sample I3 without microporous domain modelling. The 10 largest percolation paths are coloured in purple; the 100 largest percolation paths are coloured in cyan.

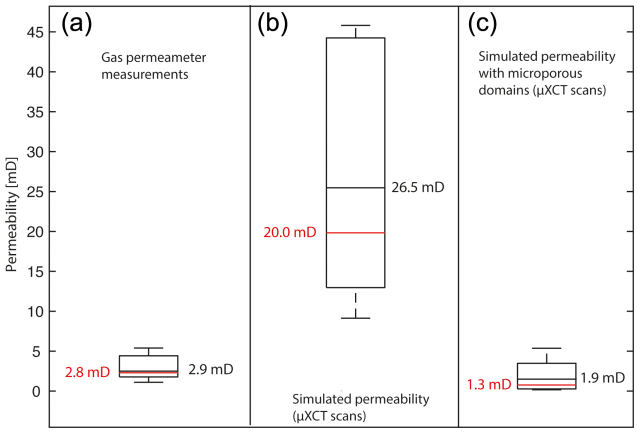

Figure 11. Comparison of measured and simulated permeabilities. The boxes indicate the upper and lower quartile of derived permeability values. Median values are coloured in red; mean values are coloured in black. **(a)** Measured permeabilities using the gas permeameter test. **(b)** Simulated permeabilities using µXCT data. **(c)** Simulated permeabilities using µXCT data with modelled microporous domains.

ter (Table 2). Histograms of the simulated fluid-flow velocities indicate a strong decrease in velocities due to the modelling of the microporous domains in sample E9 (Fig. 12). Correlation histograms of the velocities depict differences induced by the modelling. While identical fluid-flow field velocities would plot as a single straight line, the velocities, in this case, show straight lines with varying slopes. This indicates a general decrease in the fluid-flow velocities with a splitting of different flow path velocities. Points which plot as a line represent a main fluid-flow path with a direct correlation of the velocities between the original and the modelled structure's flow field. Furthermore, a wider spread of the distribution of high velocities results from microporous domain modelling. This indicates narrow pore throats where fluid-flow velocities are locally enhanced compared to the structure before the modelling.

Based on our combined analytical and numerical study, further research may help to increase the accuracy of simulated permeabilities even further. Since isotropic permeabilities of the microporous domains were applied to µXCT images, the accuracy can be improved by taking the anisotropy of clay mineral fabrics and surface topology into account. This can be done by applying anisotropic permeabilities in the calculation of the microporous domains. While this study showed a good match between the experimental and simulated permeability, the need to include heterogeneities of clay mineral layering to improve the simulations was depicted in Villiéras et al. (1997).

The presented approach might also be applicable to other rock types such as mudrocks, carbonates, etc., if the preconditions are met. The examined rock properties (e.g. permeability) should be based on the same scale dependencies as the rock analysed in this work (e.g. Grathoff et al., 2016).

5 Conclusions

Overall, the outcome of this study shows that combining µXCT and FIB-SEM imaging with numerical models constitutes a valuable and novel approach for determining physical properties of clay-bearing tight reservoir rocks. Considering the high number of accessible pores in the scans, the phenomenon of flow impingement was mainly attributed to the unresolvable nanoporosity. While permeability, which is one of the most important reservoir properties, is often determined by simulations based on µXCT scans of small samples taken from a field-scale reservoir, we were able to demonstrate that an accurate estimation for clay-rich and low-permeability rocks is only possible if nanoscale poros-

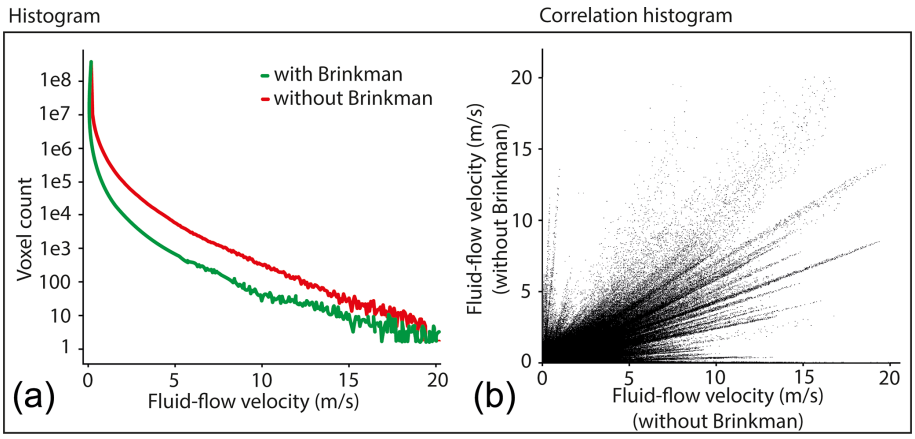

Figure 12. Comparison of unmodelled µXCT images and modelled microporous domain images **(a)**. Correlation histogram prior to and after the modelling that shows a decrease in the main fluid-flow velocities, while few velocities after the modelling were increased with a wide spread of distribution **(b)**.

ity is also included. Thus, our simulations using the Euclidian distance map approach resulted in an improved match with stationary gas permeameter measurements in contrast to permeability simulations merely based on unmodified µXCT images. Adopting this multi-method approach, we increased the accuracy of simulated permeabilities of samples measured by µXCT. These results have important implications for improved modelling of reservoirs relevant to gas and water applications. A realistic simulated permeability of a tight reservoir sandstone could only be achieved by appropriate modelling of the nanoporosity related to matrix clay minerals (illite) that occur below the µXCT resolution. The simulated permeability based on combined µXCT and FIB-SEM images and modelled microporous domains showed good agreement with the experimental results. Obtaining an even distribution of the simulated fluid-flow paths through the sample without flow impingement was necessary to obtain an accurate permeability estimation from 3D imaging. Resolving the nanopore structure and distribution of clay mineral-related features by the combined analytical and numerical modelling approach represents a tool for achieving a more accurate understanding of the fluid-flow behaviour within tight sandstones, with direct relevance to predicting the injection, storage or extraction of gas or water in a reservoir rock. Our multi-method approach can be applied to determine more accurate permeability values and flow paths for reservoir rocks with high clay mineral content if direct experimental measurements are not successful. Hence, future studies should focus on distinguishing the different morphologies of clay minerals and their related anisotropic effect on rock permeability. The permeability of the nanoporous structures depends highly on the layering of the clays and their spatial orientation on the grain surfaces and within feldspars. This approach should include a variety of various sedimentological facies, also with high porosity and permeability, to investigate whether clay mineral modelling is also a valid tool for such sedimentary rocks.

Data availability. Data can be partially accessed upon request by Arne Jacob, Markus Peltz and Frieder Enzmann.

Supplement. The supplement related to this article is available online at: https://doi.org/10.5194/se-12-1-2021-supplement.

Author contributions. The conceptualization was developed by AJ, MP, SH, FE, LNW, GG, PB and MK. The process methodology was developed by AJ and MP. The software was provided by FE while the programming was conducted by AJ and MP. The final validation of the results was done by AJ, MP, SH, FE, LNW, GG, PB and MK. Formal analysis was executed by AJ and MP. The review and editing was executed by AJ, MP, SH, FE, OM, LNW, GG, PB and MK. The visualization of the results was conducted by AJ and MP. Supervision was provided by FE, LNW, GG, PB and MK. The project was administrated by FE, LNW, GG, PB and MK.

Competing interests. The authors declare that they have no conflict of interest.

Acknowledgements. This work was supported by the German Federal Ministry of Education and Research (BMBF) “Geological Research for Sustainability (GEO:N)” program, which is part of the BMBF “Research for Sustainable Development (FONA3)” framework program. It is part of the project ResKin (Reaction kinetics in reservoir rocks, 03G0871E). We would like to thank Fabian Wilde and the staff of PETRA synchrotron facility at DESY Hamburg for their assistance with the imaging beamline P05. Jens Hornung and Meike Hintze from the TU Darmstadt are also acknowledged for

providing us with gas permeability measurements of the studied samples.

Financial support. This research has been supported by the German Federal Ministry of Education and Research (BMBF) (grant no. 03G0871E).

This open-access publication was funded
by Johannes Gutenberg University Mainz.

Review statement. This paper was edited by Florian Fusseis and reviewed by two anonymous referees.

References

Abell, A. B., Willis, K. L., and Lange, D. A.: Mercury Intrusion Porosimetry and Image Analysis of Cement-Based Materials, J. Colloid Interf. Sci., 211, 39–44, https://doi.org/10.1006/jcis.1998.5986, 1999.

Ahmad, K. M., Kristaly, F., and Docs, R.: Effects of clay mineral and physico-chemical variables on sandstone rock permeability, J. Oil Gas Petrochem. Sci., 1, 18–26, https://doi.org/10.30881/jogps.00006, 2018.

Alyafei, N., Raeini, A. Q., Paluszny, A., and Blunt, M. J.: A Sensitivity Study of the Effect of Image Resolution on Predicted Petrophysical Properties, Transp. Porous. Med., 110, 157–169, https://doi.org/10.1007/s11242-015-0563-0, 2015.

Andrä, H., Combaret, N., Dvorkin, J., Glatt, E., Han, J., Kabel, M., Keehm, Y., Krzikalla, F., Lee, M., Madonna, C., Marsh, M., Mukerji, T., Saenger, E. H., Sain, R., Saxena, N., Ricker, S., Wiegmann, A., and Zhan, X.: Digital rock physics benchmarks—Part I: Imaging and segmentation, Comput. Geosci., 50, 25–32, https://doi.org/10.1016/j.cageo.2012.09.005, 2013a.

Andrä, H., Combaret, N., Dvorkin, J., Glatt, E., Han, J., Kabel, M., Keehm, Y., Krzikalla, F., Lee, M., Madonna, C., Marsh, M., Mukerji, T., Saenger, E. H., Sain, R., Saxena, N., Ricker, S., Wiegmann, A., and Zhan, X.: Digital rock physics benchmarks–part II: Computing effective properties, Comput. Geosci., 50, 33–43, https://doi.org/10.1016/j.cageo.2012.09.008, 2013b.

Aplin, A. C., Matenaar, I. F., McCarty, D. K., and van der Pluijm, B. A.: Influence of mechanical compaction and clay mineral diagenesis on the microfabric and pore-scale properties of deep-water Gulf of Mexico mudstones, Clay. Clay. Miner., 54, 500–514, https://doi.org/10.1346/CCMN.2006.0540411, 2006.

Bear, J.: Dynamics of fluids in porous media, American Elsevier Pub. Co, New York, 1972.

Berg, S., Saxena, N., Shaik, M., and Pradhan, C.: Generation of ground truth images to validate micro-CT image-processing pipelines, Leading Edge, 37, 412–420, https://doi.org/10.1190/tle37060412.1, 2018.

Berg, S., Kutra, D., Kroeger, T., Straehle, C. N., Kausler, B. X., Haubold, C., Schiegg, M., Ales, J., Beier, T., Rudy, M., Eren, K., Cervantes, J. I., Xu, B., Beuttenmueller, F., Wolny, A., Zhang, C., Koethe, U., Hamprecht, F. A., and Kreshuk, A.: ilastik: interactive machine learning for (bio)image analysis, Nat. Methods, https://doi.org/10.1038/s41592-019-0582-9, 2019.

Brinkman, H. C.: Calculations on the flow of heterogeneous mixtures through porous media, Appl. Sci. Res., 1, 333, https://doi.org/10.1007/BF02120339, 1949.

Brunke, O., Brockdorf, K., Drews, S., Müller, B., Donath, T., Herzen, J., and Beckmann, F.: Comparison between x-ray tube-based and synchrotron radiation-based µCT, edited by: Stock, S. R., San Diego, California, USA., 2008.

Buades, A., Coll, B., and Morel, J.-M.: Non-Local Means Denoising, Image Processing On Line, 1, 208–212, https://doi.org/10.5201/ipol.2011.bcm_nlm, 2011.

Darcy, H.: Les Fontaines Publiques de la Ville de Dijon, Les Fontaines Publiques de la Ville de Dijon: Exposition et Application des Principes a Suivre et des Formulesa Employer dans les Questions de Distribution d'Eau, Dalmont, 1856.

De Boever, W., Derluyn, H., Van Loo, D., Van Hoorebeke, L., and Cnudde, V.: Data-fusion of high resolution X-ray CT, SEM and EDS for 3D and pseudo-3D chemical and structural characterization of sandstone, Micron, 74, 15–21, https://doi.org/10.1016/j.micron.2015.04.003, 2015.

Desbois, G., Urai, J. L., Hemes, S., Schröppel, B., Schwarz, J.-O., Mac, M., and Weiel, D.: Multi-scale analysis of porosity in diagenetically altered reservoir sandstone from the Permian Rotliegend (Germany), J. Petrol. Sci. Eng., 140, 128–148, https://doi.org/10.1016/j.petrol.2016.01.019, 2016.

Doebelin, N. and Kleeberg, R.: *Profex*?: a graphical user interface for the Rietveld refinement program *BGMN*, J. Appl. Crystallogr., 48, 1573–1580, https://doi.org/10.1107/S1600576715014685, 2015.

Filomena, C. M., Hornung, J., and Stollhofen, H.: Assessing accuracy of gas-driven permeability measurements: a comparative study of diverse Hassler-cell and probe permeameter devices, Solid Earth, 5, 1–11, https://doi.org/10.5194/se-5-1-2014, 2014.

Fischer, C., Dunkl, I., Von Eynatten, H., Wijbrans, J. R., and Gaupp, R.: Products and timing of diagenetic processes in Upper Rotliegend sandstones from Bebertal (North German Basin, Parchim Formation, Flechtingen High, Germany), Geol. Mag., 149, 827–840, https://doi.org/10.1017/S0016756811001087, 2012.

Gane, P. A. C., Ridgway, C. J., Lehtinen, E., Valiullin, R., Furó, I., Schoelkopf, J., Paulapuro, H., and Daicic, J.: Comparison of NMR Cryoporometry, Mercury Intrusion Porosimetry, and DSC Thermoporosimetry in Characterizing Pore Size Distributions of Compressed Finely Ground Calcium Carbonate Structures, Ind. Eng. Chem. Res., 43, 7920–7927, https://doi.org/10.1021/ie049448p, 2004.

Gao, H. and Li, H. A.: Pore structure characterization, permeability evaluation and enhanced gas recovery techniques of tight gas sandstones, J. Nat. Gas Sci. Eng., 28, 536–547, https://doi.org/10.1016/j.jngse.2015.12.018, 2016.

Gluyas, J. G. and Swarbrick, R. E.: Petroleum geoscience, Blackwell Pub, Malden, MA, USA, 2004.

Grathoff, G. H., Peltz, M., Enzmann, F., and Kaufhold, S.: Porosity and permeability determination of organic-rich Posidonia shales based on 3-D analyses by FIB-SEM microscopy, Solid Earth, 7, 1145–1156, https://doi.org/10.5194/se-7-1145-2016, 2016.

Guan, K. M., Nazarova, M., Guo, B., Tchelepi, H., Kovscek, A. R., and Creux, P.: Effects of Image Resolution on Sandstone Porosity and Permeability as Obtained from X-Ray Microscopy, Transp.

Porous. Med., 127, 233–245, https://doi.org/10.1007/s11242-018-1189-9, 2019.

Heidsiek, M., Butscher, C., Blum, P., and Fischer, C.: Small-scale diagenetic facies heterogeneity controls porosity and permeability pattern in reservoir sandstones, Environ. Earth Sci., 79, 425, https://doi.org/10.1007/s12665-020-09168-z, 2020.

Hemes, S., Desbois, G., Urai, J. L., Schröppel, B., and Schwarz, J.-O.: Multi-scale characterization of porosity in Boom Clay (HADES-level, Mol, Belgium) using a combination of X-ray µ-CT, 2D BIB-SEM and FIB-SEM tomography, Micropor. Mesopor. Mat., 208, 1–20, https://doi.org/10.1016/j.micromeso.2015.01.022, 2015.

Iliev, O. and Laptev, V.: On numerical simulation of flow through oil filters, Comput. Visual. Sci., 6, 139–146, https://doi.org/10.1007/s00791-003-0118-8, 2004.

Jacob, A., Enzmann, F., Hinz, C., and Kersten, M.: Analysis of Variance of Porosity and Heterogeneity of Permeability at the Pore Scale, Transp. Porous. Med., 130, 867–887, https://doi.org/10.1007/s11242-019-01342-7, 2019.

Jiang, S.: Clay Minerals from the Perspective of Oil and Gas Exploration, in: Clay Minerals in Nature – Their Characterization, Modification and Application, edited by: Valaskova, M., IntechOpen, 2012.

Kessler, R. M., Ellis, J. R., and Eden, M.: Analysis of Emission Tomographic Scan Data: Limitations Imposed by Resolution and Background, J. Comput. Assist. Tomo., 8, 514–522, https://doi.org/10.1097/00004728-198406000-00028, 1984.

Ketcham, R. A. and Carlson, W. D.: Acquisition, optimization and interpretation of X-ray computed tomographic imagery: applications to the geosciences, Comput. Geosci., 27, 381–400, https://doi.org/10.1016/S0098-3004(00)00116-3, 2001.

Khan, F., Enzmann, F., and Kersten, M.: Multi-phase classification by a least-squares support vector machine approach in tomography images of geological samples, Solid Earth, 7, 481–492, https://doi.org/10.5194/se-7-481-2016, 2016.

Kling, T., Vogler, D., Pastewka, L., Amann, F., and Blum, P.: Numerical Simulations and Validation of Contact Mechanics in a Granodiorite Fracture, Rock. Mech. Rock. Eng., 51, 2805–2824, https://doi.org/10.1007/s00603-018-1498-x, 2018.

Klinkenberg, L. J.: The permeability of porous Media to liquids and gases, Drilling and Production Practice, API-41-200, 1941.

Leu, L., Berg, S., Enzmann, F., Armstrong, R. T., and Kersten, M.: Fast X-ray Micro-Tomography of Multiphase Flow in Berea Sandstone: A Sensitivity Study on Image Processing, Transp. Porous. Med., 105, 451–469, https://doi.org/10.1007/s11242-014-0378-4, 2014.

Linden, S., Wiegmann, A., and Hagen, H.: The LIR space partitioning system applied to the Stokes equations, Graphical Models, 82, 58–66, https://doi.org/10.1016/j.gmod.2015.06.003, 2015.

Lindquist, W. B., Venkatarangan, A., Dunsmuir, J. and Wong, T.: Pore and throat size distributions measured from synchrotron X-ray tomographic images of Fontainebleau sandstones, J. Geophys. Res., 105, 21509–21527, https://doi.org/10.1029/2000JB900208, 2000.

Lis-Śledziona, A.: Petrophysical rock typing and permeability prediction in tight sandstone reservoir, Acta Geophys., 67, 1895–1911, https://doi.org/10.1007/s11600-019-00348-5, 2019.

Liu, G., Bai, Y., Fan, Z., and Gu, D.: Determination of Klinkenberg Permeability Conditioned to Pore-Throat Structures in Tight Formations, Energies, 10, 1575, https://doi.org/10.3390/en10101575, 2017.

Liu, M. and Mostaghimi, P.: Reactive transport modelling in dual porosity media, Chem. Eng. Sci., 190, 436–442, https://doi.org/10.1016/j.ces.2018.06.005, 2018.

Liu, M., Starchenko, V., Anovitz, L. M., and Stack, A. G.: Grain detachment and transport clogging during mineral dissolution in carbonate rocks with permeable grain boundaries, Geochem. Cosmochim. Ac., 280, 202–220, https://doi.org/10.1016/j.gca.2020.04.022, 2020.

Markussen, Ø., Dypvik, H., Hammer, E., Long, H., and Hammer, Ø.: 3D characterization of porosity and authigenic cementation in Triassic conglomerates/arenites in the Edvard Grieg field using 3D micro-CT imaging, Mar. Petrol. Geol., 99, 265–281, https://doi.org/10.1016/j.marpetgeo.2018.10.015, 2019.

Maurer, C. R., Rensheng, Q., and Raghavan, V.: A linear time algorithm for computing exact Euclidean distance transforms of binary images in arbitrary dimensions, IEEE T. Pattern Anal., 25, 265–270, https://doi.org/10.1109/TPAMI.2003.1177156, 2003.

Mayo, S., Josh, M., Nesterets, Y., Esteban, L., Pervukhina, M., Clennell, M. B., Maksimenko, A., and Hall, C.: Quantitative micro-porosity characterization using synchrotron micro-CT and xenon K-edge subtraction in sandstones, carbonates, shales and coal, Fuel, 154, 167–173, https://doi.org/10.1016/j.fuel.2015.03.046, 2015.

Menke, H., Gao, Y., Linden, S., and Andrew, M.: Using nano-XRM and high-contrast imaging to inform micro-porosity permeability during Stokes-Brinkman single and two-phase flow simulations on micro-CT images, preprint, EarthArXiv, https://doi.org/10.31223/osf.io/ubg6p, 2019.

Moosmann, J., Ershov, A., Weinhardt, V., Baumbach, T., Prasad, M. S., LaBonne, C., Xiao, X., Kashef, J., and Hofmann, R.: Time-lapse X-ray phase-contrast microtomography for in vivo imaging and analysis of morphogenesis, Nat. Protoc., 9, 294–304, https://doi.org/10.1038/nprot.2014.033, 2014.

Moulinec, H. and Suquet, P.: A FFT-Based Numerical Method for Computing the Mechanical Properties of Composites from Images of their Microstructures, in: IUTAM Symposium on Microstructure-Property Interactions in Composite Materials, edited by: Pyrz, R., Springer Netherlands, Dordrecht, 235–246, 1995.

Münch, B. and Holzer, L.: Contradicting Geometrical Concepts in Pore Size Analysis Attained with Electron Microscopy and Mercury Intrusion, J. Am. Ceram. Soc., 91, 4059–4067, https://doi.org/10.1111/j.1551-2916.2008.02736.x, 2008.

Neale, G. and Nader, W.: Practical significance of brinkman's extension of darcy's law: Coupled parallel flows within a channel and a bounding porous medium, Can. J. Chem. Eng., 52, 475–478, https://doi.org/10.1002/cjce.5450520407, 1974.

Okabe, H. and Blunt, M. J.: Prediction of permeability for porous media reconstructed using multiple-point statistics, Phys. Rev. E, 70, 066135, https://doi.org/10.1103/PhysRevE.70.066135, 2004.

Peng, S., Hu, Q., Dultz, S., and Zhang, M.: Using X-ray computed tomography in pore structure characterization for a Berea sandstone: Resolution effect, J. Hydrol., 472–473, 254–261, https://doi.org/10.1016/j.jhydrol.2012.09.034, 2012.

Peng, S., Marone, F., and Dultz, S.: Resolution effect in X-ray microcomputed tomography imaging and small pore's contribution

to permeability for a Berea sandstone, J. Hydrol., 510, 403–411, https://doi.org/10.1016/j.jhydrol.2013.12.028, 2014.

Pittman, E. D. and Thomas, J. B.: Some Applications of Scanning Electron Microscopy to the Study of Reservoir Rock, J. Petrol. Tech., 31, 1375–1380, https://doi.org/10.2118/7550-PA, 1979.

Prill, T., Schladitz, K., Jeulin, D., Faessel, M., and Wieser, C.: Morphological segmentation of FIB-SEM data of highly porous media, J. Microsc.-Oxford, 250, 77–87, https://doi.org/10.1111/jmi.12021, 2013.

Saxena, N., Hofmann, R., Alpak, F. O., Berg, S., Dietderich, J., Agarwal, U., Tandon, K., Hunter, S., Freeman, J., and Wilson, O. B.: References and benchmarks for pore-scale flow simulated using micro-CT images of porous media and digital rocks, Adv. Water Resour., 109, 211–235, https://doi.org/10.1016/j.advwatres.2017.09.007, 2017.

Saxena, N., Hows, A., Hofmann, R., O. Alpak, F., Freeman, J., Hunter, S., and Appel, M.: Imaging and computational considerations for image computed permeability: Operating envelope of Digital Rock Physics, Adv. Water Resour., 116, 127–144, https://doi.org/10.1016/j.advwatres.2018.04.001, 2018.

Shah, S. M., Gray, F., Crawshaw, J. P., and Boek, E. S.: Micro-computed tomography pore-scale study of flow in porous media: Effect of voxel resolution, Adv. Water Resour., 95, 276–287, https://doi.org/10.1016/j.advwatres.2015.07.012, 2016.

Soulaine, C., Gjetvaj, F., Garing, C., Roman, S., Russian, A., Gouze, P., and Tchelepi, H. A.: The Impact of Sub-Resolution Porosity of X-ray Microtomography Images on the Permeability, Transp. Porous. Med., 113, 227–243, https://doi.org/10.1007/s11242-016-0690-2, 2016.

Spanne, P., Thovert, J. F., Jacquin, C. J., Lindquist, W. B., Jones, K. W., and Adler, P. M.: Synchrotron Computed Microtomography of Porous Media: Topology and Transports, Phys. Rev. Lett., 73, 2001–2004, https://doi.org/10.1103/PhysRevLett.73.2001, 1994.

Tinet, A.-J., Corlay, Q., Collon, P., Golfier, F., and Kalo, K.: Comparison of various 3D pore space reconstruction methods and implications on transport properties of nanoporous rocks, Adv. Water Resour., 141, 103615, https://doi.org/10.1016/j.advwatres.2020.103615, 2020.

Ufer, K., Kleeberg, R., Bergmann, J., and Dohrmann, R.: Rietveld Refinement of Disordered Illite-Smectite Mixed-Layer Structures by a Recursive Algorithm. II: Powder-Pattern Refinement and Quantitative Phase Analysis, Clay. Clay. Miner., 60, 535–552, https://doi.org/10.1346/CCMN.2012.0600508, 2012.

Villiéras, F., Michot, L. J., Bardot, F., Cases, J. M., François, M. and Rudziński, W.: An Improved Derivative Isotherm Summation Method To Study Surface Heterogeneity of Clay Minerals †, Langmuir, 13, 1104–1117, https://doi.org/10.1021/la9510083, 1997.

Washburn, E. W.: The Dynamics of Capillary Flow, Phys. Rev., 17, 273–283, https://doi.org/10.1103/PhysRev.17.273, 1921.

Wilson, M. D. and Pittman, E. D.: Authigenic Clays in Sandstones: Recognition and Influence on Reservoir Properties and Paleoenvironmental Analysis, J. Sediment. Res., 47, 3–31, https://doi.org/10.1306/212F70E5-2B24-11D7-8648000102C1865D, 1977.

Worden, R. H. and Morad, S.: Clay Minerals in Sandstones: Controls on Formation, Distribution and Evolution, in Clay Mineral Cements in Sandstones, edited by: Worden, R. H. and Morad, S., Blackwell Publishing Ltd., Oxford, UK, 1–41, 1999.

Yoon, H. and Dewers, T. A.: Nanopore structures, statistically representative elementary volumes, and transport properties of chalk: NANOPORE STRUCTURES, SREV, AND FIB-SEM, Geophys. Res. Lett., 40, 4294–4298, https://doi.org/10.1002/grl.50803, 2013.

Zhang, D., Zhang, R., Chen, S., and Soll, W. E.: Pore scale study of flow in porous media: Scale dependency, REV, and statistical REV, Geophys. Res. Lett., 27, 1195–1198, https://doi.org/10.1029/1999GL011101, 2000.

Zhao, H., Ning, Z., Wang, Q., Zhang, R., Zhao, T., Niu, T., and Zeng, Y.: Petrophysical characterization of tight oil reservoirs using pressure-controlled porosimetry combined with rate-controlled porosimetry, Fuel, 154, 233–242, https://doi.org/10.1016/j.fuel.2015.03.085, 2015.

5.2.3 Article 3

Developing synthetic sandstones using geopolymer binder for constraining coupled processes in porous rocks

Markus Peltz, Laurence N. Warr, Sina Hale, and Philipp Blum

SN Applied Sciences

Volume 5, Article number: 87 (2023)

Published: February 19, 2023
DOI: https://doi.org/10.1007/s42452-023-05301-2

Research Article

Developing synthetic sandstones using geopolymer binder for constraining coupled processes in porous rocks

Markus Peltz[1] · Laurence Warr[1] · Sina Hale[2] · Philipp Blum[2]

Received: 13 October 2022 / Accepted: 3 February 2023
Published online: 19 February 2023

Abstract

There is a current need for developing improved synthetic porous materials for better constraining the dynamic and coupled processes relevant to the geotechnical use of underground reservoirs. In this study, a low temperature preparation method for making synthetic rocks is presented that uses a geopolymer binder cured at 80 °C based on alkali-activated metakaolin. For the synthesised sandstone, the key rock properties permeability, porosity, compressive strength, and mineralogical composition, are determined and compared against two natural reservoir rocks. In addition, the homogeneity of the material is analysed structurally by micro-computed tomography and high-resolution scanning electron microscopy, and chemically by energy dispersive X-ray spectroscopy. It is shown that simple, homogenous sandstone analogues can be prepared that show permeability-porosity values in the range of porous reservoir rocks. The advance in using geopolymer binders to prepare synthetic sandstones containing thermally sensitive minerals provides materials that can be easily adapted to specific experimental needs. The use of such material in flow-through experiments is expected to help bridge the gap between experimental observations and numerical simulations, leading to a more systematic understanding of the physio-chemical behaviour of porous reservoir rocks.

Article highlights

- A novel approach for developing synthetic sandstones at low temperatures using geopolymer binder is presented.
- A variety of material properties can be easily controlled which allows adaption to attain specific experimental requirements.
- Geopolymer-bound synthetic sandstones are an ideal material for studying thermally sensitive materials such as carbonates in reactive flow-through experiments.

Keywords Synthetic sandstone · Geopolymer · Benchmark material · Metakaolin · Alkali-activated binder · Reactive transport · Reservoir modelling

✉ Markus Peltz, markus.peltz@uni-greifswald.de; ✉ Laurence Warr, warr@uni-greifswald.de | [1]Institute of Geography and Geology, University of Greifswald, 17489 Greifswald, Germany. [2]Institute of Applied Geosciences (AGW), Karlsruhe Institute of Technology (KIT), 76131 Karlsruhe, Germany.

1 Introduction

Quantifying and modelling the processes of fluid-rock interaction in geological reservoir rocks related to the extraction or storage of georesources are an important part of effectively using Earth's upper crustal resources with minimal detriment to the environment. Reservoir rocks located close to the surface, which hold 99% of all freshwater, are increasingly impacted by the accumulation of groundwater pollutants [1, 2]. At greater depths, geological reservoir formations still host significant hydrocarbon reserves in the form of oil or methane gas that continue to provide the main source of global energy through the burning of these fossil fuels. These very same reservoirs can be used to store CO_2 as part of a carbon capture and storage (CCS) approach that is still in the process of upscaling and finding social acceptance [3]. In the quest to move away from fossil fuel dependence, geological reservoirs may also represent suitable places for the seasonal storage of renewable energy gases, such as CH_4 and/or H_2 [4], as well as provide temporary retention sites for heat [5]. Such applications are additional to the current extraction of natural geothermal energy from reservoirs characterised by high thermal gradients and enhanced levels of heat flow [6].

One of the main limitations in advancing the geological engineering of injection or extraction procedures is the difficulty in quantifying the coupled processes that occur during fluid-rock interactions in these complex natural reservoir systems [7, 8]. Porous and tight reservoir sandstones, for example, normally contain several types of minerals present in the form of detrital clasts, diagenetically formed cements or more loosely held pore-filling mineral particles. These develop during the long and complex histories of geological reservoir rocks that include sedimentation, burial diagenesis and subsequent stages of alteration related to fluid-rock interaction and rock deformation [9]. As a result, reservoir rocks are rarely simple but instead represent poly-mineralic assemblages of detrital and authigenic components that are heterogeneous on a multitude of scales, both compositionally and texturally. Such sedimentary and diagenetic variations are observable at the sub-micrometre scale as well as on the centimetre to meter scale [10].

Reservoir sandstone heterogeneities also include multiple generations of similar minerals, such as different types of carbonates, zeolites and clay minerals, which form under low temperature conditions and are often present in the same natural sample [11, 12]. These minerals commonly display diverse varieties of diagenetic textures representative of complex fluid flow behaviour, dissolution and precipitation reactions, as well as particle mobilisation and pore space modifications [13]. In the case of the formation of illite, which is a clay mineral common to sandstone reservoirs subjected to the circulation of potassium-bearing fluids, crystals of varying shape and size may form as platy grain coatings by direct replacement reactions of K-feldspar grains or as fibrous crystals that grow into the open pore space [12]. In these cases, the more complex the rock, the more challenging it becomes to understand and predict its behaviour under varying chemical and hydraulic conditions, such as the changes in porosity and permeability commonly experienced during natural water circulation. These complexities are also evident in experimental flow-through experiments conducted using natural porous rocks, where complex flow patterns, low accessible surface areas and time-dependent dynamic variations limit the applicability of reactive transport modelling [14, 15]. When models can be applied, their validation is often characterised by inconsistent results [16].

As reservoir sandstones are often too complex to easily constrain specific processes, different methods of synthesising simpler rock assemblages have been attempted [17–20]. Early studies utilised epoxy resin, which resulted in good cementation but provided a poor natural analogue [17]. Other techniques used sintered glass beads [19] or 3D-printed models [21] to successfully study particle transport and multi-phase flow in porous media. Another approach to mimic quartz cementation was to use sodium silicate solution as a binder [18, 22, 23], but this technique required rather high temperatures (> 600 °C) to produce a sufficiently strong silicate cementation [24]. Tillotson et al. [20] found that the strength of a synthetic rock can be further increased by adding kaolinite to the sodium silicate—sand mixture, which was subsequently heated beyond the dehydroxylation temperature of kaolinite during the hardening process.

One type of binder that does not require a high curing temperature are geopolymers. These are based on dehydroxylated Al- and Si-rich precursor materials, such as metakaolin, coal fly ash or ground blast furnace slag [25]. After alkali-activation, which involves the dissolution of precursor materials in concentrated NaOH or KOH solutions and the subsequent alkaline hydrolysis of the dissolved Al and Si species, low temperature curing occurs through a series of polymerisation and condensation reactions [26, 27]. In these polymer structures, alkali metal cations have a stabilising effect by compensating charge imbalances. As a consequence, binders containing amorphous geopolymer and crystalline zeolite form at temperatures < 100 °C [28, 29].

As part of recent research activities in studying the complex reactions kinetics of calcite dissolution coupled with the mobilisation of clay minerals in natural reservoir

sandstones [15], there has emerged a clear necessity for developing simpler synthetic analogues for constraining otherwise difficult to resolve coupled processes. To achieve this, the present study outlines a novel approach of preparing synthetic rocks utilising an alkali-activated metakaolin-based geopolymer binder cured at 80 °C that allows thermally sensitive minerals, such as calcite or clay minerals, to be included. Based on quantitative X-ray diffraction analyses and detailed SEM-EDX observations, it is shown that a synthetic calcite-bearing sandstone can be prepared with a binder composed of amorphous geopolymer and crystalline zeolite. Measurements of porosity, permeability and compressive strength paired with computed tomography analyses and direct numerical simulations reveal that the proposed preparation method can be used to produce a synthetic sandstone with petrophysical values in the range of natural reservoir rocks, although improvements are still required to enhance the materials compressive strength. Based on this reaction system, we provide an outlook for potential applications of this type of synthetic rock by outlining the range of parameters that can be adjusted during sample preparation for the purpose of constraining coupled reservoir-relevant properties.

When used in the present article, the term cement refers to its geologic meaning as a lithifying agent rather than to a specific type of limestone-based binder, such as Portland cement.

2 Materials and methods

2.1 Sample preparation

An illustration of the workflow employed to prepare the geopolymer-based synthetic sandstone under low temperature conditions is shown in Fig. 1a and b. The kaolin used was a well crystalline China Clay variety referred to as SPS (selected particle size) from Cornwall, UK. Based on X-ray diffraction analyses (XRD) and Rietveld refinement using the software Profex [30] it contains by weight 96.4% kaolinite, 3.2% muscovite and 0.4% of quartz. This sample, which was obtained from the University of Greifswald collection (TS number 809) was placed in a ceramic tray and heated at 600 °C for 3 h. The heat-treated powder was then cooled to laboratory conditions and subsequently ground for 30 min using an agate ball mill. The amorphous state of the metakaolin powder was confirmed by XRD by the absence of kaolinite reflections and the formation of a characteristic elevated background between 15° and 40° 2θ (Fig. 2). The amorphous XRD pattern is very similar to other metakaolin powders reported in the literature [31]. For the framework grains, a commercially available sea sand (Carl Roth, No. 8441, extra pure, < 250 µm) was used. Its purity (> 99.6% quartz with traces of titanium oxides) was confirmed by powder XRD and Rietveld analysis. For the preparation of a pure calcite source, a single large Iceland Spar crystal was crushed and ground to obtain a 63–250 µm size fraction by sieving. Based on XRD analysis and quantification it was found to consist of 99.7% calcite and 0.3% of quartz that was probably introduced during grinding.

The binder was prepared by mixing 25% NaOH (6.25 M) solution (Carl Roth, No. 4351, extra pure) and sodium silicate solution (VWR, No. 28079.320, technical grade) with metakaolin in a weight ratio of 2.5:2.5:1. This corresponds to a Si/Al molar ratio of 2.2, which is in the range of well accepted ratios for the production of geopolymers from metakaolin with high compressive strengths and short curing times [e.g. 32, 33]. Following initial tests, a specific order of mixing was adopted in order to maximise the hardening of the binder and better mimic the textures of natural sandstones. First, the metakaolin was mixed with NaOH and hand-stirred until the mixture was homogenised. This step enhanced initial dissolution of Al and Si from the powder, which is required for the subsequent condensation of Al-Si polymers. As a high 6.25 M concentration of NaOH was used, this stage of dissolution is considered to be stoichiometric and thus release similar concentrations of both Al and Si. Second, the sodium silicate solution was added to the binder and homogenised using a planetary centrifugal mixer (Thinky U.S.A. Inc., USA) for 2 min at 2000 rpm. This step adds additional reactive Si to enhance hardening during the condensation and precipitation process. Without time delay, the sea sand was then added and carefully stirred by hand until the quartz grains were evenly coated. Calcite, as an exemplary reactive component, was added during the last stage of preparation to prevent calcite grains from being excessively coated by the binder. The amount of calcite was chosen so that its dissolution during reactive transport experiments would not lead to structural instabilities.

The pre-cured mixture was calculated to contain by weight 85% quartz, 10% calcite and 5% metakaolin when only the dry components are considered. This is equivalent to 70.8% quartz, 8.3% calcite and 20.8% metakaolin binder by weight when the NaOH and sodium silicate solution are considered. For curing, the sandstone mixture was placed into cylindrical molds of either 15 or 25 mm in diameter and heated in a desiccator at 80 °C for 7 days, which was found to be the minimum time required to complete the geopolymerisation reaction. This time is consistent with values reported in literature [e.g. 29]. The bottom of the desiccator was filled with water, but the valve remained open for water to evaporate. This allowed the samples to slowly dry, which enhanced the strength of the sample material during the curing process and prevented the formation of drying cracks. While some water is required to facilitate the geopolymerisation reaction during curing, too much water

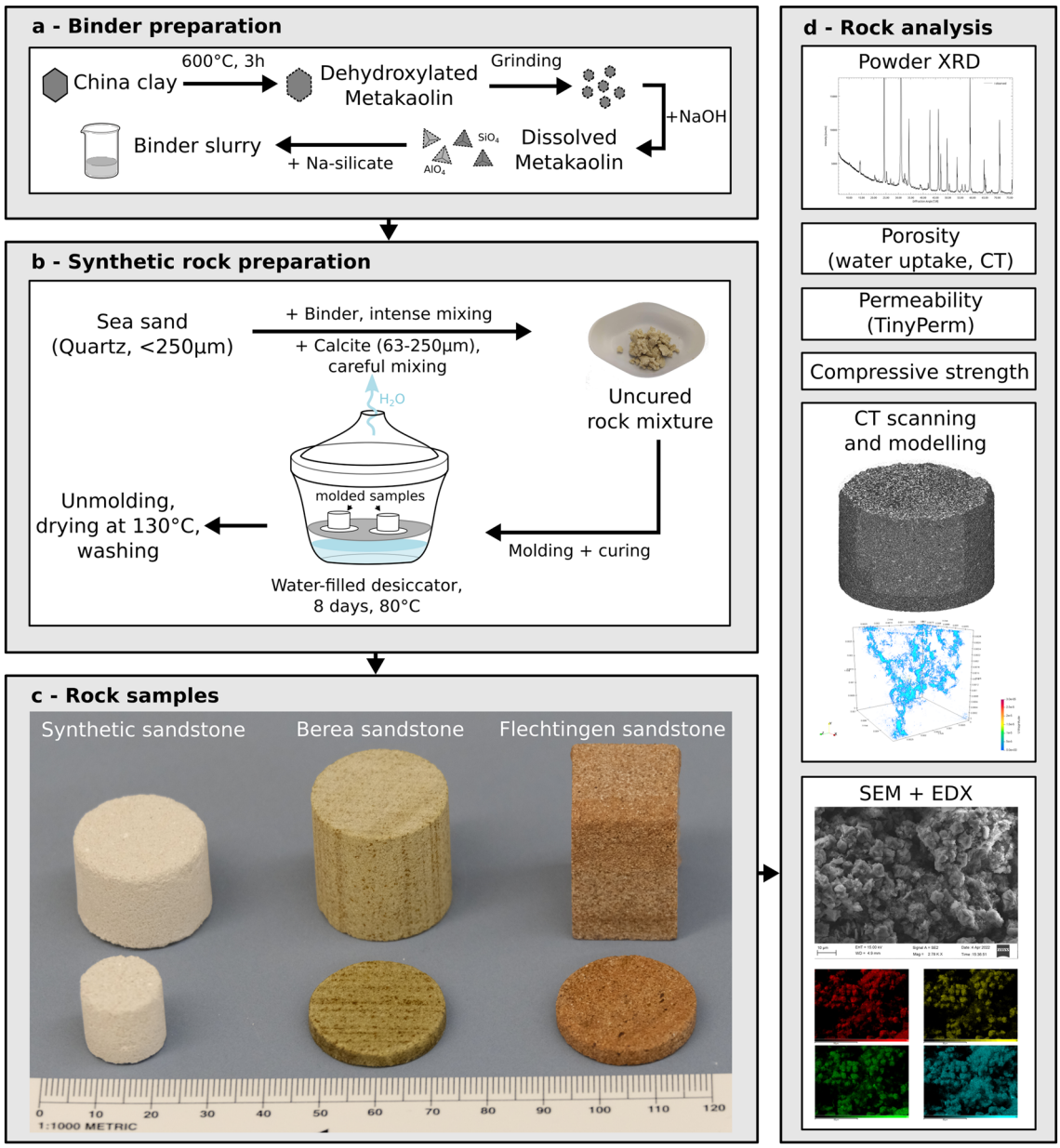

Fig. 1 **a** + **b** Schematic illustration of the workflow applied for the preparation of the binder and the synthetic rock. **c** Photographs of the synthetic sandstone sample and core samples of the Berea and Flechtingen sandstone. **d** Overview of analytical methods used to study the synthetic sandstone

can lead to dilution of the reacting alkaline solution and to the inhibition of the condensation and precipitation process [34]. Afterwards, samples were removed from the molds and dried in an oven at 130 °C for another 3 days. This latter step may not always be required, but for the material prepared in this study this step was seen to further enhance compressive strength. The final stage of preparation involved removal of any unreacted NaOH from the cured samples by washing in double-distilled water. The water was exchanged until the pH in the beaker approached that of the double-distilled water (pH 5.2). This procedure represents an important step to test the success of the geopolymer binder as insufficient reaction will lead to materials that soften and breakup during final washing.

2.2 Analytical methods and sample characterisation

2.2.1 X-ray diffraction (XRD)

The mineralogical compositions of the starting materials and the synthetic sandstone were analysed using powder

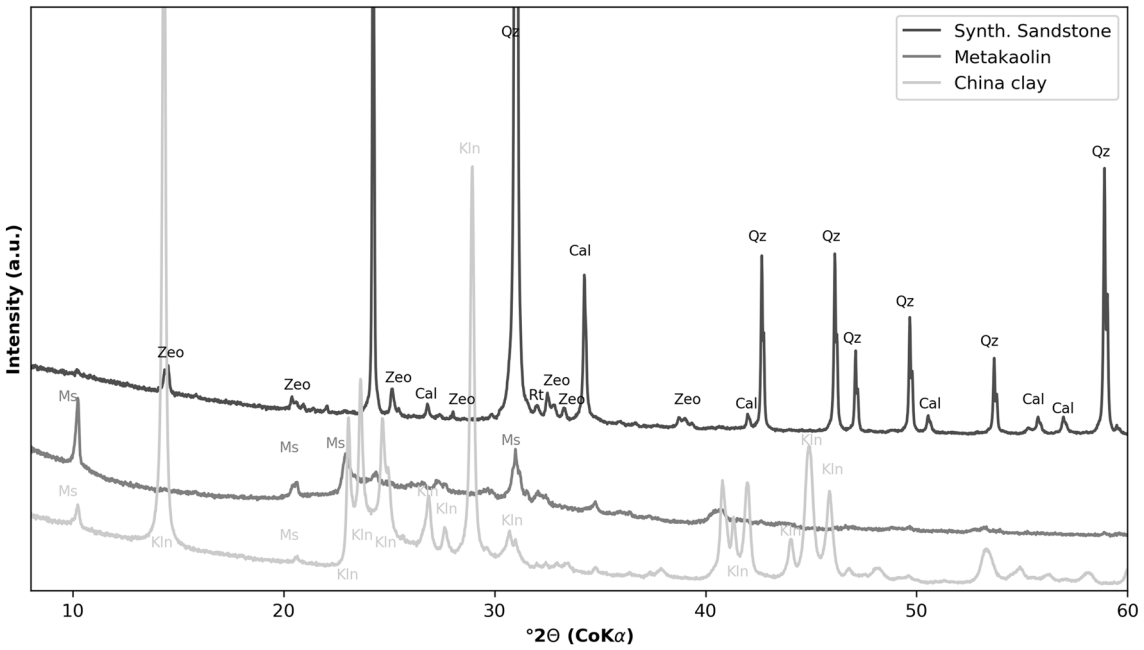

Fig. 2 X-ray diffraction patterns of the initial China clay, metakaolin after heating at 600 °C for 2 h and the micronised synthetic sandstone. (*Ms* muscovite, *Kln* kaolinite, *Qz* quartz, *Cal* calcite, *Zeo* zeolite, *a.u.* arbitrary unit)

X-ray diffraction (XRD) and Rietveld calculations. XRD patterns were measured between 3° and 80° 2θ at 1° 2θ/min using a Bruker D8 Advance diffractometer (Karlsruhe, Germany) equipped with a Lynxeye 1D stripe detector and CoKα radiation at 40 kV and 30 mA. The divergence slit was set to an opening angle of 0.5°. All samples were ground and micronised prior to the preparation of side-loaded random powders. Data was analysed using the Diffrac. EVA software (Bruker, Germany) and the PDF2.0 database. Quantification of mineral components was undertaken using Profex [30].

2.2.2 Scanning electron microscopy (SEM)

The top and bottom Pd-coated surfaces of the samples were analysed using a Zeiss Auriga (Oberkochen, Germany) field emission scanning electron microscope (SEM) operated at 15 kV and images were collected using a secondary electron Everhart-Thornley-style detector. Energy dispersive X-ray spectroscopy (EDX) was carried out at 15 kV using an Oxford X-MAX 80 mm^2 detector (Wiesbaden, Germany) to determine the chemical composition of the binder. Input count rates were limited to 25,000 counts per second. Spot measurements of varying rectangular size were limited by a count integral of 500,000 total counts. EDX mappings were collected at an image resolution of 512 × 384, a dwell time of 100 µs per pixel and with total of 20 overlain maps.

2.2.3 Permeability

The air permeability of the sample plugs was measured with the transient-flow air permeameter *TinyPerm 3* (New England Research, Inc., USA). A detailed description of the process is given in Hale et al. [35] and Hale and Blum [36].

2.2.4 Compressive strength

Uniaxial compressive strength values were approximated using a calibrated inhouse device made of a torque wrench attached to a screw clamp. A detailed description of this measurement method and calibration curves against DIN EN 12390-3 normal procedures are given in Dietel et al. [37].

2.2.5 Computed tomography (CT) and modelling

Computed tomography (CT) imaging was used to determine the porosity and microstructure of a 15 mm synthetic sandstone sample plug. Measurements were run on a YXLON CT Precision system housed at the Institute of Applied Materials—Materials Science and Engineering of the Karlsruhe Institute of Technology [38, 39]. In total, 1950 projections were acquired for the CT scan. The reconstructed dataset had a voxel size of 7.6 µm. Image processing was done using the software Avizo 9.0 (FEI, Germany) and included non-local means filtering to remove noise, ring artifact removal and cropping to a rectangular

domain (x = 1300, y = 1229, z = 1300). Five phases were distinguishable after filtering, namely pores, quartz, calcite, binder and minor amounts of titanium oxide, which showed the highest degree of X-ray absorption. These were segmented using the machine-learning software Ilastik [40]. For every 200th image, a manually formed segmentation mask was created as a training data set. The obtained phase image was statistically analysed using Avizo. Pore and binder size distributions were calculated based on the algorithm proposed by Münch and Holzer [41]. For comparison, a 25 mm Berea sandstone plug was scanned with a voxel size of 13.3 µm.

Subdomains of 384^3 voxels were used for direct numerical simulations by applying the OpenFOAM toolbox [42] to calculate the permeability of the material and analyse the flow path distribution. The SimpleFOAM solver, which uses the SIMPLE algorithm (Semi-Implicit Method for Pressure-Linked Equations) was utilised to solve the Navier–Stokes equations. For laminar flow of incompressible fluids, the conservation of mass is

$$\nabla \cdot v = 0\,, \tag{1}$$

where v is the divergence-free velocity. The momentum equation without gravitational term reads

$$\mu \nabla^2 v = \rho \left(\frac{\partial v}{\partial t} + v \cdot \nabla v \right) + \nabla p, \tag{2}$$

where μ is the dynamic fluid viscosity, ρ the density of the fluid and p the pressure field.

The mesh was generated to be congruent with a segmented connected pore voxel volume. A single-layer mesh refinement was performed at the boundary of the pore space to prevent an under-resolved mesh in the narrow pore throat regions. Between the inflow and outflow planes, which were enlarged by 10 cells as a "reservoir" in each direction, a constant pressure gradient was adopted. No slip boundary conditions were used for solid grain boundaries and symmetric boundaries were applied for the remaining domain sites. Fluid properties were set to mimic air at 21 °C. Simulations were run in the y-direction, equivalent to the direction of air permeameter measurements. To determine the permeability for each subdomain, the velocity u_y of the computed velocity field was integrated over the sample volume V without reservoirs and the absolute permeability was calculated as follows:

$$K_y = -\mu \left(\frac{1}{V} \int_V u_y dV \left(\frac{\Delta P}{l_y} \right)^{-1} \right), \tag{3}$$

where K_y is the permeability in y-direction, μ is the dynamic viscosity, ΔP the pressure gradient between inflow and outflow plane and l_y length of the domain in y-direction without reservoirs.

3 Results and discussion

3.1 Mineralogical composition

The XRD pattern of the cured synthetic sample after crushing and micronising was compared to the initial China clay and the metakaolin pattern (Fig. 2). Reflections of quartz, calcite and crystalline zeolite (likely zeolite NaP of the gismondine framework [43] or phillipsite) were observed. Traces of muscovite can be recognised by a tiny 10 Å reflection. No amorphous hump was detected in the cured sandstone sample, as detected in the original metakaolin sample, indicating close to complete dissolution of the amorphous precursor material. Based on Rietveld calculations, the cured synthetic sandstone is composed of 84 wt% quartz, 8 wt% calcite, 6 wt% zeolite and traces of muscovite and titanium oxides (Table 1). When compared to the initial composition of dry components, this shows a relative increase in the binder fraction and some minor dissolution of calcite that probably occurred during the washing of the sample in distilled water. Zeolite cements are commonly reported in natural reservoir sandstones and are indicative of high porosity and permeability preservation during diagenesis [44].

3.2 SEM and EDX

SEM images of rock fragments taken from the cured synthetic sandstone sample show that quartz grains are cemented by the geopolymer binder that consists mainly of zeolite NaP crystals with diameters between 15 and 25 µm as well as an amorphous Si-rich geopolymer phase (Fig. 3a, b). The binder is primarily located in between quartz grains and contains varying amounts of porosity, which explains the broad range of grey values observed in CT images for this phase (Fig. 3a, b). To determine its chemical composition, EDX spectra of different binder and quartz grain spots were collected (Table 2). Binder regions B1–B3 are composed of Na, Al, Si, K, Ca and O with traces of Mg detected in B1. Na, Al, Si and O can be related to the zeolite NaP. The traces of Mg and K are likely remnants of the muscovite that was introduced with the metakaolin precursor material. The low concentration of Ca observed across all spectra is considered to represent some local calcite dissolution that likely occurred during the curing of the sample under strong alkaline conditions or the washing in slightly acidic double-distilled water. Subsequently, this Ca was either incorporated in the geopolymer during

Table 1 Petrophysical properties and mineralogical composition of the synthetic sandstone plug

	Synthetic sandstone	Berea sandstone	Flechtingen sandstone
Φ_{water} (%)	22.8	13.1	5.8
Φ_{CT} (%)	12.6	12.3	6.7 ± 3.4[a]
K_{air} (md)	1610 ± 423	117 ± 49	2.9 ± 1.5[a]
K_{calc} (md)	463 ± 315	Not determined	1.3[a]
σ (MPa)	19.6	91.2	129.2
Average mineral contents (wt%)			
Quartz	84	88	64
Zeolite	6	–	–
Calcite	8	1	6
Illite/muscovite	< 1	3	13
Titanium and iron oxides	< 1	< 1	< 1
Kaolinite	–	2	–
Feldspars	–	6	16

Values for Berea and Flechtingen sandstone are provided for comparison

Φ porosity, K permeability, σ uniaxial compressive strength

[a]Data compiled from Heidsiek et al. [10], Jacob et al. [45] and Peltz et al. [12]

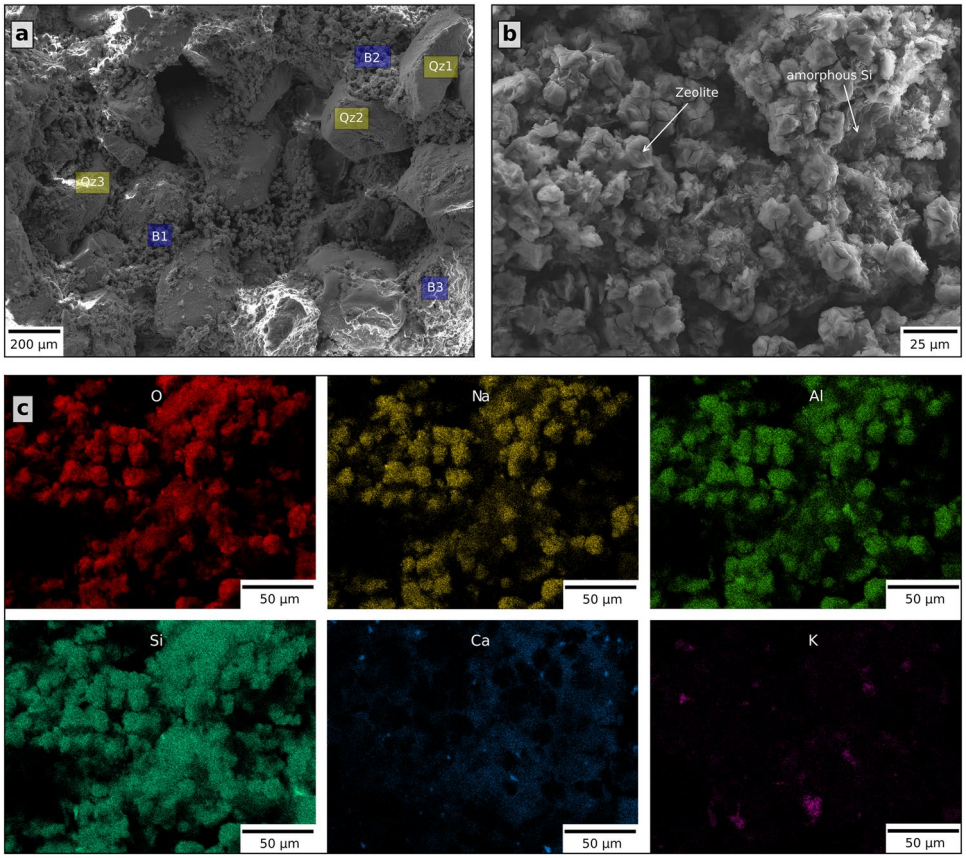

Fig. 3 **a** Low resolution secondary electron image of the synthetic sandstone. Binder is found in intergranular regions and shows varying degrees of porosity depending on the amount of pore-filling amorphous geopolymer. The locations of quartz (Qz1-3) and binder (B1-3) EDX spot analyses from Table 2 are marked by blue and yellow frames. **b + c** Close-up and selected EDX maps showing the distribution of zeolite NaP and amorphous geopolymer

Table 2 Results of EDX spot measurements

	Na	Mg	Al	Si	K	Ca	O
Qz1	0.6	–	0.5	45.2	–	1.2	52.6
Qz2	1.4	–	1.4	42.5	–	3.2	51.5
Qz3	1.3	–	2.0	41.9	–	3.4	51.4
B1	5.7	0.4	8.7	32.1	0.9	3.9	48.3
B2	8.6	–	10.1	29.3	0.9	4.0	47.1
B3	4.2	–	7.0	32.8	1.5	6.7	47.9

Locations of the spots are shown in Fig. 3. All values in weight%

the curing as indicated by areas in the mapping that correlate with Si, or reprecipitated as calcite during the drying, as shown by the peaks of Ca that do not correlate with Si but with O (Fig. 3c).

EDX mappings of a larger area were collected to determine the chemical variability of the binder (Fig. 3b, c). The visibly crystalline parts (Fig. 3b) that are formed by zeolite are composed of Na, Al, Si and O. In between these crystals, an amorphous phase can be observed, which is primarily composed of Si and Al and is likely the amorphous geopolymer. Thus, higher Si contents correspond to denser and geopolymer-rich binders as confirmed visually and chemically by comparing site B2 with B3 (Fig. 3a; Table 2).

3.3 Petrophysical properties

To compare the properties of the geopolymer-based synthetic sandstone plug to natural rock plugs of the same dimensions, air permeability K_{air}, uniaxial compressive strength σ and water displacement porosity Φ_{water} were also measured for a Berea sandstone specimen representing a porous siliciclastic reservoir rock and a Flechtingen sandstone (Upper Rotliegend, Parchim Formation) as an example for a compacted, tight sandstone (Fig. 1; Table 1).

The total porosity of the synthetic sandstone obtained from water uptake (22.8%) and from CT images (12.6%) is within the typical range reported for natural porous reservoir sandstones [9]. These porosity values indicate that a large proportion of pores cannot be resolved by CT, such as the small pores associated with the zeolite and the amorphous geopolymer binder phase. Axis connectivity of the segmented pore space exists in all spatial directions and is built-up by a single connecting pore cluster (Fig. 4a). The fluctuations of the porosity and the binder content between consecutive images are low, but an overall decrease can be observed for both parameters from top to bottom (Fig. 4b). This is accompanied by a slight increase in quartz content observed from top to bottom (Fig. 4b), which reflects some gravitational settling of quartz grains during the curing process. These variations are, however, minor when compared to that produced by the sedimentary grading of sand grains common to water-deposited sands and lithified sandstones.

Other, more local heterogeneities exist at a scale of a few 100 µm in association with clustered binder-rich regions with low porosity (Fig. 4a). It is also noticeable that the mineral phases in the upper 100 slices show large fluctuations and an increased porosity that can be viewed as an artefact of the molding process. Two additional anomalies in binder content and porosity are recognised in the regions around slice #700 and #1000, which mark regions where material was placed on top of each other during the filling of the mold. Despite these irregularities and artefacts, the overall bulk sample can be considered to be homogeneous and shows a consistent pore structure.

The calculated pore and binder size distributions (Fig. 4c) correlate well with the observed internal framework structure. The total volume fraction of the binder is 22.1% and the diameter of the binder coating between individual grains ranges between 15.2 and 22.8 nm. In comparison, the pore size distribution detected from CT imaging is broader with a peak abundance at about 38 nm (Fig. 4c).

By adding calcite as the last component during the rock mixture preparation, most calcite grains were located in open pores making them accessible for invading fluids. The textures observed are therefore similar to late-diagenetic calcites formed in reservoir sandstones [46]. In addition, the distribution of calcite shows only minor variations in texture across the specimen. This reflects that the synthetic geopolymer sample is notably more homogenous than reported from natural samples.

To check the homogeneity of the sample quantitatively, the range of permeabilities across the sample was simulated by selecting 12 sub-volumes of 384^3 voxels from three different depths and conducting separate numerical simulations (Fig. 4d). Four laterally located non-overlapping volumes were taken from the top, from below the highly porous zone at a depth of 128 voxel and from a depth of 512 voxels, respectively. All depths are related to the top face of the cubic domain. The measured and calculated permeability range shows a large fluctuation

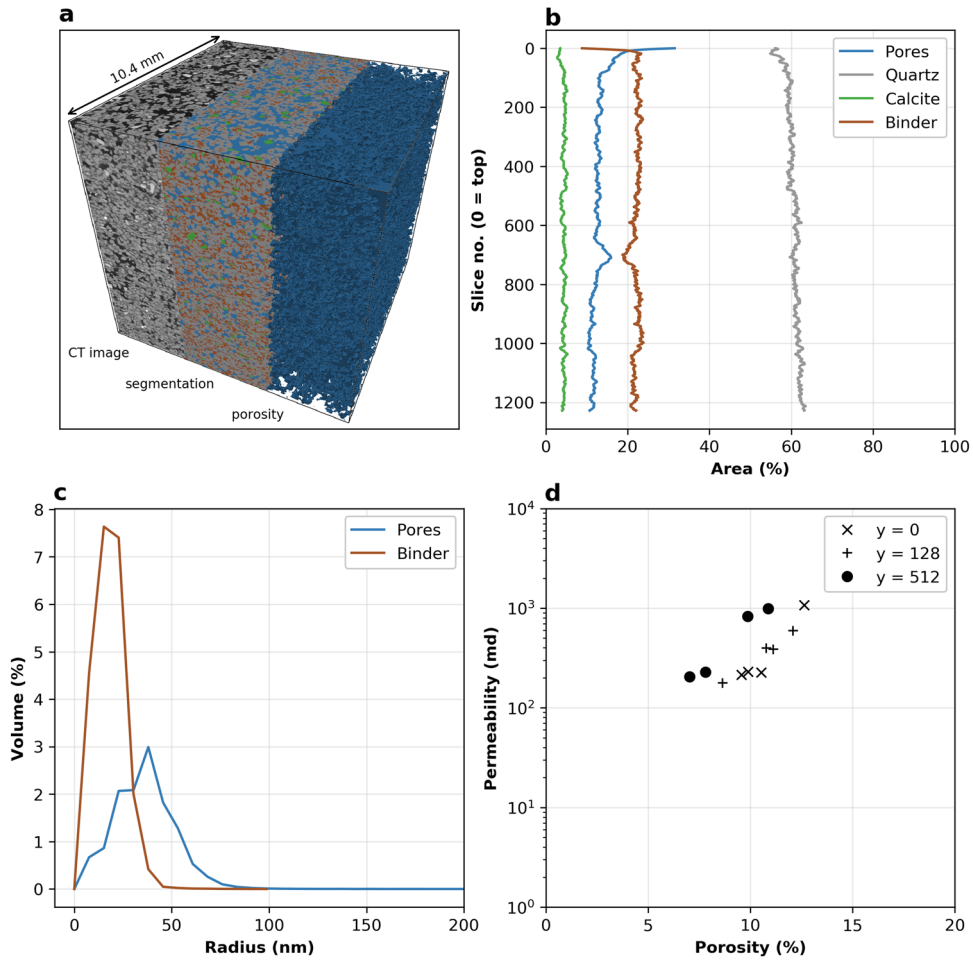

Fig. 4 **a** 3D rendering showing the processed CT image, the machine-learning based segmentation and the voxel-rendering of the connected pore space. **b** Slice-wise area distribution of the segmented phases showing a slight increase in quartz content from top to bottom. The first 100 slices are characterised by an increased porosity and solid contents indicating lower compaction at the top. **c** The calculated pore and binder size distributions indicate that the binder primarily occupies narrower intergranular regions. **d** Porosity-permeability relationship for 12 selected sub-volumes

($K_{air} = 1610 \pm 423$ md, $K_{calc} = 463 \pm 315$ md) attributable to the low degree of compaction in the top area and varying degrees of pore connectivity at the simulated scale. It was observed that the connected porosity of sub-volumes from a depth of 512 voxels was 2–3% lower but the permeability values were within the same range as those observed for sub-volumes closer to the top. This indicates that the heterogeneity of connectivity of the pore space and flow paths was similar throughout the entire sample volume. Thus, the comparatively small sub-volumes of 384^3 voxels may not capture the representative elementary volume (REV) size of the sample. However, this issue is widely known when attempting to determine the permeability of natural sandstones by modelling [47] and deviations by a factor of 2 are generally expected for smaller volumes compared to the larger samples of the same material [48]. Although values fluctuated considerably, the permeabilities of the synthetic sandstone are up to 3 orders of magnitude higher than those observed in the natural samples (Table 1), which is favourable for conducting flow-through experiments [15].

The compressive strength of 19.6 MPa measured on the synthetic sandstone was significantly lower than that determined for the Berea (91.6 MPa) and Flechtingen (129.2 MPa) sandstones (Table 1). This low strength is attributed to insufficient hardening of the binder as evident from the remains of some amorphous geopolymer detected in the specimen. Increased hardening and therefore higher compressive strength may be achieved by various factors. (1) The presence of amorphous Si-rich geopolymer indicates an excess of sodium silicate solution in the starting materials. Thus, adjusting the molar ratios of the starting materials to zeolite NaP should lead to a more complete conversion of the educts, while reducing the likely mechanically weaker amorphous content. (2) Prolonged thermal curing of the geopolymer and/or applying a compressional force during the hardening stage may further increase the compressive strength. (3) The China clay utilised in the present study contains small amounts of muscovite, which was used to determine its suitability for particle migration studies. However, due to the intensive grinding, particle sizes became too small to be observed within the framework of this sample. Hence,

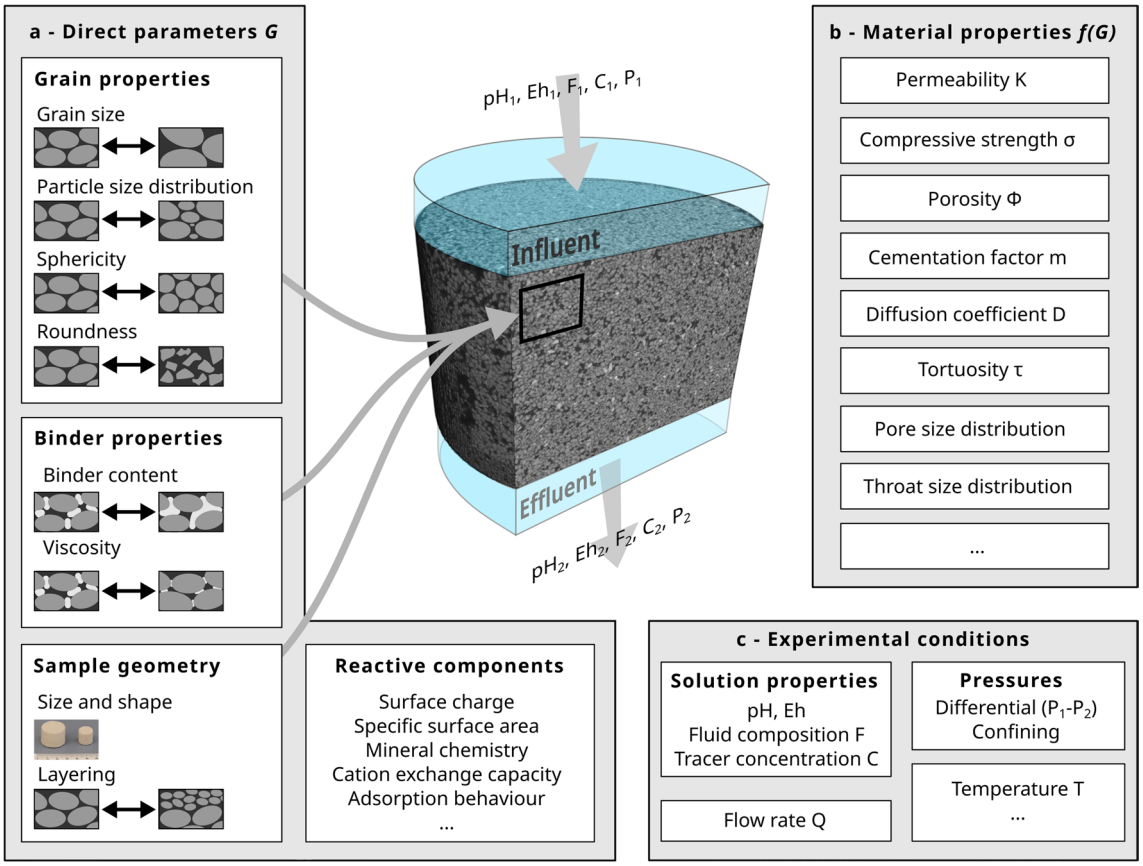

Fig. 5 Overview of parameters that can be adapted and material properties that can be constrained and investigated by flow-through experimentation of geopolymer-cemented synthetic sandstone. **a** Direct parameters *G* refer to properties that can be adjusted when preparing the sample. **b** Material properties that are a function of direct parameters. **c** Examples of experimental conditions that can be monitored or adjusted in flow-through experiments

adding more suitable particles separately that can be imagined for this purpose is recommended. Furthermore, the kaolinite could be replaced by a more disordered variety with smaller initial particle sizes and larger specific surface areas (possibly KGa2), as these are known to dissolve faster in alkaline environments [49].

3.4 Suitability for advancing experimental studies

Geopolymer-cemented synthetic sandstones containing thermally sensitive minerals have the potential of advancing experimental studies by providing more homogeneous solid materials that can be easily adapted to constrain specific reservoir rock parameters. Thus, these materials are considered to provide better analogues for reservoir rocks than synthetic rocks cured at high temperatures [17, 18, 20] or unconsolidated and consolidated sands [50, 51]. Examples of the direct parameters *G* that can be adjusted when preparing the samples, and the main corresponding reservoir-relevant properties *f(G)* that can be constrained, are summarised in Fig. 5. These, and additional parameters, are required by available reactive transport models and can be provided for verifying these by improved controlled experimentation [14, 52–54].

In this proof-of-concept study, specimens were prepared with the focus of adding a matrix calcite (8 wt%) to a highly porous framework during the final stage of mixing as an analogue to a carbonate-cemented sandstone. Similar synthetic rocks can be constructed using other temperature-sensitive minerals, such as clay minerals (e.g. kaolinites, illites, smectites, chlorites) as well as various zeolites (clinoptilolite, heulandite, erionite, mordenite, analcime) which are common to the matrix of reservoir sandstones [55, 56]. These mixtures can be used to study surface-related processes, such as adsorption, cation exchange and reactive transport that cannot be constrained when high-temperature curing procedures induce irreversible mineral alterations.

In addition to adapting mineral contents, various grain properties can be selected when preparing the mixtures that are important for studying porosity-permeability

relationships as well as controlling pore and throat size distributions and tortuosity (Fig. 5a). Basic properties that are easy to control are grain size, grain-size distribution, sphericity, roundness and surface properties [57]. Recent numerical simulations, for example, indicate that the degree of adhesion and surface roughness in porous rocks will determine whether or not small particles are mobilised at the sub-pore scale, leading to reservoir clogging [58].

A range of matrix parameters can also be controlled by adjusting the binder mixture. This is an important aspect in influencing the volume and distribution of the cement that controls porosity, permeability, diffusivity, compressive strength, as well as the rate of fluid flow (Fig. 5b, c). Combining variations in mineral content, grain and binder properties using synthetic geopolymer sandstones may also lead to improved studies relevant to inorganic and organic pollutants based on monitoring changes in the chemistry of the effluent (Fig. 5c).

Geopolymer-hardened sandstones can be prepared in range of sample sizes and shapes applying no or very low confining pressures. Thus, it is straightforward to produce highly porous synthetic sandstone using simple mineral assemblages that are often difficult to find in natural sample collections. Any inconsistencies in porosity produced at the top or bottom of the synthetic sample can be easily removed before experimentation and internal inconsistencies can be avoided by pouring the slurry into the mold as one continuous process.

4 Conclusion

This study demonstrated that homogenous synthetic sandstones can be prepared at low temperatures using geopolymer binder that have the potential to provide improved analogue materials for constraining experimental parameters that are difficult to attain from the study of natural heterogenous rocks. The low-temperature curing enables the incorporation of temperature-sensitive materials such as carbonates, zeolites or clay minerals that cannot be studied using conventional high-temperature hardening approaches. Although the maximum temperature in the present study did not exceed 130 °C, many geopolymer studies indicate that curing even at room temperature may be achievable if longer curing times are used.

The variety of parameters, such as grain and cement properties, sample geometry and mineralogical composition, that can be easily adapted during the sample preparation, allows adaption to attain specific experimental requirements. Thus, the use of synthetic geopolymer-cemented sandstones in flow-through experiments has the potential to provide needed benchmark materials and datasets for verifying reactive transport models from the pore to the Darcy scale. As some improvements in the specimen preparation are still required to reach compressive strengths equal to those of hard reservoir rocks, the material synthesised in this study is considered more useful for studying fluid-rock interactions than mechanical aspects.

Acknowledgements We thank Stefan Dietrich from the Karlsruhe Institute of Technology (KIT) for his assistance during the computed tomography (CT) imaging. A DFG-financed FIB-SEM instrument housed in the mineralogical laboratory of the University of Greifswald (Grant 173095180) was also used for this study.

Author contributions All authors contributed to the study conception and design. Material preparation, data analysis and visualisation: MP. Data collection: MP and SH. Writing—original draft: MP. Writing—review & editing: all authors. Supervision: LNW. All authors read and approved the final manuscript.

Funding Open Access funding enabled and organised by Projekt DEAL. This work was financially supported by the German Federal Ministry of Education and Research (BMBF) Geological Research for Sustainability (GEO:N) program (Grant No. 03G0900) within the framework of Research for Sustainable Development (FONA3).

Data availability The datasets generated during and/or analysed during the current study are available from the corresponding author on reasonable request.

Declarations

Competing interests The authors declare that they have no conflicts of interest.

References

1. Jackson RB et al (2001) Water in a changing World. Ecol Appl 11:1027–1045. https://doi.org/10.1890/1051-0761(2001)011[1027:WIACW]2.0.CO;2
2. Ozano K et al (2022) Groundwater: making the invisible visible. FCDO Briefing Pack on Water Governance, Finance and Climate Change, K4D Briefing Note, Brighton: Institute of Development Studies. https://doi.org/10.19088/K4D.2022.027

3. Haszeldine RS (2009) Carbon capture and storage: how green can black be? Science 325:1647–1652. https://doi.org/10.1126/science.1172246
4. Amid A et al (2016) Seasonal storage of hydrogen in a depleted natural gas reservoir. Int J Hydrog Energy 41:5549–5558. https://doi.org/10.1016/j.ijhydene.2016.02.036
5. Welsch B et al (2016) Characteristics of medium deep borehole thermal energy storage. Int J Energy Res 40:1855–1868. https://doi.org/10.1002/er.3570
6. Barbier E (2002) Geothermal energy technology and current status: an overview. Renew Sustain Energy Rev 6:3–65. https://doi.org/10.1016/S1364-0321(02)00002-3
7. Lesmes DP, Frye KM (2001) Influence of pore fluid chemistry on the complex conductivity and induced polarization responses of Berea sandstone. J Geophys Res 106:4079–4090. https://doi.org/10.1029/2000JB900392
8. Stück H et al (2013) Petrographical and petrophysical properties of sandstones: statistical analysis as an approach to predict material behaviour and construction suitability. Environ Earth Sci 69:1299–1332. https://doi.org/10.1007/s12665-012-2008-1
9. Worden RH, Burley SD (2003) Sandstone diagenesis: the evolution of sand to stone. In: Burley SD, Worden RH (eds) Sandstone diagenesis. Blackwell Publishing Ltd, Oxford, pp 1–44. https://doi.org/10.1002/9781444304459.ch
10. Heidsiek M et al (2020) Small-scale diagenetic facies heterogeneity controls porosity and permeability pattern in reservoir sandstones. Environ Earth Sci 79:1–14. https://doi.org/10.1007/s12665-020-09168-z
11. Noh JH, Boles JR (1993) Origin of Zeolite cements in the Miocene Sandstones, North Tejon Oil Fields, California. SEPM JSR, vol 63. https://doi.org/10.1306/D4267AD2-2B26-11D7-8648000102C1865D
12. Peltz M et al (2022) A FIB-SEM study of Illite morphology in Aeolian Rotliegend Sandstones: implications for understanding the petrophysical properties of reservoir rocks. Clays Clay Miner 70:84–105. https://doi.org/10.1007/s42860-022-00174-9
13. Chagneau A et al (2015) Mineral precipitation-induced porosity reduction and its effect on transport parameters in diffusion-controlled porous media. Geochem Trans 16:13. https://doi.org/10.1186/s12932-015-0027-z
14. Iliev O (2017) On the pore-scale modeling and simulation of reactive transport in 3D geometries. Math Modelling Anal 22:671–694. https://doi.org/10.3846/13926292.2017.1356759
15. Hale S et al (2022) Upscaling calcite dissolution rates in a tight reservoir sandstone. Environ Earth Sci 81(11):303. https://doi.org/10.1007/s12665-022-10399-5
16. Abd AS, Abushaikha AS (2021) Reactive transport in porous media: a review of recent mathematical efforts in modeling geochemical reactions in petroleum subsurface reservoirs. SN Appl Sci 3:1–28. https://doi.org/10.1007/s42452-021-04396-9
17. Rathore JS et al (1995) P- and S-wave anisotropy of a synthetic sandstone with controlled crack geometry. Geophys Prospect 43:711–728. https://doi.org/10.1111/j.1365-2478.1995.tb00276.x
18. den Brok SW et al (1997) Preparation of synthetic sandstones with variable cementation for studying the physical properties of granular rocks. Comptes Rendus de l'Académie des Sci Ser IIA Earth Planet Sci 325:487–492. https://doi.org/10.1016/S1251-8050(97)89866-7
19. Turner ML et al (2004) Three-dimensional imaging of multiphase flow in porous media. Physica A 339:166–172. https://doi.org/10.1016/j.physa.2004.03.059
20. Tillotson P et al (2012) Experimental verification of the fracture density and shear-wave splitting relationship using synthetic silica cemented sandstones with a controlled fracture geometry. Geophys Prospect 60:516–525. https://doi.org/10.1111/j.1365-2478.2011.01021.x
21. Patsoukis Dimou A et al (2022) Benchmarking the viability of 3D printed micromodels for single phase flow using particle image velocimetry and direct numerical simulations. Transp Porous Med 141:279–294. https://doi.org/10.1007/s11242-021-01718-8
22. Al-Homadhi ES (2002) Artificial sandstone cores production with a wide range of petrophysical properties. J King Saud Univ-Eng Sci 14:95–117. https://doi.org/10.1016/S1018-3639(18)30747-5
23. Kozhagulova A et al (2021) An integrated laboratory experiment of realistic diagenesis, perforation and sand production using a large artificial sandstone specimen. J Rock Mech Geotech Eng 13:154–166. https://doi.org/10.1016/j.jrmge.2020.09.004
24. Subasri R, Näfe H (2008) Phase evolution on heat treatment of sodium silicate water glass. J Non-cryst Solids 354:896–900. https://doi.org/10.1016/j.jnoncrysol.2007.08.037
25. Duxson P et al (2007) Geopolymer technology: the current state of the art. J Mater Sci 42:2917–2933. https://doi.org/10.1007/s10853-006-0637-z
26. Davidovits J (1991) Geopolymers. J Therm Anal 37:1633–1656. https://doi.org/10.1007/BF01912193
27. Weng L, Sagoe-Crentsil K (2007) Dissolution processes, hydrolysis and condensation reactions during geopolymer synthesis: Part I—low Si/Al ratio systems. J Mater Sci 42:2997–3006. https://doi.org/10.1007/s10853-006-0820-2
28. Muñiz-Villarreal MS et al (2011) The effect of temperature on the geopolymerization process of a metakaolin-based geopolymer. Mater Lett 65:995–998. https://doi.org/10.1016/j.matlet.2010.12.049
29. Albidah A et al (2021) Characteristics of metakaolin-based geopolymer concrete for different mix design parameters. J Mater Res Technol 10:84–98. https://doi.org/10.1016/j.jmrt.2020.11.104
30. Doebelin N, Kleeberg R (2015) Profex: a graphical user interface for the Rietveld refinement program BGMN. J Appl Crystallogr 48:1573–1580. https://doi.org/10.1107/S1600576715014685
31. Cyr M et al (2012) Use of metakaolin to stabilize sewage sludge ash and municipal solid waste incineration fly ash in cement-based materials. J Hazard Mater 243:193–203. https://doi.org/10.1016/j.jhazmat.2012.10.019
32. Li J et al (2022) Longitudinal single-sided NMR study: silica-to-alumina ratio changes the reaction mechanism of geopolymer. Cem Concr Res 160:106921. https://doi.org/10.1016/j.cemconres.2022.106921
33. Singh PS et al (2005) Geopolymer formation processes at room temperature studied by 29Si and 27Al MAS-NMR. Mater Sci Eng A 396:392–402. https://doi.org/10.1016/j.msea.2005.02.002
34. Park S, Pour-Ghaz M (2018) What is the role of water in the geopolymerization of metakaolin? Constr Build Mater 182:360–370. https://doi.org/10.1016/j.conbuildmat.2018.06.073
35. Hale S et al (2020) Method comparison to determine hydraulic apertures of natural fractures. Rock Mech Rock Eng 53:1467–1476. https://doi.org/10.1007/s00603-019-01966-7
36. Hale S, Blum P (2022) Bestimmung der hydraulischen Durchlässigkeiten eines Sandsteins mithilfe eines Luftpermeameters. Grundwasser - Zeitschrift der Fachsektion Hydrogeologie 27:57–65. https://doi.org/10.1007/s00767-021-00504-z
37. Dietel J et al (2017) The importance of specific surface area in the geopolymerization of heated illitic clay. Appl Clay Sci 139:99–107. https://doi.org/10.1016/j.clay.2017.01.001
38. Damon J et al (2022) Mechanical surface treatment of EBM Ti6Al4V components: effects of the resulting surface layer state on fatigue mechanisms and service life. Mater Sci Eng A 849:143422. https://doi.org/10.1016/j.msea.2022.143422
39. Englert L et al (2020) Investigations on printing path dependent properties of additively manufactured samples using micro

computed tomography. RPJ 26:1603–1614. https://doi.org/10.1108/RPJ-07-2019-0200
40. Berg S et al (2019) ilastik: interactive machine learning for (bio) image analysis. Nat Methods 16:1226–1232. https://doi.org/10.1038/s41592-019-0582-9
41. Münch B, Holzer L (2008) Contradicting geometrical concepts in pore size analysis attained with Electron Microscopy and Mercury Intrusion. J Am Ceram Soc 91:4059–4067. https://doi.org/10.1111/j.1551-2916.2008.02736.x
42. OPENCFD (2016) OpenFOAM, the open source cfd toolbox. User Guide
43. Hildebrando EA et al (2014) Synthesis and characterization of zeolite NaP using kaolin waste as a source of silicon and aluminum. Mater Res 17:174–179. https://doi.org/10.1590/S1516-14392014005000035
44. Weibel R et al (2019) Thermogenetic degradation of early zeolite cement: an important process for generating anomalously high porosity and permeability in deeply buried sandstone reservoirs? Mar Pet Geol 103:620–645. https://doi.org/10.1016/j.marpetgeo.2019.02.006
45. Jacob A et al (2021) Simulating permeability reduction by clay mineral nanopores in a tight sandstone by combining computer X-ray microtomography and focussed ion beam scanning electron microscopy imaging. Solid Earth 12:1–14. https://doi.org/10.5194/se-12-1-2021
46. Morad S et al (2010) The impact of diagenesis on the heterogeneity of sandstone reservoirs: a review of the role of depositional facies and sequence stratigraphy. Bulletin 94:1267–1309. https://doi.org/10.1306/04211009178
47. Arns CH et al (2005) Cross-property correlations and permeability estimation in sandstone. Phys Rev E 72:46304. https://doi.org/10.1103/PhysRevE.72.046304
48. Blunt MJ (2017) Multiphase flow in permeable media. Cambridge University Press, Cambridge
49. Werling N et al (2022) Solubility of Calcined Kaolinite, Montmorillonite, and Illite in high molar NaOH and suitability as precursors for geopolymers. Clays Clay Miner 70:270–289. https://doi.org/10.1007/s42860-022-00185-6
50. Walton IC et al (2002) Perforating unconsolidated sands: an experimental and theoretical investigation. SPE Drilling Completion 17:141–150. https://doi.org/10.2118/79041-PA
51. Dehghani A et al (2013) Experimental investigation of sand consolidation techniques: resin injection and in-situ combustion. IJOGCT 6:689. https://doi.org/10.1504/IJOGCT.2013.056738
52. Maes J, Menke HP (2021) GeoChemFoam: direct modelling of multiphase reactive transport in real pore geometries with equilibrium reactions. Transp Porous Med 139:271–299. https://doi.org/10.1007/s11242-021-01661-8
53. Molins S et al (2021) Simulation of mineral dissolution at the pore scale with evolving fluid-solid interfaces: review of approaches and benchmark problem set. Comput Geosci 25:1285–1318. https://doi.org/10.1007/s10596-019-09903-x
54. Schabernack J, Fischer C (2022) Improved kinetics for mineral dissolution reactions in pore-scale reactive transport modeling. Geochim Cosmochim Acta 334:99–118. https://doi.org/10.1016/j.gca.2022.08.003
55. Reed JK, Gipson Jr M, Vass D (1993) Hydrocarbon potential of sandstone reservoirs in the East Slovakian basin, part 2: zeolites and clay minerals. J Pet Geol 16:223–236. https://doi.org/10.1111/j.1747-5457.1993.tb00108.x
56. Wilson MJ et al (2014) The influence of individual clay minerals on formation damage of reservoir sandstones: a critical review with some new insights. Clay Min 49:147–164. https://doi.org/10.1180/claymin.2014.049.2.02
57. Kong H et al (2020) The variation of grain size distribution in rock granular material in seepage process considering the mechanical-hydrological-chemical coupling effect: an experimental research. R Soc Open Sci 7:190590. https://doi.org/10.1098/rsos.190590
58. Sadeghnejad S et al (2022) Numerical simulation of particle retention mechanisms at the sub-pore scale. Transp Porous Med 145(1):127–151. https://doi.org/10.1007/s11242-022-01843-y

5.2.4 Article 4

High-Resolution Pore Space Imaging, Mineralogical Characterization, and Sealing Capacity Estimates of Confining Units at a Geologic Carbon Storage Demonstration: The Illinois Basin–Decatur Project, USA

Jared T. Freiburg, **Markus Peltz**, Donna C. Willette, and Georg H. Grathoff

The Journal of Geology

Volume 130, 5 (335-355)

Published: December 22, 2022
DOI: https://doi.org/10.1086/722563

High-Resolution Pore Space Imaging, Mineralogical Characterization, and Sealing Capacity Estimates of Confining Units at a Geologic Carbon Storage Demonstration: The Illinois Basin–Decatur Project, USA

Jared T. Freiburg,[1,2,*] *Markus Peltz,*[2] *Donna C. Willette,*[1] *and Georg H. Grathoff*[2]

1. Illinois State Geological Survey, Prairie Research Institute, University of Illinois at Urbana-Champaign, 615 East Peabody Drive, Champaign, Illinois 61820, USA; 2. Department of Geography and Geology, University of Greifswald, Greifswald 17489, Germany

ABSTRACT

At the Illinois Basin–Decatur Project, a large-scale CO_2 capture and geologic storage demonstration project in the saline Mount Simon Sandstone in central Illinois, three overlying and laterally continuous shale formations (the Eau Claire, Maquoketa, and New Albany) are considered confining units overlying the sandstone reservoir. The Mount Simon reservoir contains internal mudstone baffles that will influence CO_2 migration pathways and future interaction with seals. Understanding the sealing properties of rock units deemed seals or confining units is vital to commercialization of geologic carbon storage. For this article, nanoscale-resolution focused ion beam scanning electron microscopy (SEM), mercury injection capillary pressure (MICP), X-ray diffraction (XRD) spectroscopy, and quantitative evaluation of minerals by SEM were used to characterize the controls on the sealing integrity of these seals and reservoir confining units. Results show that porosity and pore size generally decrease with depth, except in the carbonate-rich Maquoketa Shale. The Maquoketa contains the highest pore volume owing to abundant dolomite in the mineral matrix compared with the other mudstone and shale intervals, which are clay rich. The shallowest seal sample, the organic-rich New Albany Shale, contains the highest frequency of the smallest pore throat size and is most comparable, with respect to pore sizes and entry pressures, to the deepest black shale and primary Mount Simon reservoir seal, the Eau Claire. Point-specific MICP threshold pressure results, theoretical calculations based on a range of permeabilities, and column height calculations indicate that the internal Mount Simon mudstone and Eau Claire Shale are effective seals of CO_2 in the Mount Simon reservoir.

Introduction

Research on subsurface CO_2 storage in geological formations has been a recent global focus to mitigate the rise of anthropogenic CO_2 emissions into the atmosphere (Ciotta et al. 2020), which is a major contributing factor to global climate change (Martin-Roberts et al. 2021). Geologic carbon storage is well studied, with preferred storage in deep saline reservoirs with overlying low-permeable mud rock providing effective sealing capacity (Koide et al. 1992; Holloway 2001; Pacala and Socolow 2004; Bachu et al. 2007; Friedmann 2007; Benson and Cole 2008; Oelkers and Cole 2008; Lackner and Brennan 2009; Rackley 2017). A seal rock, considered a confining unit, is an essential component of a geologic carbon capture and storage (CCS) system. The reservoir interval is defined by its pore volume capacity and permeable matrix, while a sealing rock unit critically depends on nano-/micropore systems, which reduce/block fluid movement. In sedimentary basins, shale and its nonfissile equivalent, mudstone, by virtue of their horizontal and vertical distribution and continuity, are major controls on the vertical flow of pore fluids, preventing upward or downward leakage.

Besides being a seal for aquifers, petroleum systems, or in this case a CCS system, shale is commonly a source rock and reservoir in petroleum systems. Pore connectivity, natural or induced, is crucial to produce hydrocarbons and, inversely, critical to contain fluid migration (Liu et al. 2013). To understand the controls on the sealing properties of the confining zones of a CCS reservoir seal,

Manuscript received February 11, 2022; accepted August 19, 2022; electronically published December 22, 2022.

* Author for correspondence; email: freiburg@illinois.edu.

Journal of Geology, volume 130, number 5, September 2022. https://doi.org/10.1086/722563

the extent and connectivity of pore space must be measured and quantitatively described. Organic matter in shales can develop nano-/microporosity due to hydrocarbon generation as burial and thermal maturation increase with time (Loucks et al. 2012). While trace amounts of organic matter are present in the Eau Claire and Maquoketa Shales, the New Albany Shale contains abundant preserved organic matter. Therefore, it is critical to understand controls on pore volume and pore network development and overall mineralogy in overlying confining units.

The Illinois Basin–Decatur Project (IBDP) in Decatur, Illinois, is a large-scale demonstration of the deep saline geological storage of 1 million metric tons of CO_2 injected, stored, and actively monitored in the lowermost unit of the Cambrian Mount Simon Sandstone at a depth of approximately 2100 m (fig. 1). The Mount Simon Sandstone is locally heterogeneous, with the injection unit dominantly comprising deposited fluvial and eolian sandstones (Freiburg et al. 2014; Reesink et al. 2020). Within and overlying the injection unit, numerous well-cemented sandstones and mudstones act as localized baffles to fluid migration. Mount Simon is overlain by three deposited marine shales: the Eau Claire, Maquoketa, and New Albany, which are considered the seals at the IBDP site (Finley 2014). These three shale units are continuous, thick, geographically extensive, and predictable with respect to mineralogy and tectonics. A variety of studies have analyzed the lithology, mineralogy, petrophysics, pore size distribution and capillary entry pressure, fluid-fracture pressure, and CO_2-brine-rock interaction of shales throughout the Illinois Basin (Carroll et al. 2012; Liu et al. 2012; Neufelder et al. 2012; Lahann et al. 2013, 2014; Mastalerz et al. 2013; Yoksoulian et al. 2013; Mozley et al. 2016; Medina et al. 2020), but no study has evaluated the mineralogy, pore space, and seal capacity of all major seals at a single CCS demonstration project in the Illinois Basin, such as the IBDP.

This research provides information on the nature, controls, and variability of the pore structure and mineralogy of seals at the IBDP site. The evaluation is supported by using ultrahigh-resolution focused ion beam (FIB) scanning electron microscopy (SEM) and mercury injection capillary pressure (MICP) analysis coupled with petrographic quantitative evaluation of minerals by SEM (QEMSCAN) and X-ray diffraction (XRD). It aims to characterize the pore space and mineralogy of sealing rocks, both of which are contributing factors to the quality of a seal and its sealing capacity at this CCS project. This information is important for obtaining a Class VI permit from the Environmental Protection Agency, which is necessary to inject CO_2 into deep rock formations in the United States. Commercialization of CCS will need broader and more extensive studies to accurately predict seal capacity throughout the basin.

Geologic Background of IBDP Confining Units

The Illinois Basin is an intracratonic basin filled with Paleozoic sedimentary rocks that covers most of Illinois, southwestern Indiana, western Kentucky, and small areas of Missouri and Tennessee. Precambrian basement rocks underlying the Paleozoic strata of the Illinois Basin are dominantly made up of igneous felsic rocks of the Mesoproterozoic 1.48–1.38-Gy-old Eastern Granite-Rhyolite Province (Bickford et al. 1986) emplaced onto older crust (Freiburg et al. 2020*b*). Unconformably separated from and directly overlying the Precambrian basement is the lowermost Paleozoic formation, the Cambrian Mount Simon Sandstone (Willman et al. 1975). Among many carbonate and siliciclastic units overlying the Mount Simon are three major shales (fig. 1) that persist as laterally extensive units throughout the basin; these shales are the Eau Claire (upper Cambrian), Maquoketa (Upper Ordovician), and New Albany (upper Devonian-lower Mississippian). The Eau Claire directly overlies the Mount Simon, whereas the Maquoketa and New Albany overlie but are positioned between numerous other carbonate and siliciclastic formations. In terms of the thermal maturity of the shale samples at the well site location, the New Albany is considered immature to early mature (Lewan et al. 2002), while the Maquoketa and Eau Claire were heated as a result of burial to the low end of the oil window (Grathoff et al. 2001; Schieber 2010).

Mount Simon Sandstone. The early to middle Cambrian Mount Simon Sandstone is divided into three major sections—the upper, middle, and lower—and further into five distinct units based on changes in the depositional environment and sedimentological variability (Freiburg et al. 2014, 2016, 2020*a*). An informal sandstone unit referred to as the Argenta underlies the lower Mount Simon and unconformably overlies the Precambrian basement (Freiburg et al. 2016). The lower Mount Simon, composed largely of a subarkosic sandstone, has the best reservoir properties as a result of primary porosity preservation and secondary porosity development (Freiburg et al. 2016) and is the IBDP reservoir. The lower Mount Simon depositional facies are heterogeneous and reflect a subtle marine incursion into an alluvial/fluvial environment that transformed

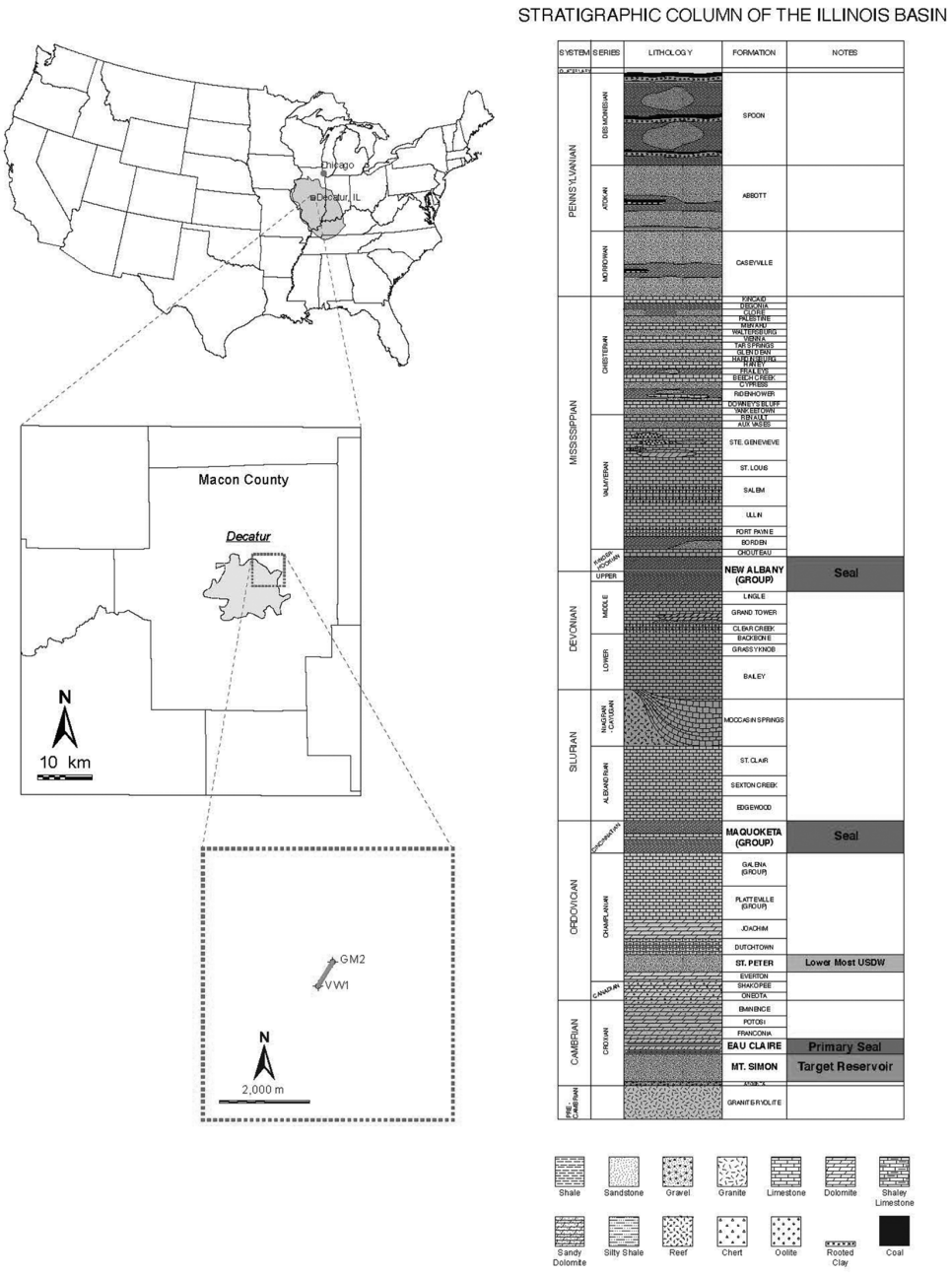

Figure 1. Location of the samples from the wells at the Illinois Basin–Decatur Project (IBDP) in Decatur, Illinois, and detailed stratigraphic column at the IBDP with target reservoir and major sealing units identified. GM2 = Geophysical Monitoring Well 2; VW1 = Verification Well 1; USDW = underground source of drinking water. A color version of this figure is available online.

upward into an eolian environment (Reesink et al. 2020). Thin mudstone beds (<2 m at IBDP) were deposited on floodplains in a braided river system (Freiburg et al. 2014). Thus, because of the anastomosing nature of the river channels, mudstones are laterally discontinuous, as observed in geophysical logs from four wells that penetrate the section within approximately 1700 m (Freiburg et al. 2014, 2016). However, locally, mudstones represent low-permeability reservoir baffles overlying the CO_2 injection zone. The mudstone interbedded within the lower Mount Simon reservoir has been referred to as a pressure baffle as a result of pressure monitoring above and below the mudstone during CO_2 injection and the lack of pressure signals traveling vertically through this tight section (Senel et al. 2014). Despite the apparent lateral variability of this mudstone being a major shortcoming for the sealing capacity of large-scale CO_2 plume containment, it has high-quality sealing properties and is characterized herein (fig. 2).

Eau Claire Formation. The Eau Claire Formation is considered the primary seal of the CCS reservoir for the IBDP (Finley 2014) and functions as a regional aquitard that impedes the exchange of groundwater or mineralizing fluids between the Mount Simon and overlying aquifers in parts of Illinois, Wisconsin, Indiana, and Ohio (Leetaru et al. 2005; Benson and Cole 2008; Neufelder et al. 2012). The Eau Claire was deposited in the upper Cambrian (Neufelder et al. 2012) and, based on the fossil record, is considered Dresbachian in age, part of the Sauk II sequence. The Eau Claire directly overlies and is conformable with the Mount Simon Sandstone and is overlain by the Galesville Sandstone (Konstantinou et al. 2014). The Eau Claire Formation is laterally extensive, underlying all of Illinois, ranging from less than 100 feet (61 m) thick in western Illinois (Willman et al. 1975) to more than 1200 feet (370 m) thick in southern Illinois (Sargent 1991). The Eau Claire is a heterolithic shallow marine succession dominated by interbedded shale, siltstone, sandstone, and dolomite (Aswasereelert et al. 2008; Yawar and Schieber 2008; Neufelder et al. 2012; Lahann et al. 2014; Palkovic 2015). Lithofacies vary widely across the basin and must be reviewed for projects considering the use of the Eau Claire as a confining unit (Lahann et al. 2014). In northwestern Illinois, the Eau Claire is dominantly made up of sandstone. In north-central Illinois, the Eau Claire is siltier and shaley. In southern to southwestern Illinois, the Eau Claire is predominantly

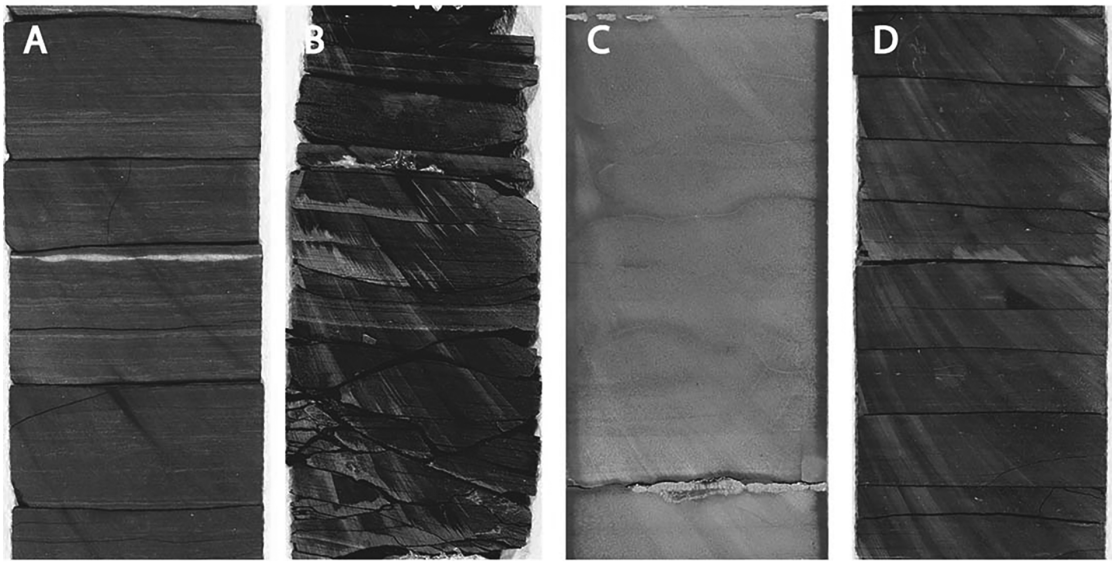

Figure 2. Sampled cores (4 inches [10 cm] in diameter) from the Illinois Basin–Decatur Project. *A*, Mudstone sample (depth: 6863 feet [2092 m]) interbedded within the Mount Simon Sandstone. *B*, Eau Claire Formation sample (depth: 5465 feet [1666 m]). *C*, Maquoketa Shale Group sample (depth: 2816 feet [858 m]). *D*, New Albany Shale Group sample (depth: 2157 feet [657 m]). A color version of this figure is available online.

dolomite and limestone and is commonly referred to as the Bonneterre Formation. At the IBDP site, the basal unit of the Eau Claire is dominantly composed of silty and sandy shale to clean shale and is approximately 50 feet (15 m) thick (Lahann et al. 2014; Palkovic 2015).

Maquoketa Shale Group. The Maquoketa is considered a secondary sealing unit of the IBDP (fig. 1). It is widespread across the US midcontinent, spanning about 680 mi (1100 km) wide (Kolata and Graese 1983). The Maquoketa is disconformable with the underlying limestones and dolomites of the Galena Group and overlain by limestones of the Silurian System. In Illinois, the Maquoketa is divided into several formations from the base to the top: Scales Shale, Fort Atkinson Limestone, Brainard Shale, and Neda Formation (Kolata and Graese 1983). Although the Scales Shale contains less clay and is the more carbonate-rich facies of the two Maquoketa Shale formations, it is the basalmost formation and would be the first to act as a seal for underlying CO_2 storage reservoirs. Thus, the Scales Shale is the focus of this study and is simply referred to as the Maquoketa Shale. It ranges from 50 to 150 feet (15 to 45 m) thick across Illinois (Willman et al. 1975). The Scales consists primarily of light gray and olive gray shale with minor amounts of olive black, brownish gray, and brownish black shale (Kolata and Graese 1983). The Maquoketa overlies formations of the Knox Supergroup and the Ancell Group, which have been proposed as prospective CCS reservoirs (Leetaru et al. 2012; Leetaru 2014; Damiani 2020) and have been used for industrial wastewater storage for decades (Freiburg and Leetaru 2012); the Maquoketa is the primary seal. At the IBDP, the Maquoketa is considered a secondary seal (Freiburg et al. 2014)

New Albany Shale Group. The New Albany Shale Group is part of the Kaskaskia sequence and forms an essentially continuous body of shale that is mostly upper Devonian in age, with the sequence beginning in the mid-Devonian and ending in the lower Mississippian. It consists of laterally extensive, organic-rich shales with consistent organofacies containing total organic carbon (TOC) values that can reach up to 13% across Illinois, western and central Kentucky, and Indiana, with highly variable maturity (Mastalerz et al. 2013). More than 140.4 billion barrels of oil have been generated from the New Albany Shale in thermally mature portions of the basin (Higley et al. 2003) supplying oil to numerous overlying Mississippian and Pennsylvanian reservoirs throughout the Illinois Basin (Barrows and Cluff 1984). The New Albany has a maximum thickness of 400 feet (121 m) but is eroded in northern Illinois and exposed in parts of western and southern Illinois. In Illinois, the New Albany is divided into several major shale formations from base to top: Blocher, Sweetland Creek, Grassy Creek, Saverton, and Hannibal (Cluff et al. 1981). The New Albany also includes a thin sandstone (Sylamore) unit and a limestone (Louisiana) unit. This study focuses on the Grassy Creek Shale, which has the highest concentration of organic carbon of any member of the New Albany Shale (Cluff et al. 1981). Natural gas has been produced from the New Albany over the past century, until the present (Partin 2004). In addition to its gas potential (Strapoc et al. 2010), the New Albany is of interest for CO_2 sequestration (Nuttall et al. 2009) and is considered a secondary seal for the IBDP (Freiburg et al. 2014). Porosity and the influence of CO_2 on the New Albany have previously been investigated using various samples across the Illinois Basin (Partin 2004; Lahann et al. 2013)

Methods

Three representative samples of shale from the major sealing units for the IBDP were selected for analyses: the Eau Claire Formation (depth: 5465 feet [1666 m]), the Maquoketa Shale (depth: 2816 feet [858 m]), and the New Albany Shale (depth: 2157 feet [657 m]; fig. 2). A fourth sample, a Mount Simon mudstone (depth: 6863 feet [2092 m]), was selected, as it represents a major baffle internal to the reservoir that may control CO_2 migration pathways (fig. 2). These samples were selected to be representative of potential sealing facies within each seal interval based on their lithology and relative position within the formations. Samples were cut from a 10-cm core from Verification Well 1 (VW1) and Geophysical Monitoring Well 2, located at the IBDP site and housed at the Illinois State Geological Survey sample library (figs. 1, 2). The petrographic, mineralogical, and routine petrophysical property analyses described below were completed for all four samples. Samples were equally split for each separate analysis.

Thin sections of each sample were analyzed and described under plane and cross-polarized light (fig. 3). Quantitative electron mineralogy analysis using QEMSCAN was completed by SGS Laboratory in Vancouver, Canada. This included qualitative mineralogy, mineralogical distribution mapping, and particle size analysis. Mineral distribution maps consisting of several stitched frames with pixelwise mineralogy information were collected for carbon-coated polished rock samples at a resolution of 5 μm for New Albany, Eau Claire, and Maquoketa and

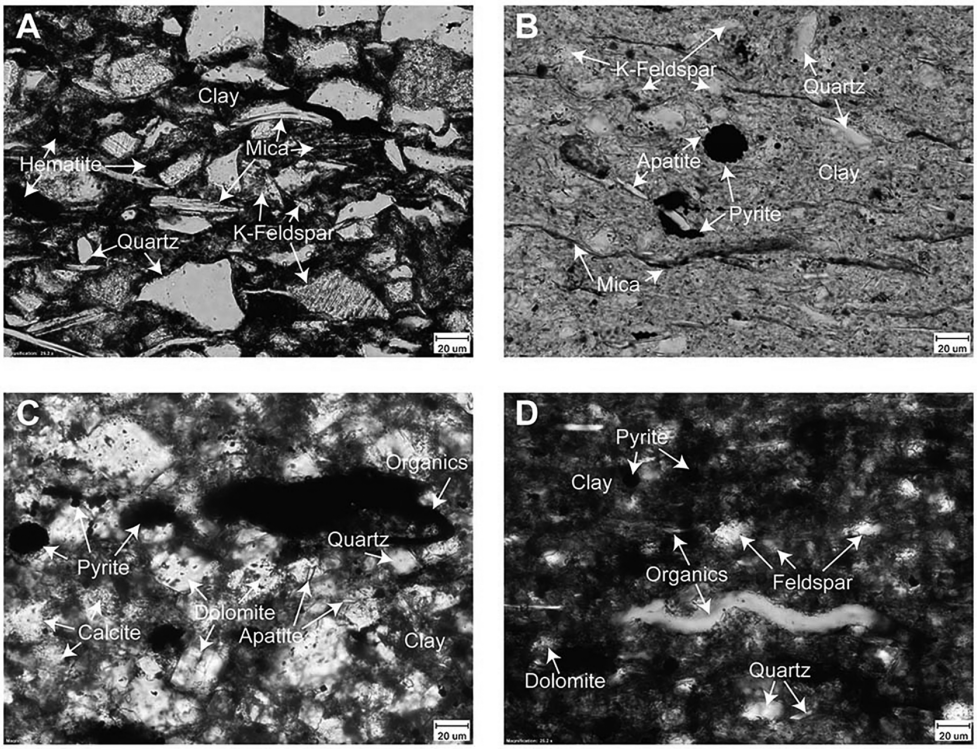

Figure 3. Thin section photomicrographs from the core samples (fig. 2). *A*, Mount Simon mudstone with a hematite and illitic clay matrix hosting abundant quartz, K-feldspar, and mica. *B*, Shale from the Eau Claire Formation with an illitic clay matrix hosting mica, quartz, K-feldspar, apatite, and pyrite. *C*, Argillaceous dolomite from the Maquoketa Shale Group with dolomite, calcite, and illitic clay matrix with minor pyrite, quartz, apatite, and organics. *D*, Shale from the New Albany Shale Group with an illitic clay-rich matrix hosting minor quartz, feldspar, pyrite, dolomite, and organics. A color version of this figure is available online.

10 μm for Mount Simon. Because of the rich abundance of the clay-sized mineral grains, QEMSCAN mapping was used for contextual mineral distribution and rock texture analyses and not for mineral identification or quantification. Rather, XRD analyses were used for mineral identification, quantitative mineralogy, and clay fraction analysis (<2 μm). As all samples were epoxy resin impregnated and coated with carbon before measurements, no organic matter was detected by QEMSCAN.

Samples for XRD were analyzed with a Bruker D8 Advance instrument with Bragg-Brentano θ-θ geometry equipped with a Lynxeye 1D stripe detector. Step-scanned data were collected at 30 mA and 40 kV from 3°–40° 2θ (oriented preparations) and 4°–80° 2θ (random powders) with a fixed rate of 2° per minute and a step size of 0.02° 2θ for each sample. Quantitative Rietveld refinements were realized using the BGMN/Profex software (Doebelin and Kleeberg 2015).

To complement textural analyses, FIB SEM with energy-dispersive spectroscopy (EDS) was carried out in clay-rich intergranular regions that were otherwise difficult to resolve by QEMSCAN alone. Measurements were completed with a Zeiss Auriga equipped with an Oxford Instruments X-MAX 80 EDS detector and an FE cathode. Secondary electron (SE) and energy-selective backscattered electron (BSE) image stacks were collected at 1 kV to minimize charging artifacts near the edges and organic matter. Image resolution was 1024 × 768 in the *x* and *y* directions. During the serial sectioning, a beam current of 500 pA was used for cutting about 25-nm-thick slices. SE and BSE image stacks were allowed to differentiate between mineral phases. As gray-level normalization was performed on the polished surfaces before the start of the serial sectioning process, the ability to differentiate between distinct phases depends strongly on the range of gray levels of each individual sample. Therefore,

for some samples it was possible to distinguish between quartz grains and clay mineral matrix, whereas this was not possible for samples containing organic matter as well as dense metal oxides. Differences in mineral quantities between the FIB SEM and the XRD/QEMSCAN analyses result from the size of the samples analyzed and the FIB SEM approach to specifically analyzing the intergranular clay matrix. FIB SEM volume of analysis is generally 10 μm × 10 μm × 10 μm, equivalent to only 1–4 pixels in QEMSCAN maps. Therefore, detrital grains such as quartz and feldspar coarser than clay size are generally highly underestimated in FIB SEM because of the size of the FIB SEM area of investigation. Coarse-grained particles are avoided when selecting the region of investigation to avoid a single grain filling the entire volume of investigation. Silty laminae, such as those observed in QEMSCAN (fig. 4), were avoided for FIB SEM analysis.

The identification of the minerals during FIB SEM was based on EDS mappings collected before and after the serial sectioning process. Images were analyzed with Avizo 9.3 and ImageJ. After alignment of the image stack, filters were applied to enhance the image quality for segmentations. The filters used for image analysis included a fast Fourier transform filter to remove curtaining artifacts, shading, and background correction and a nonlocal means filter to remove noise. Segmentations were done by using thresholds on gray values and improved by hand using the Avizo segmentation editor. Pore space was binarized and qualitatively and quantitatively analyzed. All objects of <5 voxels were considered noise and thus removed from the binary image. Image-based pore size distributions (PSDs) were calculated based on the continuous PSD (cPSD) approach (Münch and Holzer 2008).

Porosity was further measured by MICP using a Micromeritics AutoPore IV 9520 mercury porosimeter at Schlumberger Reservoir Laboratories in Houston, Texas. Samples were subjected to drainage-only mercury injection to measure routine properties and pore throat size distribution. TOC data were available for the Eau Claire and New Albany samples and are included with the XRD data.

A first approximation of the sealing capacity (column height of supercritical CO_2 [$scCO_2$] that the

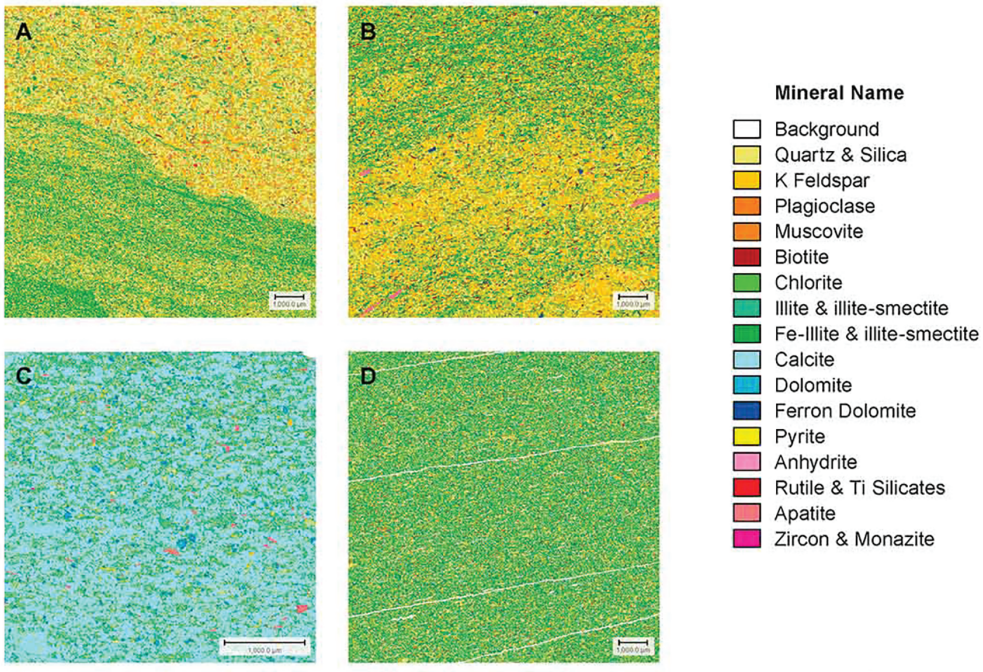

Figure 4. Quantitative evaluation of minerals by scanning electron microscopy mineral phase assemblage maps of selected samples. *A*, Mount Simon mudstone with abundant quartz, K-feldspar, and illite. *B*, Eau Claire Shale with abundant K-feldspar, quartz, illite, and illite-smectite. *C*, Maquoketa argillaceous dolomite showing abundant calcite and minor dolomite and illite. *D*, New Albany Shale with abundant quartz, illite, and illite-smectite.

seals can retain before leakage occurs) of the samples is evaluated using permeability estimates, which span the range of values calculated from petrophysical analyses. This evaluation is determined from previous experimental research in which statistically significant relationships between air permeability (md) and air threshold pressure (psi) are evident (Dewhurst et al. 2002; Li et al. 2005).

The correlation between $scCO_2$ threshold pressure (psi) and N_2 threshold pressure (psi) is key to approximating the sealing capacity for $scCO_2$. Mean pressure in relation to $scCO_2$ is 42.7% of that measured in relation to air or N_2. Using equation (1), the relation is

$$P_{tscCO_2} = \left[0.427 \times \left(e^{3.02} \times k_{seal}{}^{-0.434}\right)\right], \quad (1)$$

where P_{tscCO_2} is the threshold pressure (psi) and k_{seal} is permeability (md).

Substitution of equation (1) into the standard evaluation of column height in equation (2), or the height of a hydrocarbon or $scCO_2$ column the seal can hold before breakthrough, is as follows (Daniel and Kaldi 2008):

$$h_{scCO_2}\,\max = \frac{\left[0.427 \times \left(e^{3.02} \times k_{seal}{}^{-0.434}\right)\right] - \left(e^{3.02} \times k_{res}{}^{-0.434}\right)}{\left[\left(\rho_f - \rho_{scCO_2}\right) \times 0.433\right] \times 0.3048}, \quad (2)$$

where k_{seal} is seal permeability (md), k_{res} is reservoir permeability (md), ρ_f is density of the reservoir brine, and ρ_{scCO_2} is density of $scCO_2$ at reservoir temperature and pressure.

A range of permeability values for each sample interval were calculated using temperature, pressure, and density values determined from the IBDP well data. Comparison of the New Albany Shale is not possible using this formulation as at formation temperature and pressures, CO_2 is in gas phase, not sc.

A rigorous evaluation of threshold pressures using detailed MICP data created a range of minimum to maximum $scCO_2$ column heights based on a range of CO_2 contact angles and Hg/air threshold pressures. This provides additional insight into seal capacity and leakage potential. Generally, before 2006, $scCO_2$/water/rock interfaces in the subsurface were assumed to have a contact angle (θ) of 0°, as water was thought to be the wetting phase (Daniel and Kaldi 2008). More recent experimental studies using quartz, mica, and clay substrates and $scCO_2$ immersed in brine indicate that these substrates become less water wet in the presence of $scCO_2$—that is, at contact angles varying from 0° to 40° (Sarmadivaleh et al. 2015). An increase in contact angle ranging from 30° to 60° becomes more pronounced at higher pressures up to 20 mPa. For the purposes of this study, a range of column heights were calculated using contact angles of 0°, 20°, 40°, and 60° to bracket the wettability uncertainty. In addition, on the basis of the sample MICP entry pressure (Hg/air), the threshold pressure of the CO_2/brine system was modified by 20% (either low or high) to capture some of the variability in the pore volume and permeability of the changing seal composition and resultant diagenesis. This allowed a maximum/minimum comparison of column heights relative to the data derived from the sample.

Variability of capillary pressure using a range of contact angles follows the equation for a wettability transformation from an air/mercury system to brine (after Schowalter 1979):

$$P_{b/CO_2} = P_{a/m}(\sigma_{b/CO_2} \cos\theta_{b/CO_2})/(\sigma_{a/m} \cos\theta_{a/m}), \quad (3)$$

where P_{b/CO_2} is the capillary pressure in the brine/CO_2 system; $P_{a/m}$ is the capillary pressure in the air/mercury system; σ_{b/CO_2} and $\sigma_{a/m}$ are the interfacial tensions (IFTs) of the brine/CO_2 and the air/mercury systems, respectively; and θ_{b/CO_2} and $\theta_{a/m}$ are the contact angles of the brine/CO_2/substrate and air/mercury/substrate systems, respectively.

Calculation of the column height uses the standard equation

$$h_{scCO_2}\,\max = (Pth_s - Pth_r)/(\rho_f - \rho_{scCO_2}) \times 0.433, \quad (4)$$

where Pth_s is the entry pressure of the seal in the $scCO_2$/brine system, Pth_r is the entry pressure of the reservoir in the $scCO_2$/brine system, $\rho_f - \rho_{scCO_2}$ is the density difference between the brine and $scCO_2$, 0.433 is the normal hydrostatic gradient of water (psi/foot), and h_{scCO_2} max is the maximum column height or seal capacity (Daniel and Kaldi 2008). The IFT used in the Hg/air to brine/CO_2 conversion for each sample is based on studies indicating that it typically ranges between 21 and 27 dyn/cm under $scCO_2$ conditions (Espinoza and Santamarina 2010).

Results and Discussion

Complementation of Methods. Integration of mineralogical and pore size characterization analytical methods for samples in this study gives diverse results that offer important two-dimensional (2D) and three-dimensional (3D) data critical to evaluation of the sealing properties of the seals. The methods applied complement each other in various ways, but limitations may also give rise to contradicting results.

Regarding the quantitative mineralogy, XRD offers the most accurate results for the samples in this study (table 1) but lacks determination of trace mineral components such as apatite, which is often overlooked because of its low crystallinity (Kaufhold et al. 2002). QEMSCAN can detect these trace components if particles are sufficiently large (>2 μm) but lacks accuracy when identifying clay-sized minerals. For example, the Mount Simon contains significant amounts of nanocrystalline hematite, which was shown by FIB SEM to be enriched in the clay mineral matrix. Although close-up measurements down to a resolution of 2.6 μm were run by QEMSCAN for this sample, it was insufficient to resolve illite and hematite individually, which resulted in the false identification of Fe-illite. QEMSCAN quantifications also become error prone when chemically similar minerals, such as K-feldspar and illite (Mount Simon and Eau Claire) or calcite and dolomite (Maquoketa), are the main components of the rock.

Thus, QEMSCAN results give a 2D semiquantitative evaluation of the mineralogy of a single surface of the sample (table 2). An important aspect of this evaluation is obtaining a spatial distribution of minerals in the scanned surface, which may play an important role in pore space distribution. This spatial distribution, when assigned correctly, assists in understanding detrital and diagenetic relationships to pore space development and assists in mapping the 3D mineral framework and pore space network by FIB SEM. The qualitative mineralogical data from FIB SEM obtained through two EDS analysis mappings per sample were less accurate than those from QEMSCAN, as major grayscale grouping on electron images (table 3) was required. These grayscales represent dominant minerals and groups of minerals that have similar backscattered signatures. Despite these limitations, FIB SEM allowed the reconstruction of pore space and organic matter distribution. QEMSCAN was not capable of resolving nanoscale pore space in the samples studied, and the QEMSCAN sample preparation, which included epoxy resin embedding and carbon coating, prevented efficient organic matter identification. MICP and FIB SEM porosity analyses correlated well for the Maquoketa, where it can be assumed that pore throats below the resolution for FIB SEM exist within the imaged clay mineral matrix. For Mount Simon and Eau Claire, the MICP- and FIB SEM–examined pore spaces likely do not concur, as imaged pores show no signs of interconnectivity. Overall, the results discussed below indicate important values contributed from each analysis performed, but careful consideration should be given to analytical limitations.

Mount Simon (Mudstone). The mudstone is made up of silt-sized particles composed of angular to subrounded grains of quartz, K-feldspar, hematite, and muscovite in a clay matrix (fig. 3). XRD indicates that approximately 44.1% of the sample is composed of clay minerals, with the other 55.9% being nonclay minerals. The clay-rich matrix is composed of 1Md illite (39.3%), with minor amounts of well crystalline 1M illite (3%). XRD and the 2D QEMSCAN are qualitatively consistent except for trace components such as apatite and zircon, which are detected only by QEMSCAN. Furthermore, hematite, which is quantified at 4% by XRD analyses, was not detected by QEMSCAN but was accounted for as an iron-rich illite or Fe-illite (table 2). FIB SEM images show that these iron oxides are observed as clusters of nano- to micrometer-sized prismatic crystals (fig. 5*A*) that are aligned relatively horizontally within the clay-mineral matrix. The same fabric is observed at a larger scale in thin section and QEMSCAN analysis. The amount of iron oxides observed by FIB SEM is anomalously high compared with the XRD and petrographic results (fig. 6) and accounts for a large fraction (25.3%) of the sampled volume. This high amount of hematite is likely accurate in this specific sectioned matrix-dominated volume of the sample, as the hematite is easily identified because of the high backscatter intensity, although some overestimation may occur as a result of charging artifacts. However, a relative enrichment of iron oxides can be observed visually in the central region of the volume analyzed (fig. 5*A*), indicating a heterogeneous distribution throughout the clay mineral matrix. Feldspars are included in the undifferentiated matrix in the FIB SEM results.

FIB SEM images (fig. 6) indicate minimal porosity within the mudstone, at approximately 0.01% of the sample volume (table 3). Pores are almost exclusively interparticle pores. One slit-shaped pore is observed and is likely the result of clay desiccation during sample drying. All other pores are more irregular to spherical and are most common in clay matrix, where hematite crystals are absent and may occur as intraparticle pore space from partial dissolution in detrital grains such as feldspar (fig. 6). MICP analyses reveal 0.005% effective porosity. A median pore throat of 7.5 nm is observed with MICP (table 3); this is below the resolution limits of the FIB SEM (fig. 8). The calculated cPSD shows the narrowest range of pore sizes and the smallest number of pores. Overall, mineralogy and rock fabric analyses by QEMSCAN and FIB SEM on the one hand and pore space analyses by FIB SEM and MICP on the other hand do not draw a complementary picture of the rocks' flow paths. Pores imaged by FIB

Table 1. X-ray Diffraction and Total Organic Carbon Analysis Results (wt%) of the Illinois Basin–Decatur Project Seals

Formation	Lithology	Quartz	K-feldspar	Plagioclase	Dolomite	Ferroan dolomite	Hematite	Pyrite	Anatase
Mount Simon	Mudstone	32.6	19.5	.0	1.0	.0	4.0	.0	.6
Eau Claire	Shale	10.9	16.8	.0	.0	.0	.0	.7	.3
Maquoketa	Shale	15.3	5.5	2.2	17.3	30.6	.0	.9	.0
New Albany	Shale	28.0	4.1	5.0	.0	3.1	.0	3.0	.0

Formation	Rutile	Sum nonclay	Kaolinite	Chlorite	Illite 1M	Illite 1Md/ Illite-rich illite-smectite	Mica/ muscovite 2M	Sum clay	Total organic carbon
Mount Simon	.0	55.9	.0	.0	3.0	39.3	.0	44.1	na
Eau Claire	.0	28.5	.0	6.2	4.9	60.2	.0	71.3	.2
Maquoketa	.1	72.0	.0	5.0	.0	20.9	2.2	28.0	na
New Albany	.7	38.5	.0	10.0	1.6	20.4	24.1	53.1	8.3

SEM within the clay-mineral matrix are too isolated to be connected by pore throats measured by MICP, and increasing the image resolution would thus not result in finding and resolving these throats within the clay matrix. Therefore, it is more probable that these throats are found at the boundary between the silica and clay-rich layers shown by QEMSCAN (fig. 4*A*) than within the clay-mineral matrix. Of all the samples observed, the Mount Simon mudstone has an exponentially higher entry pressure than all the shales (table 3) and the lowest observed porosity, thus making it the best immediate seal relative to CO_2 migration.

Eau Claire. The Eau Claire sample is a shale made up of clay-sized grains of angular to subrounded quartz, K-feldspar, and minor plagioclase, pyrite, calcite, biotite, and dolomite suspended in a dominantly clay matrix (table 1). Chlorites are generally the coarsest particles, forming fine platelets elongated parallel to bedding in the clay matrix.

Table 2. Quantitative Evaluation of Minerals by Scanning Electron Microscopy Results (wt%)

Formation	Depth	Lithology	Grain density	Quartz and silica	K-feldspar	Alkali feldspar	Plagioclase	Calcite	Dolomite
Mount Simon	6860.60	Mudstone	2.679	40.5	22.8	.0	.0	.0	.0
Eau Claire	5462.50	Shale	2.673	22.0	41.7	.0	.4	.0	.0
Maquoketa	2784.00	Shale	2.721	5.0	2.3	.1	.8	60.0	2.6
New Albany	2143.02	Shale	2.785	21.0	6.1	.0	2.4	.0	.5

Formation	Ferroan dolomite	Fe oxide and siderite	Pyrite	Barite	Rutile and Ti silicates	Ilmenite	Apatite	Zircon
Mount Simon	.0	.1	.0	.0	.3	.1	.1	.1
Eau Claire	.4	.0	.8	.0	.2	.0	1.1	.0
Maquoketa	.8	.0	1.0	.0	.1	.0	1.7	.0
New Albany	.1	.0	7.7	.0	.3	.0	.1	.0

Formation	Muscovite	Biotite	Sericite	Illite and illite-smectite	Fe-illite and illite-smectite	Kaolinite	Chlorite	Total
Mount Simon	.9	.9	5.9	9.8	18.2	.0	.1	100.0
Eau Claire	.5	5.1	.0	7.8	19.6	.0	.4	100.0
Maquoketa	.8	.4	.0	23.1	.0	.5	.8	100.0
New Albany	1.1	5.7	.0	31.4	22.3	.3	1.0	100.0

Table 3. Porosity and Pore Data from Mercury Intrusion Capillary Pressure and Focused Ion Beam Scanning Electron Microscopy (FIB SEM)

Formation	Lithology	Hg injection effective porosity (%)	Median pore throat (nm)	Hg/air entry pressure (psi)	Air/brine entry pressure (psi)
Mount Simon	Mudstone	.005	7.5	7180	1658
Eau Claire	Shale	.019	13.7	617	120
Maquoketa	Shale	.047	9.1	435	84
New Albany	Shale	.039	8.9	694	135

Formation	Swanson permeability (mD)	FIB SEM sample volume (nm^3)	FIB SEM pore volume (nm^3)	FIB SEM pore fraction (%)	FIB SEM pores (n)
Mount Simon	<.01	1347.59	.13	.01	113
Eau Claire	<.01	3398.97	3.66	.11	1165
Maquoketa	<.01	2327.38	25	1.07	8947
New Albany	<.01	2356.9	1.73	.07	743

Apatite is observed in thin section (fig. 3*B*) and QEMSCAN (fig. 4*B*) but was not detected by XRD. Most of the sample is composed of clay, with the greatest total percentage of clay minerals (71.3%) relative to all other samples analyzed. The clay is a mixture of 1M illite (4.9%) and illite-rich, mixed, layered illite-smectite (60.2%), with minor percentages of chlorite (6.2%) detected (table 1). Trace amounts of organic carbon (0.2%) were detected only by TOC analyses. Contrary to the XRD results, QEMSCAN detected an elevated K-feldspar content in more than 40% of the scanned thin section. Much less clay is detected relative to the XRD results, implying that illitic clay minerals may be counted as K-feldspar in the QEMSCAN. This problem arises from the assignment of a single phase to a pixel during the final step of data processing, although chemically similar mixed phases per pixel can be identified by QEMSCAN (Rokosh et al. 2016). The high clay content in XRD is supported by FIB SEM, with nearly all the sample analyzed as undifferentiated clay matrix (fig. 6).

Pore space in the Eau Claire sample is minimal, as indicated by approximately 0.11% of the total FIB SEM sample volume. MICP analyses detected 0.019% pore volume. Reconstructed pore space in the FIB SEM model suggests that pores are largely associated with the coarse detritus, as slit-shaped pores are commonly found along grain boundaries. This implies that desiccation of the sample at clay-grain interfaces or depressurization after drilling may play a role in the porosity observed in this sample. No connectivity of these pores was observed throughout the analyzed domain, but their spatial proximity indicates that connecting pore throats below the resolution limits may exist. Furthermore, disconnected spherical to ellipsoidal pores are commonly observed in the segmented pore space of the Eau Claire, which likely does not contribute to the effective porosity. The median pore throat diameter detected with MICP is 13.7 nm, which is the largest among the samples studied. Entry pressure of brine/air is considerably lower at 120 psi compared with the mercury/air entry pressure (table 3). Despite the slightly higher effective porosity than the internal Mount Simon mudstone sample, the Eau Claire has the lowest effective porosity among all the major shale intervals analyzed.

Maquoketa. The results of this study indicate that the Maquoketa sample is an argillaceous dolomite to dolomitic marl on the basis of its dominant mineral composition of dolomite (table 1). The dolomite is clay sized (<63 μm) and is the dominant mineral, along with clay, making up the matrix of the sample (fig. 3). Subhedral dolomite is commonly associated with anhedral crystals of calcite. QEMSCAN suggests that the dominant mineral is calcite, which contradicts XRD results. Data from XRD analyses show 17.3% dolomite and 30.6% ferroan dolomite and are supported by petrographic examination (fig. 3*C*). Clay minerals appear to be common in thin section (fig. 3) and are quantified by QEMSCAN as 25.6% of the total, with 23.1% illite and mixed, layered illite-smectite and minor quantities of muscovite, biotite, kaolinite, and chlorite (fig. 4; table 2). XRD results show a total clay content of 28%, with about 20.9% 1Md illite, 5% chlorite, and 2.2% detrital 2M muscovite (table 1). No kaolinite was observed in the thin section and XRD. QEMSCAN- and XRD-derived clay quantities are in good agreement for the Maquoketa. Besides dominant percentages of dolomite, the Maquoketa sample includes minor quartz, K-feldspar, pyrite, and apatite, as observed in thin section, QEMSCAN, and XRD. FIB SEM supports the predominance of dolomite within the sample, with minor framboidal

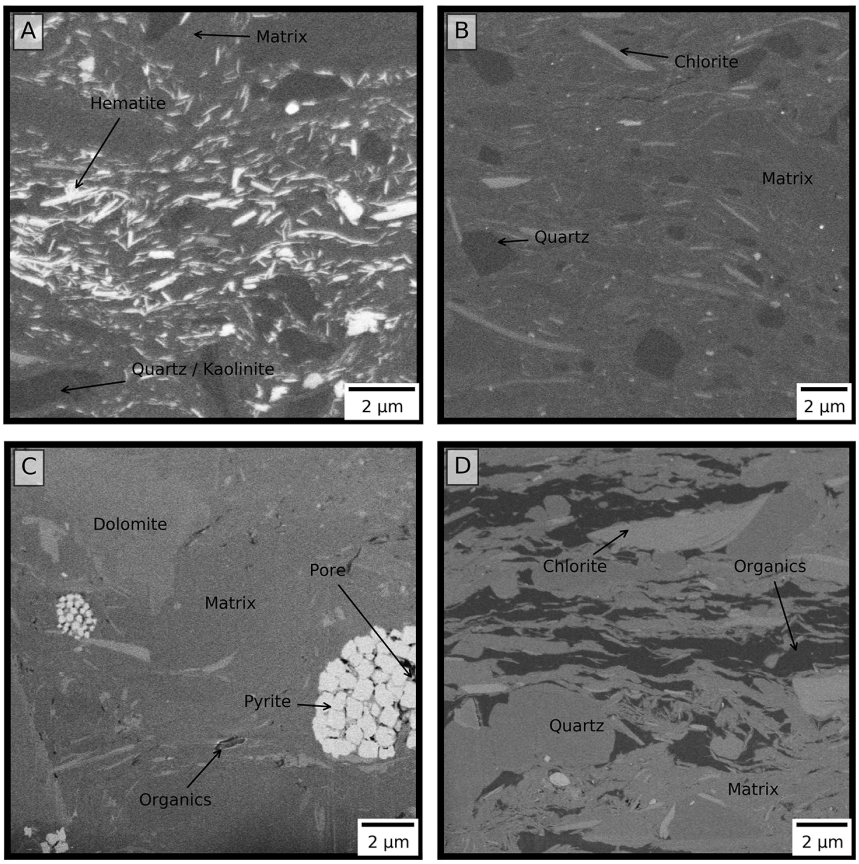

Figure 5. Select backscattered electron images of ion-polished surfaces and segmented volume fractions. *A*, Mount Simon sample shows intergranular matrix with varied mineralogy. Bright laths of hematite are abundant throughout much of the sample. *B*, Eau Claire sample showing platy chlorites in lighter colors and subrounded quartz grains within the dense, indistinguishable clay matrix. *C*, Maquoketa sample with highest pore space volume. The largest pore clusters are concentrated in framboidal pyrite. The matrix is composed of illitic clay minerals and platy chlorites in between abundant angular dolomite grains. *D*, New Albany sample, showing abundant organic material. Pore space is often located in and around organic matter and oriented along the bedding plane.

pyrite, clay, and trace organics (fig. 6). Trace organic material (0.3 vol%) is observed in electron imaging (fig. 5) as well as in thin section (fig. 3). Within the area of FIB SEM observation, large clusters of framboidal pyrite make up large areas of the sampled section (figs. 5, 6). Pore space is abundant between individual crystals in the framboids (fig. 6).

Of all the samples analyzed, the Maquoketa has the highest measurable pore space (figs. 6, 8; table 4). The highest concentration and degree of connectivity of pore space occur within the pyrite framboids. Other pore space is attributed to dolomite pores (fig. 6). FIB SEM indicates that the Maquoketa has the highest median pore radii of all samples (table 3), and pores occur in higher frequency relative to the other samples (fig. 7). MICP analyses indicate that the median pore throat of 9.1 nm is relatively small compared with the other samples and even smaller than that of the deeper Eau Claire sample (fig. 7; table 3). The Maquoketa has the lowest threshold entry pressures relative to the other major seal intervals, which is attributed to the more abundant and widely distributed pore spaces. Pores and pore throat diameters across the sample show the broadest distribution among the samples analyzed (fig. 7*A*, 7*B*). In contrast to the other samples, large connected pore clusters are observed (fig. 8*A*, 8*C*) despite the lack of axis connectivity. Pore size and cluster appearance

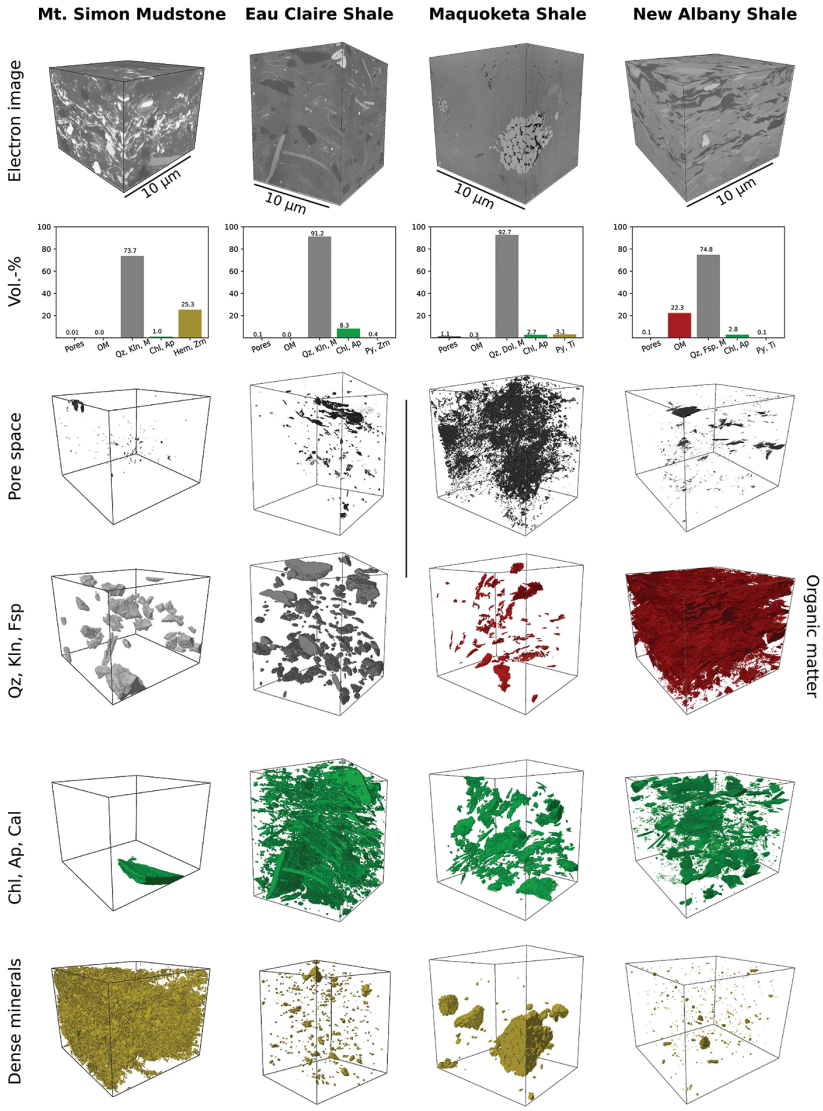

Figure 6. Three-dimensional focused ion beam scanning electron microscopy segmentation of the four samples analyzed. Segmentation and isolation of mineral phases are controlled by backscattered electron (BSE) contrast. Minerals such as quartz (Qz), kaolinite (Kln), feldspar (Fsp), and dolomite (Dol) are isolated and segmented when BSE is sufficient. In organic-rich samples, BSE is insufficient, and these minerals are not isolated and segmented. Mineral abbreviations after Warr (2021). Ant = anatase; Ap = apatite; Cal = calcite; Chl = chlorite; Hem = hematite; M = indistinguishable mineral matrix; OM = organic matter; Py = pyrite; Ti = titanium; Zrn = zircon.

are directly related to the pore host mineral. For example, pyrite framboids host the largest and most connected pore clusters (fig. 8*C*), whereas smaller pores with low connectivity are related to clay minerals and dolomite. However, the overall homogeneous and broad distribution of pore space in the FIB SEM models indicates a widespread connectivity of pores with pore throat sizes slightly below the applied resolution, as confirmed by MICP.

New Albany. The New Albany sample is composed of clay-sized quartz, K-feldspar, plagioclase, and mica detritus as well as common organic material (fig. 3). Micas are preferentially aligned parallel to lamination and are dominated by muscovite

Table 4. Rock and Fluid Properties for Seal Samples Taken at Verification Well 1, Illinois Basin–Decatur Project

Formation (sample)	Depth of sample TVDSS (m)	Pressure at sample depth (psi, mPa)	Temperature at sample depth (°F, °C)	Salinity at sample depth (ppm)	CO_2 density (g/cm^3)	Brine density (g/cm^3)	Interfacial tension (mN/m, dyn/cm)	Contact angle (°)	Seal threshold pressure (air/Hg; psia)	Reservoir threshold pressure (air/Hg; psia)
Mount Simon mudstone	2091.7	2753.10, 18.98	120.23, 49.02	20,2900	.78	1.145	27	0–60	7180	10
Eau Claire Shale	1666.0	2064.27, 14.23	111.26, 44.03	145,500	.744	1.10	26	0–60	617	10
Maquoketa Shale	858.0	1219.0, 8.40	91.38, 32.99	140,000	.64	1.10	24	0–60	435	10
New Albany Shale	658.0	934.8, 6.45	84.29, 29.05	135,000	.21	1.10	43	0–60	694	10

Note. Includes pressure, temperature, and salinity data for the selected samples; threshold pressures measured from mercury injection capillary pressure analyses; and calculated brine and CO_2 densities. The table also lists interfacial tension and contact angles used in seal capacity calculations. TVDSS = true vertical depth subsea.

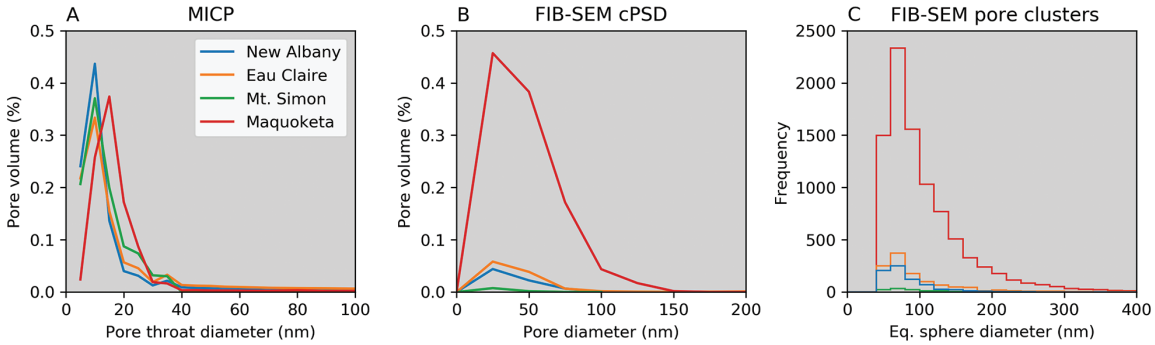

Figure 7. *A*, Graph of mercury injection capillary pressure (MICP) data, showing the volume (%) of pore throat diameter. The New Albany sample has the most abundant pore throats in the finest size range (0–5 nm). The Maquoketa sample has more abundant large pore throats than any of the other samples. *B*, Continuous pore size distribution (cPSD) calculated from binarized electron image stacks. The highest porosity and the largest pore radii are observed in the Maquoketa sample. *C*, Frequency distribution of the volume of individual pore clusters measured from binarized focused ion beam (FIB) scanning electron microscopy (SEM) image stacks. The most and the largest pore clusters are observed in the Maquoketa sample. The lowest number of pores and the narrowest range of pore sizes are found in the Mount Simon sample. New Albany and Eau Claire show similar pore and cluster size distributions.

(24.1%), which may be locally altered to chlorite (7.1%). The matrix is largely composed of 1Md illite (20.4%), with minor 1M illite (1.6%) and chlorite (fig. 4; table 1). Minor dolomite and trace pyrite are observed throughout (table 2) and may be of diagenetic origin. Pyrite occurs as single crystals, framboids, and aggregates of the two (fig. 6). Dolomite cements and single crystals are observed in FIB SEM slices, with multiple generations observed in single crystals. Of all the samples observed, the New Albany has the highest organic matter content (fig. 6; table 1).

The FIB SEM–observed pore volume in the New Albany is the second lowest, just above the Mount Simon mudstone (table 3). Effective porosity in the New Albany, however, is the second highest, just below the Maquoketa. The MICP-measured median pore throat is 8.9 nm (table 3). The MICP-measured threshold entry pressure is comparable to that of the Eau Claire (table 3). Much of the pore space in the New Albany is observed to be within close proximity to or inside organic material (fig. 6) forming predominantly slit-shaped pores. At the IBDP site location, the New Albany–calculated organic matter transformation ratio is approximately 0.60–0.65. This indicates that some oil and gas generation has occurred, as noted by D. C. Willette. Thus, porosity generation in the New Albany is likely related to the volume change of organic material during oil/gas generation. Organoporosity development can occur in both organic macerals and generated bitumen as incipient petroleum generation occurs. Under lower maturity levels, pore network development occurs as a volume change (loss) in organic macerals and in void-filling solid bitumen (Valentine et al. 2021). While the definition of bitumen and residual oil can be problematic, it is recognized that the first phase of petroleum maturation from kerogen involves the generation of bitumen (Lewan and Roy 2011). However, no kerogen decomposition in the form of organic matter–hosted pores was observed, which is related to the low maturity of the New Albany Shale formation (Lewan et al. 2002). Higher maturity generally leads to an increase in organic matter–hosted porosity (Klaver et al. 2016), with spherical to sponge-like pore structures (Misch et al. 2019). The organic material observed by FIB SEM forms large interconnected networks. Flow texture, the location of pores, and general appearance are similar to findings of Cardott et al. (2015) for postoil solid bitumen residues of a Woodford Shale sample with low thermal maturity. However, an exact determination of the type of organic matter was not part of this study. Therefore, a precise distinction between the various types of solid kerogen and bitumen remains speculative. Pore space is dominantly elongated linear space parallel to bedding and directly adjacent to organic material, further suggesting pore space generated during the kerogen volume change to bitumen. The elevated total organic content throughout the sample and the direct relationship of organic macerals and pore space likely result

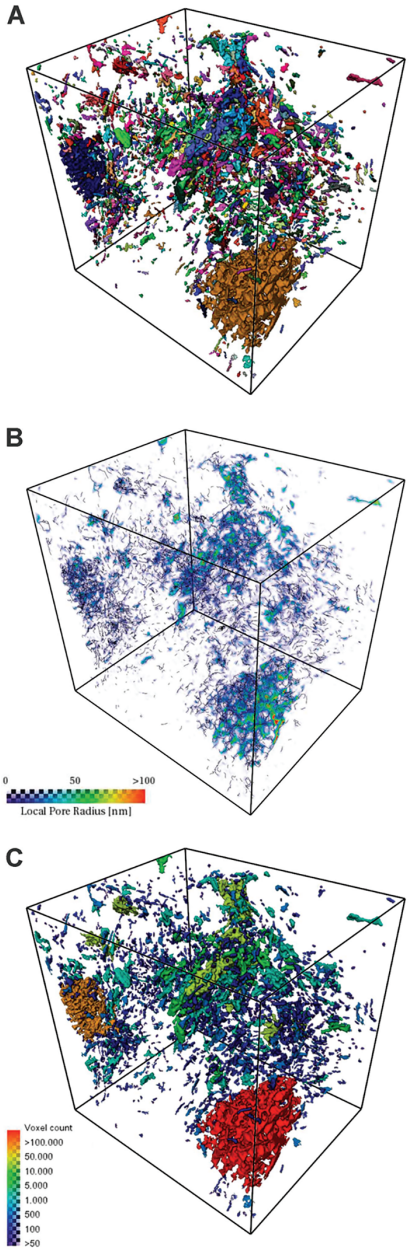

Figure 8. Images of Maquoketa pore space segmentations obtained from focused ion beam scanning electron microscopy. *A*, Pore clusters individually colored to show the connectivity of face, side, or edge (pores with <50 voxels are not shown). *B*, Pore space colored to represent individual pore radii (all voxels are shown, with smallest radii shown as slightly translucent). *C*, Pores colored to show the quantity of voxels in connected pore networks.

in the high effective porosity or pore connectivity observed in the sample (table 3).

Seal Capacity. Internal mudstones within the Mount Simon—as well as the Eau Claire Shale, Maquoketa Shale, and New Albany Shale—are considered confining units to vertical CO_2 migration from the Mount Simon storage reservoir at the IBDP. As is the case with sandstones, the mineralogy and diagenetic alteration of shales can vary both vertically and horizontally within a few feet in the subsurface. This will induce rock properties such as porosity and permeability to fluctuate, sometimes by a couple of orders of magnitude. This will also affect the interpretation of MICP analytical results, as in the case of VW1, where one sample from each potential sealing formation was selected as representative.

A range of permeability values for each seal interval were calculated using temperature, pressure, and density values determined from the VW1 well data. Table 4 lists the calculated brine density (ρ_f) and $scCO_2$ density (ρ_{scCO_2}) of Mount Simon mudstone ($\rho_f = 1.15 g/cm^3$ and $\rho_{scCO_2} = 0.78 g/cm^3$), Eau Claire Shale ($\rho_f = 1.10 g/cm^3$ and $\rho_{scCO_2} = 0.74 g/cm^3$), and Maquoketa Shale ($\rho_f = 1.10 g/cm^3$ and $\rho_{scCO_2} = 0.64 g/cm^3$). Comparison of the New Albany Shale is not possible using this formulation because the formation temperature and pressures of CO_2 were in the gas phase instead of sc.

Theoretical $scCO_2$ column heights across a range of permeabilities were determined for the Mount Simon mudstone and Eau Claire Shale (fig. 9). An almost identical correspondence of values was calculated between the two intervals, with deviations of column heights ranging between 20 and 200 feet (6–61 m). However, estimates derived for the Maquoketa indicate column heights ranging between 100 and 800 feet (30.5–244 m) lower than the other two shale intervals. This is due to the lower $scCO_2$ density at the Maquoketa interface and lower threshold pressures. In addition, the FIB SEM and MICP data indicate that the Maquoketa contains the largest pore volume and lowest air/brine threshold pressure relative to the other two intervals. Therefore, the sealing capacity for CO_2 migration, while still possible, is less than that for the Mount Simon mudstone and Eau Claire Shale.

Theoretical sealing capacity estimates shown in figure 9 indicate that the Mount Simon mudstone and Eau Claire Shale will hold $scCO_2$ column heights at least one to two orders of magnitude in excess of reservoir thickness. Seal permeabilities between 0.02 and 0.0001 md may hold a $scCO_2$ column between approximately 1000 and 10,000 feet (305–3048 m). In contrast, the Maquoketa Shale (for a

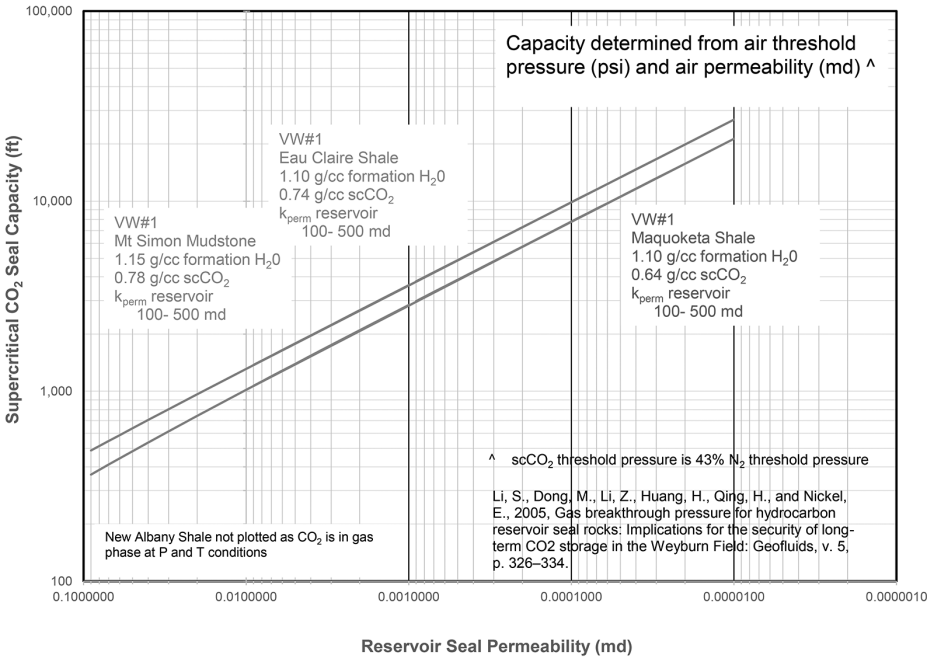

Figure 9. Approximation of seal capacity for the Mount Simon mudstone, Eau Claire Shale, and Maquoketa Shale using permeability as the major variable (after Li et al. 2005). k_{perm} = permeability; P = pressure; T = temperature; VW#1 = Verification Well 1. A color version of this figure is available online.

similar range of permeabilities) may hold between 750 and 8000 feet (229–2438 m) of $scCO_2$. These are theoretical estimates that will be compared to point-source MICP analyses. It is important to note that MICP analytical results constrain only a snapshot of a limited petrophysical representation of the seal interval.

Column height calculations from point-specific MICP calculations are at least an order of magnitude less than the theoretical calculations spanning ranges of permeability values. Table 5 lists the ranges for column heights calculated for all seal samples in which MICP analyses were run. Similar to the first approximation results, the seal capacities of the Mount Simon mudstone and Eau Claire Shale seals support the largest columns relative to the other shale intervals. The Mount Simon mudstone may support columns ranging between 2587

Table 5. Calculated Minimum, Sample Value, and Maximum Supercritical CO_2 Column Heights Relative to Seal Capacity Based on Mercury Intrusion Capillary Pressure Analyses of One Sample from the Mount Simon Mudstone, Eau Claire Shale, Maquoketa Shale, and New Albany Shale

	CA = 0° (feet [m])			CA = 20° (feet [m])			CA = 40° (feet [m])			CA = 60° (feet [m])		
Formation	Min	Sample	Max	Min	Sample	Max	Min	Sample	Max	Min	Sample	Max
Mount Simon mudstone	2587 (788)	3235 (986)	3883 (1183)	2431 (741)	3040 (927)	3649 (1112)	1982 (604)	2478 (755)	2974 (906)	1294 (394)	1617 (493)	1941 (592)
Eau Claire Shale	219 (67)	275 (84)	331 (101)	206 (63)	258 (79)	311 (95)	168 (51)	211 (64)	253 (77)	110 (34)	138 (42)	165 (50)
Maquoketa Shale	110 (34)	139 (42)	167 (51)	104 (32)	130 (40)	157 (48)	85 (26)	106 (32)	128 (39)	55 (17)	69 (21)	84 (26)
New Albany Shale[a]	166 (51)	209 (64)	251 (77)	156 (48)	196 (60)	236 (72)	127 (39)	160 (49)	192 (59)	83 (25)	104 (32)	125 (38)

Note. The variability of the column heights was calculated using a range of contact angles (CAs) and threshold pressures (20% variability relative to sample value).
[a] Column heights for the New Albany Shale are an approximation. At formation temperature and pressure, CO_2 will be in the vapor phase.

and 3883 feet (788–1183 m) using a contact angle of 0°, which is approximately one order of magnitude larger than column heights calculated for the Eau Claire Shale. As the table indicates, larger contact angles of the $scCO_2$/water/rock interface result in diminished seal column capacity. In general, as the contact angle increases to 60°, the amount of column the seal can seal before breakthrough is reduced by approximately one-half. Since the pressure at sample depths for the Mount Simon and Eau Claire ranges between 14 and 19 mPa (2064–2753 psi), it is likely that a contact angle between 20° and 40° is reasonable. Therefore, the calculated minimum seal capacity could range between 1982 and 2431 feet (604–741 m) for the Mount Simon mudstone and 168 and 206 feet (51–63 m) for the Eau Claire Shale. These estimates of seal capacity exceed total reservoir interval thicknesses within the Mount Simon.

Of the sampled intervals, the Maquoketa Shale has the lowest calculated seal capacity relative to $scCO_2$ (table 5). This is also the case using the theoretical calculations depicted in figure 9. On the basis of the mineral characterization and pore network modeling described above, this result is consistent with the seal providing a lower seal capacity relative to $scCO_2$. It should be noted that the Maquoketa Shale and New Albany Shale are considered nonprimary seals and that there are no reservoirs of note (rocks with elevated porosity and permeability) directly beneath the seals. In the case of the New Albany Shale, because of formation pressures and temperatures, any CO_2 present would be in the vapor phase. For these reasons, column heights calculated for these intervals are approximations and should be considered preliminary.

Conclusion

The three major seals overlying the Mount Simon Sandstone CCS reservoir, as well as an internal confining unit in the reservoir, are highly heterogeneous with respect to mineralogy and thus have very different pore networks and varied permeabilities that must be considered when evaluating a site for geologic CCS. MICP threshold pressure results, theoretical calculations based on a range of permeabilities, and column height calculations confirm this observation and indicate that all samples analyzed will provide a seal with variable sealing capacity for an underlying reservoir.

1. The Eau Claire sample is the best confining unit. The Eau Claire has the lowest effective porosity despite its median pore throat being higher and fluid/gas entry pressure being lower than those of the New Albany. This slightly lower entry pressure may be the result of more abundant pore volume in Eau Claire than in the New Albany.

2. The New Albany sample is the second-best seal on the basis of membrane capillary forces. It has the second-highest effective porosity and the highest fluid/gas entry pressure. It has the smallest reported median pore throat size (MICP), the lowest shale porosity according to FIB SEM analysis, and the smallest overall pore volume. It is considered a secondary seal at the IBDP location because of its vertical distance from the primary CO_2 reservoir. However, at reservoir pressures and temperatures, CO_2 will be in the vapor phase, not sc. Therefore, estimates of sealing efficacy and capacity are approximations.

3. The Maquoketa sample is ranked last of the three samples. It has the highest effective porosity and the lowest fluid/gas entry pressure. The Maquoketa has the second-largest pore throat size and the broadest range of pore sizes. Analyses indicate that the Maquoketa has the highest pore connectivity of all samples analyzed (FIB SEM), largely a result of connected pore throats in framboids and perhaps to a lesser extent the abundance of rigid carbonate grains within the sample preserving the pore volume.

4. The mudstone internal to the Mount Simon reservoir exhibits the best sealing properties relative to all the samples analyzed. However, the interval is not ranked or considered a major seal because of its lack of lateral continuity. Despite this, the mudstone is an excellent baffle and should prevent any localized vertical CO_2/fluid migration. The mudstone has exponentially lower effective porosity (MICP) as well as entry pressure relative to the other samples. Although the FIB SEM porosity is similar to that of the Eau Claire and New Albany, the median pore range is smaller than that of all samples. The mudstone also exhibits the smallest pore volume of all samples analyzed.

5. Point-specific MICP threshold pressure results, theoretical calculations based on a range of permeabilities, and column height calculations indicate that the Mount Simon mudstones and Eau Claire Shale are effective seals of $scCO_2$ in the Mount Simon reservoir. As the mudstones are laterally discontinuous, they should be considered baffles (where present) for $scCO_2$ migration. The Maquoketa Shale and New Albany Shale seals are considered nonprimary seals and will provide additional sealing capacity. However, column height calculations are considered approximations since a porous reservoir for CO_2 migration is absent beneath the formations, and in the case of the New

Albany Shale, reservoir conditions indicate that CO_2 will exist in the vapor phase.

6. Last, a variety of methodologies are beneficial when evaluating confining units. Petrographic examinations of thin sections, including QEMSCAN, are useful for determining mineral distribution and textural results but yield qualitative mineralogy. Quantitative mineralogy, including accurate qualitative clay mineralogy, is resolved with XRD, while trace components can be reliably identified by QEMSCAN. Textural analysis, including matrix and pore space evaluation, is further supported by FIB SEM, which yields higher-resolution data than QEMSCAN in a 3D aspect. Evaluation of effective pore space is complemented by MICP. Together, these methods provide interrelated nano- to centimeter-scale information that improves our understanding of the integrity of a variety of confining units.

ACKNOWLEDGMENTS

We greatly appreciate the reviewer's constructive comments, which greatly improved this article. This research was supported by the Midwest Geological Sequestration Consortium, which is funded by the US Department of Energy through the National Energy Technology Laboratory via the Regional Carbon Sequestration Partnership program (contract DE-FC26-05NT42588) and by a cost share agreement with the Illinois Department of Commerce and Economic Opportunity and the Office of Coal Development through the Illinois Clean Coal Institute.

REFERENCES CITED

Aswasereelert, W.; Simo, J. A.; and LePain, D. L. 2008. Deposition of the Cambrian Eau Claire Formation, Wisconsin: hydrostratigraphic implications of fine-grained cratonic sandstones. Geosci. Wis. 19(1): 1–21.

Bachu, S.; Bonijoly, D.; Bradshaw, J.; Burruss, R.; Holloway, S.; Christensen, N. P.; and Mathiassen, O. M. 2007. CO_2 storage capacity estimation: methodology and gaps. Int. J. Greenh. Gas Control 1(4):430–443.

Barrows, M. H., and Cluff, R. M. 1984. New Albany Shale Group (Devonian-Mississippian) source rocks and hydrocarbon generation in the Illinois Basin. *In* Demaison, G., and Murris, R. J., eds. Petroleum geochemistry and basin evaluation. Am. Assoc. Pet. Geol. Mem. 35:111–138.

Benson, S. M., and Cole, D. R. 2008. CO_2 sequestration in deep sedimentary formations. Elements 4(5):325–331.

Bickford, M. E.; Van, W. R.; and Zietz, I. 1986. Proterozoic history of the midcontinent region of North America. Geology 14(6):492–496.

Carroll, S. A.; McNab, W. W.; Dai, Z.; and Torres, S. C. 2012. Reactivity of Mount Simon sandstone and the Eau Claire Shale under CO_2 storage conditions. Environ. Sci. Technol. 47(1):252–261.

Cardott, B. J.; Landis, C. R.; and Curtis, M. E. 2015. Post-oil solid bitumen network in the Woodford Shale, USA: a potential primary migration pathway. Int. J. Coal Geol. 139(1):106–113. https://doi.org/10.1016/j.coal.2014.08.012.

Ciotta, M.; Peyerl, D.; Barrozo, L.; Anna, L. S.; dos Santos, E. M.; Bermann, C.; Grohmann, C.; Moretto, E. M.; and Tassinari, C. 2020. An overview of carbon capture and storage atlases around the world. Environ. Geosci. 27(1):1–8.

Cluff, R. M.; Reinbold, M. L.; and Lineback, J. A. 1981. New Albany Shale Group of Illinois. Ill. State Geol. Surv. Circ. 518.

Damiani, D. 2020. Safe geologic storage of captured carbon dioxide: two decades of DOE's carbon storage R&D program in review. Washington, DC, US Department of Energy Office of Fossil Energy. https://www.osti.gov/servlets/purl/1779871.

Daniel, R. F., and Kaldi, J. G. 2008. Evaluating seal capacity of caprocks and intraformational barriers for the geosequestration of CO_2. *In* Petroleum Exploration Society of Australia Eastern Australian Basin Symposium, 3rd (Sydney, 2008), p. 475–484.

Dewhurst, D. N.; Jones, R. M.; and Raven, M. D. 2002. Microstructural and petrophysical characterization of Muderong Shale: application to top seal risking. Pet. Geosci. 8:371–383.

Doebelin, N., and Kleeberg, R. 2015. Profex: a graphical user interface for the Rietveld refinement program BGMN. J. Appl. Crystallogr. 48(5):1573–1580.

Espinoza, D. N., and Santamarina, J. C. 2010. Water-CO_2 mineral systems: interfacial tension, contact angle, and diffusion: implications to CO_2 geological storage. Water Resour. Res. 46:WO7537.

Finley, R. J. 2014. An overview of the Illinois Basin–Decatur Project. Greenh. Gases 4(5):571–579.

Freiburg, J. T.; Holland, M. E.; Malone, D. H.; and Malone, S. J. 2020*a*. Detrital zircon geochronology of basal Cambrian strata in the deep Illinois Basin, USA: evidence for the Paleoproterozoic–Cambrian tectonic and sedimentary evolution of central Laurentia. J. Geol. 128(3):303–317.

Freiburg, J. T., and Leetaru, H. E. 2012. Controls on porosity development and the potential for CO_2 sequestration or wastewater disposal in the Cambrian Potosi Dolomite (Knox Group): Illinois Basin. *In* Annual Eastern Section American Association of Petroleum Geologists Meeting, 41st (Cleveland, 2012).

Freiburg, J. T.; McBride, J. H.; Malone, D. H.; and Leetaru, H. E. 2020*b*. Petrology, geochronology, and geophysical

characterization of Mesoproterozoic rocks in central Illinois, USA. Geosci. Front. 11(2):581–596.

Freiburg, J. T.; Morse, D. G.; Leetaru, H. E.; Hoss, R. P.; and Yan, Q. 2014. A depositional and diagenetic characterization of the Mt. Simon Sandstone at the Illinois Basin–Decatur Project carbon capture and storage site, Decatur, Illinois, USA. Ill. State Geol. Surv. Circ. 583.

Freiburg, J. T.; Ritzi, R. W.; and Kehoe, K. S. 2016. Depositional and diagenetic controls on anomalously high porosity within a deeply buried CO_2 storage reservoir—the Cambrian Mt. Simon Sandstone, Illinois Basin, USA. Int. J. Greenh. Gas Control 55:42–54.

Friedmann, S. J. 2007. Geological carbon dioxide sequestration. Elements 3(3):179–184.

Grathoff, G. H.; Moore, D. M.; Hay, R. L.; and Wemmer, K. 2001. Origin of illite in the lower Paleozoic of the Illinois Basin: evidence for brine migrations. Geol. Soc. Am. Bull. 113(8):1092–1104.

Higley, D. K.; Henry, M. E.; Lewan, M. D.; and Pitman, J. K. 2003. The New Albany Shale petroleum system, Illinois Basin: data and map image archive from the material-balance assessment. U.S. Geol. Surv. Open-File Rep. 2003-37.

Holloway, S. 2001. Storage of fossil fuel-derived carbon dioxide beneath the surface of the Earth. Annu. Rev. Energy Environ. 26(1):145–166.

Kaufhold, S.; Dohrmann, R. B.; Ufer, K.; and Meyer, F. M. 2002. Comparison of methods for the quantification of montmorillonite in bentonites. Appl. Clay Sci. 22(3): 145–151.

Klaver, J.; Desbois, G.; Littke, R.; and Urai, J. L. 2016. BIB-SEM pore characterization of mature and post mature Posidonia Shale samples from the Hils area, Germany. Int. J. Coal Geol. 158:78–89.

Koide, H.; Tazaki, Y.; Noguchi, Y.; Nakayama, S.; Iijima, M.; Ito, K.; and Shindo, Y. 1992. Subterranean containment and long-term storage of carbon dioxide in unused aquifers and in depleted natural gas reservoirs. Energy Convers. Manag. 33(5–8):619–626.

Kolata, D. R., and Graese, A. M. 1983. Lithostratigraphy and depositional environments of the Maquoketa Group (Ordovician) in northern Illinois. Ill. State Geol. Surv. Circ. 528.

Konstantinou, A.; Wirth, K. R.; Vervoort, J. D.; Malone, D. H.; Davidson, C.; and Craddock, J. P. 2014. Provenance of quartz arenites of the early Paleozoic midcontinent region, USA. J. Geol. 122(2):201–216.

Lackner, K. S., and Brennan, S. 2009. Envisioning carbon capture and storage: expanded possibilities due to air capture, leakage insurance, and C-14 monitoring. Clim. Change 96(3):357–378.

Lahann, R.; Mastalerz, M.; Rupp, J. A.; and Drobniak, A. 2013. Influence of CO_2 on New Albany Shale composition and pore structure. Int. J. Coal Geol. 108:2–9.

Lahann, R.; Rupp, J.; and Medina, C. 2014. An evaluation of the seal capacity and CO_2 retention properties of the Eau Claire Formation (Cambrian). Environ. Geosci. 21(3):83–106.

Leetaru, H. 2014. Maquoketa shale caprock integrity evaluation. DOE/FE002068-9. Washington, DC, US Department of Energy.

Leetaru, H.; Brown, A.; Lee, D.; Senel, O.; and Coueslan, M. 2012. CO_2 injectivity, storage capacity, plume size, and reservoir and seal integrity of the Ordovician St. Peter Sandstone and the Cambrian Potosi Formation in the Illinois Basin. DOE/FE0002068-1. Washington, DC, US Department of Energy.

Leetaru, H.; Morse, D. G.; Bauer, R.; Frailey, S.; Keefer, D.; Kolata, D.; Korose, C.; et al. 2005. Saline reservoirs as a sequestration target. *In* Finley, R., ed. An assessment of geological carbon sequestration options in the Illinois Basin. DE-FC26-03NT41994. Washington, DC, US Department of Energy, p. 253–324.

Lewan, M. D.; Henry, M. E.; Higley, D. K.; and Pitman, J. K. 2002. Material-balance assessment of the New Albany–Chesterian petroleum system of the Illinois Basin. Am. Assoc. Pet. Geol. Bull. 86(5):745–778.

Lewan, M. D., and Roy, S. 2011. Role of water in hydrocarbon generation from type-I kerogen in Mahogany oil shale of the Green River Formation. Org. Geochem. 42(1):31–41.

Li, S.; Dong, M.; Li, Z.; Huang, H.; Qing, H.; and Nickel, E. 2005. Gas breakthrough pressure for hydrocarbon reservoir seal rocks: implications for the security of long-term CO_2 storage in the Weyburn Field. Geofluids 5:326–334.

Liu, F.; Ellett, K.; Xiao, Y.; and Rupp, J. A. 2013. Assessing the feasibility of CO_2 storage in the New Albany Shale (Devonian-Mississippian) with potential enhanced gas recovery using reservoir simulation. Int. J. Greenh. Gas Control 17:111–126.

Liu, F.; Lu, P.; Griffith, C.; Hedges, S. W.; Soong, Y.; Hellevang, H.; and Zhu, C. 2012. CO_2-brine-caprock interaction: reactivity experiments on Eau Claire Shale and a review of relevant literature. Int. J. Greenh. Gas Control 7:153–167.

Loucks, R. G.; Reed, R. M.; Ruppel, S. C.; and Hammes, U. 2012. Spectrum of pore types and networks in mudrocks and a descriptive classification for matrix-related mudrock pores. Am. Assoc. Pet. Geol. Bull. 96(6):1071–1098.

Martin-Roberts, E.; Scott, V.; Flude, S.; Johnson, G.; Haszeldine, R. S.; and Gilfillan, S. 2021. Carbon capture and storage at the end of a lost decade. One Earth 4(11):1569–1584.

Mastalerz, M.; Schimmelmann, A.; Drobniak, A.; and Chen, Y. 2013. Porosity of Devonian and Mississippian New Albany Shale across a maturation gradient: insights from organic petrology, gas adsorption, and mercury intrusion. Am. Assoc. Pet. Geol. Bull. 97(10):1621–1643.

Medina, C. R.; Mastalerz, M.; Lahann, R. W.; and Rupp, J. A. 2020. A novel multi-technique approach used in the petrophysical characterization of the Maquoketa Group (Ordovician) in the southeastern portion of the Illinois Basin: implications for seal efficiency for the geologic sequestration of CO_2. Int. J. Greenh. Gas Control 93:102883.

Misch, D.; Gross, D.; Hawranek, G.; Horsfield, B.; Klaver, J.; Mendez-Martin, F.; Urai, J. L.; et al. 2019. Solid bitumen in shales: petrographic characteristics and implications for reservoir characterization. Int. J. Coal Geol. 205:14–31. https://doi.org/10.1016/j.coal.2019.02.012.

Mozley, P. S.; Heath, J. E.; Dewers, T. A.; and Bauer, S. J. 2016. Origin and heterogeneity of pore sizes in the Mount Simon Sandstone and Eau Claire Formation: implications for multiphase fluid flow. Geosphere 12(4):1341–1361.

Münch, B., and Holzer, L. 2008. Contradicting geometrical concepts in pore size analysis attained with electron microscopy and mercury intrusion. J. Am. Ceram. Soc. 91(12):4059–4067.

Neufelder, R. J.; Bowen, B. B.; Lahann, R. W.; and Rupp, J. A. 2012. Lithologic, mineralogical, and petrophysical characteristics of the Eau Claire Formation: complexities of a carbon storage system seal. Environ. Geosci. 19(3):81–104.

Nuttall, B. C.; Drahovzal, J. A.; Eble, C. F.; and Bustin, R. M. 2009. Regional assessment of suitability of organic-rich gas shales for carbon sequestration: an example from the Devonian shales of the Illinois and Appalachian Basins, Kentucky. *In* Grobe, M.; Pashin, J. C.; and Dodge, R. L., eds. Carbon dioxide sequestration in geological media—state of the science. Am. Assoc. Pet. Geol. Stud. Geol. 59:173–190.

Oelkers, E. H., and Cole, D. R. 2008. Carbon dioxide sequestration: a solution to a global problem. Elements 4(5):305–310.

Pacala, S., and Socolow, R. 2004. Stabilization wedges: solving the climate problem for the next 50 years with current technologies. Science 305(5686):968–972.

Palkovic, M. J. 2015. Depositional characterization of the Eau Claire Formation at the Illinois Basin–Decatur Project: facies, mineralogy, and geochemistry. MS thesis, University of Illinois, Champaign.

Partin, T. 2004. Demand for high price spurs a new era of drilling for New Albany Shale gas wells in Harrison County, Indiana. *In* Schieber, J., and R. Lazer, eds. Devonian black shales of the eastern US: new insights into sedimentology and stratigraphy from the subsurface and outcrops in the Illinois and Appalachian Basins. Indiana Geol. Surv. Open-File Stud. 04-05.

Rackley, S. A. 2017. Carbon capture and storage. Amsterdam, Butterworth-Heinemann.

Reesink, A. J. H.; Best, J.; Freiburg, J. T.; Webb, N. D.; Monson, C. C.; and Ritzi, R. W. 2020. Interpreting prevegetation landscape dynamics: the Cambrian Lower Mount Simon Sandstone, Illinois, USA. J. Sediment. Res. 90(11):1614–1641.

Rokosh, C. D.; Anderson, S. D. A.; and Pawlowicz, J. G. 2016. QEMSCAN analysis of various lithologies from tight- and shale-gas plays in Alberta. Alberta Energy Regul./Alberta Geol. Surv. Spec. Rep. 99.

Sargent, M. L. 1991. Sauk sequence: Cambrian system through lower Ordovician series. *In* Leighton, M. W.; Kolata, D. R.; Oltz, D. F.; and Eidel, J. J., eds. Interior cratonic basins. Tulsa, OK, Am. Assoc. Pet. Geol. Mem. 51:75–86.

Sarmadivaleh, A.; Al-Yaseri, Z.; and Iglauer, S. 2015. Influence of temperature and pressure on quartz-water-CO_2 contact angle and CO_2-water interfacial tension. J. Colloid Interface Sci. 441:59–64.

Schieber, J. 2010. Common themes in the formation and preservation of intrinsic porosity in shales and mudstones—illustrated with examples across the Phanerozoic. *In* SPE Unconventional Gas Conference (Pittsburgh, 2010). Richardson, TX, Soc. Pet. Eng.

Schowalter, T. T. 1979. Mechanics of secondary hydrocarbon migration and entrapment. Am. Assoc. Pet. Geol. Bull. 63:723–760.

Senel, O.; Will, R.; and Butsch, R. J. 2014. Integrated reservoir modeling at the Illinois Basin–Decatur Project. Greenh. Gases 4(5):662–684.

Strapoc, D.; Mastalerz, M.; Schimmelmann, A.; Drobniak, A.; and Hasenmueller, N. R. 2010. Geochemical constraints on the origin and volume of gas in the New Albany Shale (Devonian-Mississippian), eastern Illinois Basin. Am. Assoc. Pet. Geol. Bull. 94(11):1713–1740.

Valentine, B. J.; Hackley, P. C.; and Hatcherian, J. J. 2021. Hydrous pyrolysis of New Albany Shale: a study examining maturation changes and porosity development. Mar. Pet. Geol. 134:105368.

Warr, L. N. 2021. IMA-CNMNC approved mineral symbols. Mineral. Mag. 85:291–320.

Willman, H. B.; Atherton, E.; Buschbach, T. C.; Collinson, C. W.; Frye, J. C.; Hopkins, M. E.; Lineback, J. A.; and Simon, J. A. 1975. Handbook of Illinois stratigraphy. Ill. State Geol. Surv. Bull. 95.

Yawar, Z., and Schieber, J. 2008. Facies and depositional settings of Eau Claire Formation (Cambrian) mudstones in northwestern Indiana. Geol. Soc. Am. Abstr. Program. 40:A433.

Yoksoulian, L. E.; Freiburg, J. T.; Butler, S. K.; Berger, P. M.; and Roy, W. R. 2013. Mineralogical alterations during laboratory-scale carbon sequestration experiments for the Illinois Basin. Energy Proced. 37:5601–5611.

5.3 Further publications

- Grathoff, G.H., **Peltz, M.**, Enzmann, F. and Kaufhold, S. (2016): Porosity and permeability determination of organic-rich Posidonia shales based on 3-D analyses by FIB-SEM microscopy. *Solid Earth*, 7, 1145-1156.

  DOI: 10.5194/se-7-1145-2016

- Gussone, N., Böttcher, M.E., Conrad, A., Fiebig, J., **Peltz, M.**, Grathoff, G.H. and Schmidt, B. (2020): Calcium isotope fractionation upon experimental apatite formation. *Chemical Geology*. 551, 119737.

  DOI: 10.1016/j.chemgeo.2020.119737

- Warr, L.N., Podlech, C., Kandler, J. and **Peltz, M.** (2020): Developing buoyant and biocompatible nanoclays for the removal of hydrocarbon pollution from aqueous systems. *Applied Clay Science*, 201, 105917.

  DOI: 10.1016/j.clay.2020.105917

- Podlech, C., Matschiavelli, N., **Peltz, M.**, Kluge, S., Arnold, T., Cherkouk, A., Meleshyn, A., Grathoff, G.H and Warr, L.N. (2021): Bentonite Alteration in Batch Reactor Experiments with and without Organic Supplements: Implications for the Disposal of Radioactive Waste. *Minerals*, 11, 932.

  DOI: 10.3390/min11090932

5.4 Conference contributions

- **Peltz, M.**, Grathoff, G.H., Warr, L.N. and Obst, K. (2015): The influence of CO_2-charged brine on mineralogy and pore space of caprocks: An XRD and FIB-SEM study on Toarcian claystones. *GeoBerlin 2015*, Berlin, Germany. Poster

- **Peltz, M.**, Grathoff, G.H., Enzmann, F. and Kaufhold, S. (2017): Permeability anisotropy determined from 3D nano-scale pore structures of organic-rich shales *Interpore 2017*, Rotterdam, Netherlands. Presentation

- **Peltz, M.**, Jacob, A., Hale, S., Blum, P., Enzmann, F., Warr, L.N. and Grathoff, G.H. (2019): Influence of sub-micrometer porosity on permeability of Rotliegend sandstones. *Interpore 2019*, Valencia, Spain. Pitch presentation

- **Peltz, M.**, Hale, S., Grathoff, G.H., Blum, P., and Warr, L.N. (2022): Illite morphologies in aeolian Rotliegend sandstones: insights into the stability and clogging of particles during high-pressure flow-through experiments. *Mid European Clay Conference 2022*, Kliczkow, Poland. Presentation

Acknowledgements

Mein größter Dank gilt meinem Betreuer Prof. Laurence Warr, der mir die Möglichkeit zur Erstellung dieser Arbeit bot und mich stets und ständig unterstützte und motivierte.

Weiterhin möchte ich mich bei meinem Kollegen Georg Grathoff bedanken, welcher schon während meines Studiums alle Hebel in Bewegung setzte, um Kontakte herzustellen und neue Projekte zu planen. Ohne sein Engagement wäre es nicht zu meiner Arbeit im ResKin-Projekt gekommen.

Mein Dank gilt weiterhin allen Kolleginnen und Kollegen, mit denen ich während ResKin und ResKin_Move zusammenarbeiten durfte. Ich danke Sina Hale, Arne Jacob, Marcel Reinhardt, Prof. Philipp Blum, Cornelius Fischer, Ricarda Rohlfs, Prof. Andreas Lüttge, Marcos Toro, Torben Prill, Prof. Oleg Iliev und allen die ich vergessen habe. Mein ausdrücklicher Dank gilt zudem der Mainzer Gruppe um Prof. Michael Kersten und Prof. Frieder Enzmann für die Einführung in Porenraumsimulationen und die Einladung zur Synchrotronstrahlzeit am DESY. Dem Bundesministerium für Bildung und Forschung danke ich für die finanzielle Förderung der Projekte ResKin und ResKin_Move, die die Forschungen im Rahmen dieser Arbeit ermöglichten.

Weiterer Dank gilt den Kolleginnen und Kollegen vom Institut für Geographie und Geologie der Uni Greifswald, die mich im Laufe der Zeit auf die ein oder andere Art unterstützten, insbesondere Robert Mrotzek, Silvia Weinert, Mike Steinich, Sebastian Lorenz und Prof. Michael Böttcher. Außerdem danke ich meinen HiWis Yerko, Jacqueline und Tobias. Weiterer Dank gilt Jared Freiburg vom Illinois State Geological Survey.

Meiner Familie gilt besonderer Dank, da sie mir zu jeder Zeit ihre volle Unterstützung und den nötigen Rückhalt boten, um mich ganz auf meine Arbeit zu konzentrieren. Danke Hubi, Mutti, Lene und Lykke! Tiefer Dank gilt weiterhin meinem Bruder Christian, welcher mir stets ein Vorbild ist, und mich jederzeit sowohl mental als auch wissenschaftlich unterstützte.

Meine tiefste Dankbarkeit gilt der wichtigsten Person in meinem Leben, meiner Freundin Carolin. Danke für deine Unterstützung, deinen Rückhalt, deine Geborgenheit und Liebe, die mir stets halfen weiter zu machen, auch wenn der Akku längst leer war.